Deliverable Report D1.42

Methodology for Feed-Forward Control Strategies using Nacelle or Blade Based Sensors and Distributed Control

Agreement n.:	308974
Duration	November 2012 – October 2017
Co-ordinator:	DTU Wind

The research leading to these results has received funding from the European Community's Seventh Framework Programme FP7-ENERGY-2012-1-2STAGE under grant agreement No. 308974 (INNWIND.EU)

Document information

Document Name:	D1.42 Methodology for feed-forward control strategies using nacelle or blade based sensors and distributed control
Document Number:	Deliverable D 1.42
Author:	Mikel Iribas – CENER Morten H. Hansen, Mahmood Mirzaei, Carlo Tibaldi, Anand Natarajan – DTU Ervin Bossanyi – DNV-GL Adam Stock, Peter Jamieson, William Leithead – Univ. of Strathclyde, David Schlipf - Univ. of Stuttgart
Document Type	Report
Dissemination level	PU
Review:	Anand Natarajan
Date:	Aug 30, 2015
WP:	1
Task:	4
Approval:	Approved by Project Coordinator

Table of Contents

1.0 Overview of State of the art in LIDAR assisted control

Recent developments in LIDAR technology have led to much interest in the possibility of improving wind turbine control by making use of a turbine-mounted LIDAR system to sense the approaching wind field before it reaches the turbine, providing preview information which might help the controller to improve turbine performance. The principle motivation is the potential for increased energy capture, and reduced turbine loading leading to lower capital and operating costs and increased lifetime. The changed relationship between energy capture and loading implies a potential for re-optimisation of the wind turbine design in an integrated design process leading to lower levelised cost of energy (LCoE).

However, such a reduction in LCoE depends on the capital cost of the LIDAR being low enough to be outweighed by the value of the potential benefits. Furthermore the LIDAR should not reduce the reliability of the system. This means that the LIDAR equipment itself must be highly reliable, and it also means that the controller should have a strategy to allow the turbine to continue operating and generating power even if the LIDAR signal is degraded or unavailable, whether because of LIDAR malfunction or because of atmospheric conditions causing a poor signal (e.g. because of fog, precipitation, or very clean air with insufficient particles or aerosols to provide a strong enough reflected signal). If the turbine design loads are based on the availability of a functioning LIDAR, continued operation while the LIDAR signal is unavailable may require some de-rating of the turbine to remain within the design load envelope.

LIDAR types and characteristics

The principal commercially-available LIDARs currently under consideration for wind turbine control include both continuous-wave and pulsed devices. The most significant difference between these is that pulsed LIDARs can measure the line-of-sight wind speed at multiple ranges simultaneously through electronic processing of the reflected signal, while the continuous-wave systems can only measure at a single range at any instant, although the range can be changed by inserting or removing optical elements in the beam path electro-mechanically. However, continuous-wave systems are generally capable of higher sampling rates. Both systems can measure only the line-of-sight (LoS) wind speed, i.e. the wind speed component resolved in the beam direction and averaged over some length of the beam.

Most work to date has used nacelle-mounted LIDARs, which for upwind turbines has the disadvantage that the beam is sometimes obscured by a passing blade, and the nacelle structure imposes limitations on LIDAR mounting position to avoid obstruction of the beam by the nacelle itself. Beam obstruction is easily dealt with in the LIDAR signal processing but inevitably reduces signal quality in some sense. This problem is avoided if the LIDAR is mounted in the spinner, although there may be disadvantages in terms of ease of installation and access, vibration, communications etc.

In all cases, the effectiveness of the LIDAR for control enhancement depends in a very significant way on the ability to sample the whole swept area of the rotor; a single fixed beam staring at a single point ahead of the turbine is far less effective than if multiple beams are used, or a single movable beam

scanning the swept area. Circular scanning is easily achieved by means of a rotating prism, and more complex scans can be achieved using two prisms rotating at different speeds, or using movable mirrors. Such scanning requires electro-mechanical components which are liable to reduce reliability and increase maintenance requirements, but can potentially cover more of the swept area to give better estimates of rotor-average wind speed, direction, shear gradients and localised gusts.
Some experiments have also been conducted using short-range blade-mounted LIDARs to detect local inflow just ahead of the blade leading edge. Other possible configurations include the use of three movable LIDAR beams with different origins but all focussing at a single remote point so that the full three-component wind vector can be measured; co-ordinated movements of the three beam angles and measurement ranges can then be used to move the focus point and scan around the swept area.
A different approach is used in one commercial product, using cross-correlation of backscattered light instead of the Doppler shift to detect turbulent structures.

LIDAR applications in turbine control

A number of different ways in which LIDAR could be used to enhance wind turbine control have been proposed:

- As a way to increase energy capture from a given rotor:
  - LIDAR can provide an estimate of wind direction, which may be better than using the traditional nacelle-mounted wind vane(s) and might therefore result in more precise alignment of the nacelle with the wind direction. Since yaw response has to be fairly slow, this application is unlikely to benefit significantly from the preview capability of LIDAR, but only from the substitution of spatial averaging for time averaging leading to better estimation of rotor-average yaw misalignment. Improved yaw control might also reduce some of the asymmetric loading caused by yaw misalignment.
  - LIDAR could be used to improve the ability of the controller to track maximum C_p in below-rated wind conditions. The large rotor inertia prevents the rapid rotor speed changes which may be needed to maintain optimum tip speed ratio, so a preview of approaching wind speed may be used to improve trajectory planning over time horizons of a few seconds, although any significant increase in energy capture might still require large torque variations to drive the rotor accelerations needed to track optimum tip speed ratio, which could drive up fatigue loads and reduce power quality.
  - LIDAR estimation of approaching asymmetry in the wind field, and/or short-range local flow measurements using blade-mounted LIDARs, could be used in below-rated wind speeds to modify the individual pitch angles to optimise angles of attack (and/or the settings of ailerons or other blade-distributed aerodynamic control devices), potentially leading to a small gain in energy capture.
  - In the transition region just below rated wind speed, the fine pitch angle is often increased slightly to minimise rotor thrust variations, at the expense of a small loss of energy capture.

LIDAR wind speed preview could potentially improve the trade-off between energy and loads in this region.

- Similarly, for a turbine design in which high wind speed de-rating is used to reduce loads at the expense of some energy capture, the energy-loads trade-off could potentially be improved.

- As a way to reduce loads:
  - Above or around rated, LIDAR wind speed preview has the potential to allow smoother and better-optimised collective pitch response, improving the trade-off between tightness of speed / power regulation and thrust-related loading. The resulting reduction in tower base fatigue loading could be a very significant benefit.
  - LIDAR measurement estimation of approaching asymmetry in the wind field, and/or short-range local flow measurements using blade-mounted LIDARs, could be used to modify the individual pitch angles to minimise loading caused by differential thrust load variation across the rotor in above-rated wind speeds, enhancing or possibly replacing the conventional individual pitch techniques based on load measurements.
  - Such LIDAR measurements could similarly be used to supplement and/or replace the measurements from load sensors, pressure taps, Pitot tubes etc. which are proposed for controlling distributed aerodynamic devices on 'smart' rotor blades.
  - Some of the measures described above for increasing energy capture might also be used to reduce loading, or at least improve the trade-off between energy and loads.

Further general comments follow on the applications which have been most studied to date.

Yaw control

There is much actual and anecdotal evidence of energy losses due to poor yaw alignment of wind turbines in the field, which has led to claims for large energy gains when LIDAR is used for yaw control. However this poor performance is often only for a small proportion of turbines and yaw control can also work very well, even when only using a nacelle wind vane. It is clearly important to ensure that the yaw system is correctly set up and well-calibrated, and in this case the energy gains from using LIDAR may be rather small at best.

Even with an ideal strategy which achieves perfect yaw misalignment at all times, the maximum available gain in annual energy capture compared to a well-calibrated conventional yaw controller may be less than 1% **Error! Reference source not found.**. Of course this would still be very valuable, but n practice it is unlikely that a LIDAR would achieve much of this benefit, if any, (a) because the LIDAR direction estimation based on LoS measurement is imperfect, and cannot easily distinguish between a wind direction and a horizontal shear gradient, and (b) because the 'ideal' yaw strategy implies fast yawing which is not possible in practice (it would cause excessive gyroscopic and other loads, and prohibitive yaw actuator duty).

However, in practice most poor yaw performance probably comes from poor wind vane calibration. Good calibration is difficult and time-consuming, and may not always be done satisfactorily. It should depend on rotor speed and pitch angle, as the wind vane is behind the rotor 2. Therefore a LIDAR could be a very useful and convenient tool for wind vane calibration during turbine commissioning, and also for re-calibration once poor yaw control has been detected; but it may be difficult to justify the cost of a permanently-mounted LIDAR if it is used only for yaw control, although it could make sense to use it in this way if it is also providing some of the other benefits described here.
Since LIDAR-based yaw control is unlikely to be a key factor in improving the cost-effectiveness of large offshore wind turbines, it is not a focus of the INNWIND.EU project.

Peak C_p tracking

While the LIDAR wind speed preview measurement allows predictive control of generator torque to maintain optimum tip speed ratio, any increase in energy capture is likely to be very small, and achievable only at the expense of huge power and torque excursions needed to accelerate and decelerate the rotor to follow wind speed variations 3. This is therefore not a focus of the INNWIND.EU project.

Collective pitch control

The use of LIDAR for enhanced collective pitch control offers clear scope for reducing significant thrust-related design loads 3, and should certainly be considered within the project. The load reductions should be possible without detriment to energy capture, and may even facilitate some small increase by avoiding compromises which might have been needed, for example in the region close to rated wind speed.

Individual pitch and smart rotor control

Since LIDAR estimates of flow asymmetry are imperfect, and since conventional methods using load sensors are already quite effective, the scope for further reductions in asymmetric rotor loads using LIDAR may be limited [3], especially in the case of smart rotor control where the actuator response is significantly faster than for full-span pitch control and so the benefit of preview is likely to be further reduced.

Fatigue and extreme load reduction

Where LIDAR is used to reduce fatigue loads, it is relatively straightforward to assess the implications. Only the average rate of fatigue damage accumulation over the lifetime is important. Even if the LIDAR is unavailable for some fraction of the time, for whatever reason, this can be taken into account.
It is tempting to think that if fatigue loads are being reduced, there should also be a reduction in extreme operational loads caused by turbulence (as opposed to extreme loads caused by malfunctions, grid loss, non-operational conditions, etc.). However, even if this is true and the extreme loads happen to be design-driving, it may be difficult to take advantage of this in reducing the design load envelope, for a number of reasons as discussed in [3]. One problem is the need to understand the probability of availability of a good LIDAR signal at the moment when the extreme load happens – even if the

probability of unsuitable atmospheric conditions is low, one would have to be sure that such conditions are not highly correlated with the very conditions which might give rise to that extreme wind event. A bigger problem is how to define that extreme wind event itself: current extreme gusts are specified only in terms of changes in speed, direction and shear parameters at the turbine rotor, but if LIDAR preview is used to mitigate the effect of the gust one would also have to specify the spatial structure of the gust and how it moves during the LIDAR look-ahead time. Current gust specifications are already very arbitrary and physically unrealistic, and to extend the specification to include these effects is to stretch credibility still further. One possibility currently being investigated is to generate simulated turbulent wind fields with embedded gusts; but even these models are likely to use Gaussian assumptions which are most likely to break down in extreme conditions.

Algorithms for LIDAR-assisted control

Deliverable D1.41 deals with the processing of LIDAR LoS measurements to provide estimates of those rotor-averaged quantities which may be useful for control enhancement, such as wind speed, direction, horizontal and vertical shear, etc. This section provides a very brief summary of some of the proposed algorithms for using these estimated rotor-averaged quantities to improve control action. Yaw control is not included, because the LIDAR is essentially used as an improved wind vane – preview is of little benefit and so there is little need for new algorithms; although because of the spatial averaging effect of the LIDAR it is certainly possible to use reduced averaging times, if this should prove to be advantageous.

The main emphasis in the literature to date has been on algorithms for using wind speed preview in the pitch controller, and sometimes also in the torque controller.

Perhaps the simplest approach is to use simple feed-forward control, in which the preview wind speed is used with the optimal steady-state operating curve to determine the control action which would be optimum in steady-state terms at the end of the preview period, and then to bias the demands coming from the normal dynamic control algorithm so as to move towards this target. This extremely simple approach has already been shown to work surprisingly well in the case of above-rated collective pitch control. In 4, an additional pitch rate is applied proportional to the rate of change of the preview wind speed, while 3 uses an additional pitch rate demand calculated to achieve the desired change in pitch angle at the end of the preview time. Some promising field test results with these simple algorithms are becoming available, e.g. **Error! Reference source not found.**. The pitch rate demand calculated from he LIDAR preview is capable of improving the rotor speed regulation significantly; the gain of the normal pitch feedback controller which regulates rotor speed can therefore be decreased, and this leads to a significant reduction in thrust-related loading, in particular the tower base overturning moment.

More rigorous feed-forward approaches can also be used; in particular a model-inverse feed-forward controller uses an approximate inverse of the plant model to calculate the pitch action which would lead to the correct plant response given the expected wind speed from the LIDAR preview. Since the plant model is not normally invertible, different methods of deriving an approximate inverse have been investigated 5.

A much more sophisticated approach is possible with model predictive control (MPC) **Error! eference source not found.**. This is particularly well-suited to make use of preview information, including simultaneous previews at different ranges, because the preview information can be fed into

the predicted future behaviour of the system over the prediction horizon. The ability of MPC to take into account constraints such as pitch actuator position, rate and acceleration limits also makes it particularly useful, although the computational expense of such algorithms may be a limiting factor.

The following sections detail the implementation of these different types of control algorithms for the 10 MW INNWIND.EU reference turbine, starting with the traditional collective pitch feedback control. The final section looks at advanced means of control for the 20 MW multi rotor concept that was designed in Task 1.3.

2.0 Offshore wind turbine Control

According to INNWIND.EU project goals, all the development of the controls are based and evaluated on the 10MW reference wind turbine as mounted on a Jacket designed in WP 4.1 and WP 4.3. The controllers that are developed are typical either Fortran or Matlab/Simulink platforms, but the aeroelastic software used for loads prediction are various ranging from HAWC2, Bladed, FAST etc. and therefore the controls modules may need to be replicated in different aeroelastic modules. The Simulink platform has been used wherever possible for ease of portability to connect to different aeroelastic software.

A reasonable set of load cases for evaluating the controller actions on the baseline turbine is made based on the IEC offshore wind turbine standards [8]. This set of load cases is representative enough to evaluate the performance of the Wind Turbine and Control options, with a high degree of detail. These set of load cases includes fatigue load cases, extreme load cases, fail cases, etc. as described in the IEC 61400-3 Ed.1 standard [8]. Also working on the same reference wind turbine definition and load cases is a good starting point. Even more, in order to be able to execute all the proposed load cases, a supervisory controller for the baseline was developed, to make possible the simulations of actuator faults, grid loss, yaw errors, normal stops, emergency stops, etc. The following sections detail upgraded versions of the reference controller, that was developed to mitigate the loads on the components of the reference wind turbine without using advance control techniques such as Individual Pitch Control (IPC) or Lidars. This therefore provides the limit of loads reduction using conventional control techniques.

2.1. DTU Upgraded Baseline Controller for Offshore

The offshore 10 MW turbine which was mounted on a jacket structure had different natural frequencies as compared to the land version of the turbine for which the original reference controlled was designed to and also significantly high fatigue loads. Therefore an upgrade of the baseline controller was undertaken wherein a resonance exclusion zone (to avoid 3p excitation of the support structure), peak thrust shaver and tower top fore-aft damper were added to lower the fatigue loads and better tune the controller to the new structural frequencies. A Simulink based implementation of this upgraded controller compatible with GH Bladed was developed by University of Stuttgart, and validated in cooperation with DTU. The supervisory control therein was developed was developed by CENER, in order to make possible the execution of the event based load cases described.

The controller is only considering low speed shaft (LSS) measures of rotational speeds and torques, i.e., model of gearbox or other details of drivetrain are not considered in this design. The controller still could be used for turbines with a gearbox, when the torques and speeds are transformed between the LSS and HSS using the gear ratio. Furthermore, the gearbox modes need not be taken into account, as they were not considered during drivetrain damper design.

Strategy and architecture

A diagram of the entire controller is shown in Figure 2.1. The routes of this diagram that are active when the turbine is operating below rated power, herein called *partial load* operation, are shown in Figure 2.2. The routes that are active in *full load* operation are shown in Figure 2.3. These two regions of operation are first described before the switching between is explained.

Partial load operation

This section is extensively adopted from [9] as the functionality is identical. The strategy for optimal C_P tracking in partial load operation is based on a balance between generator and aerodynamic torques to obtain a close to optimal tip speed ratio. To avoid the feedback of higher frequency dynamics (e.g. the drivetrain torsion mode), the torque reference $Q_{ref,k}$ at the current step k is computed based on a second order low-pass filtered LSS generator speed as $K\overline{\Omega}_k$. This feedback is enforced by setting the torque limits for the PID controller to $Q_{g,min,k} = Q_{g,max,k}=K\overline{\Omega}_k^2$ whenever the filtered rotational speed $\overline{\Omega}_k$ is not close to the minimum speed Ω_{min}, or the rated speed Ω_0. When the rotational speed is close to its bounds, these torque limits will open according to the interpolation factors $\sigma_{min,k}$ and $\sigma_{max,k}$. The torque reference will then be given by the PID controller based on the speed error $e_{Q,k} = \overline{\Omega}_k - \Omega_{set,k}$, where the set point is the minimum, or rated speed. Because the rotor speed is bounded, the power loss can often be minimized be performing some adjustment of the minimum pitch. A first order low-pass filtered wind speed measured at hub height $\overline{V}_k$ is used as parameter for varying the minimum pitch angle $\theta_{min,k} = \theta_{min}\,\bar{V}_k$ based on a look-up table provided by the user. The $\theta_{min}(\bar{V}_k) = 0;\ \forall\,\bar{V}_k$ for this particular controller design, therefore this functionality is omitted and $\theta_{min,k}$ is set to zero.

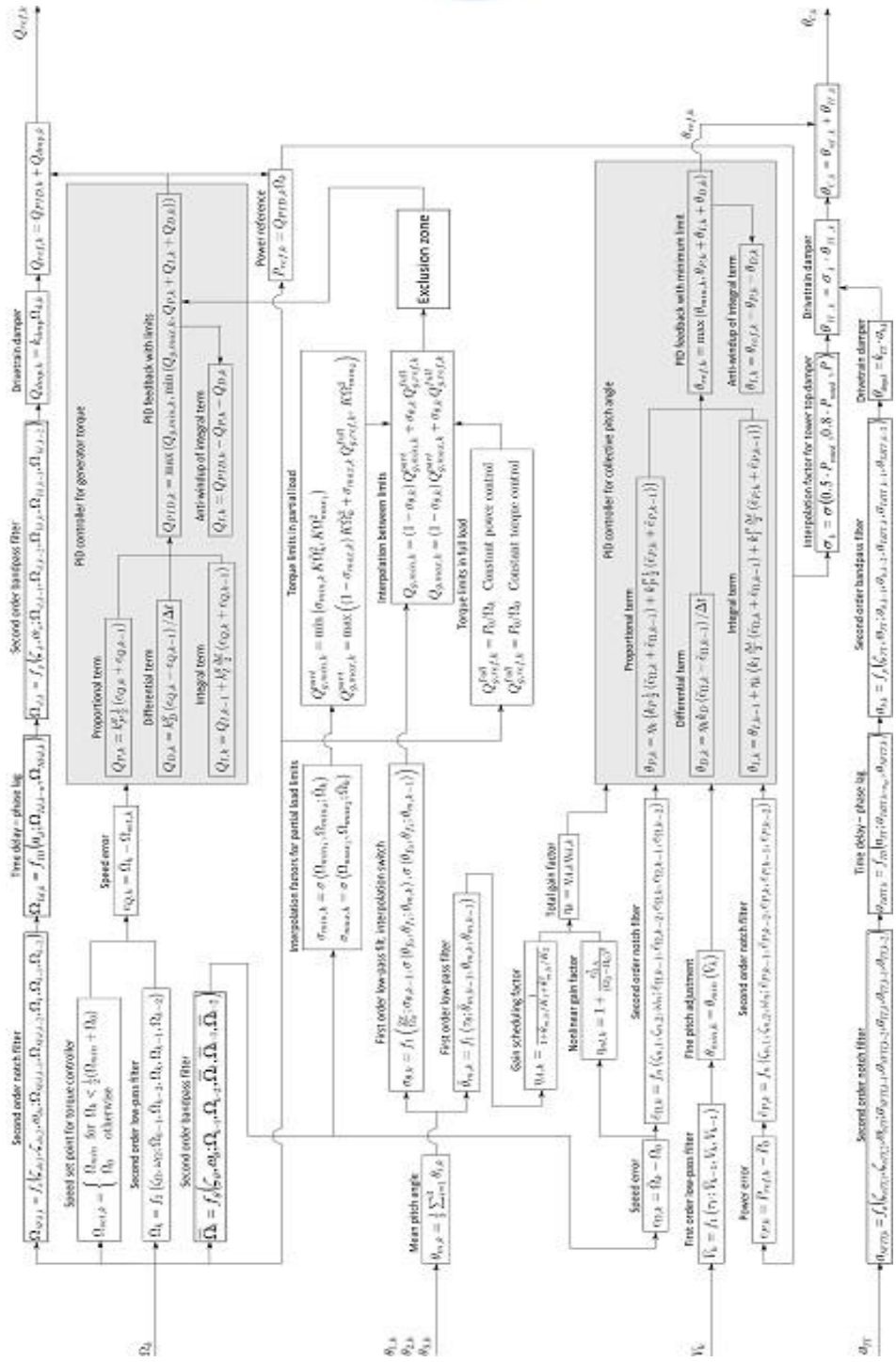

Figure 2.1: Diagram of the discrete controller. Note that *k* denotes the current time step

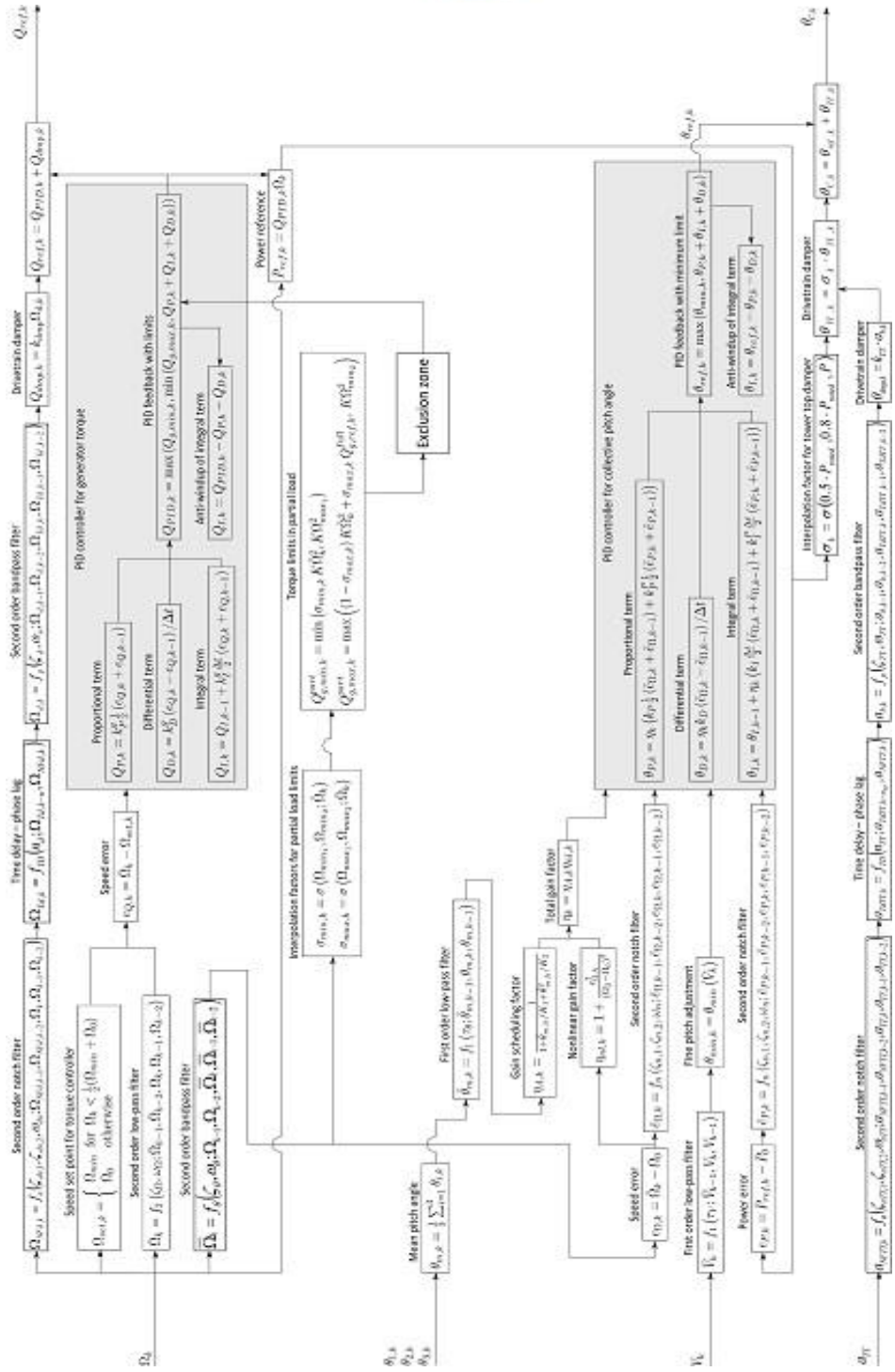

Figure 2.2: Active routes during partial load operation in the controller diagram in Figure 2.1

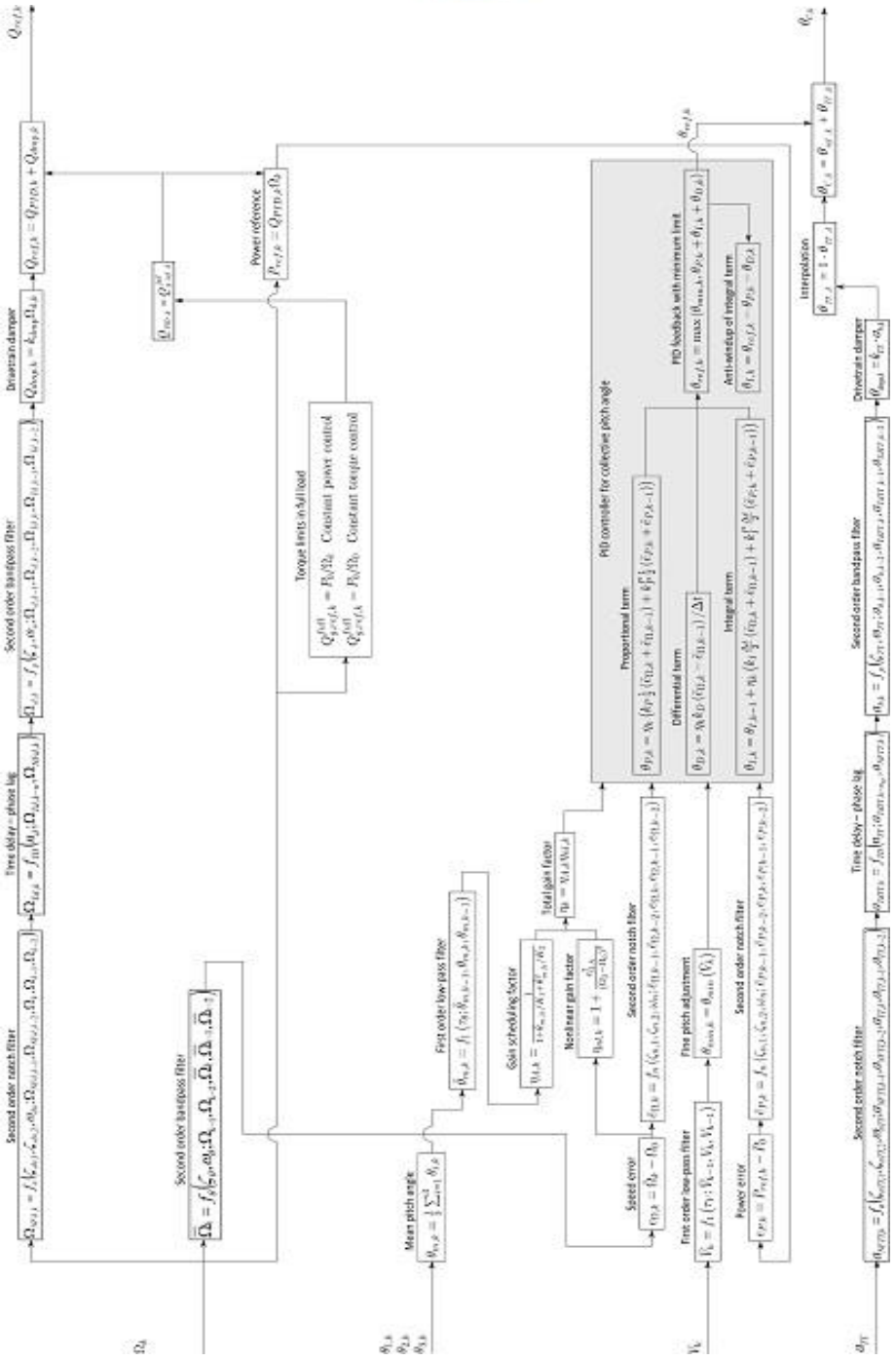

Figure 2.3: Active routes during full load operation in the controller diagram in Figure 2.1.

The interpolation factors for the opening of the torque limits are based on how close the second order low-pass filtered generator speed is from its minimum and rated speeds. The limits can be opened gradually over an interval as described by the function

$$\sigma\left(x_0, x_1; x\right) = \begin{cases} 0 & \forall x < x_0 \\ a_3 x^3 + a_2 x^2 + a_1 x + a_0 & \forall x \in [x_0 : x_1[\\ 1 & \text{otherwise} \end{cases}, \qquad \text{Eq. 1}$$

where the coefficients of the spline are

$$a_3 = \frac{2}{\left(x_0 - x_1\right)^3}, \quad a_2 = \frac{-3\left(x_0 + x_1\right)}{\left(x_0 - x_1\right)^3}, \quad a_1 = \frac{6 x_1 x_0}{\left(x_0 - x_1\right)^3}, \quad a_0 = \frac{\left(x_0 - 3x_1\right) x_0^2}{\left(x_0 - x_1\right)^3} \qquad \text{Eq. 2}$$

The function is programmed such that if $x_0 \geq x_1$then the σ-function becomes

$$\sigma\left(x_0, x_0; x\right) = \begin{cases} 0 & \forall x < x_0 \\ 1 & \text{otherwise} \end{cases} \qquad \text{Eq. 3}$$

Figure 2.4 shows an example of the σ-function where $x_0 = 1$ and $x_1 = 2$. In an actual implementation of the controller, this smooth function with a third order polynomial may be an unnecessary complexity, which can be replaced by a linear interpolation function.

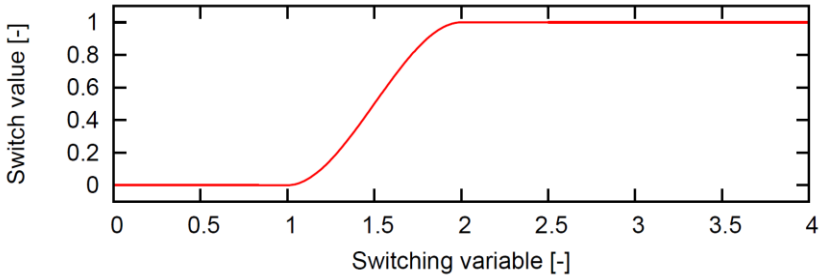

Figure 2.4: Example of the σ-function Eq. 1where $x_0 = 1$ and $x_1 = 2$

Figure 2.5 shows the torque limits in partial load operation of the DTU 10~MW RWT, where the minimum speed is 5~rpm and rated speed is 9.6~rpm. Several operational regions can be seen here. Namely the bellow minimal rotational speed region, variable speed region with exclusion zone functionality, transient variable to constant speed region and finally constant speed region. The generator torque limits are set to be open in bellow minimal rotor speed, where the maximal torque limit is set to

$$Q_{g,max} = max \begin{cases} K \cdot \Omega_{min}^2 \\ K \cdot \bar{\Omega}_k^2 \end{cases} \qquad \text{Eq. 4}$$

and minimal torque is equal to zero. The generator torque limits are closed approximately 5% above the minimum speed Ω_{min} and start opening again at 90% and are fully open at 95% of the rated speed. If the exclusion zone functionality is active, the torque limits starts to open at 95% of the exclusion zone minimal speed $\omega_L$and are closed approximately 5% above the exclusion zone maximal speed ω_H.

Where the spline function is used to guarantee smooth transient. The maximal torque limit is set to $Q_{g,max}$ 5% above the $T_{G_{\omega_L}}$ and the minimal torque is set to $Q_{g,min}$ 95% of the $T_{G_{\omega_H}}$.

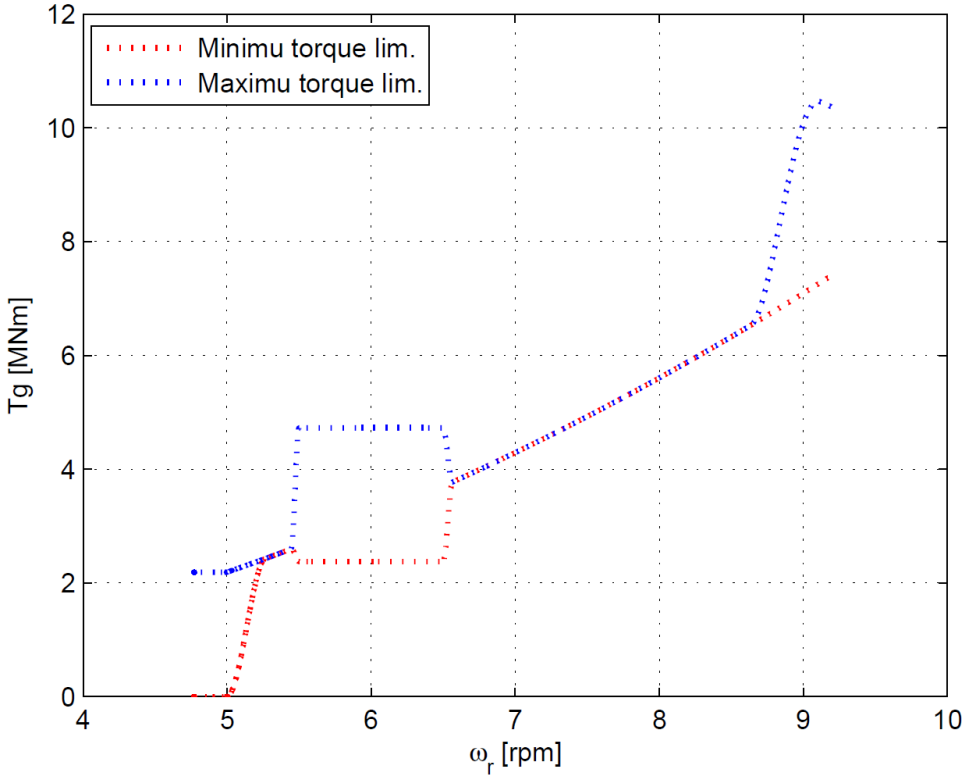

Figure 2.5: Torque limits in partial load operation of the 10MW RWT, where the minimum speed is 5 rpm and rated speed is 9.6 rpm. The limits are set to be closed approximately 5% above the minimum speed and start opening again at 90% and are fully open at 95% of rated speed.

Full load operation

This section is extensively adapted from [9]. In full load operation, the torque limits are closed around the torque given by the selected power control strategy, either constant power P_0/Ω_k, or constant torque P_0/Ω_0, where P_0 is the rated power. Note that the unfiltered measured LSS generator speed Ω_k is used for computation of the reference torque in the constant power control.

The pitch reference angle is obtained from a combined PI feedback of the generator speed and power errors, and a possible differential feedback of the speed error. The speed error is obtained as the difference between the second order low-pass filtered LSS generator speed and the rated speed. The power error is the difference between the reference power $P_{ref,k} = Q_{ref,k}\Omega_k$and the rated power P_0. Both errors are notch filtered around the frequency specified by the user as the free-free drivetrain frequency. This frequency is assumed to be constant although HAWCStab2 eigenvalue analysis often

show a small variation with operational point (wind speed). Note that both errors contribute to the same proportional term ($\theta_{P,k}$) and same integral term ($\theta_{I,k}$). The latter is important because it ensures that the reference pitch angle is kept at the minimum pitch angle until rated power is reached; assuming that the right weighting between the integral speed error gain k_I and power error gain k_I^P has been selected by the user.

The anti-windup is performed such that the controller will react quickly with increased pitch angle if the reference power signal suddenly increased above the rated power level: In each time step, the minimum pitch limit is enforced on the reference pitch which is the sum of the proportional, differential, and integral terms $\theta_{ref,k} = \max(\theta_{min,k}, \theta_{P,k} + \theta_{D,k} + \theta_{I,k})$. The value of the integral term to be used for the integration in the next time step is then recalculated as $\theta_{I,k} = \theta_{ref,k} - \theta_{P,k} - \theta_{D,k}$, which only makes a change to the integral term if the reference pitch is on the minimum limit $\theta_{ref,k} = \theta_{min,k}$. Below rated power, where the proportional term is negative because the rotational speed error is kept close to zero by the torque PID controller, the integral term will therefore be positive. If the reference power is increased and becomes close to rated power (due to the reaction of the torque PID controller to an increased wind speed), then the proportional term will then come close to zero whereas the integral will still be positive and the resulting pitch reference angle will be positive, whereby large power and speed variations are avoided. Note that the same anti-windup scheme is used in the torque PID controller.

The first order low-pass filtered mean of the blade pitch angles $\bar{\theta}_{m,k}$ is used for scheduling of the gains of the pitch PID controller. A quadratic dependency of the aerodynamic torque gain with collective pitch angle is assumed as

$$\frac{\partial Q_A}{\partial \theta} = \left.\frac{\partial Q_A}{\partial \theta}\right|_{\theta=0} \left(1 + \frac{\theta}{K_1} + \frac{\theta^2}{K_2}\right) \qquad \text{Eq. 5}$$

where Q_A denotes the aerodynamic torque, θ is the collective pitch angle, and $\left.\frac{\partial Q_A}{\partial \theta}\right|_{\theta=0}$ is the aerodynamic gain at zero pitch. The parameters of this expression K_1 and K_2 can be obtained from curve fitting to the derivative of the aerodynamic torque with respect to collective pitch angle assuming quasi-steady aerodynamics and *frozen wake* (constant induced velocities) as

$$\frac{\partial Q_A}{\partial \theta} = \frac{1}{2}\rho B \int_0^R c(r)U(r)^2 \left(C'_L(\alpha(r))\sin\varphi(r) - C'_D(\alpha(r))\cos\varphi(r)\right) rdr \qquad \text{Eq. 6}$$

where *B* is the number of blades, *R* is the outer radius of the rotor, *c(r)* is the radial chord distribution, *U(r)* is the mean steady state relative inflow velocity along the blade, C'_L and C'_D are the gradients of the lift and drag coefficient curves evaluated at the mean steady state angle of attack $\alpha(r)$ along the blade, and $\varphi(r)$ is the spanwise distribution of inflow angles relative to the rotor plane.

Figure 2.6 shows the aerodynamic torque gradients obtained from HAWCStab2 for the DTU 10~MW RWT together with the fit of the quadratic expression Eq. 5. Often, a linear fit is sufficient and it is assumed when the user enters $K_2 = 0$ (note that K_1 then is the angle where the aerodynamic gain is

doubled). The gain scheduling factor based on the filtered mean pitch angle $\eta_{A,k}$ is the inverse of the expression in the parenthesis of Eq. 5. A nonlinear gain factor $\eta_{nl,k}$ based on the generator speed error is also added for increased sensitivity of the pitch PID controller by large speed excursions.

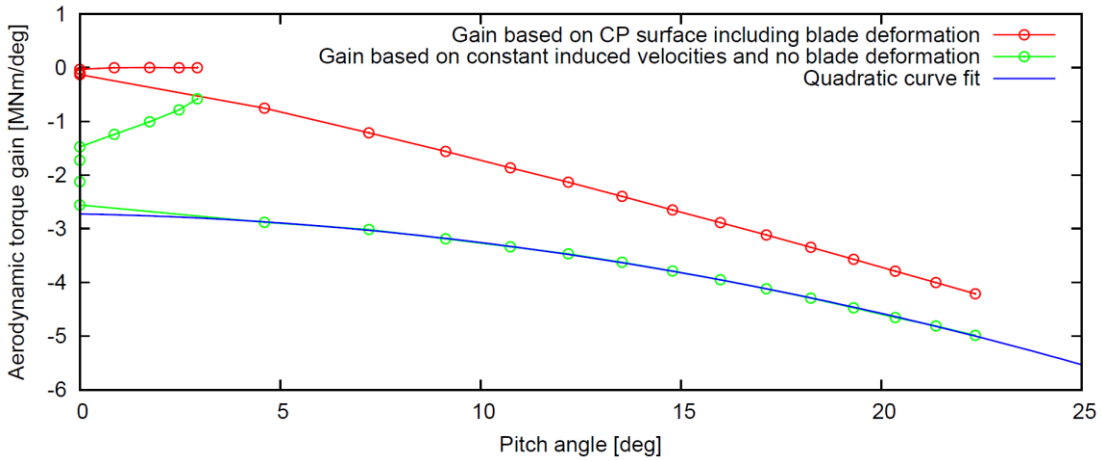

Figure 2.6: Aerodynamic torque gains for the DTU 10~MW RWT obtained from HAWCStab2, adopted from [9].

Switching between partial and full load operation

The switching between partial and full load control of the generator torque is based on a first order low-pass filtered switching variable $\sigma_{\theta,k}$ that is driven by a σ-function evaluation using the measured mean pitch angle θ_m. The time constant is the rotational period at rated speed. As explained above, the anti-windup of the combined integral term of the pitch PID controller will ensure that the reference pitch angle raises above its minimum value when the torque PID controller of generator speed results in a reference power close to the rated power level. The user can define at how many degrees above the minimum pitch this switching shall occur. Good experiences have been obtained with a hard switch at $\theta_{f_1} = \theta_{f_2} = \theta_{min,k} + 0.5$ deg (1 deg value is used when thrust peak shaving functionality is active).

Drivetrain damper

The measured generator LSS speed Ω_k is fed through a band-stop filter with the frequency ω_{dn} as center frequency, to avoid drivetrain to rotor mode coupling. The filtered speed $\Omega_{NFd,k}$ phase is corrected by phase lag (implemented as time delay) to compensate for phase shift during signal processing and natural phase lag of wind turbine systems. Such a signal is further filtered using band-pass filter with the free-free drivetrain torsional frequency ω_n as center frequency. The filtered speed $\Omega_{d,k}$ is multiplied by a gain factor k_{dmp} and added to the torque feedback from the PID controller to give the generator torque reference. Note that this drivetrain damper is always active when $k_{dmp} > 0$. The performance of drivetrain damper can be seen from Figure 2.7, where the drivetrain mode is actively stabilized by damper.

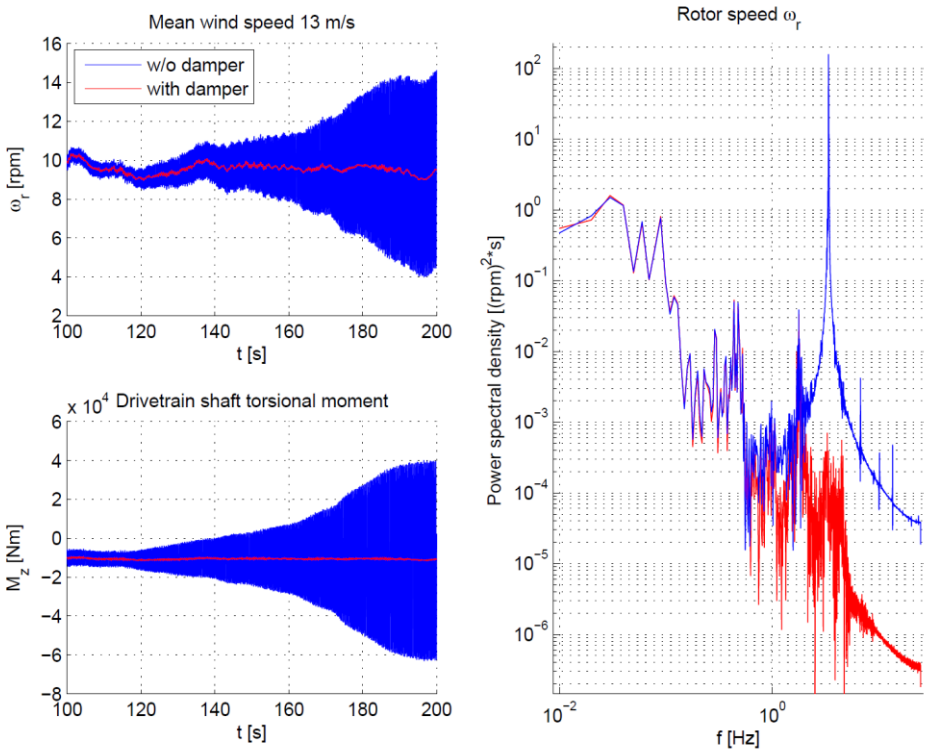

Figure 2.7: Drivetrain damper.

Tower top fore-aft damper

Similar hierarchy as applied for drivetrain damper is used for tower top fore-aft damper. The measured tower top acceleration a_{TT} is fed through a band-stop filter with the frequency ω_{nTT} as center frequency, to avoid excitation of foundation structure at *3p* frequency by feedback loop. The filtered signal $a_{NFTT,k}$ phase is corrected by phase lag (implemented as time delay) to compensate for phase shift during signal processing and natural phase lag of wind turbine systems. Such a signal is further filtered using band-pass filter with the first tower fore-aft mode frequency ω_{TT} as centre frequency. The filtered acceleration $a_{b,k}$ is multiplied by a gain factor k_{TT} and added to the collective pitch angle feedback from the PID controller. Note that tower top damper starts operating at 50% of rated power and is fully active for generated power higher than 80% of rated power, smooth transient is guaranteed by interpolation factor based on generated power. The additional damping of first tower mode in fore-aft direction can be assessed from Figure 2.8. The open loop and closed loop time series are plotted in left figure and frequency domain responses are potted in right figure. The assessment of active damping in time domain is really hard due to multiple modes close to tower first fore-aft mode, but significant reduction of particular mode amplitude can be clearly seen in frequency domain.

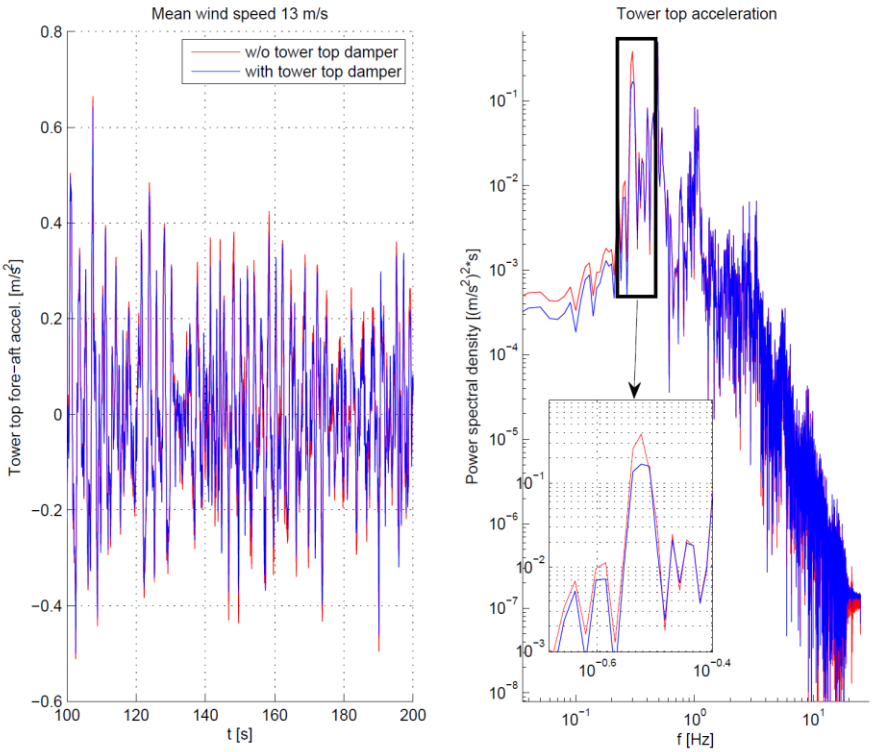

Figure 2.8: Tower top fore-aft damper.

Exclusion zone

The exclusion zone functionality prevents foundation structure to rotor 3p resonance by avoiding rotor to operate at critical rotational speed. The functionality logic is based on finite-state machine with diagram presented in f. States *0* and *3* are variable speed regimes below exclusion zone minimal speed and above exclusion zone maximal speed. States *1* and *2* are constant speed regimes of exclusion zone, where wind turbine rotor speed is stabilized on ω_L or ω_H by appropriate switching of reference speed for generator torque PID controller. Notice that reference speed switching during transient from state *1* to state *2* and other way around is done with time constant τ_{EZ} . The torque dependency on rotor speed can be seen from Figure 2.10. Finally the exclusion zone functionality can be seen from Figure 2.11, where the rotor speed, tower top fore-aft and side to side acceleration is displayed for active and deactivated exclusion zone.

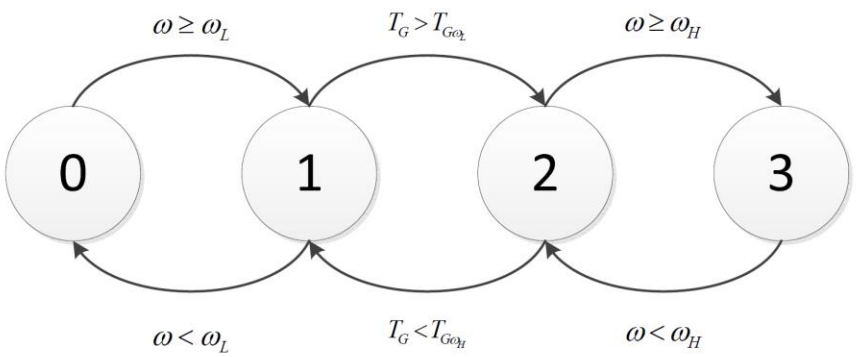

Figure 2.9: Exclusion state automat.

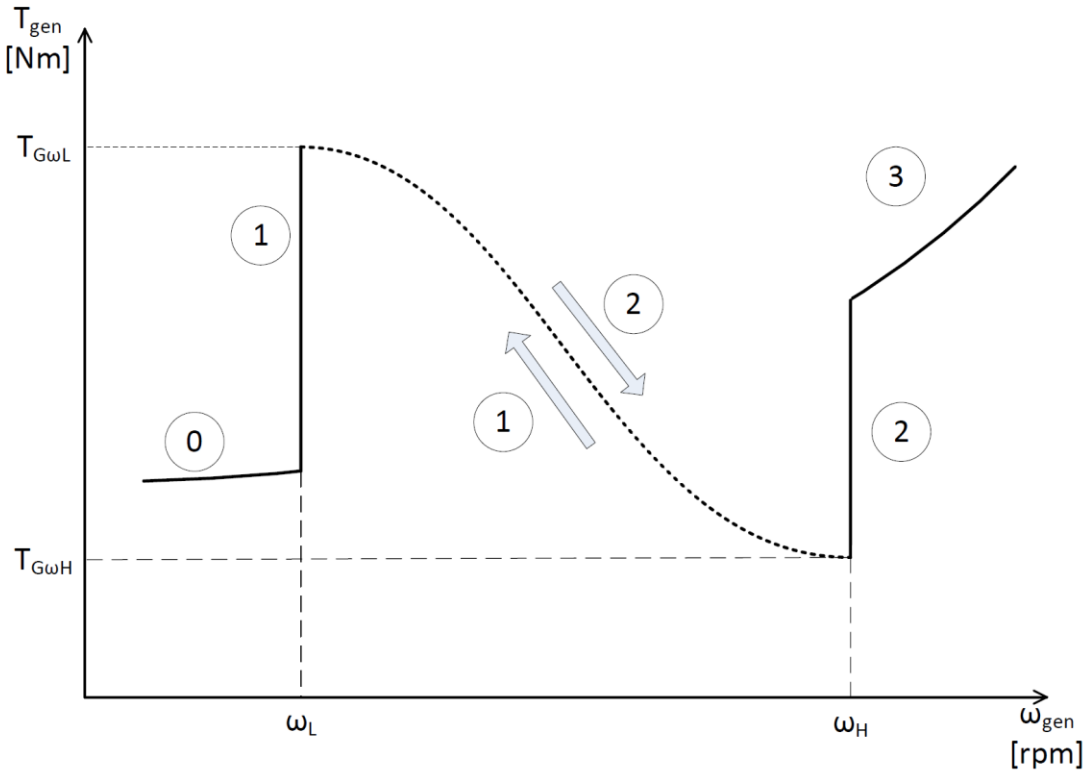

Figure 2.10: Exclusion zone torque curve.

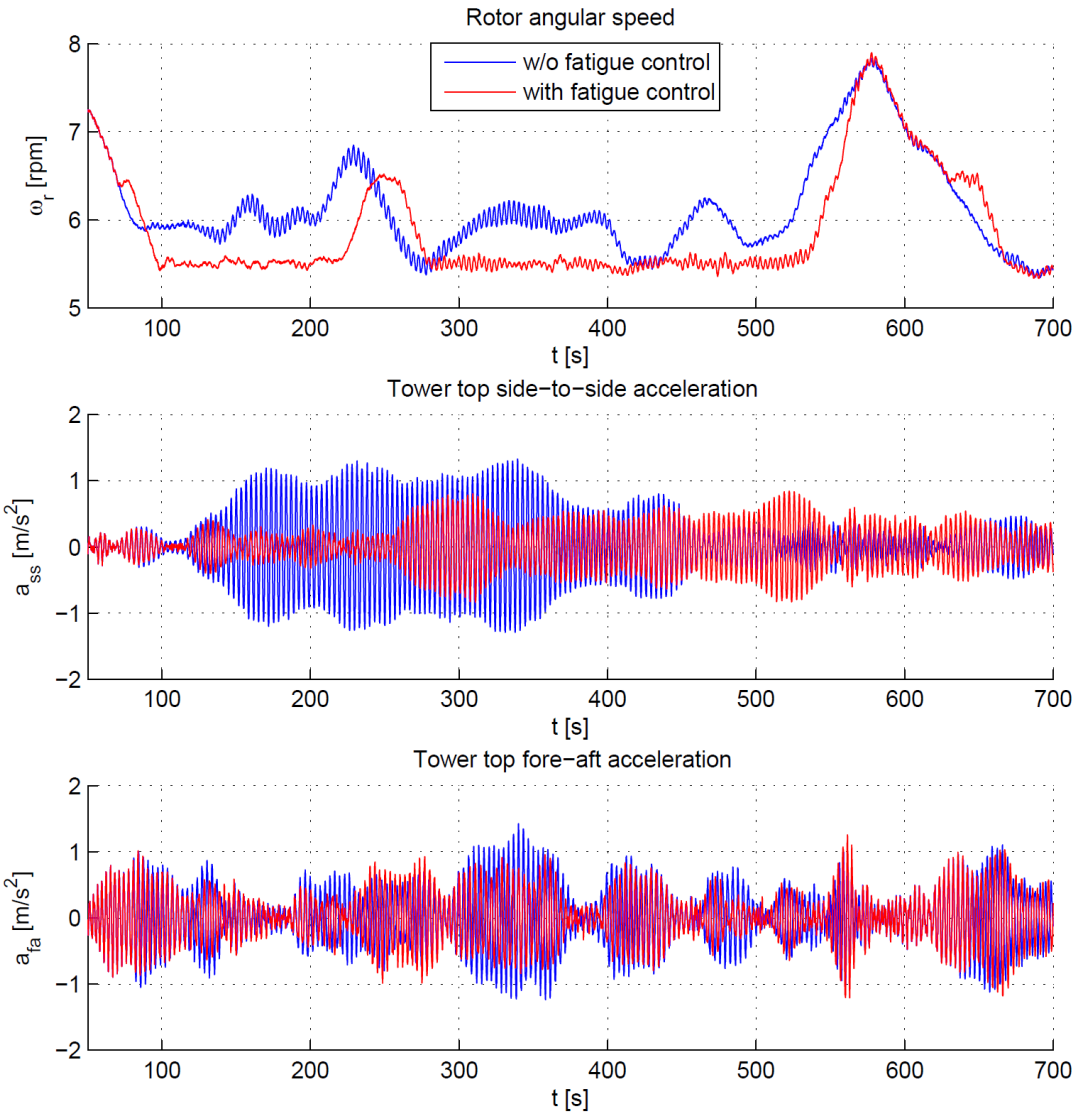

Figure 2.11: Exclusion zone.

As can be seen in Fig. 2.11, even though the tower top accelerations are greatly reduced with the exclusion zone, there is still potential for further reduction in the excitations of the tower by tuning the exclusion zone.

Parameters to be tuned

The rotor speed exclusion zone requires five different tuning parameters:

1. Low rotor speed limit
2. High rotor speed limit

3. Reference generator torque for low rotor speed limit
4. Reference generator torque for high rotor speed limit
5. Time constant for smooth transitions

The first two parameters represent the limits between which the turbine should operate the least possible to avoid resonance between the 3P excitation and the first tower lateral mode.
The third and fourth parameters are the reference generator torque values that are used to enable a fast transition of the rotor speed across the rotor speed exclusion zone. The torque value for the low rotor speed limit is the maximum torque value the controller has to use to keep the rotor speed at the low rotor speed value. The torque value for the high rotor speed limit is the minimum torque value the controller has to use to keep the rotor speed at the high rotor speed value.
The fifth parameter is a time constant to enable smooth variation of the rotor speed reference value used for the generator torque feedback between the regions.

Tuning

The first lateral tower frequency of the jacket mounted version of the DTU 10MW RWT is equal to 0.31 Hz. If an exclusion zone about the tower frequency of ± 10% is imposed the corresponding values of the low rotor speed limit and the high rotor speed limit are 0.584 and 0.714 rad/s, respectively.
The reference generator torque for low rotor speed limit should be close to the generator torque value obtained with the $k\Omega^2$ controller for a rotor speed equal to the high rotor speed limit. When this value is selected, the transition to the high speed limit occurs when the generator torque is high enough to guarantee the desired tip-speed-ratio, set from the $k\Omega^2$ controller, at the high speed value. Similarly the reference torque for the high rotor speed limit can be set close to the value of the $k\Omega^2$ controller for the low rotor speed limit. These reference torque values, when k equals to $1.301\ 10^7$ Nms^2 and the previously mentioned rotor speed limits are selected, are 4437 and 6632 kNm.
The time constant has to be selected to compromise between a fast transition across the region that leads to large variations of the reference generator torque, and to a slow transition that can lead to high tower vibrations. A new compromise of 25s has been found.

Comparison

Two comparisons are reported: a simple test case where a uniform wind ramp is applied to see the wind turbine behaviour when operating across the exclusion zone and the response to turbulent wind at different mean wind speeds.
The below figure shows the wind turbine response to a wind ramp close to the exclusion zone and compares the old and new tuning. The new tuning leads to lower lateral tower base bending moment vibrations for this case. This reduction is achieved with a higher high rotor speed limit and a faster transition across the exclusion zone.

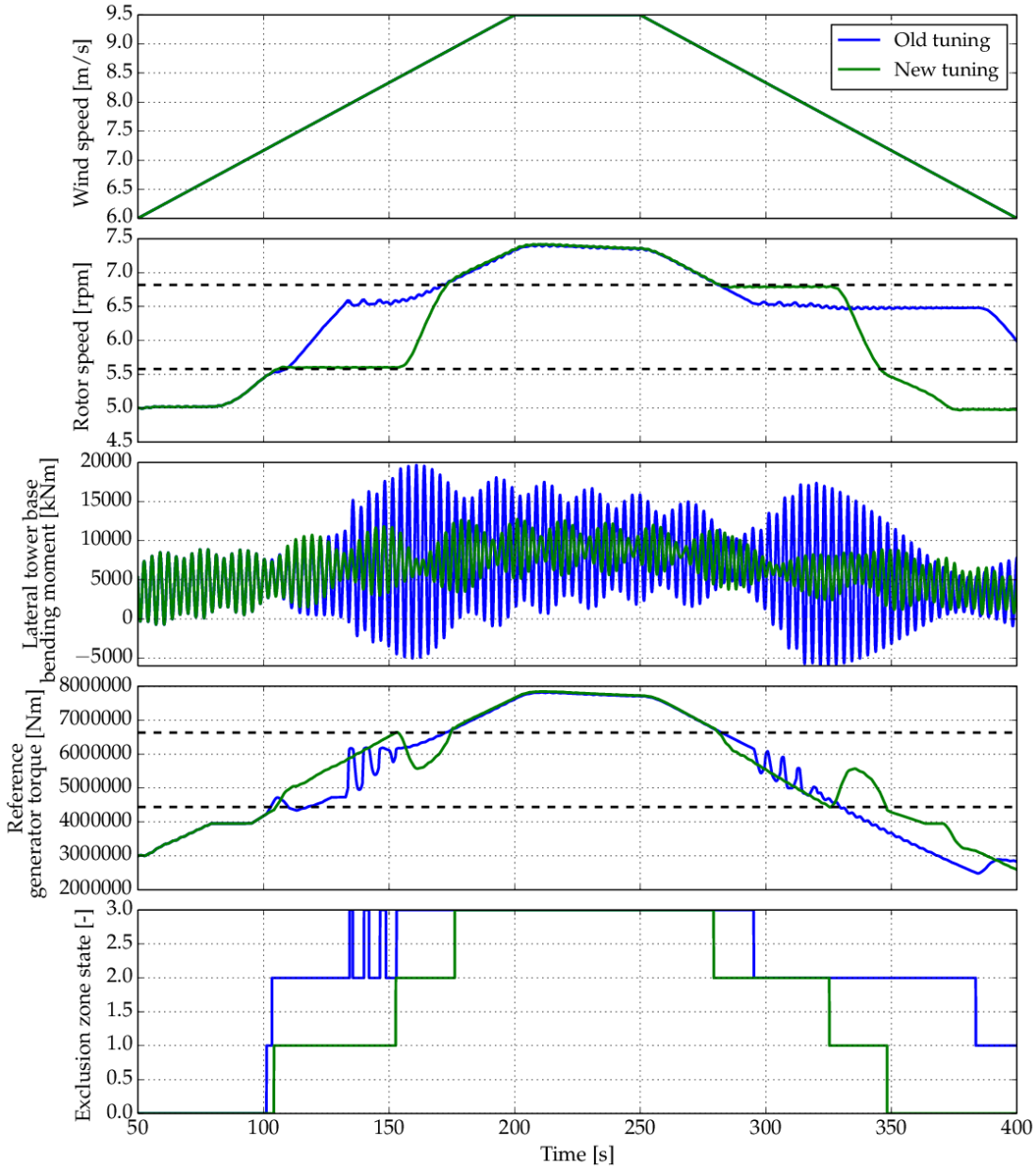

Figure 2.122 Wind turbine response during a wind ramp. Comparison between the old and new exclusion zone controller tuning.

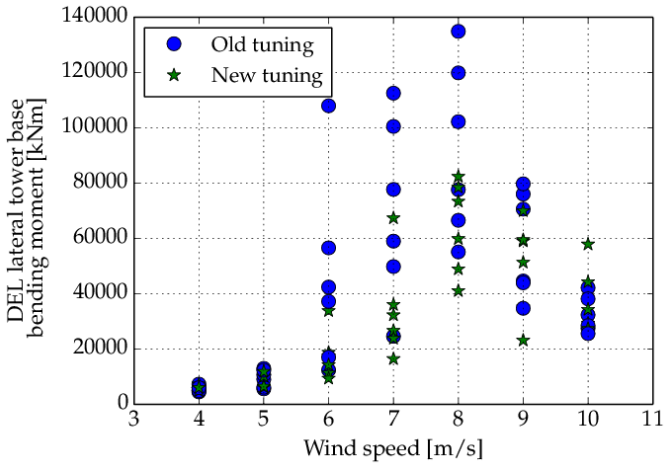

Figure 2.13: Damage equivalent load of the lateral tower base bending moment. Comparison between the old and the new exclusion zone controller tuning. Wind speed from 4 to 10 m/s and six turbulence seeds.

Figure.13 shows a comparison of the lateral tower base bending moment damage equivalent load obtained with the two exclusion zone controller tuning. The loads are computed from simulations with turbulent wind at different mean wind speeds and with six different turbulent seeds. Between 5 and 9 m/s the new tuning leads to a reduction in the fatigue loads of the tower for all the cases. At 8 m/s the load reduction reaches 80%. At 10m/s some cases show higher loads but, at this wind speed, the loading is lower than at the wind speeds where the new tuning improves the performances.

Thrust peak shaving

The aerodynamic thrust force has its maximum closed to rotor rated speed Ω_0, where the wind speed reaches its maximum for collective pitch angle at its minimal value (see Figure, blue curve). This introduces high extreme and fatigue loading for several wind turbine sub-components. The thrust force response to the blade pitching has negative trend (for particular wind speed, with increasing pitch angle the thrust force is reduced) and therefore collective pitch angle can be used to reduce maximal thrust. However the power production of wind turbine is also reduced as collective pitch angle differ from optimal one. Hence it is important to keep the thrust reduction to power reduction trade off in mind during thrust peek shaving design. The thrust peek shaving functionality can be implemented as altered minimal pitch angle lookup table, where higher pitch angle would be required as wind turbine approaches rated wind speed. The thrust peek shaver is implemented by dis-engaging of power error feedback loop for pitch PID, in case of DTU10MW offshore controller. This results in natural increase of pitch activity right before wind turbine hit rated wind speed. The comparison of collective pitch angle as function of wind speed, with and without thrust peek shaving function, can be seen from Figure4.

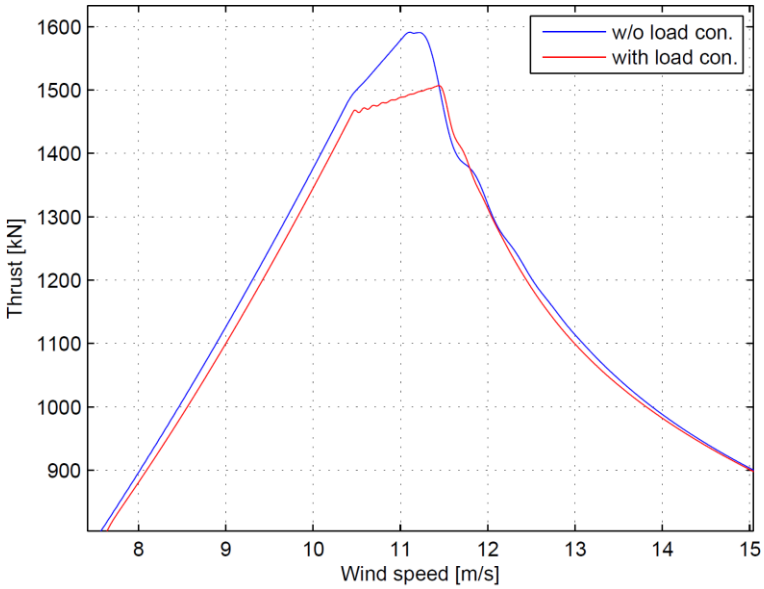

Figure 2.14: Thrust force as function of wind speed.

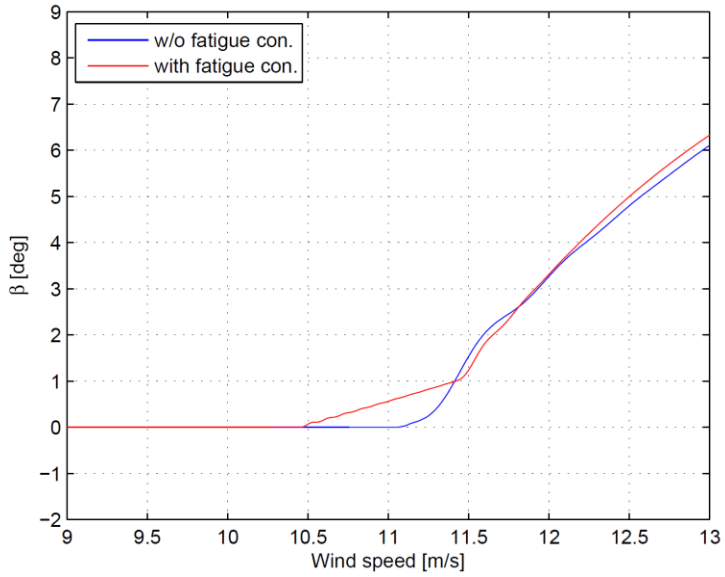

Figure 2.15: Collective pitch angle as function of wind speed.

Additional non-linear pitch control term

This term should only be active during extreme event where severe over-speed can occur.

$$\dot{\theta}_+ = \dot{\theta}_+ + k_{os}(\dot{\tilde{\Omega}}_k/\Omega_{os} + e_{\Omega,k}/\dot{\Omega}_{os}) \quad , \text{for } (\dot{\tilde{\Omega}}_k/\Omega_{os} + e_{\Omega,k}/\dot{\Omega}_{os}) > 1$$
$$\dot{\theta}_+ = \dot{\theta}_+ \quad , \text{for } (\dot{\tilde{\Omega}}_k/\Omega_{os} + e_{\Omega,k}/\dot{\Omega}_{os}) \leq 1 \qquad \text{Eq. 7}$$

This control block is only active if $(\Omega_{os}, \dot{\Omega}_{os}, k_{os}) \neq 0$.

2.2 Cyclic Pitch Control

The cyclic pitch controller (or individual pitch controller) is basically a controller added on top of the collective pitch controller described above to reduce variations in the blade root bending moment. The collective pitch controller is part of the DTU basic controller [9]. This section describes the basic benefits of cyclic pitch control and its implementation at the 10 MW scale. Here we use the term cyclic as the pitch variation is prescribed through a time invariant function of the azimuth angle. Therefore, cyclic means that the same pitch angle pattern as a function of the azimuth angle is applied to the individual blades. Looking at the time series of the cyclic pitch of the blades, they are periodic with the same shape, only with 120 degrees of phase shift:

$$\begin{aligned}\theta_1(\psi) &= \theta^c + \theta^i(\gamma, \psi) \\ \theta_2(\psi) &= \theta^c + \theta^i(\gamma, \psi - 2\pi/3) \\ \theta_3(\psi) &= \theta^c + \theta^i(\gamma, \psi - 4\pi/3)\end{aligned} \quad (1)$$

In which $\theta_k, k = 1,2,3$ are the pitch of the blades, $\theta^c$is the collective pitch and θ^i is the cyclic term of the pitch of the blades. The cyclic pitch function is found by optimizing the parameters of a parameterized periodic function:

$$\theta^i(\gamma, \psi) = \theta^i(\gamma, \psi + 2\pi) \quad (2)$$

In which the function θ^i is parameterized using the parameter vector γ. ψ is the azimuth angle and the equation above basically indicates that the cyclic pitch function is periodic in azimuth angle, with a period of 2π.

An example of the cyclic pitch of the three blades is given in figure 2.15:

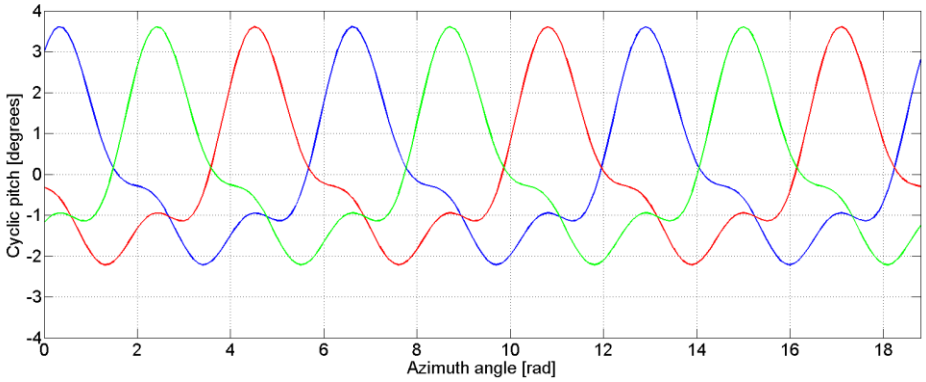

Figure 2.15 Cyclic pitch of the 3 blades

Calculating the cyclic pitch

In order to calculate the cyclic pitch values, the controller solves the following optimization problem:

$$\min_{\gamma} \sqrt{\sum_{i=1}^{N}(M_x - \mu_M)^2} \qquad (3)$$

As mentioned in the previous section, γ is the vector of parameters in the cyclic pitch function. M_x is the flapwise blade root bending moment, $\mu_M$is the mean value of M_x and N is the number of samples in one period. The optimizer determines the vector γ and runs a HAWC2 [10] simulation. It holds until the simulation reaches steady state, then one cycle of the flapwise bending moment is measured (a vector with size *N*) and its standard deviation is calculated. Here we can use any other measures, such as infinity-norm or 1-norm of the deviation from the mean value to measure the fluctuations of the blade root bending moment. The calculated number is returned back to the optimizer as the value of the objective function. Two ways for parameterizing the cyclic pitch is used: Fourier series and periodic splines. They will be explained in their respective sections. Figure 13.16 shows how the iteration is done on the optimization of the parameters of the cyclic pitch.

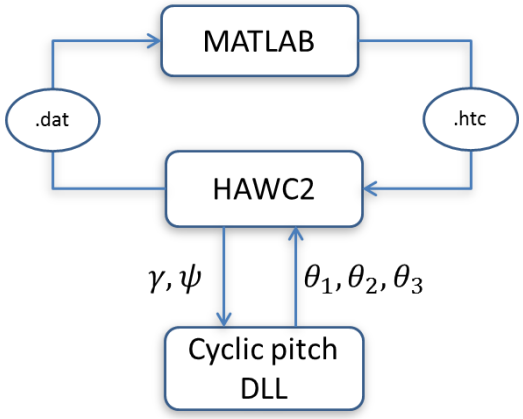

Figure 13.16 **The optimization loop using MATLAB and HAWC2**

The MATLAB block calculates a value for the vector γ, the value is given to HAWC2 through initialization function of DLLs in the htc file. A HAWC2 simulation is run until it reaches steady state. In order to check if the steady state condition is satisfied, two consecutive cycles of one of the output channels, e.g. flapwise blade root bending moment, are compared and if the difference is below a threshold, the program gives a flag that the steady state is reached. There the data file which contains all the output channels of the HACW2 simulation is passed to MATLAB. MATLAB analyzes the data, extracts the last cycle of the flapwise blade root bending moment and calculates its variance (or other chosen norms) and returns the value to the optimizer as the obtained value of the cost function. The cyclic pitch controller is developed as a HAWC2 DLL which is initialized by HAWC2 and the parameter vector γ. Thereafter, in each HAWC2 iteration, the DLL is called and given the azimuth angle of the turbine. The DLL then returns the cyclic pitch value for the individual blades. Figure shows the procedure where the cyclic pitch controller is called.

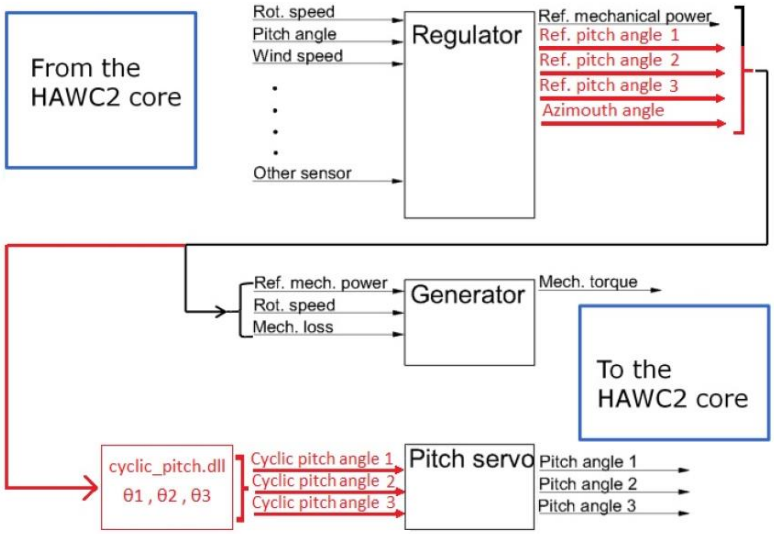

Figure 2.17 The configuration of the cyclic pitch controller DLL in HAWC2

Parameterization of the cyclic pitch

In this section the different methods of parameterization of the cyclic pitch controller are explained.

Fourier series method

In this method it is assumed that the cyclic pitch can be modeled as Fourier series. The parameters of the function are the coefficients a_k and b_k of the Fourier series below:

$$\theta_1^i(\psi) = \sum_{k=1}^{N} a_k \sin(k\psi) + b_k \cos(k\psi)$$
$$\theta_2^i(\psi) = \sum_{k=1}^{N} a_k \sin(\psi - 2\pi/3) + b_k \cos(k\psi - 2\pi/3) \quad (4)$$
$$\theta_3^i(\psi) = \sum_{k=1}^{N} a_k \sin(k\psi - 4\pi/3) + b_k \cos(k\psi - 4\pi/3)$$

For each simulation scenario, different values of *N* are chosen and the performance of the cyclic pitch controller is assessed. It is clear that as the *N* increases and the Fourier series include terms with higher frequencies the cyclic pitch controller has more degrees of freedom to decrease the variations of the blade root bending moment. Therefore it can achieve better performance in calculating sharp pitch demands to compensate for fast variations of the blade effective wind speed, such as the case with tower shadow. In fact even one pair of parameters (a_1 and b_1) are sufficient to compensate for the wind shear with a reasonable performance, however when the tower shadow and partial wake are included more terms are necessary. The results of these analyses are given in the respective sections.

Cubic spline method

A spline is basically a mathematical function that is piecewise affine with polynomial functions. Periodic spline can give a better tool for our purpose. Because, it can give sharp enough pitch signals to compensate for steep changes in the blade effective wind speed. The steep changes in wind speed can be the result of for example tower shadow. A periodic spline returns a smooth transition from one period to the next period as well as the smooth curve in the spline interval. The following equation shows the parameterization of the periodic spline function:

$$S(x) = \begin{cases} C_1(x), & x_0 \le x \le x_1 \\ C_2(x), & x_1 \le x \le x_2 \\ \vdots & \\ C_n(x), & x_{n-1} \le x \le x_n \end{cases} \tag{5}$$

$$C_i(x) = a_i + b_i(x - x_i) + c_i(x - x_i)^2 + d_i(x - x_i)^3 \tag{6}$$

In the above equations the following conditions must hold in order to have a smooth spline:

$$\begin{aligned} & C_i(x_k) = C_{i+1}(x_k) \\ & \left.\frac{dC_i}{dx}\right|_{x_k} = \left.\frac{dC_{i+1}}{dx}\right|_{x_k} \\ & \qquad \vdots \\ & \left.\frac{d^m C_i}{dx^m}\right|_{x_k} = \left.\frac{d^m C_{i+1}}{dx^m}\right|_{x_k} \end{aligned} \tag{7}$$

$$\text{For} \quad k = 1, \ldots, n-1 \text{ and } i = 1, \ldots, n$$

And the following equations must hold in order to have a smooth transition between the consecutive periods:

$$\begin{aligned} & C_1(x_0) = C_n(x_n) \\ & \left.\frac{dC_1}{dx}\right|_{x_0} = \left.\frac{dC_n}{dx}\right|_{x_n} \\ & \qquad \vdots \\ & \left.\frac{d^m C_1}{dx^m}\right|_{x_0} = \left.\frac{d^m C_n}{dx^m}\right|_{x_n} \end{aligned} \tag{8}$$

which basically means the curve should be continuous at the period point as well as differentiable to the degree *m*. *m* is an arbitrary value and determines the degree of smoothness we require. **Figure** shows a spline curve with 8 points.

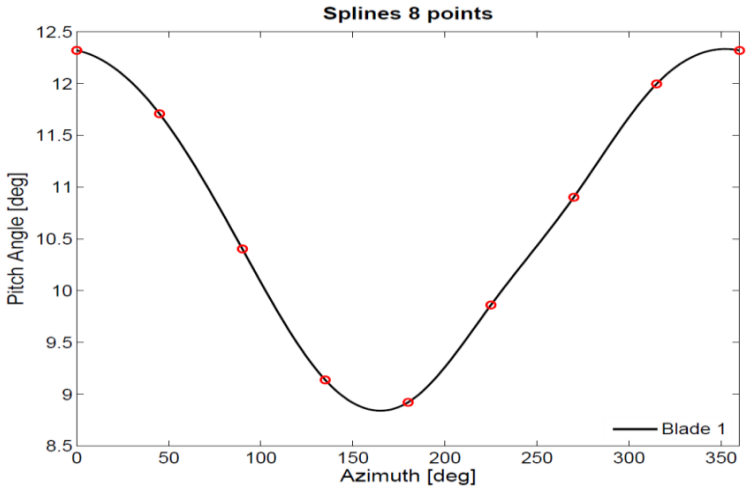

Figure 2.18 Sample of a periodic spline curve using 8 points

Simulation cases

In this section the simulation results are presented. In each simulation case a certain wind profile is considered and the optimization of the cyclic pitch variables, with parameterization using both Fourier series and spline are given. In the case with wind shear only, the spline method is not applied as the Fourier parameterization gives good enough performance. For each parameterization case, different numbers of parameters are chosen and the results are compared. As mentioned earlier, as the number of parameters increase, the performance of the cyclic pitch controller in reducing flapwise blade root bending moment increases, however the performance comes at the cost of more computationally expensive calculations.

Wind shear

A constant wind speed of *15 m/s* and shear factor of *0.2* is considered. **Figure** shows the wind speed variations as a function of the azimuth angle measured by a sensor placed at *r=63m* at the blade.

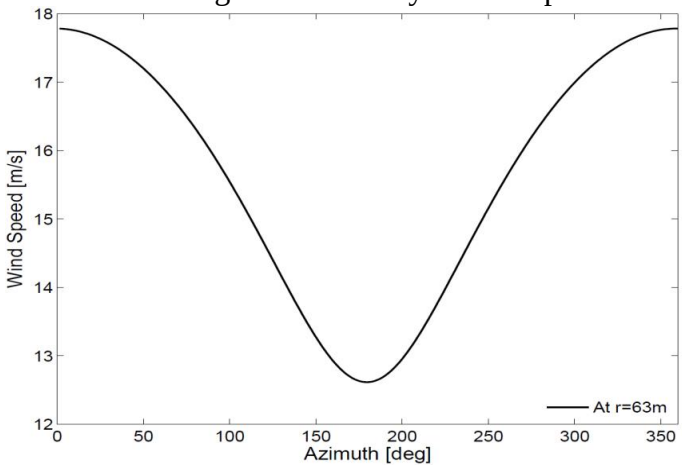

Figure 2.19 Wind speed as a function of the azimuth angle measured at r=63m of the blade

Figure shows the calculated pitch of the blades for different harmonic values. The harmonic number basically shows the different number of *N* in the equation 4.

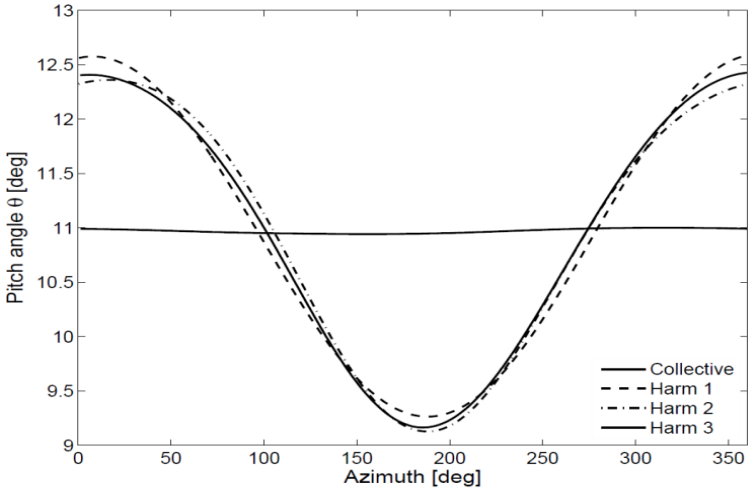

Figure 2.20 Calculated cyclic pitch angle of the baldes using Fourier parameterization method

The below figure shows the flapwise blade root bending moments for different cyclic pitch functions.

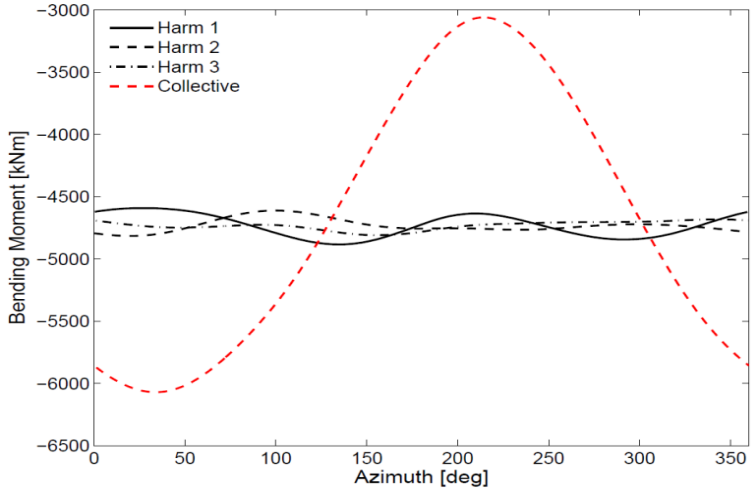

Figure 2.21 Flapwise blade root bending moment for cyclic pitch control with different number of Fourier parameters

Wind shear and tower shadow

In this simulation case a constant wind speed with a value of *15 m/s* and a shear factor of *0.2*, as well as the tower shadow are considered. **Figure** shows the wind speed variations as a function of the azimuth angle measured by a sensor placed at *r=63m* at the blade.

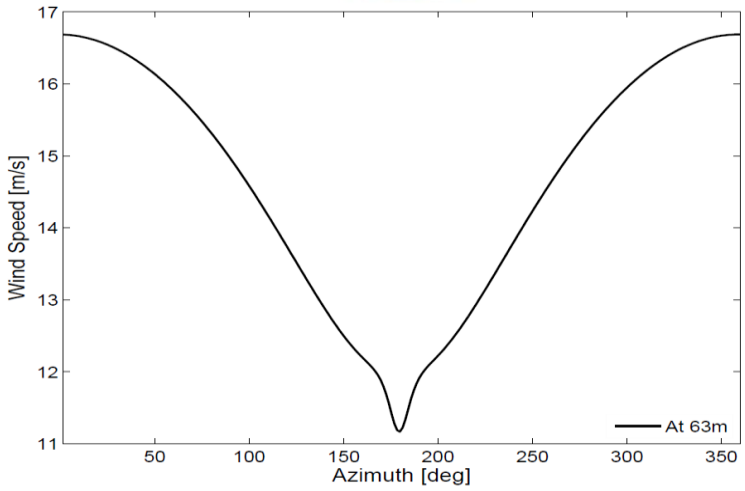

Figure 2.22 Wind speed as a function of the azimuth angle measured at r=63m of the blade

Figure below figure depicts the calculated pitch of the blades for different harmonic values in the Fourier parameterization case and different spline points for the spline parameterization case. The number of points in the spline curve is basically the number of affine spline functions which is *n* in the equation 5.

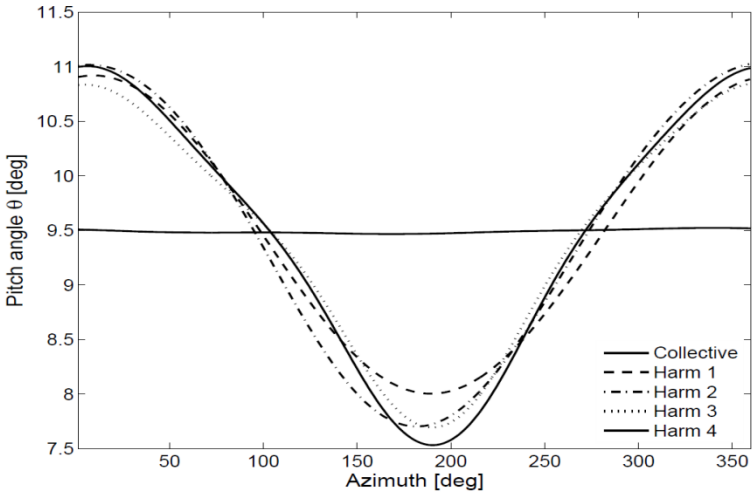

Figure 2.23 Calculated cyclic pitch angle of the blades using Fourier parameterization method

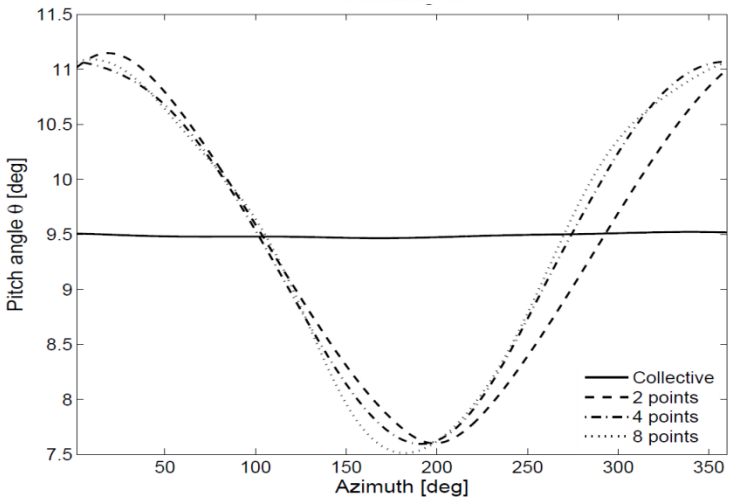

Figure 2.24 Calculated cyclic pitch angle of the baldes using periodic spline parameterization method

Figur 2.25 is a plot of sample flapwise blade root bending moments for the different pitch signals given in figure **Figure** . Figure 15 shows the same channel with pitch signals of figure **Figure** are used.

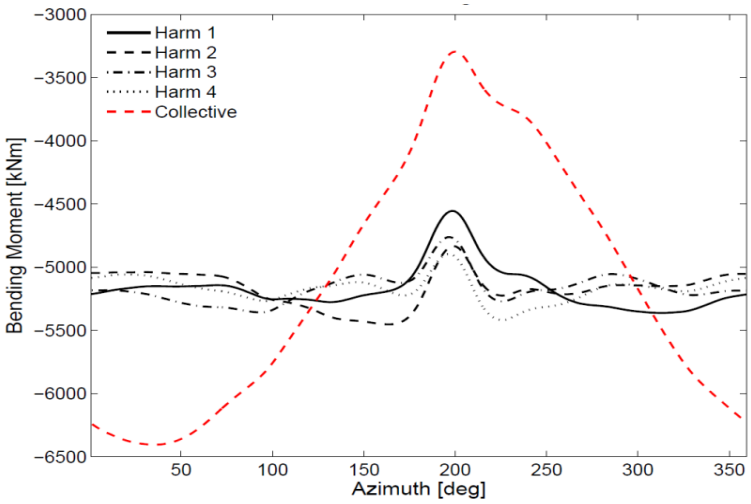

Figure 14 Flapwise blade root bending moment for cyclic pitch control with different number of Fourier parameters

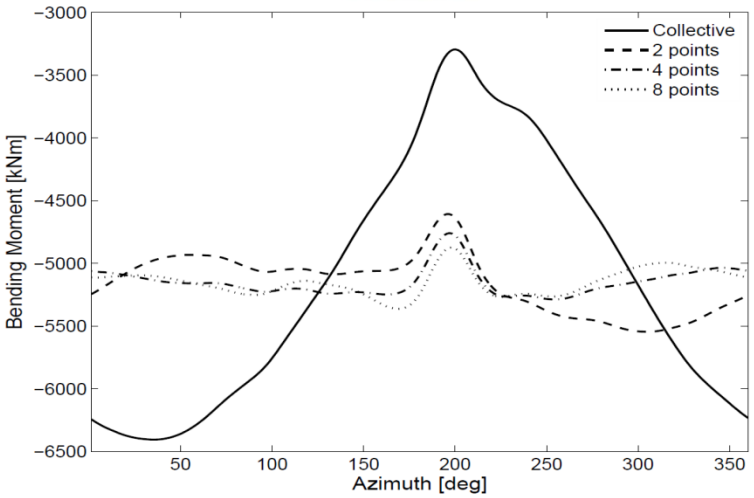

Figure 15 Flapwise blade root bending moment for cyclic pitch control with different number of periodic spline parameters

Wind shear, tower shadow and partial wake

In this simulation case a constant wind speed with a value of *15 m/s* and a shear factor of *0.2*, as well as the tower shadow are considered. Besides, the turbine is placed in a partial wake which is produced using Dynamic Wake Meandering Model (DWM)[11] built in HAWC2 code. The below figure shows the wind speed variations as a function of the azimuth angle measured by a sensor placed at *r=63m* at the blade. As it can be seen in the figure, there is a big reduction in the measured wind speed as the blade passes through the wake from azimuth angle around 225 degrees to 325 degrees. This results in large variations of the blade root bending moment. The variations can be alleviated using the given cyclic pitch controller.

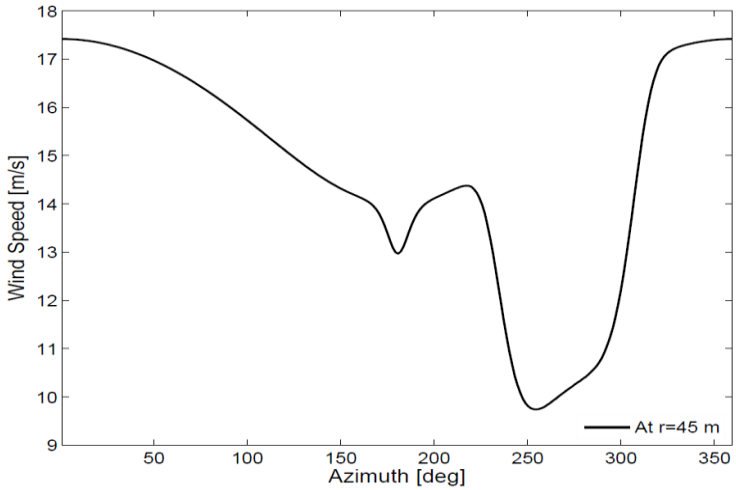

Figure 2.27 Wind speed as a function of the azimuth angle measured at r=63m of the blade

Figure below figure depicts the calculated pitch of the blades for different harmonic values in the Fourier parameterization case:

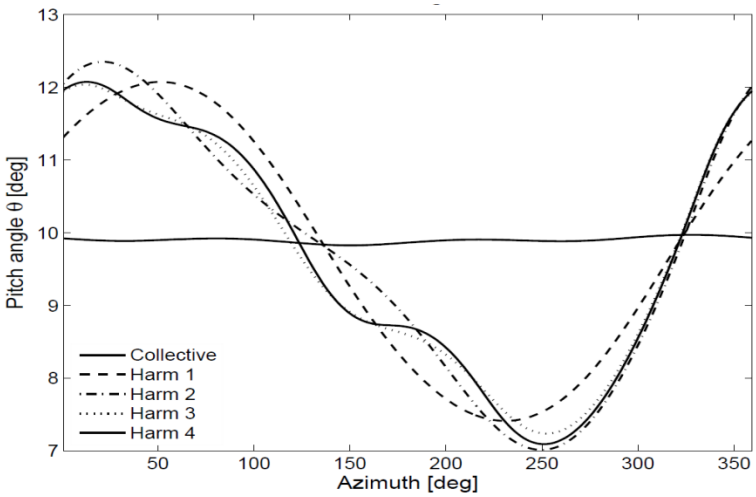

Figure 2.28 Calculated cyclic pitch angle of the blades using Fourier parameterization method

Figure 162.29 and 2.30 shows the flap wise blade root bending moments for the different pitch signals of the Fourier and spline parameterizations:

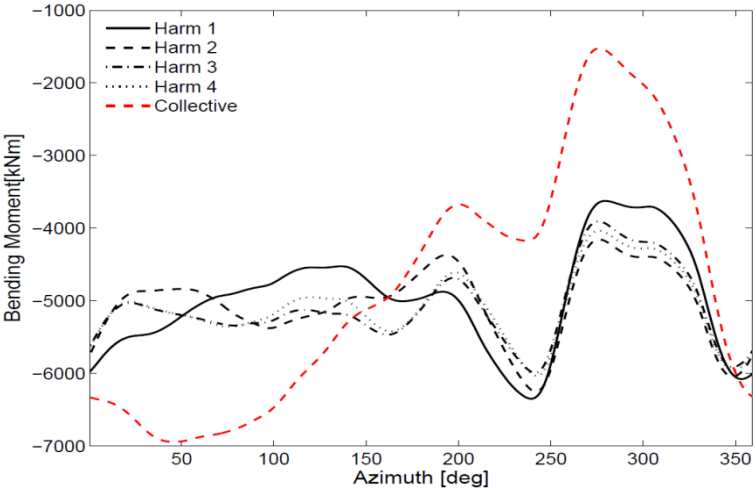

Figure 16 Flapwise blade root bending moment for cyclic pitch control with different number of Fourier parameters

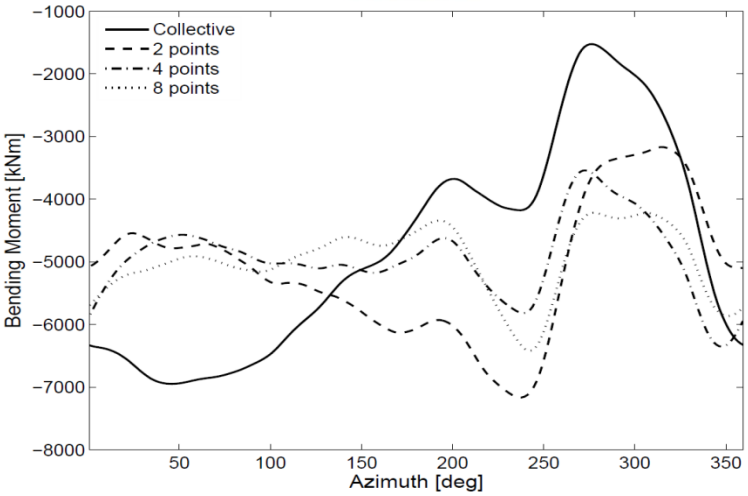

Figure 2.30 Flapwise blade root bending moment for cyclic pitch control with different number of periodic spline parameters

The above presentation depicts typical results on the performance achievable using cyclic pitch control to reduce variations on the blade root bending moment due to wind shear and tower shadow and partial wake effects. An optimization framework was setup to find the best possible cyclic pitch track. The obtained controller is only for performance assessment of an ideal cyclic pitch controller. If it is to be used jointly with Lidar wind observations, then the only case where we can make use of this controller is when the LIDAR can be proven to provide nearly perfect measurement of the effective wind speed of the individual blades. This analysis did not include load reductions from normal or extreme turbulent wind, since essentially cyclic pitch control is only reducing the sheared effect of the wind on the loads.

3.0 LIDAR Feed Forward control

3.1 LIDAR measurements and configuration for feed-forward control

For any feedback control loop, the measurement is a critical issue, since the control performance will be as good as the measurement could be, for the best case. This is not different for feed-forward control. And this is even more complicated for LIDAR based control, since the LIDAR devices provides many wind speed measurements, at different distances from the nacelle, in planes and several in plane points, however. Actually, this set of measurements is not useful by itself, since all this information needs to be transformed into a unique value, in case we want to develop feed-forward control based on collective pitch control. Even more, this value should be the best representation of the real wind suffered by the Rotor. This is sometimes known as the effective wind speed. For the case of INNWIND.EU 10MW, offshore (jacket supported), the LiDAR configuration used is shown in Table 3.1.

Table 3.1.- Features of LiDAR configuration

LiDAR configuration		
Type		Pulsed
Beams		1
Sample Rate [Hz]		50
Range	Nº Focal distances	5
	Focal distances [m]	102.5 to 222.5
Scan Mode		Circular Scan
Angle to Centerline [deg]		20
Assume perfect alignment		yes

With the idea of obtaining the most valuable and comparable results, some partners involved in LiDAR control development decided to use the same LiDAR emulator. Then, these INNWIND.EU partners involved on LIDAR based control development have used GH Bladed LIDAR measurements.

In order to have useful values for collective pitch feed-forward control, we need to have the best approximation for the effective wind speed coming to the rotor. Then this information goes into the feed-forward algorithm which modifies the pitch demand and/or torque demand. Then, the first step is to get a good estimation of the incoming inflow, based on the LIDAR measurements.

The basic idea is to get an estimation of incoming wind based on measurements at different distances and different plane positions. This could be understood as a volume wind measurements. In this case, the measurements of the wind are only in the component of the laser beam direction, line-of-sight wind speed - ***vlos***. Then it should be considered each measurement, compute the line-of-sight wind speed, using a pulse length, ***l***, of 60m in several points along the laser beam and apply a weighting function. Figure 3.17 shows the weighting function used for the simulated pulsed LiDAR.

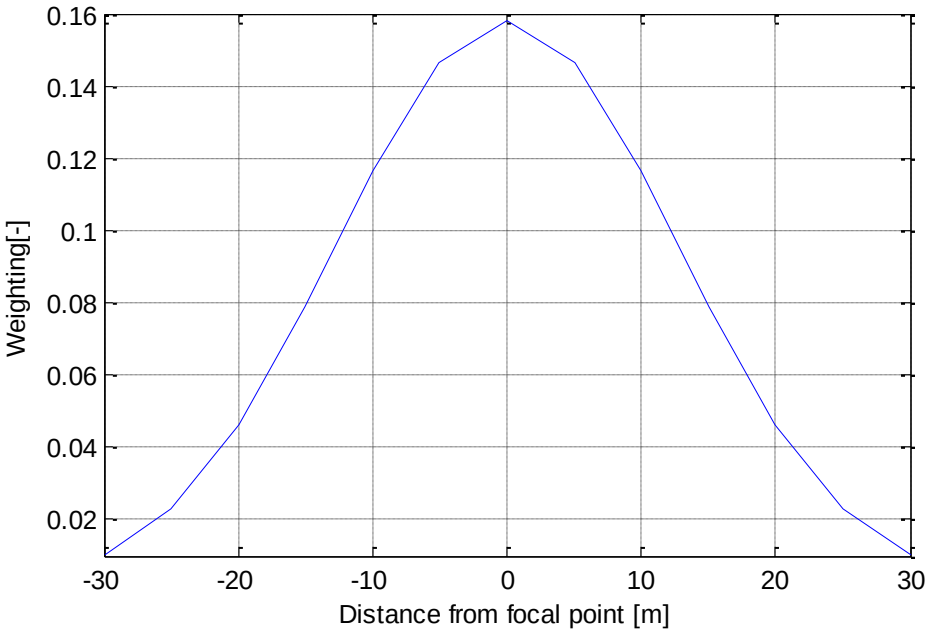

Figure 3.17.- Weighting function for the simulated pulsed LiDAR of INNWIND.EU

The line-of-sight winds speeds measurements provided by GH Bladed LiDAR emulator should then be used to reconstruct the wind field. The LiDAR measures the wind speed projected along the LiDAR's instantaneous line-of-sight unit pointing vector $\begin{bmatrix} l_{xi} & l_{yi} & l_{zi} \end{bmatrix}^T$. The line-of-sight winds speeds $v_{los,i}$ of each focus point can be modeled by:

$$v_{los,i} = l_{xi}u_i + l_{yi}\ v_i + l_{zi}w_i \qquad (1)$$

where $[u_i\ v_i\ \ w_i]^T$ is the wind speed vector. The incoming wind component for each focus point is reconstructed using the assumption of perfect alignment with the wind, then $v_i = w_i = 0$. Then, provided that we assume the turbine is perfectly aligned with the wind, the estimated lateral and vertical wind components are assumed to be zero and the longitudinal component u_i for each focus point *i* can be calculated as:

$$u_i = \frac{v_{los,i}}{l_{xi}} \qquad (2)$$

where $l_{xi} = \cos\varphi_i \cdot \cos\theta_i$ with φ_i , θ_i are the azimuth and elevation angle of the LiDAR beam, line-of-sight vector.

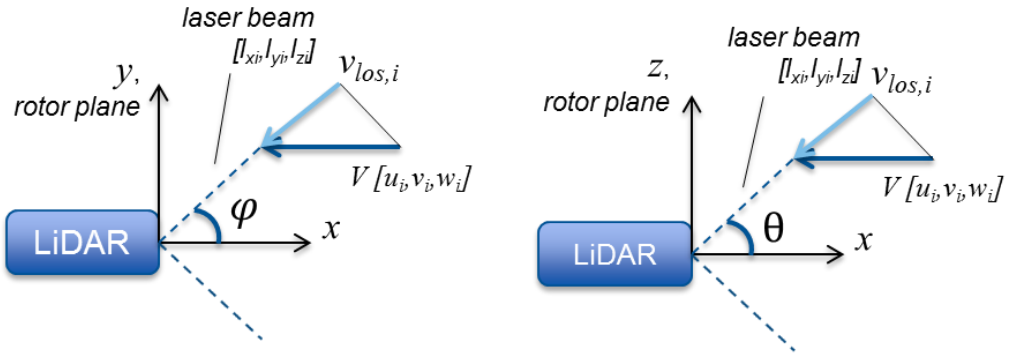

Figure 3.18.- LiDAR coordinate system from top and lateral views

This formulation may be implemented for all focal distances. Then, average for each plane of each focal distance can be computed. In this way, a time series for each focal distance is available simultaneously, and they are shifted or delayed according to Taylor's frozen turbulence hypothesis. For this time shift, details like delays of the LiDAR measurements, processing and the preview time needed for feedforward control, or even Wind Turbine dynamics may be considered. Now the time series of the focal distances are shifted, and these time series need to be combined to obtain one wind speed V_{0L}, the effective LiDAR wind speed, which is afterwards used for the feedforward control. Now, the estimated effective wind speed is available and can be considered as any other measurement in a control problem.

The first and most extended need for any control measurement is to avoid high frequency activity which may introduce undesired pitch activity on the control loops. Then a low pass filter is proposed to filter the V_{0L}. This filter may be of constant bandwidth, as usual in other control problems, or may be adaptive as suggested in [1].

Once the procedure for data treatment is agreed, this should be checked. Due to the available aeroelastic codes like GH Bladed, this is possible in simulation environment. As a check of accuracy of the LiDAR setup configuration, and the data processing, in Figure 3.19, in black is depicted the rotor average longitudinal wind speed provided by Bladed and in red, the obtained value of estimated wind speed by the already explained procedure and LiDAR measurements. In Figure 3.19 it is easy to see the coherence between values provided by GH Bladed and the one obtained. Of course that there are always some differences, but the correlation between signals is clear. Nevertheless, the goodness of the measurement may also be validated later based on the profits and improvements on the control loop and loads reduction on the INNWIND.EU 10MW offshore wind turbine.

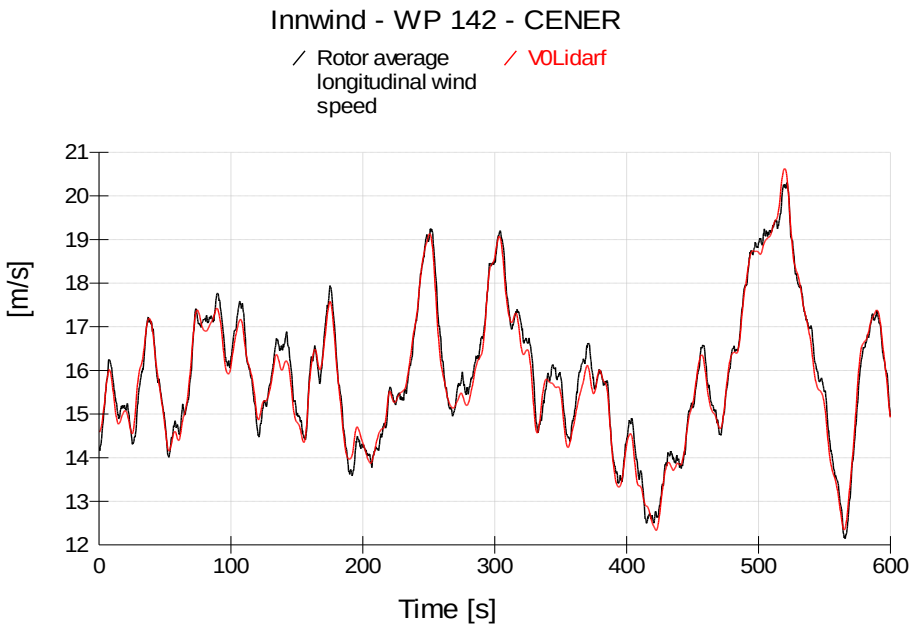

Figure 3.19.-Lidar rotor effective wind speed fitting to rotor average longitudinal wind speed

3.2 CENER FEEDFORWARD CONTROL

A full solution for a control loop requires a strategy which tries to cover all the performance needs, which implies reduction in both fatigue and extreme loads, as well as increased energy production, all of which may not be feasible, when combined. In the frame of INNWIND.EU project, CENER developed three different solutions which help in fatigue and extreme loads reduction, although no specific algorithm for increase energy production was developed. These solutions integrate together to get benefits in terms of loads. These are:

- FF1, works with pitch performance limits.
- FF2, operates over rotor speed set point, trying to improve the extreme loads envelope
- FF3, deals with a pitch speed demand contribution, in order to reduce fatigue and extreme loads, in cooperation with previous control concepts

These strategies are adapted and tuned to work with CENER's feedback control and for the 10 MW wind turbine. The combination of these three strategies assisted by LiDAR enhances the control performance of 10MW INNWIND.EU reference offshore wind turbine, jacket supported.

3.2.1 Feedforward Pitch Limits – FF1

When a wind gust hits the wind turbine, its rotor is accelerated and feedback control system tries to correct the speed error. This correction is limited by the wind turbine dynamics. With LiDAR measurements, it is possible to know the time a gust can strike the turbine, and then it may allow control system take action to protect the turbine before the gust affects it.

A simple and non-aggressive strategy is to set limits to the collective pitch angle which the control system may demand, according to the wind speed data reported by the LiDAR. In this algorithm, from LiDAR effective wind speed measurement, the control constructs maximum and minimum pitch angle limits. Figure 3.20 shows this feedforward control block.

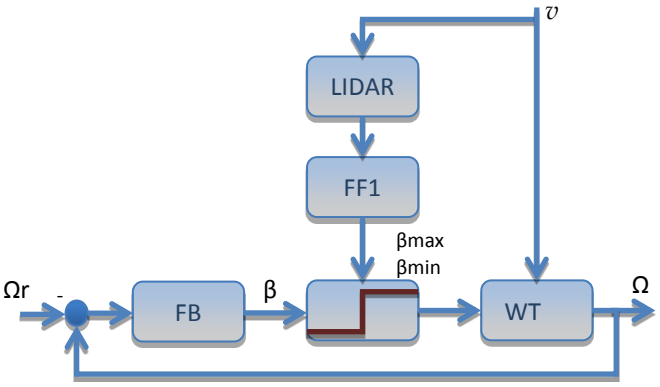

Figure 3.20.- Pitch Limitation feed forward strategy.

In normal operating conditions, aerodynamic static torque corresponds with the minimum between optimum and rated torque, Figure 3.21. These pitch angle limits are calculated from a minimum and maximum pre-determined aerodynamic torques. This calculation is carried out first with aerodynamic equations and secondly with a 3D look-up table (Cp-lambda-pitch angle).

First the aerodynamic desired torque Q_{est} is calculated as follows:

$$\Omega_{opt} = \frac{\lambda_{opt} \cdot v_0}{R} \quad (3)$$

$$Q_{est} = \min \begin{cases} K_{opt} \cdot \Omega_{opt}^2 \\ Q_{rated} \end{cases} \quad (4)$$

Where Ω_{opt} is the optimum rotor speed, λ_{opt} the optimum tip speed ratio, R the rotor radius, and $v_0 = v_{0L}(\tau + t)$ is the effective wind speed obtained by LiDAR measurements at preview time τ. Q_{rated} is the rated torque, and K_{opt} the optimal torque gain.

And from (3) and (4) $\frac{Cp}{\lambda^3}$ is obtained for β_{min} and $ß_{max}$:

$$\beta_{\max} : Q_{est} \cdot tol = \frac{1}{2}\rho\pi R^5 \frac{Cp}{\lambda^3}\Omega_r^{\,2} \quad (5)$$

$$\beta_{\min} : Q_{est} \cdot \frac{1}{tol} = \frac{1}{2}\rho\pi R^5 \frac{Cp}{\lambda^3}\Omega_r^{\,2} \quad (6)$$

Where ρ is the density of air, R is the rotor radius, Ωr is the rotor speed, λ is the tip speed ratio and Cp is the power coefficient. V_0 is the effective wind speed obtained from LiDAR measurements at a preview time τ_{FF1}

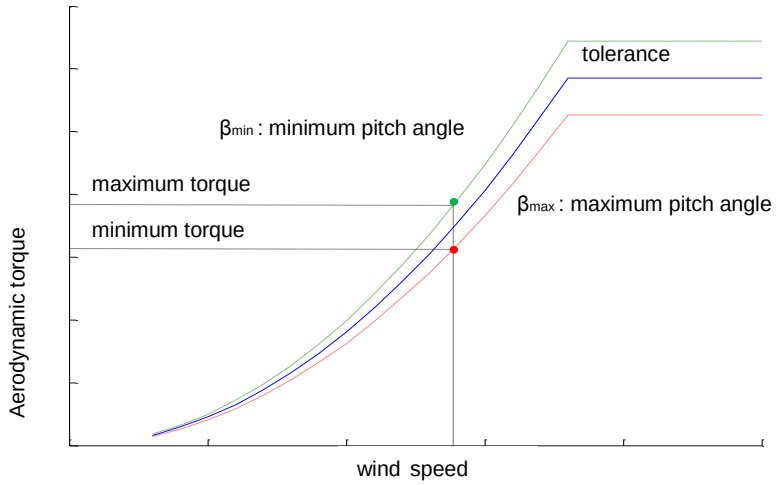

Figure 3.21.- Aerodynamic static torque vs wind speed

Finally with 3D look-up table (Cp-lambda-pitch angle), outputs $ß_{min}$ and $ß_{max}$. The objective is to force the control system to maintain the turbine in a state such that the expected aerodynamic torque will be between (*tol*) and (1/*tol*) times its optimum value, with *tol* a tolerance. Note that a large value of *tol* will result in this strategy having no effect, while a small value of *tol* will prevent the control system from regulating the rotor speed.

Figure 3.22 shows results for one ultimate load case of IEC standard, Normal operation with Extreme Operating Gust. The lower pitch angle limit obtained from this algorithm anticipates the gust and help the turbine to overcome it. As a result, load reduction is attained (see results section) and the turbine can continue operating.

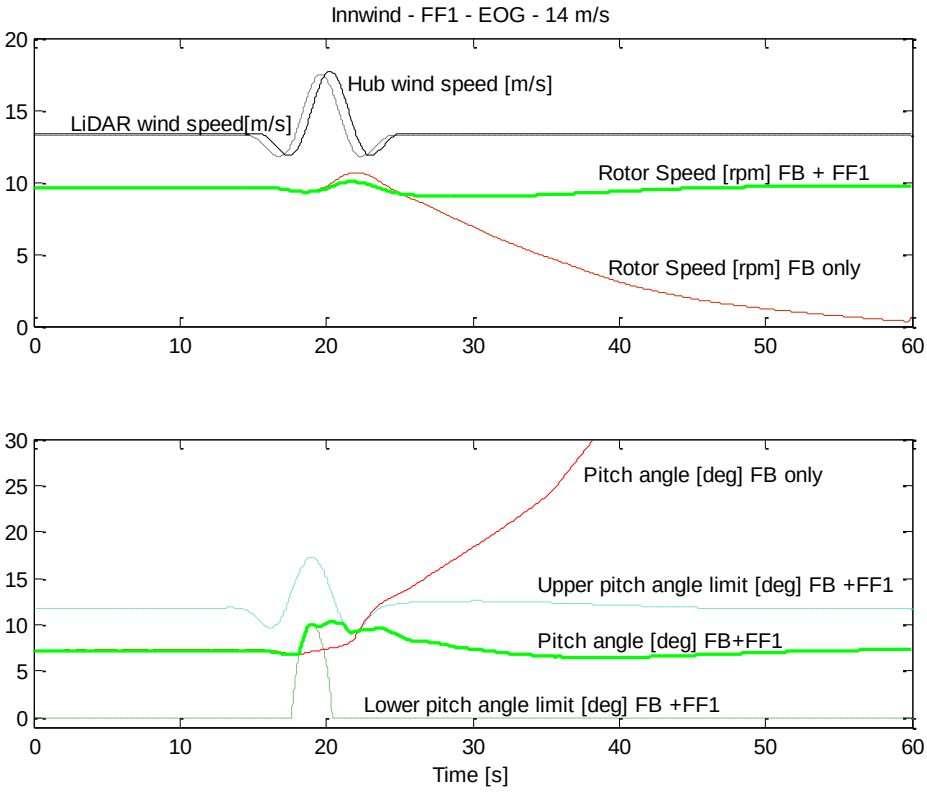

Figure 3.22.- Wind gust overcome with the assistance of FF1 strategy

3.2.2 Feedforward set point modification – FF2

It is well known that a full feedforward control strategy consists of two different blocks, as shown on Figure 3.23. The most extended feedforward solutions for Wind Turbine nowadays focus on *FFd* block, but it is also possible trying to work on *FFr*. However, this option is normally used for tracking problems, and taking into account that Wind Turbine control problems is more a pure disturbance rejection problem, *FFr* algorithm is refused. In addition, if we think about modifying rotor speed, commonly known as derating, this will cause reduction on power production, so *FFr* tends to be forgotten.

Although this is true, in some cases a temporally rotor speed set point modification could be interesting for extreme loads alleviation, without affecting in a negative way to power production, neither to fatigue loads. This is true since otherwise, the Wind Turbine may simply stop.

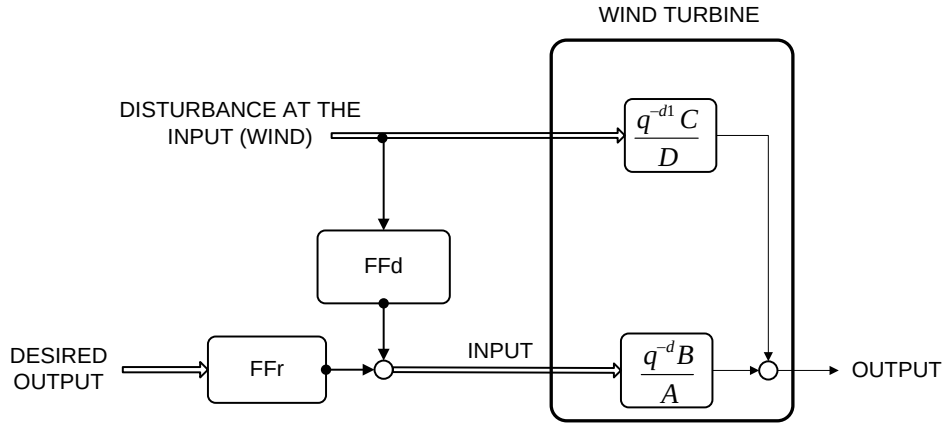

Figure 3.23.- Full feedforward control scheme

Then, trying to make use of *FFr*, this strategy is designed to reduce turbine loads and increase energy capture by preventing rotor overspeeds and shut downs. The algorithm was presented in [16] and here has been updated and improved for the INNWIND.EU 10 MW RWT.

A variable speed, pitch-controlled wind turbine typically operates with a constant speed setpoint at wind speeds above that for which the turbine is rated. The use of a LiDAR device allows the control system to adapt the speed at which the turbine operates to the wind conditions. The controller receives the LiDAR measurement, which anticipates the incoming wind speed. If a high wind approaches, the setpoint speed is reduced to protect the turbine. Otherwise, the speed is maintained to maximize the power output.

This idea is not too much different of a classical derating manoeuvre, but there is an important difference. A classical derating is based on statistics or low frequency filtered data of wind anemometers, pitch blade angles or similar ways of making a measurement of a mean wind, which has already passed through the Wind Turbine. This is different in the sense that the idea is similar, but trying to avoid undesired incoming winds, protecting the wind turbine, and not reducing power production.

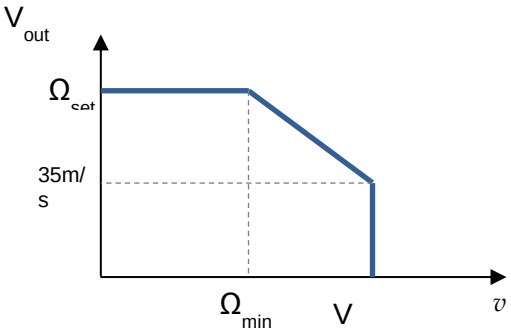

Figure 3.8.- Setpoint look up table of FF2 strategy

Figure shows the setpoint look up table of FF2 strategy, where Ω_{ar} is the above rated generator speed, 50.265 rad/s, Ω_{min} is the lower generator speed, 26.179 rad/s and V_{out} is the cut-out wind speed, 25m/s. Figure 3.24 shows simulation results of a power production load case from IEC 61400-3 standard. Here due to the high turbulent wind speed, ETM, the baseline controller achieves an over speed threshold at 39.16 s and the supervisory system shutdown the turbine. This shut down, and the loss of power production can be avoided with strategy FF2 enabled. The LiDAR system anticipates the wind speed increase and the generator speed setpoint is reduced, the pitch reacts increasing its value and preventing an overspeed and the subsequent shutdown.

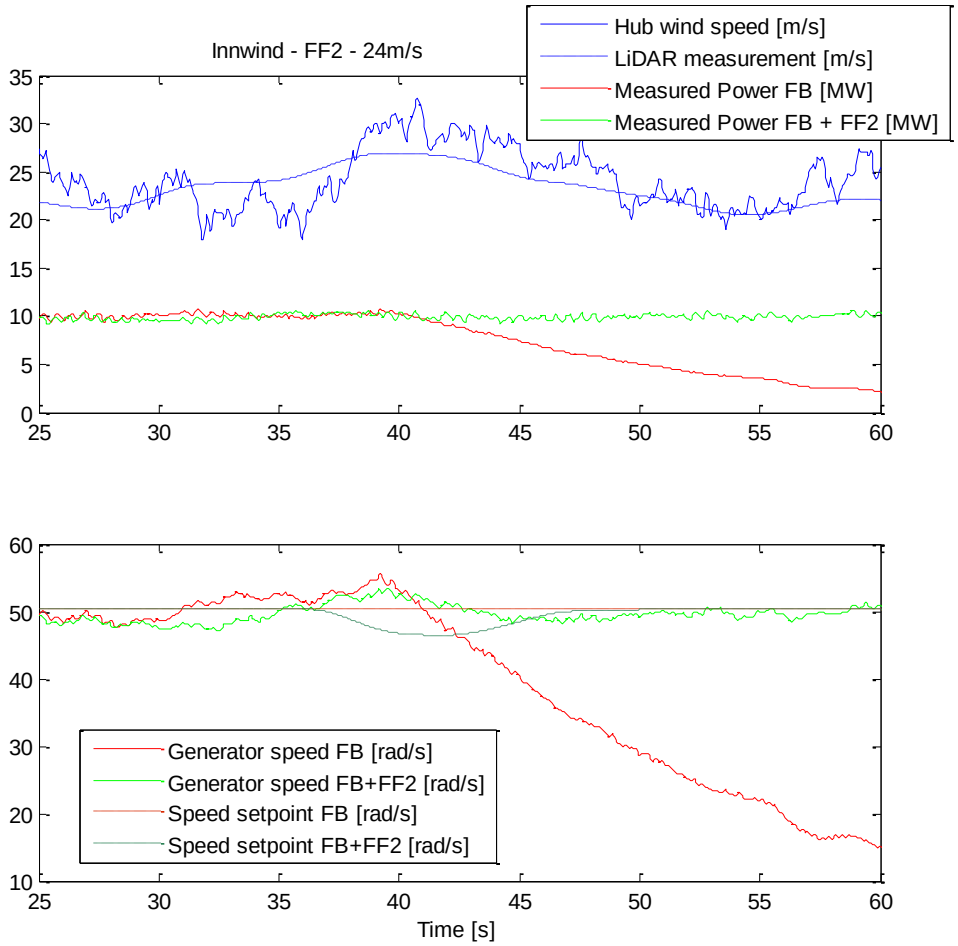

Figure 3.24.- DLC 13, ETM at 24m/s, with and without FF2 strategy

Figure 25 shows another simulation results for one ultimate load case of IEC 61400-3 standard, Power production plus loss of electrical grid connection. An unexpected grid loss fault happens 21.5 seconds into the simulation, when a severe wind gust is about to reach the turbine. The baseline controller is

oblivious to this gust, and is consequently operating the turbine at its rated speed when the safety system takes over and shuts the turbine down.

The LiDAR-assisted control system with the Strategy FF2 enabled, on the other hand, anticipates a high wind gust reaching the turbine, and therefore operates the turbine at a lower speed, in order to protect it. The take-over does eventually occur, and the safety system proceeds to shutting the turbine down, starting from a lower speed than in the standard control case. The resulting hub bending moment, as well as other loads not shown here, is clearly less severe.

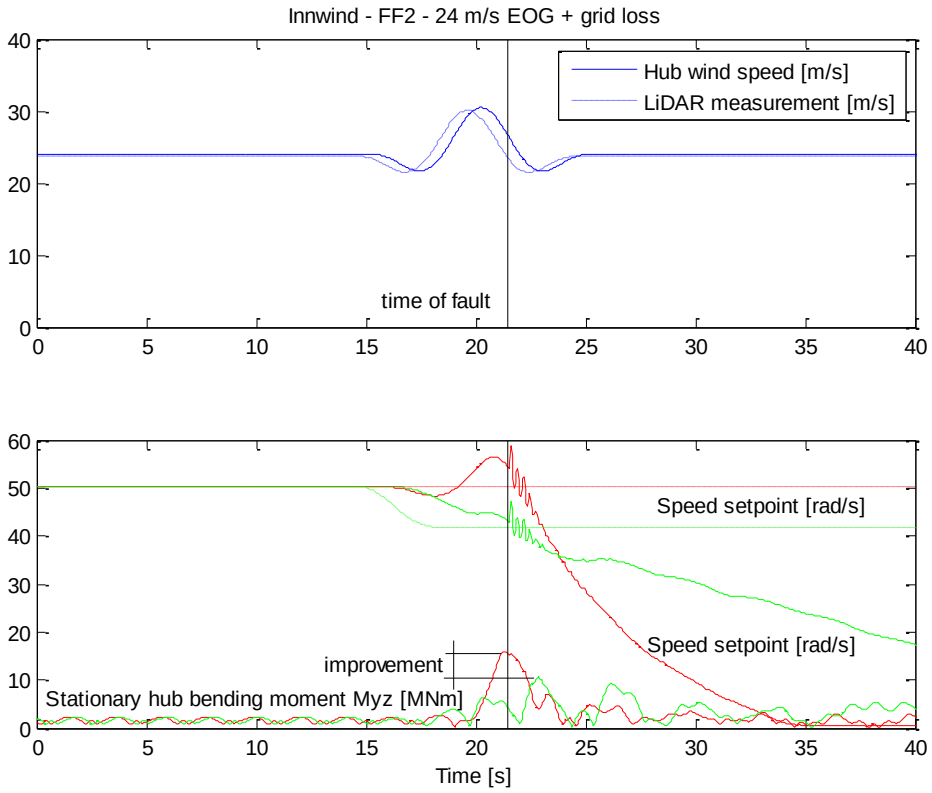

Figure 25.- DLC 23, EOG + grid loss, with and without FF2 strategy

3.2.3 Feedforward pitch rate contribution – FF3

Based on classical feedforward control scheme, Figure 3.23, FF3 focus on a more classical approach for LiDAR based controller, combining CENER's baseline feedback controller with a feed-forward based on analytical static gain for the 10 MW INNWIND.EU Wind Turbine.

In order to have a clear view of control performance in terms of loads, for a 10MW wind turbine, we added an IPC controller to the CENER's baseline controller. This will give the research community, but also manufactures' of Wind Turbine and components, a clear overview of a realistic load envelope. In this sense, we can analyze independently the effects of each loop in an independent way, since we will show the loads with the same control scheme than INNWIND.EU baseline controller, plus LIDAR and plus IPC. For more details on load calculations see section 6 on the load comparison results.

This feed-forward algorithm is focused on fatigue load reduction, and operates together with FF1 and FF2 structure in order to also obtain an extreme load reduction. This algorithm is easy and straightforward to implement and tune, which helps for a real implementation.

The developed FF3 algorithm is based on Predictive Disturbance Compensation (PDC) control theory. Theoretically, and provided the actuator has enough energy, in case some disturbances are known, they can be exactly compensated by feed-forward controller, FF3. This is true if the influence of the disturbance on the output is perfectly known, and the relation between the actuator and the controlled variable is also known and invertible. This means that we should know the transfer function between generator speed and the actual wind, and also the transfer function between the pitch angle and generator speed, which should in addition be invertible.

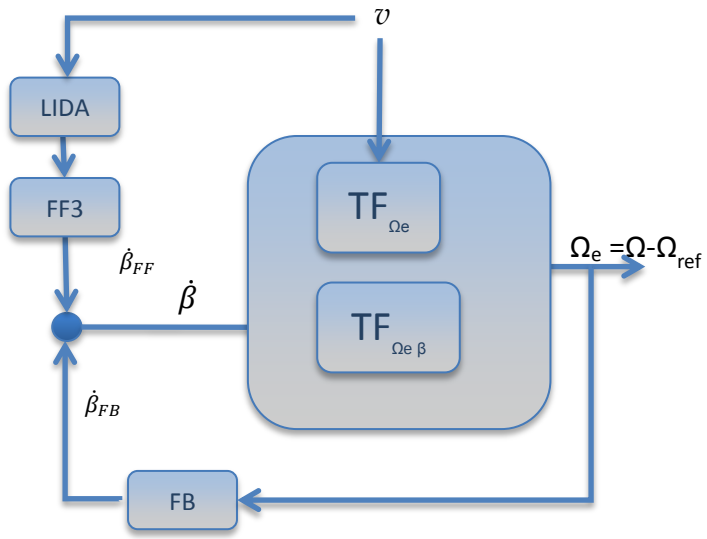

Figure 3.26.- Disturbance compensation feed-forward strategy with linearized wind turbine model

According to Figure 3.26 we have:

$$\Omega e = \frac{TF_{\Omega e\beta} \cdot FF3 \cdot v + TF_{\Omega eV} \cdot v}{1 - TF_{\Omega e\beta} \cdot FB} \quad (7)$$

The objective of the feedforward control is to get to a generator speed error,Ωe, equal to zero. In order to get this, theoretically, we can solve for the feedforward controller FF3 by setting numerator of (7) equal to zero. Then, we have:

$$FF3 = -TF_{\Omega e\beta}{}^{-1} \cdot TF_{\Omega eV} \quad (8)$$

However, it is well known that $TF_{\Omega e\beta}$ contains non-minimum phase zeros. Then, this would lead to an unstable FF3 feedforward compensator. Then, the result coming from eq. (8) cannot be implemented. Then, different solutions can try to solve this problem but always with different degrees of success. The first and simplest approach to eq. (8) is moving to a static compensation. Then, this static approach can be obtained based on:

$$\dot{\beta}_{FF}(t) = \frac{d\beta}{dv} \cdot \frac{dv}{dt} = \frac{d\beta}{dv_{ss}}\,(v_0(t-\tau_s)) \cdot \dot{v}_0(t-\tau_s) \quad (9)$$

Where v_0 is the effective wind speed obtained with LiDAR measurements, and τ_s is the preview time to apply the feed-forward contribution. $\dot{v}_0$ is the time derivative of v_0.

The feedforward gain, $\frac{d\beta}{dv_{ss}}$, in (9) can be obtained from aerodynamic information of the Wind Turbine, normally expressed as a static curve. Then, $\frac{d\beta}{dv_{ss}}$ can be implemented as look up table, and could be understood as the relation between the steady state effective wind and the steady state pitch angle.

However, it is also possible to get this $\frac{d\beta}{dv_{ss}}$ gain from linearized models coming from aeroelastic tools. From these tools, we can obtain the transfer function $TF_{\Omega eV}$, this is the transfer function from wind speed disturbance to rotor speed response. The same is also possible for the transfer function $TF_{\Omega e\beta}$ from the demanded pitch rate to the rotor speed response. The ratio between these magnitudes is equal to the required feed-forward gain, [13]. Here both methods are used and the control feed-forward gain $\frac{d\beta}{dv_{ss}}$ is shows in Figure 3.27. The gain in transition region, from region 2 to region 3, is smoothed to avoid peaks on region 2 region 3 transitions, which indeed may increase fatigue loads instead of reducing them.

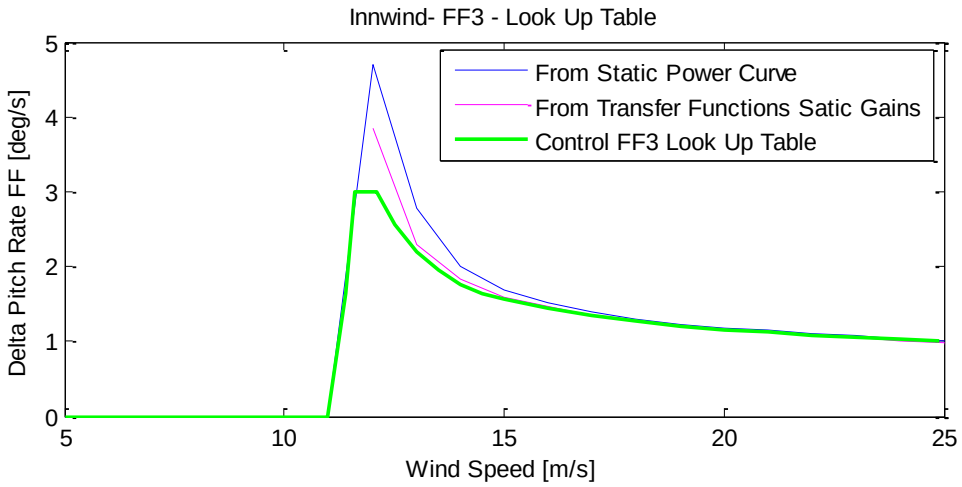

Figure 3.27.- Feed-forward gain per wind speed

The predictive time shift, **preview time**, in this case, is chosen to overcome the transition time due to pitch actuator dynamics. INNWIND.EU pitch actuator is modelled as 2nd order, from:

$$\frac{d^2\beta e(t)}{dt} + 2\varsigma\omega \cdot \frac{d\beta e(t)}{dt} + \omega^2 \cdot \beta_e(t) = \omega^2 \cdot \beta_d(t) \quad (10)$$

Where the input β_d, is the blade pitch angle demanded, and β_e is the output effective blade pitch angle. ω is the natural frequency and ς is the damping factor. The INNWIND.EU pitch actuator model is:

$$\omega = 1.6 \text{ Hz} \quad \text{and} \quad \varsigma = 0.8$$

Then, based on the pitch actuator model, the selected preview time to compensate the pitch actuator delay is 0.6 s, likes shows Figure 3.28.

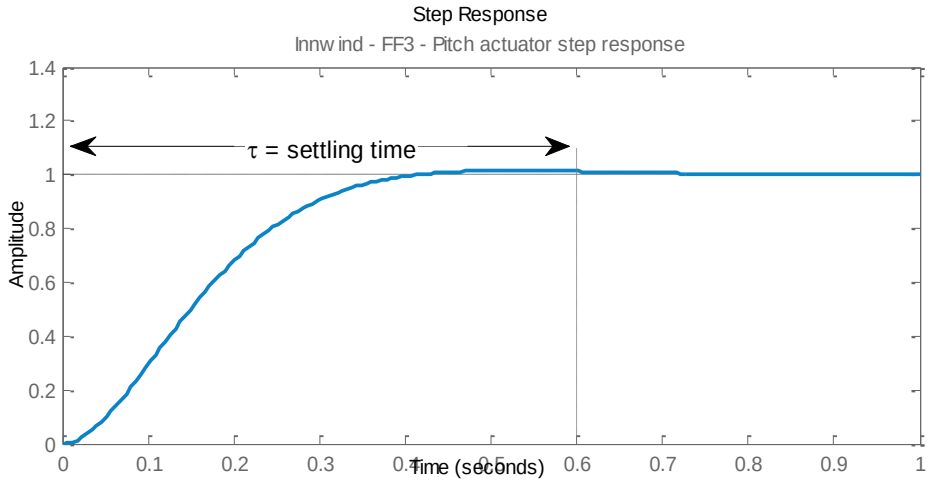

Figure 3.28.- Step response of pitch actuator model, settling time

Figure 3.29 shows a simulation results for one fatigue load, 16 m/s mean wind speed case of IEC 61400-3 standard. In this plot, we include results coming from the feedforward solution, FF3 in light green. In red we plot the same feedback controller, CENER's one, without the feedforward solution. We can see a significant reduction of 63.4% in standard deviation of rotor speed. Then we can conclude that speed regulation is enhanced with this FF3 feedforward strategy. Figure 3.30 shows the frequency content of these rotor speeds and how this reduction is achieved by feedforward loop. As was expected from the beginning, the major effect of feedforward control takes place at low frequencies, thanks to a much better disturbance rejection in the rotor speed.

However, also the objective of a control loop like this feedforward LiDAR based control is to reduce rotor excursions, this is not enough as a clear objective for Wind Turbine designers or manufactures. The only analysis of the rotor speed is not enough. A more deeply analysis is a must to get a real view of the impact in terms of loads reduction and power increase, in order to get the real goodness of the development, which is the reduction of the cost of energy.

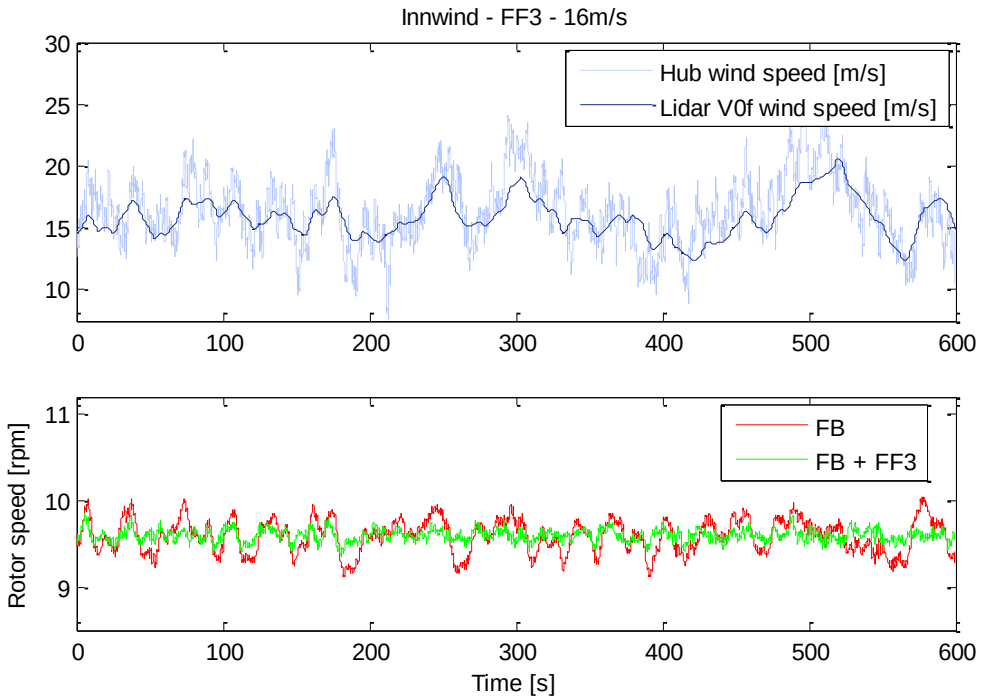

Figure 3.29.- Feed-forward speed regulation, FB vs FB+FF3 rotor speed, normal production load case DLC12 with 16 m/s mean wind speed

In order to give a detailed analysis of this control concept, a reduced set of load cases inspired on IEC-61400-1 Ed 3 standard is used. These set of load cases, include normal power production load cases, as well as actuator fails, grid loss, extreme operating gusts, etc.

This full load analysis is provided in more details in section 6, but it seems reasonable to balance between control performance in terms of rotor speed control, and reduction of loads on the Wind Turbine. This analysis suggests that using this FF3 feedforward algorithm in combination with the feedback pitch control, this last one may be redesigned and its specifications relaxed in order to achieve more load reductions, even some deteriorating the rotor speed control occurs in certain load cases.

Figure 3.31 shows the plot of Bode magnitude with the frequency characterization of the disturbance rejection of the control loop. In blue, we plot the sensitivity function for CENER's baseline controller, in green the same plot but with the feedforward control included. In light blue line is represented the sensitivity of the control system, including the feedforward control, but with CENER's baseline controller redesigned taking into account feedforward effects. This redesign, also affects in a negative way to rotor speed regulation, will improve loads reduction.

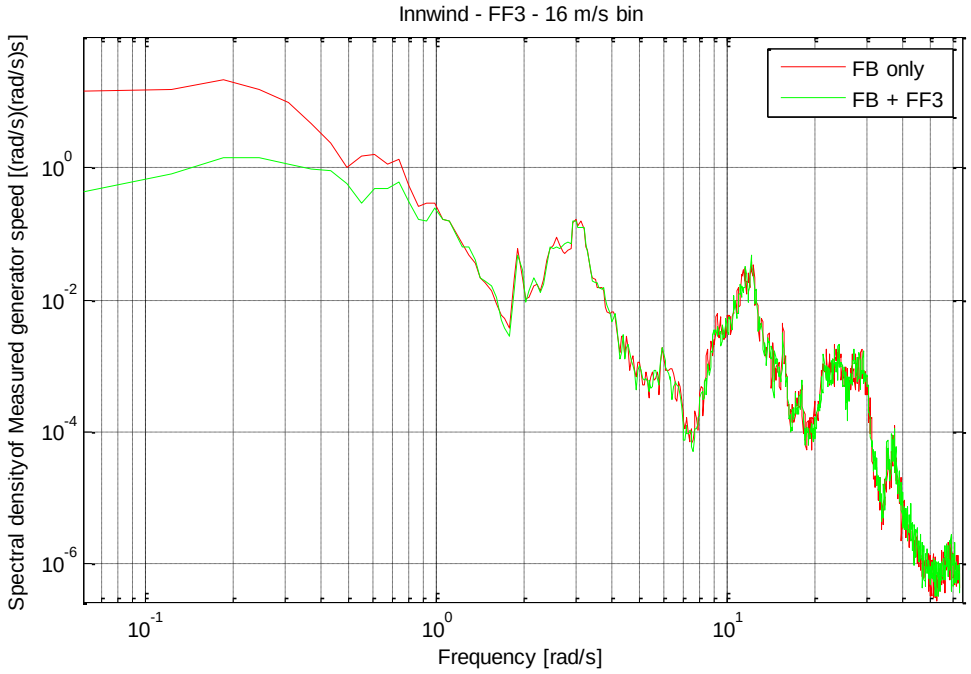

Figure 3.30.- Autospectral density of Measured generator speed [rad/s], FB vs FB+FF3, normal production load case DLC12 with 16 m/s mean wind speed

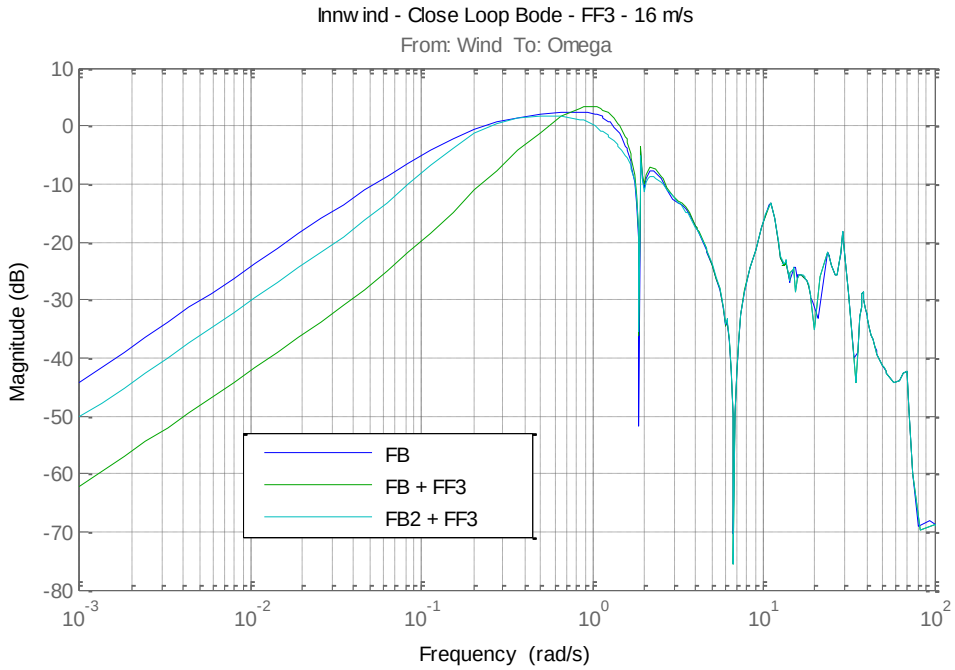

Figure 3.31.- Close loop Bode diagram from wind speed to generator speed of: feedback only controller FB, feedback + feedforward controller FB + FF3, and with new relaxed feedback +

Figure 3.32 shows the differences in terms of rotor speed and tower base loads with these three different controllers. Here it is clearly observed that rotor speed variations are reduced with the new feedback control parameterization and the obtained loads are lower for tower base bending moments.

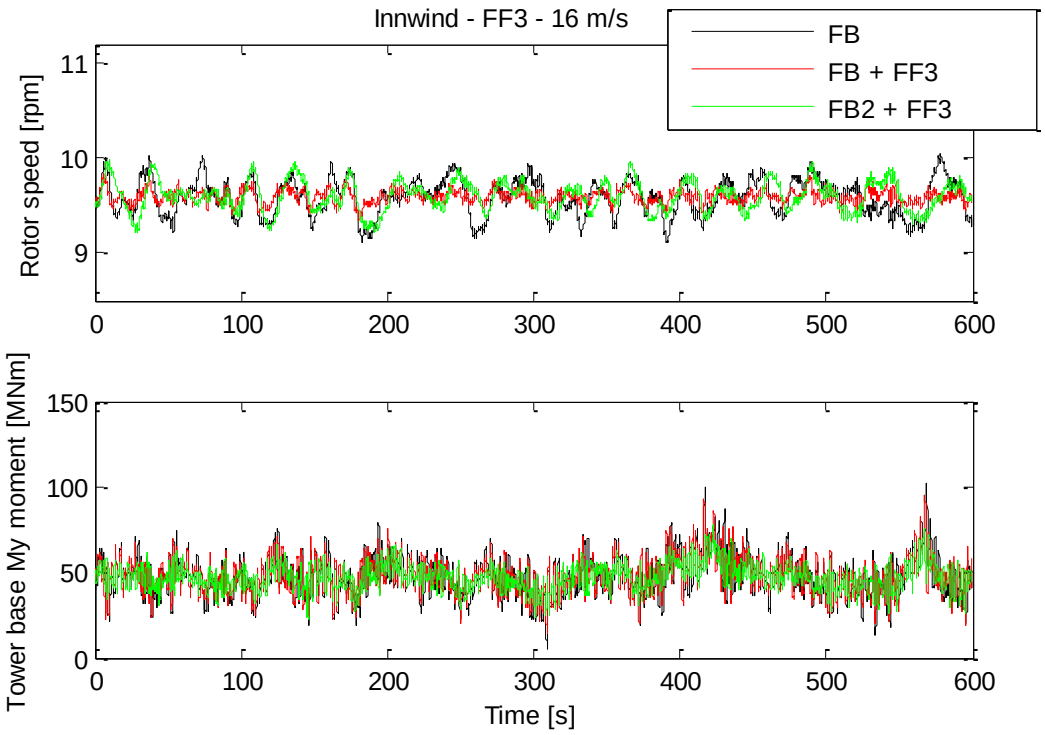

Figure 3.32.- Rotor speed [rpm] and Tower base bending moment [MNm] of: feedback controller FB, feedback + feedforward controller FB + FF3, and with new feedback parametrization + feedforward controller, FB2 + FF3.

The speed regulation with the new control setting of FB+FF3 controller is still better than the original feedback FB, obtaining a reduction of 18.96 % in standard deviation of rotor speed. Furthermore, now the damage equivalent loads (DEL) of this 10 min simulation show a significant reduction, see Table 3.2 for 16m/s case for details.

Table 3.2: DEL (N=2E06) for the complete 10 min simulation of Figure 3.32

DEL 16 m/s	FB [Nm]	FB+FF3 % above FB	FB2+FF3 % above FB
Tower Base My (m=4)	7.41E+07	-10.04	-20.02
Blade Root My (m=10)	2.50E+07	-0.36	-9.52

4.0 Model predictive control (MPC) with LIDAR measurements

In this work we are reporting the preliminary results of using LIDAR assisted MPC on the 10MW reference wind turbine.

Model predictive control (MPC) has been an active area of research and has been successfully applied on different applications in the last decades [7]. The reason for its success is its straightforward ability to handle constraints. Moreover it can employ feed-forward measurements in its formulation which is a key feature we will employ in this work. This ability helps us to use LIDAR measurements in the controller. Besides, MPC can easily be extended to MIMO systems. Wind turbine control is basically a MIMO control problem, although traditionally the different inputs and outputs are paired and separate control loops are used to overcome the control problem. In this work we treat the problem as a MIMO control problem, so the controller is aware of the interactions between different inputs and outputs and automatically compensate for it where necessary.

The main drawback of MPC is its on-line computational complexity which has kept its application to systems with relatively slow dynamics for a while. Fortunately with the rapid progress of fast computations, better optimization algorithms, off-line computations using multi-parametric programming [14] and dedicated algorithms and hardware, its applications have been extended to even very fast dynamical systems such as DC-DC converters [15].

Basically MPC uses a model of the plant to predict plants future behavior in order to compute appropriate control signals to control outputs/states of the plant. To do so, at each sample time MPC uses the current measurement/estimates of outputs/states and solves an optimization problem. The result of the optimization problem is a sequence of control inputs of which only the first element is applied to the plant and the procedure is repeated at the next sample time with new measurements [16]16. This approach is called receding horizon control. Therefore basic elements of MPC are:

- A model of the plant to predict its future
- A cost function which reflects control objectives
- Constraints on inputs and states/outputs
- An optimization algorithm
- The receding horizon principle

Depending on the type of the model which can be linear, hybrid and nonlinear, the control problem is called linear MPC, hybrid MPC, nonlinear MPC respectively. Nonlinear MPC is normally computationally very expensive and generally there is no guarantee that the solution of the optimization problem of MPC is a global optimum. In this work we extend the idea of linear MPC using a linear plant whose parameters vary as a function of a scheduling variable. Besides the disturbance to the

system is known beforehand and therefore the controller can take appropriate actions before the disturbance affects the outputs. There are some assumptions that restrict our solution to a specific class of problems. The scheduling variable is assumed to be known for the entire prediction horizon. And the operating point of the system mainly depends on the scheduling variable.

Wind Turbine Modeling

In order to design and simulate a closed loop system with a model based controller, we need two types of models. One model is the high fidelity simulation model which should be as accurate as possible in modeling the overall behavior of the plant. This model includes all the possible nonlinearities and dynamics of the real system.
The second model is called the design model which should be as simple as possible, yet it should be able to capture the most important dynamics and behavior of the system. Normally the design models are linearized and used locally around a linearization point. In the next two sections both the high fidelity simulation model and the linearized design model will be explained in details.

High Fidelity Simulation

In order to close the loop and test performance of the controller we need a simulation model. The simulation model behavior should be as close to the behavior of the real system as possible. Normally the simulation models include all degrees of freedom and the nonlinearities that can be modeled mathematically. There is the possibility of using different simulation models developed by different research institutes to verify closed loop behavior in different simulation scenarios. In this work FAST (Fatigue, Aerodynamics, Structures, and Turbulence) 17 is used as the simulation model and the 10MW reference wind turbine 10is used as the plant. FAST is a publicly available program for simulating wind turbine behaviors. The FAST code is an aero-elastic simulator capable of predicting both the extreme and fatigue loads of two- and three-bladed horizontal-axis wind turbines. In the simulation model 10 degrees of freedom are enabled which are: generator, drivetrain torsion, 1st and 2nd tower fore-aft, 2nd tower side-side, 1st and 2nd blade flapwise, 1st blade edgewise degrees of freedom.

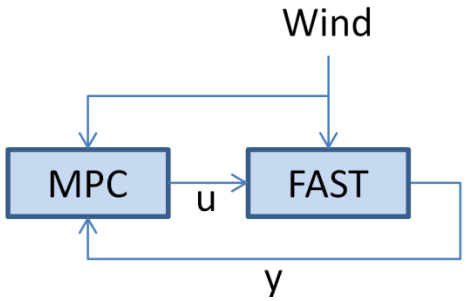

Figure 0-1 Closed loop system

Design model

In this section the nonlinear model and important degrees of freedom are explained. Afterwards the linearization procedure is described and a linear parameter varying model is derived for use in the model predictive controller.

Nonlinear model

For modeling purposes, the whole wind turbine can be divided into four subsystems: Aerodynamics subsystem, mechanical subsystem, electrical subsystem and actuator subsystem. The aerodynamic subsystem converts wind forces into mechanical torque and thrust on the rotor. The mechanical subsystem consists of the drivetrain, tower and blades. Drivetrain transfers rotor torque to the electrical generator. The tower holds the nacelle and withstands the thrust force. Blades transform wind forces into toque and thrust. The generator subsystem converts mechanical energy to electrical energy and finally the blade-pitch and generator-torque actuator subsystems are part of the control system. To model the whole wind turbine, models of these subsystems are obtained and at the end they are connected together. Figure below shows the basic subsystems and their interactions.

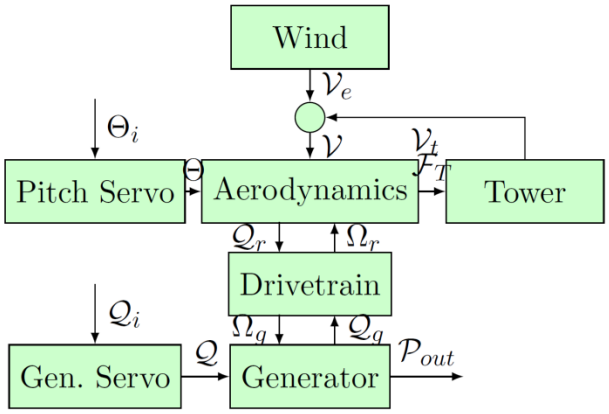

Figure 0-2 Wind turbine subsystem

T

he dominant dynamics of the wind turbine come from its flexible structure. Several degrees of freedom can be considered to model the flexible structure, but for control design, just a few important degrees of freedom are usually considered. In Figure 0-3, the essential degrees of freedom, which are normally being considered in the design model, are shown. In this work we have considered two degrees of freedom, namely the rotational degree of freedom (DOF) and the tower fore-aft motion.
Nonlinearity of the wind turbine model mostly comes from its aerodynamics. Blade element momentum (BEM) theory is used to numerically calculate aerodynamic torque and thrust on the wind turbine. Having aerodynamic torque and modeling the tower fore-aft degrees of freedom with simple mass-spring-damper, the whole system equation with 2 degrees of freedom becomes:

$$J_r\dot{\Omega} = Q_r - N_g Q_g \quad (9)$$

$$M_t\ddot{X}_t = Q_t - C_t \dot{X}_t - K_t X_t \quad (10)$$

$$P_e = Q_g \Omega_g \quad (11)$$

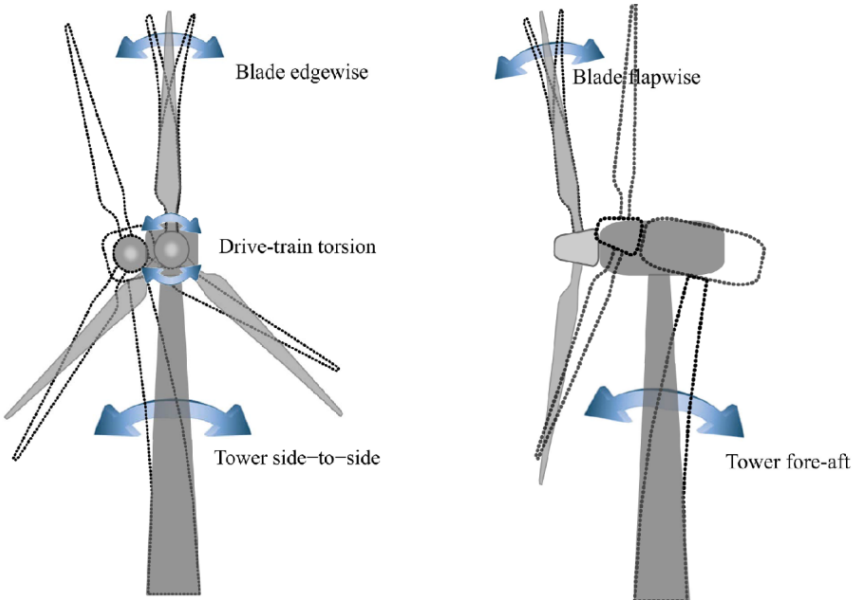

Figure 0-3 Basic degrees of freedom in a wind turbine

In which Qr and Qt are aerodynamic torque and thrust. Jr is the rotor moment of inertia, ψ is the drivetrain torsion, Qg is the generator torque and Ng is the gearbox ratio. The tower mass, damping and stiffness factors are represented by M_t, Ct and Kt, respectively, and Pe and Xt are the generated electrical power and tower displacement, respectively. Values of the parameters can be found in [10]. The Torque and thrust are nonlinear functions of the rotational speed Ω_r, the effective wind speed V_e and the blade pitch Θ.

$$Q_r = \frac{1}{2}\frac{1}{\Omega_r}\rho\pi R^2 V_e^3 C_p(\Theta, \Omega_r, V_e) \quad (12)$$

$$Q_t = \frac{1}{2}\rho\pi R^2 V_e^2 C_t(\Theta, \Omega_r, V_e) \quad (13)$$

Linearized model

For controller design purposes we need to linearize the nonlinear model given in equations 1 to 3. The nonlinear terms are the aerodynamic torque and generated power. As mentioned before the aerodynamic torque is a nonlinear function of effective wind speed V_e, rotational speed Ω_r and pitch of

the blade Θ. This nonlinear function is determined by a lookup table. The lookup table is produced using blade element momentum theory (BEM) algorithm. The generated power is nonlinear because it is a product of its two inputs, namely rotational speed and generator torque. The linearized state space model becomes:

$$\Delta Q_r(\omega,\theta,v_e) = \underbrace{\frac{\partial Q_r}{\partial \omega}}_{\alpha_1}\Delta\omega + \underbrace{\frac{\partial Q_r}{\partial \theta}}_{\beta_{11}}\Delta\theta + \underbrace{\frac{\partial Q_r}{\partial v_e}}_{\beta_{12}}\Delta v_e \tag{14}$$

$$\Delta Q_t(\omega,\theta,v_e) = \underbrace{\frac{\partial Q_t}{\partial \omega}}_{\alpha_2}\Delta\omega + \underbrace{\frac{\partial Q_t}{\partial \theta}}_{\beta_{21}}\Delta\theta + \underbrace{\frac{\partial Q_t}{\partial v_e}}_{\beta_{22}}\Delta v_e \tag{15}$$

$$\Delta P_e = \underbrace{\frac{\partial P_e}{\partial \omega_g}}_{Q_{g_0}}\Delta\omega_g + \underbrace{\frac{\partial P_e}{\partial Q_g}}_{\omega_{g_0}}\Delta Q_g \tag{16}$$

in which the linearization is done as follows:

$$\left.\frac{\partial Q_r}{\partial \theta}\right|_{(\theta^*,\omega_r^*,v_e^*)} = \frac{1}{2}\frac{1}{\omega_r}\rho\pi R^2 v_e^3 \left.\frac{\partial C_p}{\partial \theta}\right|_{(\theta^*,\omega_r^*,v_e^*)} \tag{17}$$

$$\left.\frac{\partial Q_r}{\partial \omega_r}\right|_{(\theta^*,\omega_r^*,v_e^*)} = \frac{1}{2}\rho\pi R^2 v_e^3 \left.(-\frac{1}{\omega_r^2}C_p + \frac{1}{\omega_r}\frac{\partial C_p}{\partial \omega_r})\right|_{(\theta^*,\omega_r^*,v_e^*)} \tag{18}$$

$$\left.\frac{\partial Q_r}{\partial v_e}\right|_{(\theta^*,\omega_r^*,v_e^*)} = \frac{1}{2}\frac{1}{\omega_r}\rho\pi R^2 \left.(3v_e^2 C_p + v_e^3\frac{\partial C_p}{\partial v_e})\right|_{(\theta^*,\omega_r^*,v_e^*)} \tag{19}$$

To get a linear model of the system we need to linearize the nonlinear model explained above around its operating points, which are determined by wind speed averaged on the rotor area. Wind speed changes along the blades and with the azimuth angle (angular position) of the rotor. This is because of wind shear, tower shadow and stochastic spatial distribution of the wind field. Therefore a single wind speed does not exist to be used and measured in order to find the operating point. We bypass this problem by defining a fictitious variable called effective wind speed (Ve), which shows the effect of wind on the rotor disc of the wind turbine. Using the linearized aerodynamic torque and thrust, state space matrices for the 3 DOFs linearized model become:

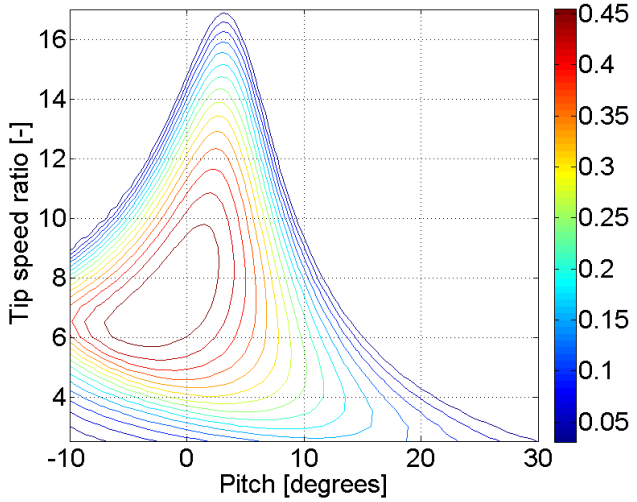

Figure 4-4 Cp curve of the wind turbine

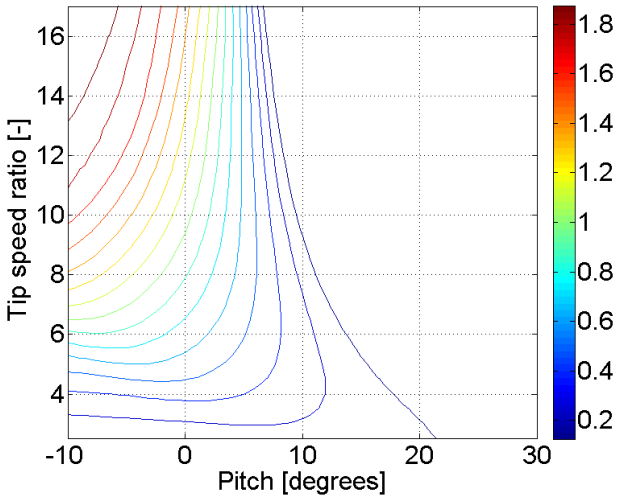

Figure 0-5 Ct curve of the wind turbine

$$\dot{\omega}_r = \frac{\alpha_1(v_e)}{J_r}\omega_r + \frac{\beta_{11}(v_e)}{J_r}\theta + \frac{\beta_{12}(v_e)}{J_r}(v_e - v_t) - Q_g \quad (20)$$

$$\dot{x}_t = v_t \quad (21)$$

$$\dot{v}_t = \frac{\alpha_2(v_e)}{M_t}\omega_r + \frac{\beta_{21}(v_e)}{M_t}\theta + \frac{\beta_{22}(v_e)}{M_t}(v_e - v_t) - \frac{C_t}{M_t}v_t - \frac{K_t}{M_t}x_t \quad (22)$$

$$P_e = Q_{g0}\omega_g + \omega_{g0}Q_g \quad (23)$$

In which the lower-case variables are deviations away from the steady state of the upper-case variables given in the equations 1 to 3. Consequently, the parameters of the linearized model are functions of wind speed, which in our approach acts as a scheduling variable. A detailed description of the model and linearization is given in [18].

Linear parameter varying model

According to the model given in the equations 12 to 15, the matrices of the state space model become:

$$A(\gamma) = \begin{pmatrix} \frac{\alpha_1(v_e)}{J_r} & 0 & \frac{\beta_{12}(v_e)}{J_r} \\ 0 & 0 & 1 \\ \frac{\alpha_2(v_e)}{M_t} & -\frac{K_t}{M_t} & -\frac{C_t}{M_t} \end{pmatrix} \quad (24)$$

$$B(\gamma) = \begin{pmatrix} \frac{\beta_{11}(v_e)}{J_r} & \frac{\beta_{12}(v_e)}{J_r} \\ 0 & 0 \\ \frac{\beta_{21}(v_e)}{M_t} & \frac{\beta_{22}(v_e)}{M_t} \end{pmatrix} \tag{25}$$

$$C(\gamma) = \begin{pmatrix} 1 & 0 & 0 \\ Q_{g0} & 0 & 0 \\ \frac{\beta_{22}(v_e)}{M_t} & -\frac{K_t}{M_t} & -\frac{C_t}{M_t} \end{pmatrix} \tag{26}$$

$$D(\gamma) = \begin{pmatrix} 0 & 0 \\ 0 & \omega_0 \\ \frac{\beta_{21}(v_e)}{M_t} & \frac{\beta_{22}(v_e)}{M_t} \end{pmatrix} \tag{27}$$

in which $x = (\omega_r \quad x_t \quad \dot{x}_t)$, $u = (\theta \quad Q_g)$, $y = (\omega_r \quad P_e \quad \dot{x}_t)$ are states, inputs and outputs respectively. Now that we have the linearized state space model of the system, we can proceed to use this model in the control design procedure.

Controller Design

In this section we begin by explaining model predictive control (MPC) and different components of it in general. Then we will present the linear MPC formulation. After explaining linear model with known disturbance, we will explain how the MPC problem of such system with can be formulated.

Model predictive control

Generally the nonlinear dynamics of a plant could be modeled as the following difference equation:

$$x_{k+1} = f(x_k, u_k, d_k) \tag{28}$$

With x k ,u k and d k as states, inputs and disturbances respectively. Using the nonlinear model, the nonlinear MPC problem can be formulated as:

$$\begin{aligned} \min_{u} \quad & \ell(x_N) + \sum_{i=0}^{N-1} \ell(x_{k+i|k}, u_{k+i|k}) \\ \text{Subject to} \quad & x_{k+1} = f(x_k, u_k, d_k) \\ & u_{k+i|k} \in \mathbb{U} \\ & \hat{x}_{k+i|k} \in \mathbb{X} \end{aligned} \tag{29}$$

Where l denotes some arbitrary norm and U and X show the set of acceptable inputs and states. As it was mentioned because of the nonlinear model, this problem is computationally too expensive. One way to avoid this problem is to linearize around an equilibrium point of the system and use linearized model instead of the nonlinear model. We can also employ the fact that we know the future values of the disturbance to the system, namely the wind speed.

Linear MPC formulation

The problem of linear MPC can be formulated as:

$$\begin{aligned} \min_{u_0, u_1, \ldots, u_{N-1}} \quad & \|x_N\|_{Q_f} + \sum_{i=0}^{N-1} \|x_{k+i|k}\|_Q + \|u_{k+i|k}\|_R \\ \text{Subject to} \quad & x_{k+1} = Ax_k + Bu_k \\ & u_{k+i|k} \in U \\ & \hat{x}_{k+i|k} \in X \end{aligned} \tag{30}$$

Assuming that we use norms 1, 2 and ∞, the optimization problem becomes convex providing that the sets U and X are convex. Convexity of the optimization problem makes it tractable and guarantees that the solution is the global optimum. The problem above is based on a single linear model of the plant around one operating point. However, for some plants the assumption of a linear model does not hold for long prediction horizons. This is because the plant operating point changes, for example on the basis of disturbances that act as a scheduling variable. An example could be a wind turbine for which wind speed acts as a scheduling variable and changes the operating point of the system.

Wind turbine control is a challenging problem as the dynamics of the system changes based on wind speed which has a stochastic nature. In this paper, we use the wind speed as the scheduling variable. With the advances in the LIDAR technology, it is possible to measure wind speed ahead of the turbine and this enables us to have the scheduling variable of the plant for the entire prediction horizon. As it was mentioned in section before, wind turbines are nonlinear dynamical systems and if we use the nonlinear model directly in the MPC formulation, the optimization problem associated with the MPC becomes non-convex. In general, non-convex optimization problems are very complicated to solve and there is no guarantee that we could achieve a global optimum. One way to avoid complex and non-convex optimization problems is to linearize the system around an equilibrium point and use the obtained linearized model as an approximation of the nonlinear model. However, for wind turbines,

assumption of the approximate linear model does not hold for long prediction horizons. This is because the operating point of the system changes as a function of wind speed which, as mentioned, has a stochastic nature. In the next section we formulate the MPC problem using the linearized state space model with varying parameters as a function of wind speed.

Problem formulation

The linear parameter varying (LPV) model of the nonlinear system is of the following form:

$$\tilde{x}_{k+1} = A\tilde{x}_k + B\tilde{u}_k + B_d\tilde{d}_k \tag{31}$$

This model is formulated based on deviations from the operating point. However we need the model to be formulated in absolute values of inputs and states. Because in our problem the operating point changes as a function of the scheduling variable, we need to introduce a variable to capture its behavior. In order to rewrite the state space model in the absolute form we use $\tilde{x}_k = x_k - x_k^0$, $\tilde{u}_k = u_k - u_k^0$ and $\tilde{d}_k = d_k - d_k^0$ where x_k^0, $u_k^0$and d_k^0 are values of states, inputs and disturbance at the operating point. Therefore, the LPV model becomes:

$$x_{k+1} = x_{k+1}^0 + A(x_k - x_k^0) + B(u_k - u_k^0) + B_d(d_k - d_k^0) \tag{32}$$

which can be written as:

$$x_{k+1} = Ax_k + Bu_k + B_d d_k + f_k \tag{33}$$

with

$$f_k = x_{k+1} - (Ax_k^0 + Bu_k^0 + B_d d_k^0) \tag{34}$$

Now having the linear model (in fact this is an affine model) of the system we can proceed to compute the state predictions.

$$x_{k+1} = Ax_k + Bu_k + f_k \tag{35}$$

$$\begin{aligned} x_{k+2} &= Ax_{k+1} + Bu_{k+1} + f_{k+1} \\ &= A(Ax_k + Bu_k + f_k) + Bu_{k+1} + f_{k+1} \\ &= A^2x_k + ABu_k + Af_k + Bu_{k+1} + f_{k+1} \end{aligned} \tag{36}$$

$$\begin{aligned} x_{k+3} &= Ax_{k+2} + Bu_{k+2} + f_{k+2} \\ &= A(A^2x_k + ABu_k + Af_k + Bu_{k+1} + f_{k+1}) + Bu_{k+2} + f_{k+2} \\ &= A^3x_k + A^2Bu_k + A^2f_k + ABu_{k+1} + Af_{k+1} + Bu_{k+1} + f_{k+1} \end{aligned} \tag{37}$$

$$\begin{aligned} y_k &= Cx_k + Du_k + g_k \\ y_{k+1} &= Cx_{k+1} + Du_{k+1} + g_{k+1} \end{aligned} \tag{38}$$

Now that we know how to calculate the state and output predictions we can stack the predictions in one vector as below:

$$
\begin{aligned}
X &= \begin{pmatrix} x_{k+1} & x_{k+2} & \dots & x_{k+N} \end{pmatrix}^T \\
U &= \begin{pmatrix} u_k & u_{k+1} & \dots & u_{k+N-1} \end{pmatrix}^T \\
Y &= \begin{pmatrix} y_k & y_{k+1} & \dots & y_{k+N-1} \end{pmatrix}^T \\
D &= \begin{pmatrix} d_k & d_{k+1} & \dots & d_{k+N-1} \end{pmatrix}^T \\
F &= \begin{pmatrix} f_k & f_{k+1} & \dots & f_{k+N-1} \end{pmatrix}^T \\
G &= \begin{pmatrix} g_k & g_{k+1} & \dots & g_{k+N-1} \end{pmatrix}^T
\end{aligned}
\tag{39}
$$

Using the stacked notation the state and output predictions can be written as functions of the current state, the input sequence (stack of it), and the disturbance:

$$
\begin{aligned}
&X = \Phi_x x_k + \Gamma_u U + \Gamma_d D + \Gamma_f F \\
&Y = CX + DU + \Phi_g G \\
&\quad \Longrightarrow \\
&Y = C\Phi_x x_k + C\Gamma_u U + C\Gamma_d D \\
&\quad + C\Gamma_f F + DU + \Phi_g G
\end{aligned}
\tag{40}
$$

in which the matrices are:

$$
Y = \begin{pmatrix} y_k \\ y_{k+1} \\ \vdots \\ y_{k+N-1} \end{pmatrix} \qquad U = \begin{pmatrix} u_k \\ u_{k+1} \\ \vdots \\ u_{k+N-1} \end{pmatrix} \qquad D = \begin{pmatrix} d_k \\ d_{k+1} \\ \vdots \\ d_{k+N-1} \end{pmatrix}
$$

$$
F = \begin{pmatrix} f_k \\ f_{k+1} \\ \vdots \\ f_{k+N-1} \end{pmatrix} \qquad G = \begin{pmatrix} g_k \\ g_{k+1} \\ \vdots \\ g_{k+N-1} \end{pmatrix}
\tag{41}
$$

$$
\Phi_x = \begin{pmatrix} I \\ A \\ A^2 \\ \vdots \\ A^{N-1} \end{pmatrix} \qquad \Phi_g = \begin{pmatrix} I \\ I \\ I \\ \vdots \\ I \end{pmatrix}
\tag{42}
$$

$$
\Gamma_u = \begin{pmatrix} B & 0 & \dots & 0 \\ AB & B & \dots & 0 \\ \vdots & \vdots & \ddots & \vdots \\ A^{N-2}B & A^{N-3}B & \dots & B \end{pmatrix} \qquad \Gamma_f = \begin{pmatrix} I & 0 & \dots & 0 \\ A & I & \dots & 0 \\ \vdots & \vdots & \ddots & \vdots \\ A^{N-2} & A^{N-3} & \dots & I \end{pmatrix}
\tag{43}
$$

$$\Gamma_d = \begin{pmatrix} B_d & 0 & \dots & 0 \\ AB_d & B_d & \dots & 0 \\ \vdots & \vdots & \ddots & \vdots \\ A^{N-2}B_d & A^{N-3}B_d & \dots & B_d \end{pmatrix}$$

After computing the state predictions as functions of control inputs, we can write down the optimization problem similar to a linear MPC problem as a quadratic program, more details can be found in [19].
The problem of linear MPC can be formulated as:

$$\begin{aligned} \min_{U} \quad & Y^T Q Y + U^T R U \\ \text{Subject to:} \quad & U \in \mathbb{U} \\ & X \in \mathbb{X} \end{aligned} \tag{44}$$

Control objectives
The most basic control objective of a wind turbine is to maximize captured power during the life time of the wind turbine that is to maximize captured power when wind speed is below its rated value. This is also called maximum power point tracking (MPPT). However when wind speed is above rated, control objective becomes regulation of the outputs around their rated values while trying to minimize dynamic loads on the structure. These objectives should be achieved against fluctuations in wind speed which acts as a disturbance to the system. In this work we have considered operation of the wind turbine in above rated (full load region). Therefore, we try to regulate rotational speed and generated power around their rated values and remove the effect of wind speed fluctuations.

The PI Controller
The PI controller is very similar to the reference turbine controller. In this configuration there are different controllers that are responsible for different operating regimes. There is a partial load controller that makes sure the wind turbine is producing maximum power for wind speeds below rated. This controller basically adjusts the rotational speed of the turbine using the generator torque to maintain a constant and optimal tip speed ratio. In the partial load region the collective pitch of the blades is kept constant and at its optimal value. This means the rotational speed of the rotor should be adjusted as a linear function of the wind speed. This is done through a controller called K-ω. Following the optimum tip speed ratio cannot hold in the entire partial load region as the rotational speed of the wind turbine is constraint from below by the minimum rotational speed and from above by the rated rotational speed. For these cases a PI controller that regulates the rotational speed using the generator torque is employed.
As for the full load region, there is another controller that regulates the rotational speed and power using collective pitch of the blades and the generator torque. The simulation cases in this work are basically in the full load region where the full-load controller is active. Therefore, we only give details of the full load controller here.

The objective of the full load controller is to regulate the rotational speed and the generated power around their respective rated values. This is achieved with a controller that adjusts the pitch of the blades to maintain a constant aerodynamic power and the generator reaction torque to keep the generated power constant. The pitch controller is a gain scheduled PI controller that reacts on the rotational speed error.

Simulations

In this section, simulation results for the obtained controllers are presented. The controllers are implemented in MATLAB and tested on the high fidelity wind turbine simulation software FAST using the model of the 10MW reference wind turbine 10. There are two simulation scenarios, one with the extreme operating gust and one with the normal operation with the full load stochastic wind speed. As the work with the Lidar-assisted model predictive controller is not finalized and we are still in the development phase, we have made some simplifying assumptions. The wind profile is assumed to be uniform on the rotor plane. This means that although the wind speed is stochastic in time, it has the same value over all the rotor area. The same assumption is also used for simulating the extreme operating gust.

Extreme operating gust

In this simulation case the response of the wind turbine with the Lidar-assisted MPC and the PI controller to the extreme operating gust (EOG) are compared. Figures 4.6-4.11 show the simulation results. As it can be seen from the Figures, the proposed approach give a better response in terms of less extreme deviations from the operating points for the rotational speed, generated power and the tower fore-aft position.

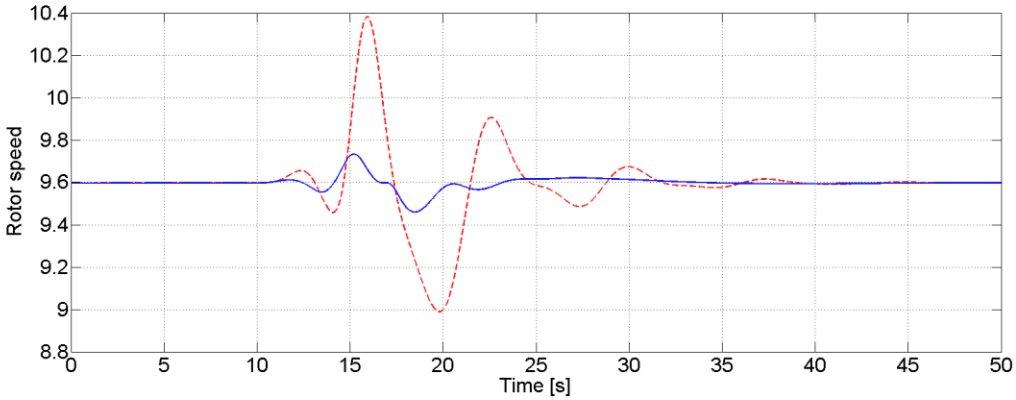

Figure 0-6 Rotational speed of the rotor (red-dashed is the PI controller, solid-blue is the MPC)

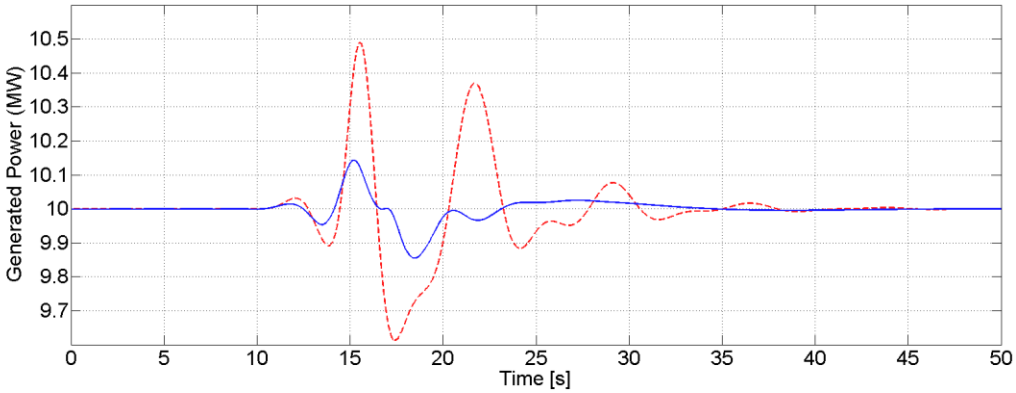

Figure 0-7 The generated power (red-dashed is the PI controller, solid-blue is the MPC)

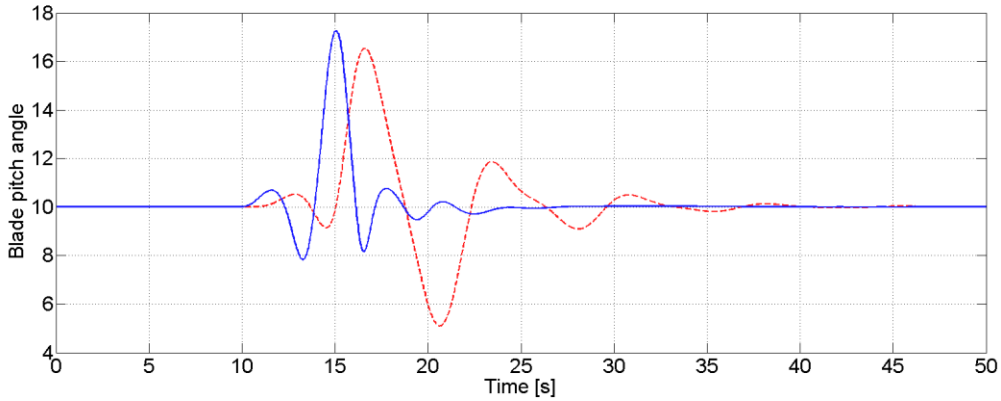

Figure 0-8 The blade pitch (red-dashed is the PI controller, solid-blue is the MPC)

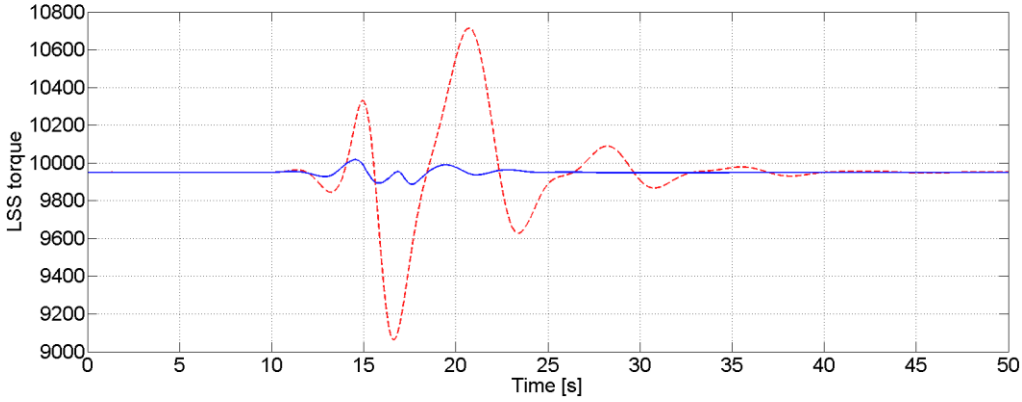

Figure 0-9 The generator re-action torque (red-dashed is the PI controller, solid-blue is the MPC)

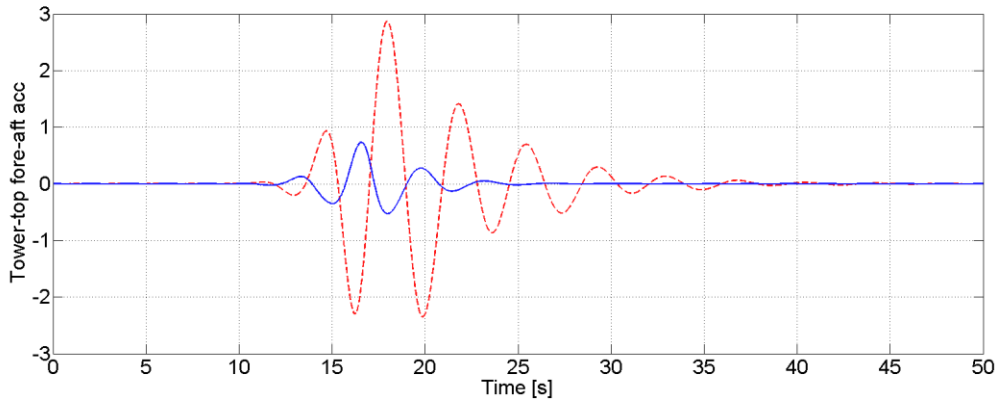

Figure 4-10 Tower fore-aft acceleration (red-dashed is the PI controller, solid-blue is the MPC)

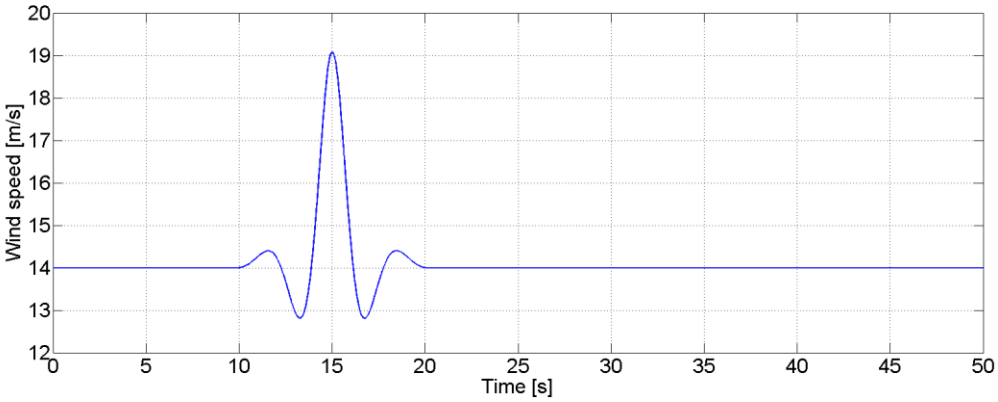

Figure 0-11 The wind speed

Stochastic Wind

In this case, simulations are done using turbulent wind speed, with Kaimal model in the software TurbSim[20] is used to generate the wind profile. In order to stay in the full load region, a realization of turbulent wind speed is used from category C of the turbulence categories of the IEC 61400-1 Ed. 3 [21] with the mean wind speed of 18m/s. Control inputs are collective pitch of the blades θ and generator reaction torque Qg . System outputs are rotor rotational speed ωr , electrical power Pe and tower fore-aft acceleration that are plotted in Figures 12-16. Table 1 shows a comparison of the results between the proposed approach and the PI controller. For comparisons, we have used pitch travel to take into account an approximation of the damage on the pitch actuator. Standard deviations (SD) of the rotational speed and generated power are also compared. As it in the table 1 and Figures 12-16, the proposed approach gives better regulation on rotational speed and generated power (smaller standard deviations) while maintaining a smaller pitch activity and less deviations on tower fore-aft acceleration.

Table 4.3 Comparison of the performance of the two controllers

Parameters	MPC+LIDAR	PI
SD of ωr (rad/s)	0.0829	0.3181
SD of Pe (M Watts)	0.0918	0.3181
Pitch travel (degrees)	0.723e3	1.007e+03
SD of tower fore-aft acc.(m/s2)	0.1180	0.5041

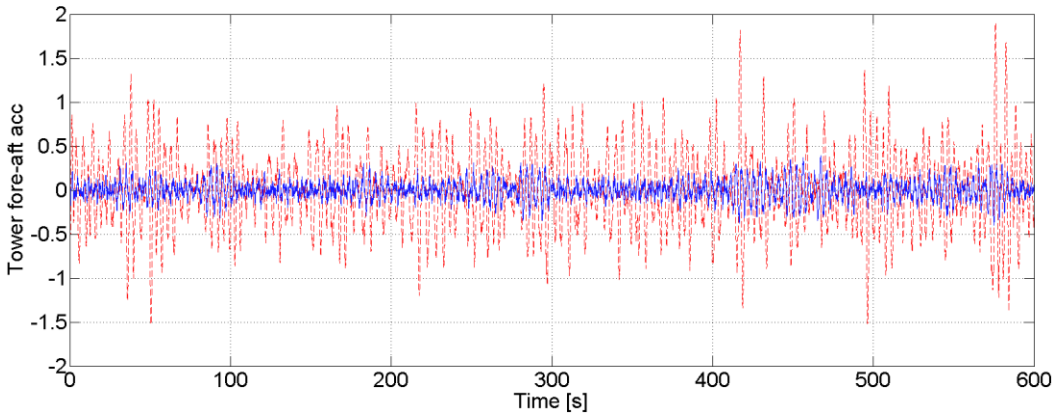

Figure 0-12 Tower fore-aft acceleration (red-dashed is the PI controller, solid-blue is the MPC)

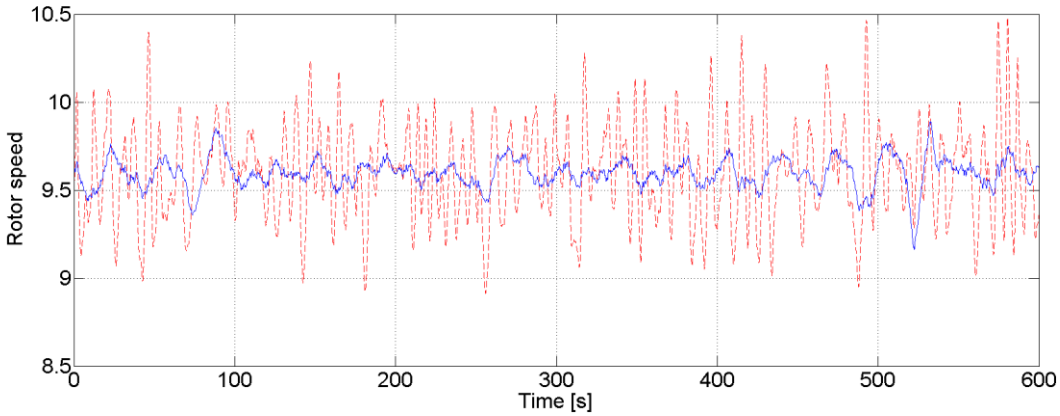

Figure 0-13 Rotational speed of the rotor (red-dashed is the PI controller, solid-blue is the MPC)

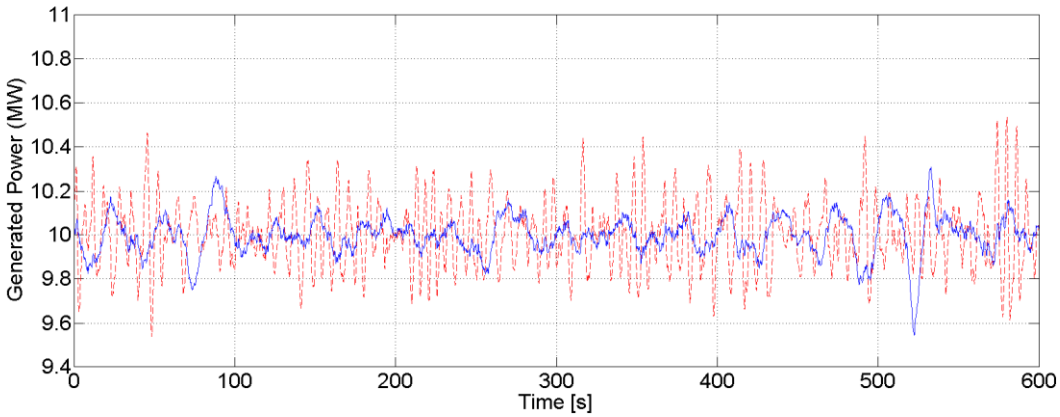

Figure 0-14 The generated power (red-dashed is the PI controller, solid-blue is the MPC)

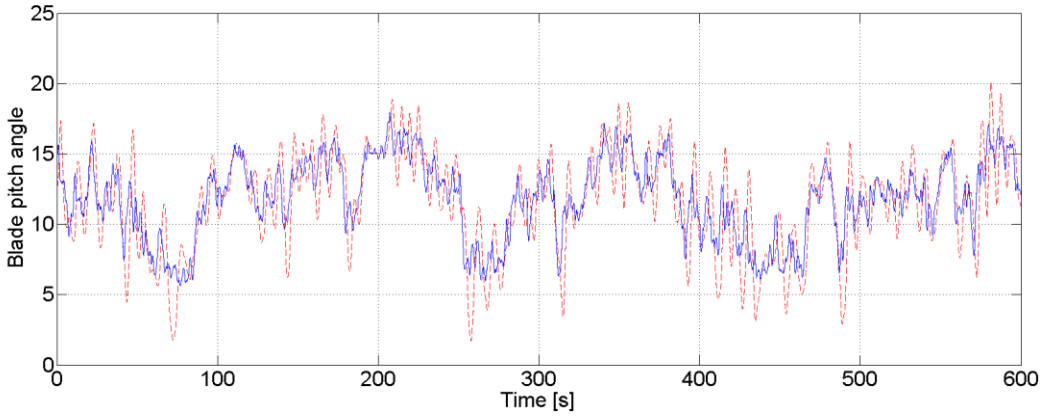

Figure 0-15 Blade pitch (red-dashed is the PI controller, solid-blue is the MPC)

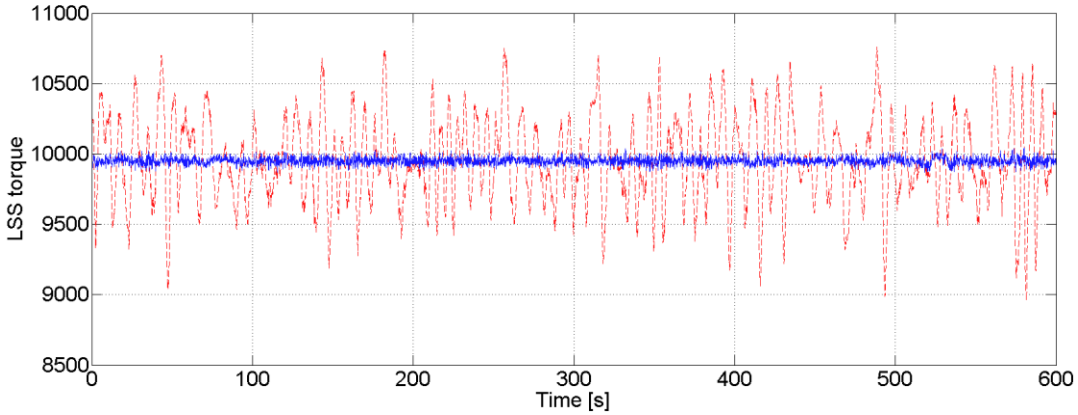

Figure 0-16 Generator re-action torque (red-dashed is the PI controller, solid-blue is the MPC)

Summary of MPC based Control

The implemented a Lidar-assisted model predictive control (MPC) on the DTU-10MW reference wind turbine was simulated with model test cases. HAWCStab2 is used to obtain the design model for MPC and simulations are done using NREL-FAST aero-servo-elastic code.
The results show that the proposed approach gives a superior performance in terms of regulation of the rotational speed and the generated compared to the gain scheduled PI controller. The tower fore-aft loads are also reduced as well as the pitch activity. The results show that there are certainly good potentials in model based control of wind turbines using LIDAR measurements. However, as these results are obtained making some simplifying assumptions, further analysis is needed to confirm that similar results can be achieved in more realistic frameworks.

The simplifying assumptions are as follows. It is assumed that the wind field is uniform in the rotor area. This assumption simplifies calculating the effective wind speed. Besides, the LIDAR we have employed gives a perfect measurement of the wind field to the controller. Normally it is not possible to measure the effective wind speed on the rotor accurately. This is because LIDARs can only measure the line of sight (LOS) wind speeds. Another simplifying assumption is on the wind flow advection time. It is assumed that the time advection time is known accurately. The advection time is the time it takes for the wind flow to travel from the LIDAR measurement plane to the rotor plane. In this work we have also assumed that the turbulence is frozen and it does not evolve as it moves toward the wind turbine.

5.0 Guidance on Supervisory Control

In order to be able to run a full load analysis for the INNWIND.EU reference Wind Turbine, it is mandatory to have a supervisory control which is able to detect a fault condition with the Wind Turbine, like over speed, overpower, misalignment, grid loss, pitch failure etc., and shut down the wind turbine following a specific rule.

In addition, IEC-61400-1 standard defines different load cases which specify failures, like pitch to feather or to fine, sensor errors, electrical faults etc. So it is also mandatory to have the capability to force these errors and be able to run those design load cases for the developed control strategies, in order to get the correct design extreme loads for the wind turbine.

These two capabilities are developed and explained how to use it for a Matlab/Simulink environment implementation in section 2.1. This software is also available on the INNWIND.EU website at (WP1->Task 1.4-> INNWIND Controller DLLs->Simulink DLLs) and as open source code, can be used for future advances and improvements on the supervisory control.

5. 1 Supervisory control

5.1.1 Blocks diagram of the supervisory control

The supervisory control, with the capabilities of forcing errors, for emulating problems on Wind Turbine, and warranty the Wind Turbine stability and shut down it, is implemented in four following blocks, depicted on Figure .

1 Checking Alarms Block.

Checking Alarms Block implements a set of triggers, to check if the wind turbine is working in a safe condition. The alarms will be triggered as a result of failure or wrong function of the controller, or of the effects of an internal, or external failure, or dangerous event. The activation thresholds, shall be set in such a way that the design load limits are not exceeded for each component.

2 Management Alarms Block.

In this block, alarm management is performed to determine the priority and type of shutdown procedure. Emergency stop state has priority over normal stop state, and normal stop state has priority over normal control state. This block decides the next wind turbine state, deciding if normal control operation should keep on running or which alarms should be activated to shut down the Wind Turbine.

3 Events Generation Block.

It is implemented a scheduling block of shutdown and faults events to simulate ultimate errors on Wind Turbine systems. This block give the capability of running simulations of all design load cases defined by IEC 61400 standards.

4 Supervisory Actions Block.

Supervisory Actions block, implements the shutdowns procedures and fault events. Once supervisory logic detects the fault, an alarm is triggered, and the supervisory shutdown procedure decides which the commanded action to each actuator is: pitch actuators demands, generator-convertor torque demand and brakes.

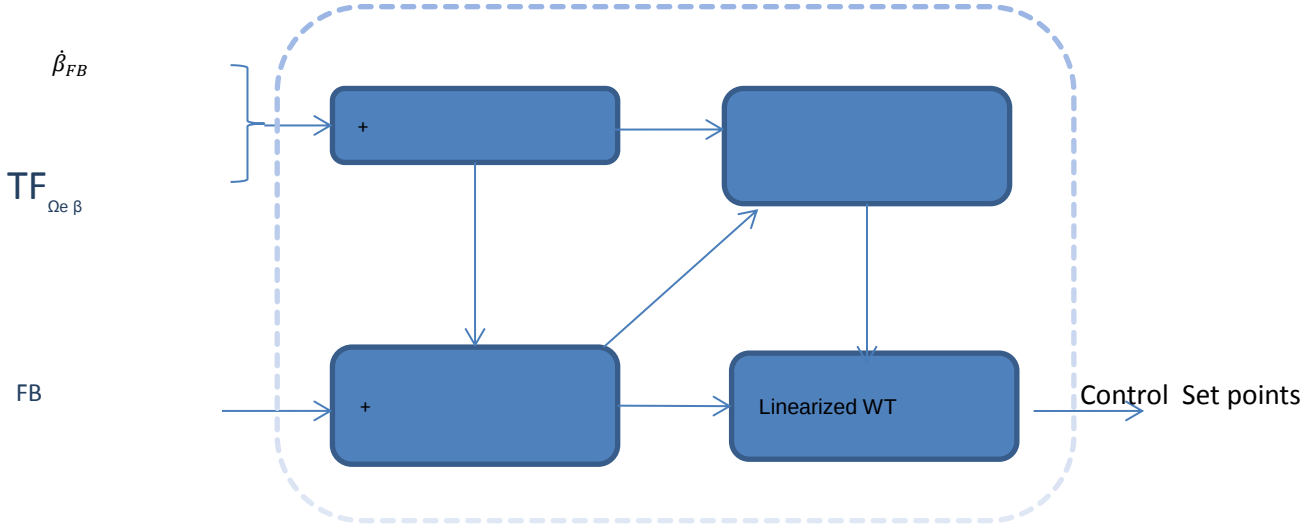

Figure 5.1 Supervisory Block

5.1.2 Alarms Setups

Over Speed and Over Power

As IEC standards recommends, there are two different thresholds both over speed and over power alarms. The Over Speed thresholds are:

i. Parameter.Cener.MaxOverSpeed_S1: Generator Over Speed alarm threshold n4 [rad/s]
ii. Parameter. Cener.MaxOverSpeed_S2: Generator Over Speed alarm threshold nA [rad/s]

while Over Power thresholds are:

i. Parameter. Cener.MaxOverPower_S1: Electrical Over Power alarm threshold p4 [W]
ii. Parameter. Cener.MaxOverPower_S2: Electrical Over Power alarm threshold pA [W]

If an over speed or over power occurs, exciding n4 or p4, then normal stop procedure is activated. In case the normal shut down procedure cannot control the Wind Turbine, and nA or pA thresholds are exceeded, then emergency stop procedure is activated. An example of how it works is shown on Figure where supervisory acts when an over speed alarm is triggered.

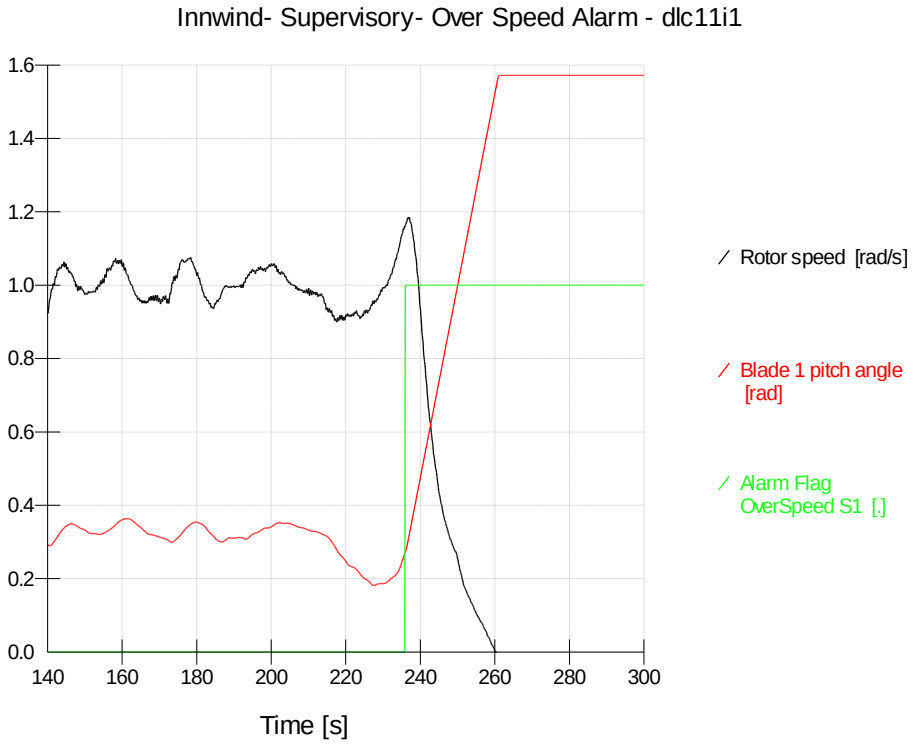

Figure 5.2 Over Speed Alarm

Yaw Error

Another classical problem is a misalignment of the Wind Turbine which should be detected, and corrected if possible or shut down the Wind Turbine, if the misalignment is too high. If the misalignment is higher than the parameter "*Parameter.Cener.MaxYawError*", in rad, during "*Parameter.Cener.YawErrorDuration*", in seconds, then the supervisory control will force a normal shut down procedure. An example of this is shown on Figure , where the threshold value is 0.5236 rad, 30 deg, during 2 seconds.

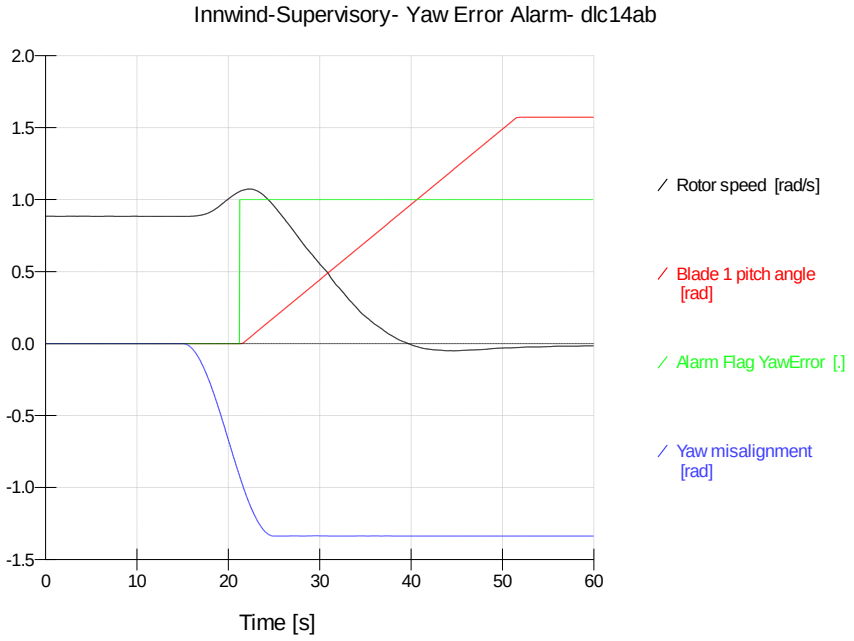

Figure 5.3 Yaw Error Alarm

Difference between blades

Depending on Wind Turbine loads and operation, it may occur that the blade angles are different for the three blades. For this implementation of supervisory controller, if the turbine is operating with a difference between measured pitch angles between two blades over

"*Parameter Cener.MaxPitchBladesDiff_Collective***"** radians, during

"*Parameter. Cener.PichBladesDiff_Duration_Collect*" seconds, then the turbine will shut down by a normal stop. An example is shown on Figure , where the maximum difference between blade pitch angles is set to 0.01745 rad, 1 deg, during 0.5 seconds. In this case, a pitch runaway is detected. This is a classical design load case defined by IEC standards, group 2.1 "*Power production plus occurrence of fault*".

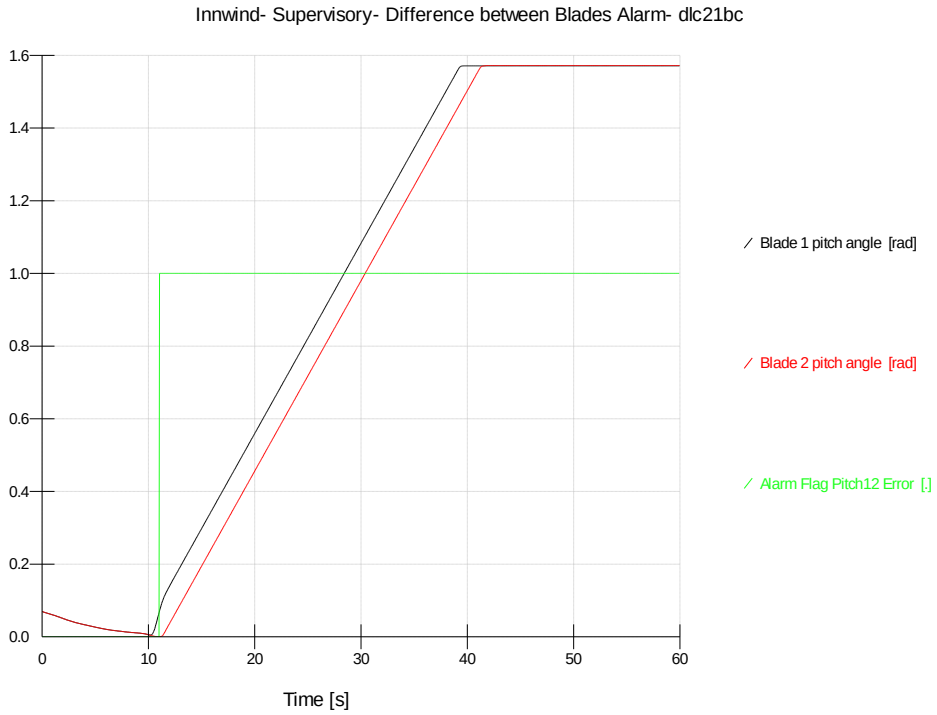

Figure 5.4 Difference between Blades Alarm

Difference between measured and demanded pitch

If the turbine is operating and during "*Parameter.Cener.PitchSetPointDiff_Duration*" seconds with differences between measured pitch angle and demanded pitch exceeds over "*Parameter. Cener.MaxPitchSetPointDiff_Collective*", then the Wind turbine will go into a Normal Stop shutdown procedure. This alarm may detect problems for pitch angle demand tracking or a blade runaway faul. An example is shown on Figure . This case shows supervisory action when difference between measured and demanded pitch alarm is triggered, simulation is from a load case of 2.1 group "*Power production plus occurrence of fault*", with all blades pitch runaway to fine fault.

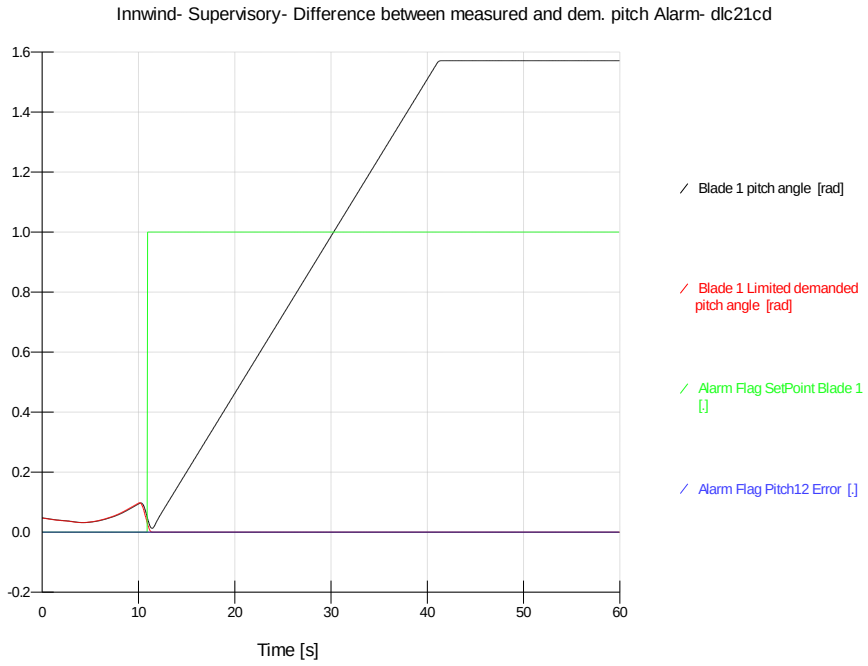

Figure 5.5 Difference between measured and demanded pitch Alarm

Grid Loss

If grid loss Alarm is enabled, "*Parameter. Cener.GridLossEnabled*" and Supervisory control detects a grid loss the turbine will go into a Normal Stop shutdown. Figure shows the supervisory action when a grid loss alarm is triggered. This is design load case of group 2.3, "*Power production plus loss of electrical grid connection*", where a grid loss occurs at 5.6 seconds after the beginning of an extreme operating gust at 13.4m/s.

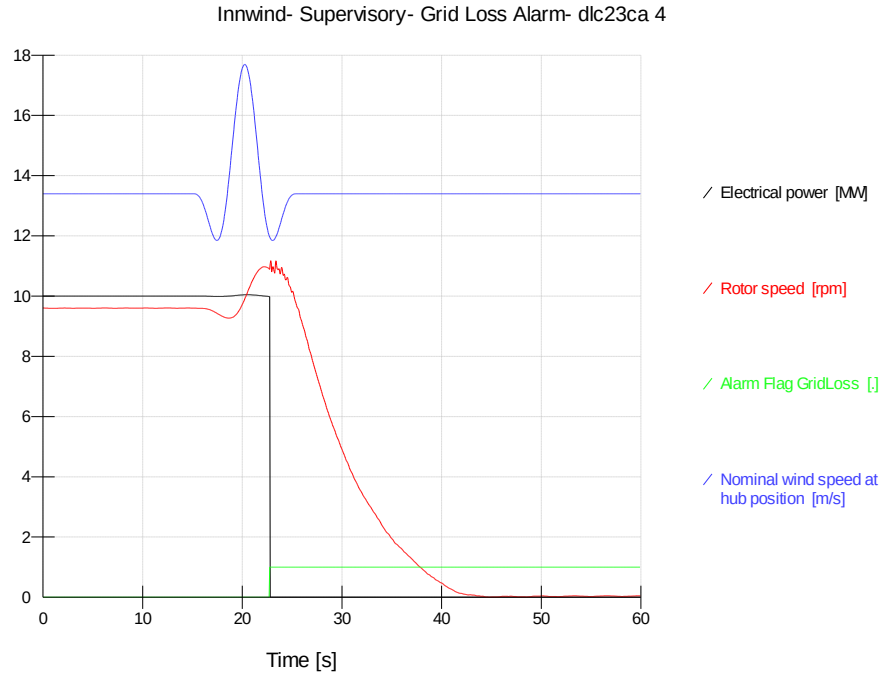

Figure 5.7 Grid Loss Alarm

5.1.3 Events Setups

The supervisory control block includes procedures to simulate normal stop, emergency stop and faults defined by external controller. This procedure can be parameterized in this realization of supervisory controller.

Normal Stop

If Normal Stop event is enabled, "*Parameter. Cener.NormalStopE_enabled =1*", the turbine will start a Normal Stop shutdown at the scheduled time. The parameters which characterize this manoeuvre are:

i. *Parameter.Cener.NormalStopE_enabled:* Normal Stop event (0: enabled; 1: disabled)
ii. *Parameter.Cener.TimeNormalStopE:* Initial time to start Normal Stop event [s]

Figure 5.7 shows Normal Stop event. Simulation is from a load case of 4.1 group "*Normal Shutdown*", Normal stop occurs at 15 second of the simulation, which has 11.4m/s steady wind condition.

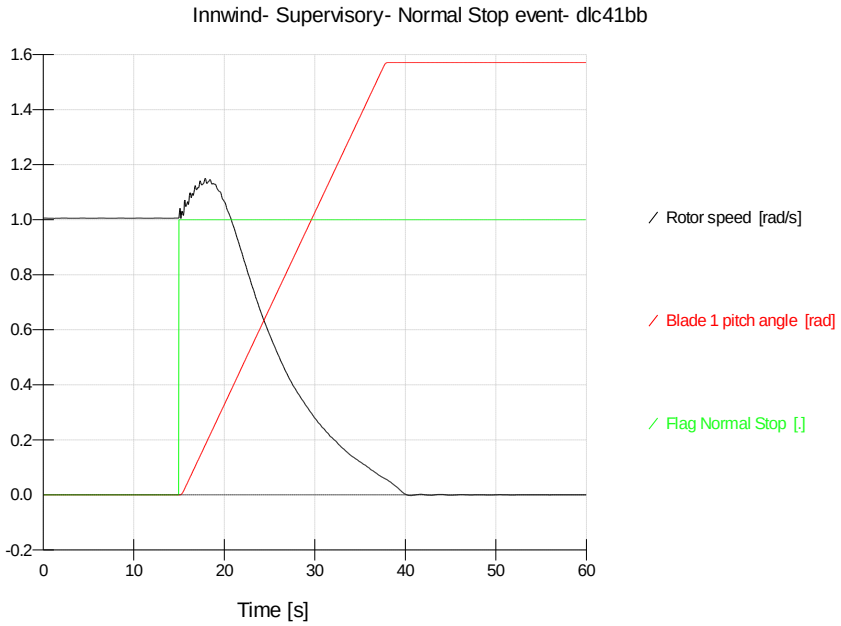

Figure 5.7 Normal Stop Event

Emergency Stop

The procedure to simulate emergency shutdown load cases is included. If Emergency Stop event is enabled, "*Parameter.Cener.EmergencyStopE_enabled = 1*" the turbine will start an Emergency Stop shutdown at the scheduled time.

i. *Parameter.Cener.EmergencyStopE_enabled:* Emergency Stop event (0: enabled; 1: disabled)
ii. *Parameter.Cener.TimeEmergencyStopE:* Initial time to start Emergency Stop event [s]

Figure shows an Emergency Stop event. Simulation is from a load case of 5.1 group "*Emergency Shutdown*", Emergency stop occurs at 15 seconds of simulation time, with 11.4m/s turbulent wind condition.

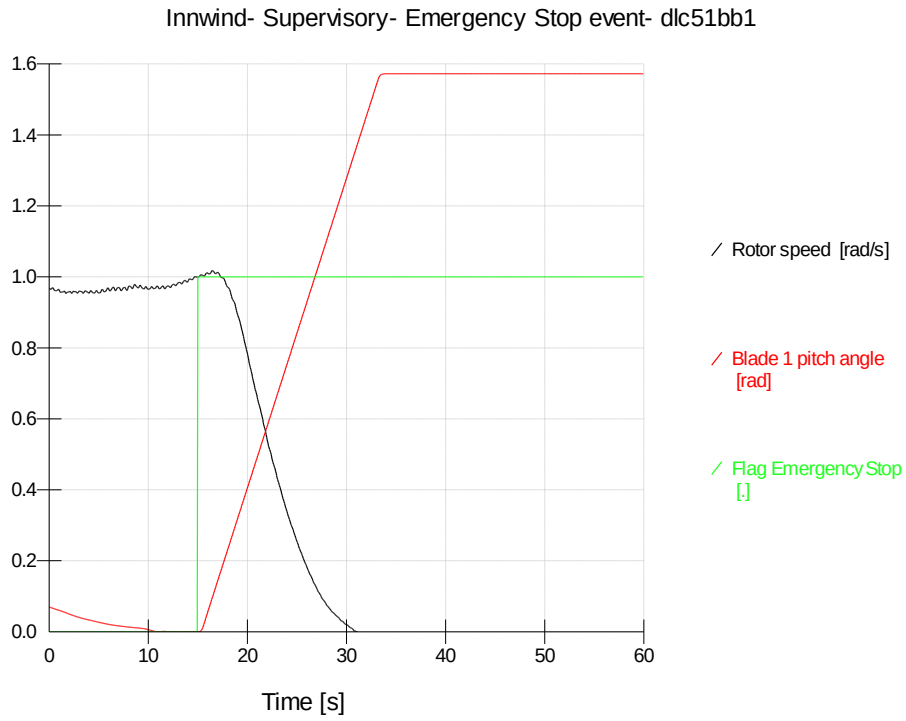

Figure 5.8 Emergency Stop Event

Grid Loss Fault

The procedure to simulate a grid loss is included. If Grid Loss event is enabled, "*Parameter.Cener.GridLossE_enabled =1*", a grid loss will occur at the scheduled time:

i. *Parameter. Cener.GridLossE_enabled:* Grid Loss event (0: enabled; 1: disabled)
ii. *Parameter. Cener.TimeGridLossE:* Initial time to start Grid Loss event [s]

Figure shows Grid Loss fault.

Pitch runaway to feather fault

The procedure to simulate a pitch runway to feather fault is included. If Blade1ToFeather fault is enabled, "*Parameter.Cener.Blade1ToFeatherE_enabled =1*" the fault will occur with the chosen pitch rate, "*Parameter. Cener.Event_PitchRateToFeather*" at the scheduled time:

i. *Parameter. Cener.Blade1ToFeatherE_enabled:* Blade 1 Pitch Runaway To Feather event (0: enabled; 1: disabled)

ii. *Parameter.Cener.Blade2ToFeatherE_enabled:* Blade 2 Pitch Runaway To Feather event (0: enabled; 1: disabled)
iii. *Parameter.Cener.Blade3ToFeatherE_enabled:* Blade 3 Pitch Runaway To Feather event (0: enabled; 1: disabled)
iv. *Parameter.Cener.TimeBlade1ToFeatherE:* Initial time to start Blade1 Pitch Runaway To Feather event [s]
v. *Parameter.Cener.TimeBlade2ToFeatherE:* Initial time to start Blade 2 Pitch Runaway To Feather event [s]
vi. *Parameter.Cener.TimeBlade3ToFeatherE:* Initial time to start Blade 3 Pitch Runaway To Feather event [s]
vii. *Parameter.Cener.Event_PitchRateToFeather:* Pitch rate at pitch runaway to feather [rad/s]

Figure and Figure show Blade 1 pitch runaway to feather event. The fault occurs at 10 s into simulation, when difference between blades alarm is triggered turbine starts a Normal Shutdown procedure, in simulation example at 11s.

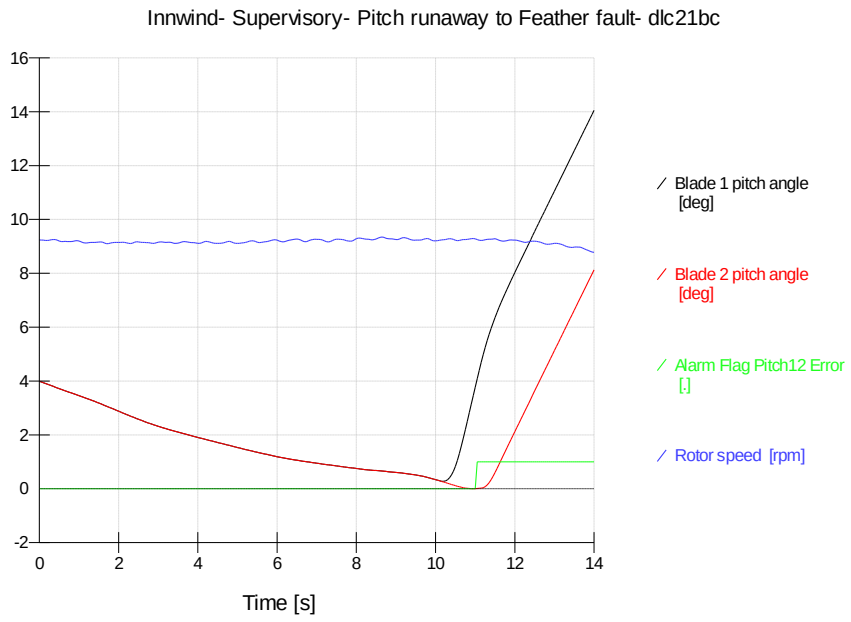

Figure 5.10. Pitch Runaway to Feather fault

Pitch runaway to feather fault

The procedure to simulate a pitch runway to fine fault is included. If Blade1ToFiner event is enabled, "*Parameter.Cener.Blade1ToFineE_enabled =1*", the fault will occur with the chosen pitch rate "*Parameter.Cener.Event_PitchRateToFine*" at the scheduled time

i. *Parameter. Cener.Blade1ToFineE_enabled:* Blade 1 Pitch Runaway To Fine event (0: enabled; 1: disabled)
ii. *Parameter. Cener.Blade2ToFineE_enabled:* Blade 2 Pitch Runaway To Fine event (0: enabled; 1: disabled)
iii. *Parameter. Cener.Blade3ToFineE_enabled:* Blade 3 Pitch Runaway To Fine event (0: enabled; 1: disabled)
iv. *Parameter.Cener.AllBladesToFineE_enabled:* All Blades Pitch Runaway To Fine event (0: enabled; 1: disabled)
v. *Parameter.Cener.TimeBlade1ToFineE:* Initial time to start Blade 1 Pitch Runaway To Fine event[s]
vi. *Parameter.Cener.TimeBlade2ToFineE:* Initial time to start Blade 2 Pitch Runaway To Fine event[s]
vii. *Parameter.Cener.TimeBlade3ToFineE:* Initial time to start Blade 3 Pitch Runaway To Fine event[s]
viii. *Parameter.Cener.TimeAllBladesToFineE:* Initial time to start All Blades Pitch Runaway To Fine event[s]
ix. *Parameter.Cener.Event_PitchRateToFine:* Pitch rate at pitch runaway to fine[rad/s]

Figure shows Blade 1 pitch runaway to fine fault. The fault occurs at 10 s into simulation, when difference between blades alarm is triggered turbine starts a Normal Shutdown procedure. Simulation is from a load case of 2.1 group "*Power production plus occurrence of fault*", with 13.4m/s turbulent wind condition.

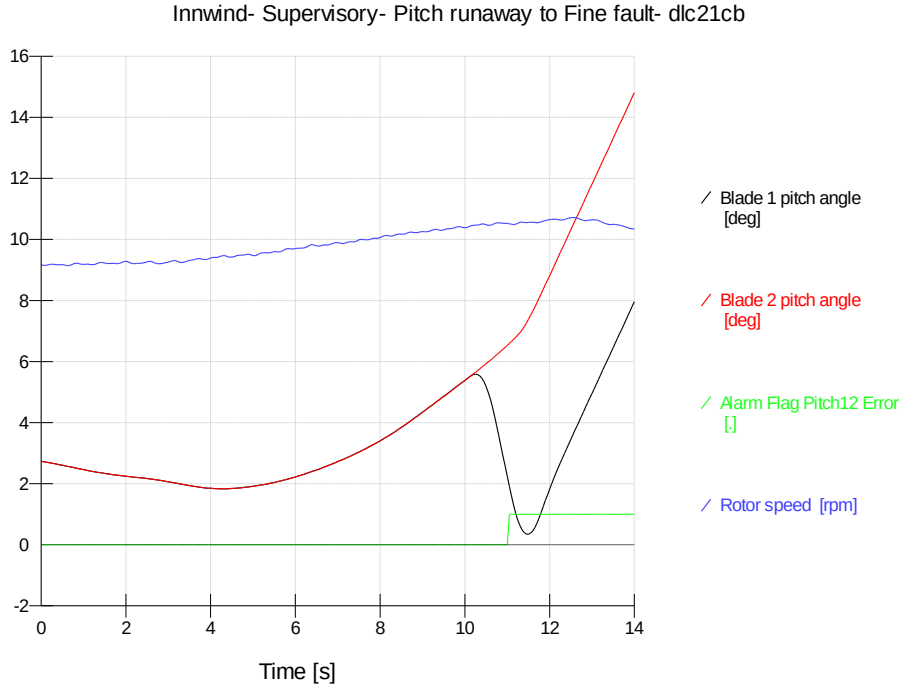

Figure 5.11. Pitch Runaway to Fine fault

Speed transducer fault

The procedure to simulate generator speed transducer fault is included. With the external parameter, "*Parameter.Cener.SpeedTransducerFaul_enabled = 1*" this fault is enabled. The time for failure, "*Parameter.Cener.TimeSpeedTransducerFault*", and constant value which the transducer reports after it has failed, "*Parameter.Cener.SpeedTransducerFault_ConstantSpeed*", have to be defined.

i. *Parameter. Cener.SpeedTransducerFaul_enabled:* Speed transducer Fault event (0: enabled; 1: disabled)
ii. *Parameter. Cener.TimeSpeedTransducerFault:* Initial time to start speed transducer fault event [s]
iii. *Parameter.Cener.SpeedTransducerFault_ConstantSpeed:* Constant Speed measured during speed transducer fault [rad/s]

Figure shows Speed transducer fault. The fault occurs at 10 s of the simulation. The erroneous speed measurement leads turbine to over speed, over speed alarm is triggered and turbine starts a Normal

Stop shutdown. Simulation is from a load case of 2.1 group "*Power production plus occurrence of fault*", with 13.4m/s turbulent wind condition.

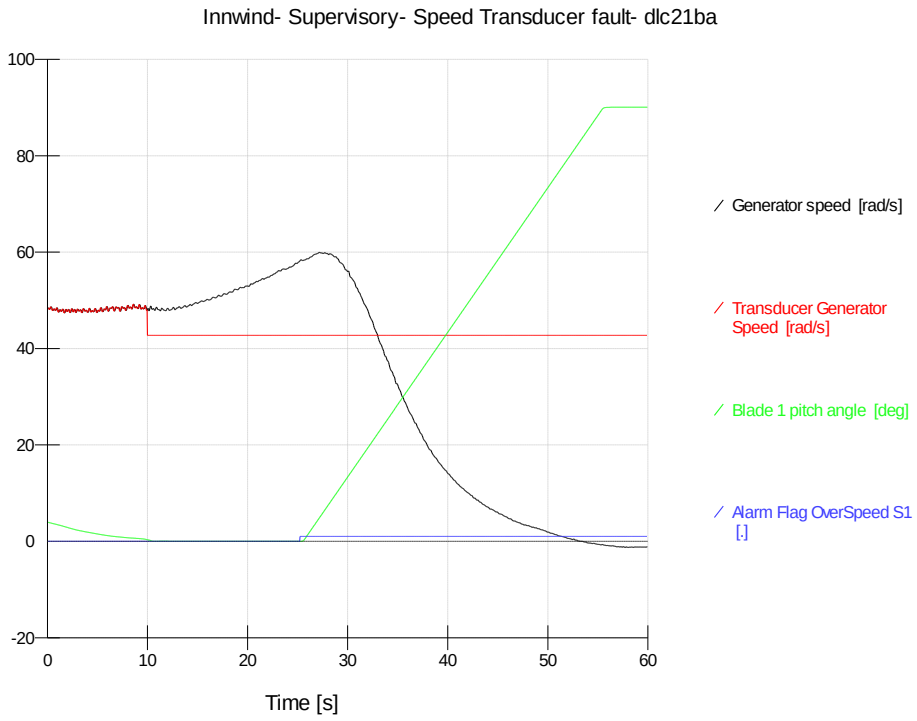

Figure 5.12. Pitch Runaway to Fine fault

5.1.4 Shutdown Setups

The supervisory algorithm includes two shutdown procedures. Normal Stop or Emergency Stop is initiated depending on the particular event. During the shutdown procedure, it should be solved which are the torque demand, and the pitch demand for each pitch actuator. As a starting point, these are the following actions implemented for this first open source supervisory control.

Normal Stop setup

As manoeuvre for the Torque demand, the torque demand is kept constant during the first seconds of the procedure, characterized by the parameter "*Parameter. Cener.NS_RampTorqueDelay*". Then torque demand is ramped to zero at chosen rate "*Parameter. Cener.NS_TorqueRate*".

Pitch setpoint can be keeping constant, at last value before stop procedure was started, during chosen time "*Parameter. Cener.NS_RampPitchDelay*". Then blades are pitched towards feather by imposing a pitch rate for the collective pitch "*Parameter.SuperV.NS_PitchRate*". The collective pitch demand is similar, except for the fact that the pitch is sent to feather in order to stop the Wind Turbine.

i. *Parameter. Cener.NS_TorqueRate:* Torque rate for Norrmal Stop (NS)[Nm/s]
ii. *Parameter. Cener.NS_RampTorqueDelay:* Delay time, keeping constant torque setpoint, before to start ramping torque to zero during NS [s]
iii. *Parameter. Cener.NS_MaxTorque:* Maximum torque during NS [Nm]
iv. *Parameter. Cener.NS_MinTorque:* Minimum torque during NS [Nm]
v. *Parameter. Cener.NS_PitchRate:* Pitch rate for Normal Stop (NS) [rad/s]
vi. *Parameter. Cener.NS_RampPitchDelay:* Delay time, keeping constant pitch setpoint, before to start ramping torque to feather during NS [s]
vii. *Parameter. Cener.NS_MaxPitch:* Maximum pitch during NS [rad]
viii. *Parameter. Cener.NS_MinPitch:* Minimum pitch during NS [rad]
ix. *Parameter. Cener.TimeChopper:* Time keeping constant torque due to chopper during Grid Loss event [s]

Emergency Stop setup

As in the normal stop procedure, the Torque demand is kept constant during a chosen time "*Parameter. Cener.ES_RampTorqueDelay*". Then torque demand is ramped to zero at chosen rate "*Parameter. Cener.ES_TorqueRate*". Pitch demand can also be kept constant, during a chosen time "*Parameter. Cener.ES_RampPitchDelay*". Then blades are pitched towards feather by imposing a pitch rate for the collective pitch "*Parameter. Cener.ES_PitchRate*".

i. *Parameter.Cener.ES_TorqueRate*: Torque rate for Emergency Stop (ES)[Nm/s]
ii. *Parameter. Cener.ES_RampTorqueDelay*: Delay time, keeping constant torque setpoint, before to start ramping torque to zero during ES [s]
iii. *Parameter.Cener.ES_MaxTorque*: Maximum torque during ES[Nm]
iv. *Parameter.Cener.ES_MinTorque*: Minimum torque during ES[Nm]
v. *Parameter.Cener.ES_PitchRate*: Pitch rate for Emergency Stop (ES) [rad/s]
vi. *Parameter.Cener.ES_RampPitchDelay*: Delay time, keeping constant pitch setpoint, before to start ramping torque to feather during ES [s]
vii. *Parameter.Cener.ES_MaxPitch*: Maximum pitch during ES [rad]
viii. *Parameter.Cener.ES_MinPitch*: Minimum pitch during ES [rad]

5.1.5 List of Supervisory Parameters

The implemented supervisory control has been done with the aim of being able to run a set of design load cases representative enough of the offshore standards. However, it is also done with the objective of given the community research a proven solution designed and implemented with the view of making easy for future researchers to improve the algorithms, the procedures, and trying to make it easy to rebuilt or parameterize, in order to avoid a unique solution for INNWIND.EU Wind Turbine. Then, in order to be able to improve the results, there is an important list of parameters which can be used to improve the performance of the supervisory control, reducing extreme operating loads. The list of parameters, its units, and its description is detailed in
Table 5..

Table 5.1. Supervisory Parameters

Supervisory Parameters	Description	Units
Parameter.Cener .SupervisoryEnabled	Supervisory Control (0: enabled; 1: disabled)	-
Alarms setup (CheckingAlarms Block)		
Parameter.Cener.MaxOverSpeed_N4	Generator Over Speed alarm threshold n4	rad/s
Parameter.Cener.MaxOverSpeed_NA	Generator Over Speed alarm threshold nA	rad/s
Parameter.Cener.MaxOverPower_P4	Electrical Over Power alarm threshold n4	W
Parameter.Cener.MaxOverPower_PA	Electrical Over Power alarm threshold nA	W
Parameter.Cener.MaxYawError	Yaw Error alarm threshold	rad
Parameter.Cener.YawErrorDuration	Required time over threshold to set Yaw Error alarm	s
Parameter.Cener.MaxPitchBladesDiff_Collective	MaxPitchBladesDiff alarm threshold	rad
Parameter.Cener.PichBladesDiff_Duration_Collect	Required time over threshold to set PitchBladesDiff alarm	s
Parameter.Cener.MaxPitchSetPointDiff_Collective	MaxPitchSetPointDiff alarm threshold	rad
Parameter.Cener.PitchSetPointDiff_Duration	Required time over threshold to set PitchSetPointDiff alarm	s
Parameter.Cener.GridLossEnabled	Grid Loss Alarm (0: enabled; 1: disabled)	-
Supervisory Stop Modes setup (SupervisoryActions Block)		
Emergency Stop		
Parameter.Cener.ES_TorqueRate	Torque rate for Emergency Stop (ES)	Nm/s
Parameter.Cener.ES_RampTorqueDelay	Delay time, keeping constant torque setpoint, before to start ramping torque to zero during ES	s
Parameter.Cener.ES_MaxTorque	Maximum torque during ES	Nm
Parameter.Cener.ES_MinTorque	Minimum torque during ES	Nm

Parameter.Cener.ES_PitchRate	Pitch rate for Emergency Stop (ES)	rad/s
Parameter.Cener.ES_RampPitchDelay	Delay time, keeping constant pitch setpoint, before to start ramping torque to feather during ES	s
Parameter.Cener.ES_MaxPitch	Maximum pitch during ES	rad
Parameter.Cener.ES_MinPitch	Minimum pitch during ES	rad
Normal Stop		
Parameter.Cener.NS_TorqueRate	Torque rate for Norrmal Stop (NS)	Nm/s
Parameter.Cener.NS_RampTorqueDelay	Delay time, keeping constant torque setpoint, before to start ramping torque to zero during NS	s
Parameter.Cener.NS_MaxTorque	Maximum torque during NS	Nm
Parameter.Cener.NS_MinTorque	Minimum torque during NS	Nm
Parameter.Cener.NS_PitchRate	Pitch rate for Normal Stop (NS)	rad/s
Parameter.Cener.NS_RampPitchDelay	Delay time, keeping constant pitch setpoint, before to start ramping torque to feather during NS	s
Parameter.Cener.NS_MaxPitch	Maximum pitch during NS	rad
Parameter.Cener.NS_MinPitch	Minimum pitch during NS	rad
Parameter.Cener.TimeChopper	Time keeping constant torque due to chopper during Grid Loss event	s

Supervisory Parameters	Description	
Events Generation setup (EventsGeneration **Block**)		
Grid Loss		
Parameter.Cener.TimeGridLossE	Initial time to start Grid Loss event	**s**
Parameter.Cener.GridLossE_enabled	Griss loss event (0: enabled; 1: disabled)	-
Normal Stp		
Parameter.Cener.TimeNormalStopE	Initial time to start Normal Stop event	**s**
Parameter.Cener.NormalStopE_enabled	Normal Stop event (0: enabled; 1: disabled)	-
Emergency Stop		
Parameter.Cener.TimeEmergencyStopE	Initial time to start Emergency Stop event	**s**
Parameter.Cener.EmergencyStopE_enabled	Emergency Stop event (0: enabled; 1: disabled)	-
Pitch Runaway To Feather		
Parameter.Cener.Event_PitchRateToFeather	Pitch rate at pitch runaway to feather	**rad/s**
Parameter.Cener.TimeBlade1ToFeatherE	Initial time to start Blade 1 Pitch Runaway To Feather event	**s**
Parameter.Cener.Blade1ToFeatherE_enabled	Blade 1 Pitch Runaway To Feather event (0: enabled; 1: disabled)	-
Parameter.Cener.TimeBlade2ToFeatherE	Initial time to start Blade 2 Pitch Runaway To Feather event	**s**
Parameter.Cener.Blade2ToFeatherE_enabled	Blade 2 Pitch Runaway To Feather event (0: enabled; 1: disabled)	-
Parameter.Cener.TimeBlade3ToFeatherE	Initial time to start Blade 3 Pitch Runaway To Feather event	**s**
Parameter.Cener.Blade3ToFeatherE_enabled	Blade 3 Pitch Runaway To Feather event (0: enabled; 1: disabled)	-
Pitch Runaway To Fine		

Parameter.Cener.Event_PitchRateToFine	Pitch rate at pitch runaway to fine	rad/s
Parameter.Cener.TimeBlade1ToFineE	Initial time to start Blade 1 Pitch Runaway To Fine event	s
Parameter.Cener.Blade1ToFineE_enabled	Blade 1 Pitch Runaway To Fine event (0: enabled; 1: disabled)	-
Parameter.Cener.TimeBlade2ToFineE	Initial time to start Blade 2 Pitch Runaway To Fine event	s
Parameter.Cener.Blade2ToFineE_enabled	Blade 2 Pitch Runaway To Fine event (0: enabled; 1: disabled)	-
Parameter.Cener.TimeBlade3ToFineE	Initial time to start Blade 3 Pitch Runaway To Fine event	s
Parameter.Cener.Blade3ToFineE_enabled	Blade 3 Pitch Runaway To Fine event (0: enabled; 1: disabled)	-
Parameter.Cener.TimeAllBladesToFineE	Initial time to start All Blades Pitch Runaway To Fine event	s
Parameter.Cener.AllBladesToFineE_enabled	All Blades Pitch Runaway To Fine event (0: enabled; 1: disabled)	-
Speed Transducer Fault		
Parameter.Cener.TimeSpeedTransducerFault	Initial time to start speed transducer fault event	s
Parameter.Cener.SpeedTransducerFaul_enabled	Speed transducer Fault event (0: enabled; 1: disabled)	-
Parameter. Cener.SpeedTransducerFault_ConstantSpeed	Constant Speed measured during speed transducer fault	rad/s

5.2 LIDAR failure issues

If LIDAR is used in the control loop it is important to consider the failure modes of the LIDAR system. This includes the possibility of unavailability of the LIDAR signal due to external conditions as well as due to failure of the LIDAR equipment itself. The LIDAR equipment itself may well be designed for high reliability, but failures still need to be considered.
Atmospheric conditions which may result in the signal being degraded, unreliable or absent include thick fog, heavy precipitation, and very clean air which lacks sufficient particles or aerosol droplets to reflect the laser light. The prevalence of such conditions will be very site-dependent. It may also be correlated (positively or negatively) with atmospheric conditions such as wind speed or turbulence which relate to the loading, and any such correlations will also be site-dependent. In practice the probability of such conditions occurring is likely to be largely unknown.
Highly disturbed flow conditions, which might include the wakes of other nearby wind turbines for instance, may also result in poor estimation of the wind field parameters because they are far from constant over the measurement area. The fitting algorithm should be able provide a criterion such as a goodness-of-fit parameter which indicates that this is occurring.

As with any sensor, failures can be

1. detected by the sensor itself, and flagged to the controller through a status flag or signal quality indicator,
2. undetected by the sensor, but detected by the controller by means of appropriate sanity checks, or

3. completely undetected.

In the LIDAR case, these categories apply both to equipment failure and to unsuitable atmospheric conditions. Category (c) is evidently the most critical, as it may result in incorrect control action and potentially dangerous loading. Safety would then rely on some other part of the system taking action: some other controller check or, in the worst case, the turbine safety system itself. Category (b) is similar to (a) except that the fault detection may well take longer, giving more time for adverse consequences to develop in the meantime.

If a LIDAR failure is identified (including loss of signal quality or poor fit of the wind field parameters), the controller needs to take some action. If the LIDAR-assisted control is used to reduce the fatigue load envelope so that the capital cost of components can be reduced, immediate action may not be required but if the problem persists, or is expected to persist, for any length of time then some action may be needed to reduce the rate of fatigue load accumulation so that the turbine lifetime is not compromised. Stopping the turbine is probably unnecessary, but the turbine may need to revert to a ‘safe mode’ of operation without LIDAR assistance and with a reduced maximum power output such that the design load envelope is still respected. This may also mean reverting to a non-LIDAR set of controller feedback gains.

6.0 Quantification of Reduction in Extreme and Fatigue Loads

As noted in chapter 2, the developed controllers were tested using different aeroelastic software as used by different partners and also in different software environments. Results of the testing these controllers have been provided in the preceding chapters. However in order to compare the effectiveness of individual pitch control or LIDAR feed forward control against the baseline controller in the same software environment and using the same aeroelastic code, the solutions developed by CENER for the IPC and Lidar feedforward were compared with the baseline using GH Bladed aeroelastic software.

The results in chapter 3 are all realistic but were done using different software as used by different partners. Here the same effort is being done in one controlled software environment. The compared controllers are the following:

1. **INNWIND.EU Baseline controller**. Implemented in Matlab/Simulink environment which accessible from the project internal teamsite under WP1->Task1.4. This control includes classical solution for drive train damping, tower exclusion algorithm, and active tower damping algorithm for the pitch loop.
2. **CENER's Version of the baseline controller.** With the same level of complexity in terms of control loops in the INNWIND.EU baseline controller, but with further tuning of parameters
3. **CENER's baseline controller + IPC algorithm.** With the idea of giving a more detailed solution in terms of loads for bigger offshore wind turbines.
4. **CENER's baseline controller + IPC algorithm + CENER's Feedforward approach.**

6.1 Global impact in loads

In this section, a more comparative analysis of these results is presented**.** Damage equivalent loads are used to equate the fatigue damage represented by Rainflow Cycle Counting, RFCC. The method is based on the Miner's rule. The S-N curve slopes (m) used here are m=4 representing steel for tower and hub loads and m=10 representing glass reinforced plastic (GRP) for blade loads. Lifetime-integrated damage equivalent fatigue loads have been calculated for a reference frequency corresponding to 10^7 cycles in 20 years.

In Table fatigue load comparison is done between (1) INNWIND.EU baseline controller (DTU), (3) CENER baseline controller. Both controllers include the standard ways of reducing fatigue that are already used on many commercial turbines.

Table 6.1: DTU Baseline vs CENER Baseline fatigue load comparison

Lifetime Weighted Equivalent Loads		CENER Reference % Above Baseline
Blade Root (m=10)	Blade root My	-8.02
	Blade root Mxy	-6.88
Rotating hub (m=4)	Rotating hub Mx	0.36
Stationary hub (m=4)	Stationary hub Myz	-2.09
Yaw bearing (m=4)	Yaw bearing Mxy	-5.67
Tower Base (m=4)	Tower base My	-12.26
	Tower base Myz	-9.48

The results from two implementations of the baseline controllers show that the they are getting similar results.

In Table 2 the fatigue load comparison is done between the baseline controller (CENER) and the CENER baseline with individual pitch controller (CENER+IPC). As may be expected from IPC strategy, a significant reduction in blade root loads are achieved. The Blade root flap moment (My) is reduced up to 20% and blade root Mxy is reduced up to 17%, as well as similar decrease in loads at stationary hub, 16%.

Table 6.2: CENER Baseline vs CENER IPC Baseline fatigue load comparison

Lifetime Weighted Equivalent Loads		CENER IPC % Above CENER
Blade Root (m=10)	Blade root My	-20.04
	Blade root Mxy	-17.02
Rotating hub (m=4)	Rotating hub Mx	-1.27
Stationary hub (m=4)	Stationary hub Myz	-16.21
Yaw bearing (m=4)	Yaw bearing Mxy	-9.69
Tower Base (m=4)	Tower base My	1.87

In Table 6.3 fatigue load comparison is done between CENER baseline individual pitch controller (CENER+IPC) and CENER feedforward controller assisted by LiDAR (CENER+IPC+FF). This table

shows that feed-forward controller is capable of improving most of fatigue loads. In particular tower base fore-aft moment My is reduced up to an extra 8%. Reduction of 6 % is achieved for blade root My and Myz.

Table 4.3: CENER IPC Baseline vs CENER IPC + FF fatigue load comparison

Lifetime Weighted Equivalent Loads		CENER IPC+FF % Above CENER IPC
Blade Root (m=10)	Blade root My	-5.70
	Blade root Mxy	-6.53
Rotating hub (m=4)	Rotating hub Mx	-2.86
Stationary hub (m=4)	Stationary hub Myz	-0.29
Yaw bearing (m=4)	Yaw bearing Mxy	-1.08
Tower Base (m=4)	Tower base My	-7.69
	Tower base Myz	-6.23

Table 6.4 shows a more detailed analysis of load reduction between all controllers, compared all against INNWIND.EU baseline control.

Table 6.4: Summary fatigue loads comparison

Lifetime Weighted Equivalent Loads		Baseline [Nm]	CENER % Above Baseline	CENER IPC % Above Baseline	CENER IPC+FF % Above Baseline
Blade Root, (m=10)	Blade Mx	2.94E+07	-0.31	-1.7	-1.97
	Blade My	3.27E+07	-8.02	-26.45	-30.73
	Blade Mxy	3.05E+07	-6.88	-22.72	-27.67
	Blade Mz	368529	-8.53	-18.5	-23.38
Rotating hub (m=4)	Rotating hub Mx	3.84E+06	0.36	-0.91	-3.67
	Rotating hub My	3.46E+07	-2.26	-24.3	-25.03
	Rotating hub Mz	3.46E+07	-2.37	-24.2	-24.05
	Rotating hub Myz	2.10E+07	-2.09	-17.97	-18.05
Stationary hub (m=4)	Stationary hub Mx	3.84E+06	0.36	-0.91	-3.67
	Stationary hub My	2.72E+07	-2.76	-3.64	-3.71
	Stationary hub Mz	2.56E+07	-1.17	-3.71	-3.87
	Stationary hub Myz	2.10E+07	-2.09	-17.97	-18.05

Yaw bearing (m=4)	Yaw bearing Mx	4.88E+06	-4.31	-7.92	-10.43
	Yaw bearing My	2.81E+07	-2.21	-3.45	-4.13
	Yaw bearing Mxy	1.18E+07	-5.67	-14.81	-15.58
	Yaw bearing Mz	2.77E+07	-0.79	-2.67	-2.96
Blade Root, (m=10)	Blade Mx	2.94E+07	-0.31	-1.7	-1.97
	Blade My	3.27E+07	-8.02	-26.45	-30.73
	Blade Mxy	3.05E+07	-6.88	-22.72	-27.67
	Blade Mz	368529	-8.53	-18.5	-23.38
Tower Top (m=4)	Tower Mx	2.77E+07	-0.79	-2.67	-2.96
	Tower My	2.03E+07	-3.16	-3.75	-4.53
	Tower Mz	2.00E+07	-2.25	-4.14	-4.75
	Tower Myz	1.18E+07	-5.67	-14.81	-15.58
Tower Base (m=4)	Tower Mx	2.81E+07	-0.85	-2.49	-2.53
	Tower My	8.34E+07	-12.26	-10.61	-17.51
	Tower Mz	9.57E+07	-6.39	-5.63	-10.04
	Tower Myz	1.14E+08	-9.48	-8.69	-14.46

6.2 Impact on Energy Production

Tables 6.5 and 6.6 show differences in terms of control performance in rotor speed and the power production between all controllers, compared all against INNWIND.EU baseline control. From these values, as commented before, we can see that the feed forward LiDAR assisted control improves the control performance in terms of rotor speed control, while a correct tuning also shows that an important load reduction is achieved. In addition, all these improvements show that this obtained without losing energy production. Actually, the produced energy is slightly higher.

The analysis of Energy production is also done by analyzing energy production for each wind bin. In this case, detailed results on Table shows the difference between the controllers compared with the INNWIND.EU Baseline control. Here it is interesting to see that for low wind speed, 4 -6 m/s, where the control is simple, INNWIND.EU baseline control produces a little bit more of energy than CENER's controls. Then, except for the control with IPC at 10m/s, CENER's controls produce more energy. The biggest difference is at 12m/s, where CENER's controls, produce around 1.8% and 2% more than the baseline control.

Table 6.5: Annual energy production comparison

	Baseline [Wh]	CENER % Above Baseline	CENER IPC % Above Baseline	CENER IPC+FF % Above Baseline
AEP	5.41E+10	0.57 %	0.36 %	0.49 %

Table 6.6: Energy production compared to baseline controller by wind bines

Wind bin (m/s)	CENER % Above Baseline	CENER IPC % Above Baseline	CENER IPC+FF % Above Baseline
4	-0,17%	-0,17%	-0,20%
6	-0,40%	-0,40%	-0,40%
8	0,12%	0,12%	0,12%
10	0,70%	-0,21%	-0,21%
12	2,02%	1,80%	2,02%
14	0,15%	0,15%	0,15%
16	0,00%	0,00%	0,00%
18	0,00%	0,00%	1,00%
20	0,00%	0,00%	0,00%
22	0,00%	0,00%	0,00%
24	0,00%	0,00%	0,00%

6.3 Extreme load analysis

In order to analyze in detail the goodness of LiDAR based control, extreme load analysis should also be performed. In this case, as we want to isolate the effect of LiDAR control we decide to compare ultimate loads between CENER IPC and CENER IPC+FF. This is possible a suitable option, since other comparisons maybe more affected by the power production controller than by the LiDAR feedforward algorithm itself. Then, for a fair comparison, these controllers have been used here because both controllers have the same feedback and supervisory control structures with the differences of the feedforward loops added in the CENER IPC+FF controller. The details of the loads with IPC based control are provides in Appendix 1 and 2.

The supervisory control includes an advanced shut-down strategy which adapts the pitch rate to turbine behaviour and loads. With this shutdown procedure, some extreme loads dominated by the shut-down procedure are minimized, and then LiDAR assisted strategies is better analysed to realize which its real contribution to reduce ultimate loads is.

In this analysis, we realize that most ultimate loads occur in the same load cases for both controllers. Even more, it seems clear that the most dangerous load cases are DLC 1.3 group, which corresponds with power production with extreme turbulent model.

Feed forward controller CENER IPC+FF can reduce most of the ultimate loads, such as Blade root My up to 5% and Myx up to 6%. Tower base ultimate load My is dominated by DLC 6.1 load cases, in which the control system is not operating since the turbine is shutdown. Reduction of 22% is achieved in hub bending moment Myz, both rotating and stationary coordinates.

Detailed loads comparisons are depicted in Table to Table .

Table 6.7 - Ultimate load comparison: blade root

Blade Root	CENER IPC		CENER IPC FF		CENER IPC+FF % Above CENER IPC
	load case	Absolute Max [kNm]	load case	Absolute Max [kNm]	
Mx	dlc13cb1	24113	dlc13cb1	24804	2.87
My	dlc13bb1	54630	dlc13cb1	51883	-5.03
Mxy	dlc13cb1	57095	dlc13cb1	53682	-5.98
Mz	dlc23da_3	600.7	dlc13eb1	548.3	-8.72

Table 6.8 - Ultimate load comparison: hub (rotating coordinates)

Rot. Hub	CENER IPC		CENER IPC FF		CENER IPC+FF % Above CENER IPC
	load case	Absolute Max [kNm]	load case	Absolute Max [kNm]	
Mx	dlc13db1	16710	dlc13eb1	16403	-1.84
My	dlc14cb	32708	dlc13db1	35243	7.75
Mz	dlc13db1	43897	dlc13eb1	33457	-23.78
Myz	dlc13db1	47890	dlc14cb	37338	-22.03

Table 6.9 - Ultimate load comparison: hub (stationary coordinates)

Stat. Hub	CENER IPC		CENER IPC FF		CENER IPC+FF % Above CENER IPC
	load case	Absolute Max [kNm]	load case	Absolute Max [kNm]	
Mx	dlc13db1	16710	dlc13eb1	16403	-1.84
My	dlc13db1	44333	dlc13db1	35297	-20.38
Mz	dlc13eb1	31731	dlc13eb1	31552	-0.56
Myz	dlc13db1	47890	dlc14cb	37338	-22.03

Table 6.10 - Ultimate load comparison: Tower base

Tower Base	CENER IPC		CENER IPC FF		CENER IPC+FF % Above CENER IPC
	load case	Absolute Max [kNm]	load case	Absolute Max [kNm]	
Mx	dlc13eb1	34855	dlc13db1	36244	3.99
My	dlc61ab_l_1_1	171023	dlc61ab_l_1_1	171023	0.00
Mz	dlc61ab_h_1_1	221644	dlc61ab_h_1_1	221644	0.00
Myz	dlc21cd	256194	dlc21cd	253708	-0.97

Table 6.11 - Ultimate load comparison: Tower top

TowerTop	CENER IPC		CENER IPC FF		CENER IPC+FF % Above CENER IPC
	load case	Absolute Max [kNm]	load case	Absolute Max [kNm]	
Mx	dlc13eb1	34460	dlc13db1	35507	3.04
My	dlc13db1	44099	dlc13db1	36799	-16.55
Mz	dlc14cb	31986	dlc14cb	29736	-7.03
Myz	dlc13db1	50230	dlc13db1	40280	-19.81

It should be noted that many of the extreme loads can occur during storm situations when the turbine is at stand still or under specific fault conditions where the controller may not be able to react to mitigate the effect of the fault.

6.4 Fatigue Load Alleviation on Jacket substructure

The fatigue loads on the reference jacket for the INNWIND.EU 10 MW wind turbine [22] showed a strong contribution from the low wind speeds due to 3P excitation of the jacket sub structure and this leads to a low lifetime for some of the joints of the structure. Based on the normal collective pitch control with exclusion zone tuning, the jacket fatigue loads were further analyzed to quantify the reduction in damage equivalent loads due to the upgraded controller.

As a baseline, the supporting jacket is oriented such that the global main direction is along the diagonal 3-1. It has four stages of X braces. Loads have been collected for the four legs at three of their respective K-nodes: mudline (level 4), mid-height (level 2) and transition (level 0) as shown in Fig. 6.1. However, loads at only few points will be presented here.

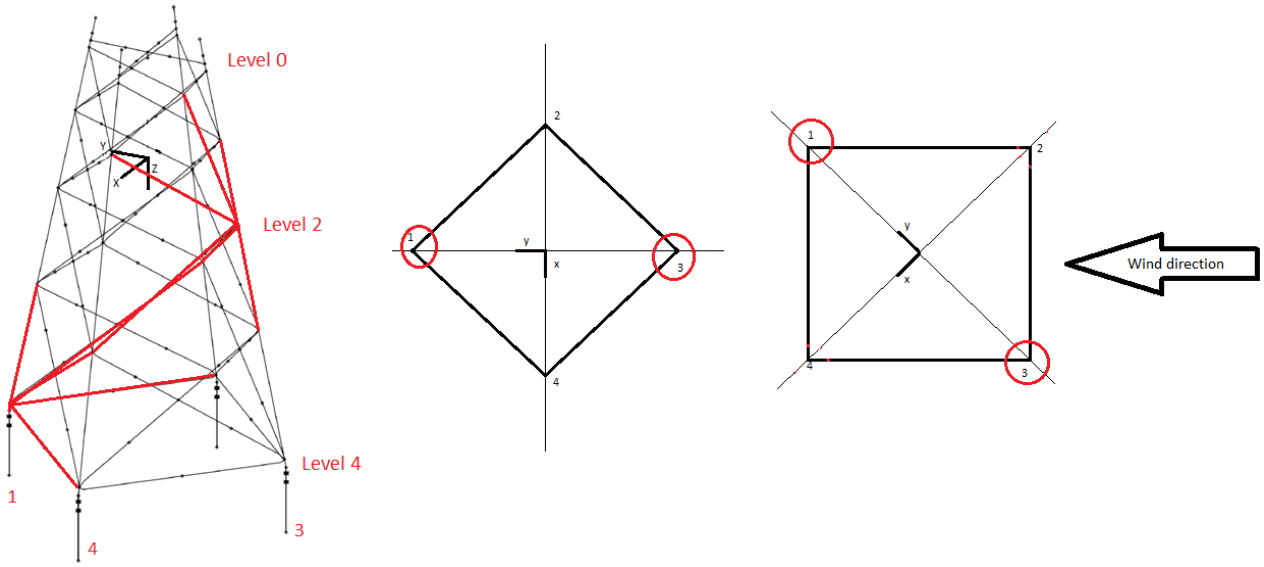

Figure 6.1. Jacket geometry

The required fatigue analysis has been conducted with the design load case 1.2 (DLC1.2) as per Ref [4]. As a baseline to check the present results, those from the INNWIND reference jacket have been used. Comparison has been done using four criteria.

1- **Tower only frequencies**. Assumed to be clamped at its bottom, the first eigen-frequencies of the tower plus Rotor and Nacelle Assembly (RNA) have been calculated by Ref [22] to be 0.32 Hz and 0.33 Hz. Respectively, the present study has obtained 0.33 Hz and 0.34 Hz. The little difference observed here is due to dissimilarities in tower geometry. See Table 6.12.

2- Whole structure frequencies. Similarly, Ref [22] produces as overall structure first frequencies 0.28 Hz and 0.29 Hz. The present study considers the jacket being mounted of 40 m depth pile and obtained 0.30 Hz and 0.30 Hz. Once more, the slight difference can be mainly attributed to geometry change. See Table 6.12.

Table 6.12: Eigen frequencies.

	Tower + RNA		Full Structure	
	1st frequency [Hz]	2nd frequency [Hz]	1st frequency [Hz]	2nd frequency [Hz]
The present study	0.33	0.34	0.30	0.30
Ref [1]	0.32	0.33	0.28	0.29
Relative difference	-3.125 %	-3.030 %	-7.143 %	-3.448 %

3- **Damage Equivalent Loads**. This study assumed a lifetime of offshore structure to be 25 years. However, results obtained from Ref [22] are for a lifetime of 20 years. They are presented for the horizontal resultant bending moments at the mudbrace level (N41). Table 4 below shows damage equivalent loads (lifetime of 20 years) as obtained for each members joining at N41. It compares equivalent loads obtained for 20 years in this study to those from Ref [22] by the means of relative deviation between the two result sets.

Table 6.12: Damage equivalent horizontal resultant bending moment at N41.

	N41_L1_down [kNm]	N41_L1_up [kNm]	N41_LB1 [kNm]	N41_LB4 [kNm]	N41_S1X4A [kNm]	N41_S4X4A [kNm]
The previous study [3]	2185.82	1633.27		258.87		569.19
The present study for 25 years	2021.62	1542.25	263.15	196.69	475.26	489.26
The present study for 20 years	1911.96	1458.37	248.86	185.96	449.40	462.78
Ref [1]	2804	2571	292 or 301	292 or 301	667 or 602	667 or 602
Relative difference	31.81%	43.28%	14.77% or 17.32%	36.32% or 38.22%	32.62% or 25.35%	30.62% or 23.13%

From Table 6.12, the relative differences in damage equivalent load for 20 years between the present and the reference analyses vary from 15% to 40 %. Although both structures have comparable eigen-frequencies and are placed in similar environment, the structure's fatigue lifetime can have a longer life due to the reduction in the fatigue damage equivalent loads. This shows that load mitigation control is important to for structural sustainability.

1 Hz Equivalent Loads : The comparison of resultant bending moments is done at the structure's interface for 6 m/s, 12 m/s and 23 m/s. Moment components at these wind speeds are obtained from linear interpolation. Relative differences vary from 16% to 25 %.

Table 6.13: 1 Hz equivalent resultant bending moments at interface.

Wind speed bin	6 m/s	12 m/s	23 m/s
The present study [kNm]	44,094	46,890	94,220
Ref [6] [kNm]	59,018	59,369	112,278
Relative difference	25.29%	21.02%	16.08%

7 Control of the Multi-Rotor Floating Wind Turbine

This task aims to bring forth innovative wind turbine concepts, analyse their performance and assess the impact at the wind turbine design level in going beyond the reference wind turbine concept. In particular, the work presented here concerns the development of a novel multi-rotor system designed to reduce the cost of energy through a wide variety of means [23].

Firstly, it was hypothesised in [23] that an MRS, with many smaller rotors, provides a more complete spatial coverage of the input turbulent wind field, allowing greater energy capture and hence improving the cost of energy. It was further hypothesised that, as each MRS rotor is a smaller entity, capable of faster response, in principle the MRS may be capable of extracting higher frequency turbulent energy than a large rotor. Preliminary test of this hypothesis suggested that for a reference TI around 5 to 6% at good offshore sites with mean wind speed of ~ 9 m/s, ~ 2% gains in energy may be obtained from operation in turbulent wind.

Secondly, simulations using a combination of CFD techniques coupled with a vortex method were completed, resulting in predictions that gains in energy capture may occur due to flow acceleration through the spaces between the rotors, resulting in a total power gain of 8%.

Thirdly, and perhaps most significantly, a breakdown of the CAPEX for a multi-rotor system was estimated and compared to that of two 10MW machines (shown in Figure 7.33).

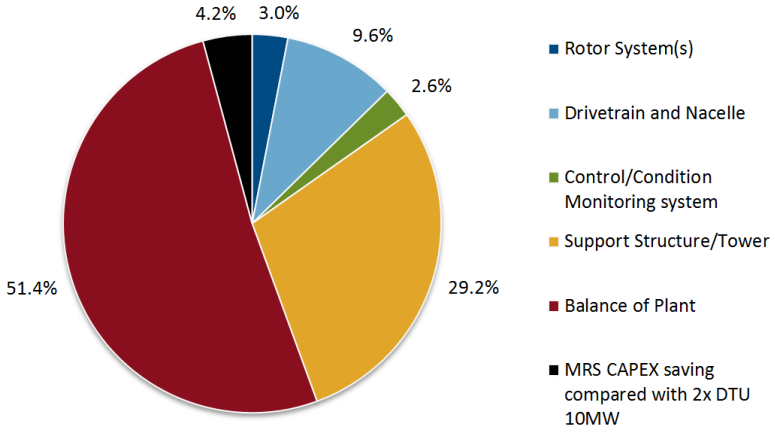

Figure 7.33: CAPEX breakdown of MRS compared to two 10MW machines of standard design

Regarding the LCOE evaluation, the previous report concluded that "*In the base case scenarios for the MRS and RWT, the LCOE of the MRS is estimated to be reduced by 15%. This is a huge benefit. To put it in perspective, if the giant blades of the 10 MW RWT were provided at no cost, the reduction in LCOE of the RWT would be only 4%.*

Also the DTU 10 MW reference turbine (RWT) is in itself a low mass advanced design aiming to capture what may be achieved in technology development of the conventional solution over the timeframe in which competing innovative technologies may appear. In the INNWIND.EU project, the

reference value for present offshore LCOE is 107 €/MWh. In relation to that value the MRS technology promises ~ 30% LCOE reduction."
Additional factors were also cited that may be even more significant than the substantial projected LCOE reduction:

1) The cost per kW of turbine components alone is not favourable with upscaling to very large machines, whereas (as illustrated in the reports sensitivity study) 20 MW is not a limit for an MRS and LCOE advantage appears to be maintained at 40 MW
2) Because the MRS predominantly utilises small rotors, familiar to the industry and de-risked the only challenges that remain for the MRS are in large structures and in floating structures but these are not new to the offshore industry
3) Economies of scale mean that producing larger numbers of smaller components, as is the case for MRS over the traditional approach, the unit reliability of MRS turbines can be better than for single large turbines and the learning curve progression, as affects cost reduction, much faster
4) Technology development with the MRS is safer and faster as new designs can be tested on just a few of the rotors/subsystems on the MRS system before roll out across the whole system.

It is clear therefore, that a multi-rotor approach or very large multi-megawatt wind turbines has large advantages in reducing the cost of energy.
The report also identified the requirement for further research into complete system engineering, a key component of which is the control of the MRS. As the MRS comprises a number of rotors whose power is amalgamated, it is reasonable to approach the MRS control problem in a similar manner to wind farm control, albeit with some additional requirements of the control system (e.g. yaw, over-turning).
The statement of work for subtask 1.3.1 of the INNWIND.EU project outlines the requirement for further, innovative concepts to be considered including multi-rotors on a common support structure, study for their feasibility focusing on the interaction effects and coordinated control. The work presented in this report aims to fulfil the requirements of this subtask.
A major part of the coordinated control of the MRS is to balance the thrust loads across the structure, in both the yaw and fore-aft directions to ensure the structure remains stable. This can be achieved by varying the thrust from the rotors on the machine to balance the moments. In addition, this opens up the possibility of using the same technique to yaw the machine to face the wind.
In addition to balancing and yawing the MRS it is possible to provide ancillary services to the grid such as droop control and synthetic inertia via wind farm level control. The scope for providing these ancillary services is explored.
Finally, an exploration of the further design issues relating to control of the multi-rotor system is presented.

7.1 Scope of the control problem

The turbines of a MRS are standard and at a scale that presents no new challenges as is the support structure. The yawing of a multi-rotor system is however the one area where special design solutions are required. Several types of yaw system are under consideration a) where the platform floats in the sea and yaws about its moorings using an underwater swivel bearing (for which there is precedent) and

b) where the MRS is on a fixed foundation and yaws from base level using some kind of mechanical bearing.
Exploiting pitch control of the many rotors in the MRS, large differences in thrust loading across each side of the array can be generated and used to produce a yawing moment. An early task was to establish the range of yaw moments that could feasibly be generated at each operational wind speed and hence yaw rates that may be possible considering the inertia and probable damping characteristics of the system.
The proposed type of yaw control based on differential rotor thrust is innovative and specific to a system with multiple rotors. In addition, the differential control of a large group of wind turbines is effectively wind farm control albeit of a wind farm of very closely spaced rotors. Such control is not yet industry standard but rather a new major research area. Thus within the limited scope of the INNWIND.EU project it was decided to focus on this combination of thrust control and turbine cluster control considering only the yaw degree of freedom. This should be fully adequate to understand yawing from a fixed foundation but clearly is only a vital preliminary for a floating system capable of 6 DOF motion.
As the number of wind farms attached to the power network increases it becomes increasingly important for wind power to provide some ancillary services, particularly synthetic inertia and droop control. As such, the potential for MRSs to provide these balancing mechanisms is explored.

7.2 Modelling of the MRS

The multi-rotor system (MRS) is comprised of 45 rotors, each rated to 444kW, giving a total rated power output for the machine of 20MW. The rotors are attached to a large steel structure, arranged as shown in Figure 7.34, with a distance of $1.05D$ between each rotor centre, where D is the rotor diameter.

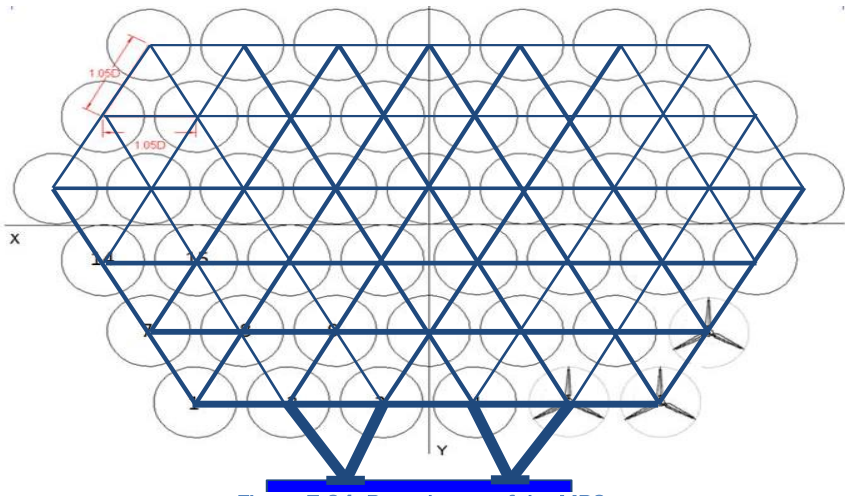

Figure 7.34: Rotor layout of the MRS

7.2.1 Rotor and Power Conversion System Modelling

Each rotor and power conversion system (RPC system) is modelled as a lumped parameter model. This model includes drivetrain dynamics, 3P and 6P loadings, blade edge and flap frequency dynamics, dynamic inflow effects, actuator dynamics.

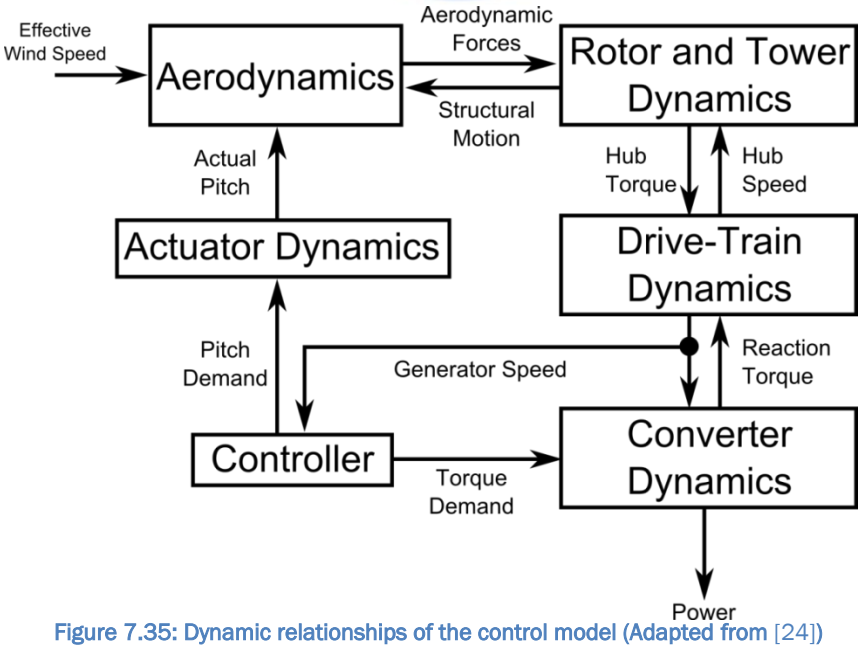

Figure 7.35: Dynamic relationships of the control model (Adapted from [24])

A diagram showing the dynamic relationships of the lumped parameter model is given in Figure 7.35. The lumped parameter model uses ordinary differential equations, with the aerodynamics based on blade element momentum theory summed across the actuator disc with a single stream tube. Using this method, the thrust on the rotor is found. The rotor dynamics are also modelled, however, as the model considers the whole rotor disc rather than each blade; individual blade dynamics are not easily modelled. This shortcoming is overcome through the derivation of a single blade model using Lagrange's equations [24,25].The drive-train and generator are modelled as a two or three lumped inertia model.

The model contains enough detail that the rotational loads on the machine (cyclic components of the dynamics at multiples of the rotor speed referred to as "*nP*", where *n* denotes the number of repetitions per rotation) up to 3P are modelled. This level of detail is required for controller design.

The model allows full design of wind turbine controllers as it contains validated models of all the major dynamics of a wind turbine. The model is general and can be used to model any horizontal axis machine. The machine chosen for use in the multi-rotor system is a 444kW direct drive machine, and the variables used in the lumped parameter model to define it are presented in Table 5.

Table 5: Variables for the RPC system

Variable	444kW
Hub Inertia	600 kgm^2
Drive Shaft Damping	730 Nms
Drive Shaft Stiffness	1434852 Nm/rad
Drive Shaft Material Damping	500000 Nms/rad
Generator Inertia	90kgm^2

Rotor Radius	20.2758 m
Effective Blade Length	14.1931 m
Distance of the Centre	8.9 m
One Blade Mass	364 kg
Flap Natural Frequency	17.1 rad/s
Edge Natural Frequency	27.206r ad/s
Rotor Inertia	75501 kgm^2
Rotor and Nacelle Mass	28497 kg

7.2.2 Wind Modelling

In addition to the RPC system models a key requirement for modelling a MRS system is to model the wind field across the MRS correctly, including any correlation of the turbulence and the effects of wind shear.

As stated in section 7.2.1 the model of the rotor requires an effective wind speed time series. The effective wind speed time series is found by initially generating a field of point wind speeds and converting the point wind speeds at each RPC system hub into effective wind speeds. The effective wind speeds are then used as inputs to the RPC system models, which in turn calculate key parameters such as the thrust and power output.

Simplification is necessary when building a control strategy for such a complex system, as not only will the creation and tuning become less complex but the computational time will be reduced enabling faster progression for the model. A clustering together of the rotors is suggested so that the control system is simplified but an accurate physical model is still represented. An averaging of effective wind speeds is proposed as the input for these clusters of rotors.

It is expected that any control system developed using the clusters would be easily converted for use on a model of 45 individual RPC systems. In this manner, controller design is made quicker and more straightforward, as simulation time is greatly reduced using the cluster approach.

A short study is completed to investigate the effect of averaging the effective wind speed over a cluster of three wind turbines in order to ensure that this approach is a reasonable approximation of the full dynamics.

The rotors are gathered in 17 clusters shown in Figure 7.36. The clustering is designed such that each cluster consists of no more than three rotors, and all rotors in a cluster are located next to one another. The larger a cluster becomes, the less accurate the approximation, as the large area will result in great variation in wind speeds and the model would risk becoming over simplified. Conversely, if the cluster are made too small then the processing time increases such that controller design becomes impractical.

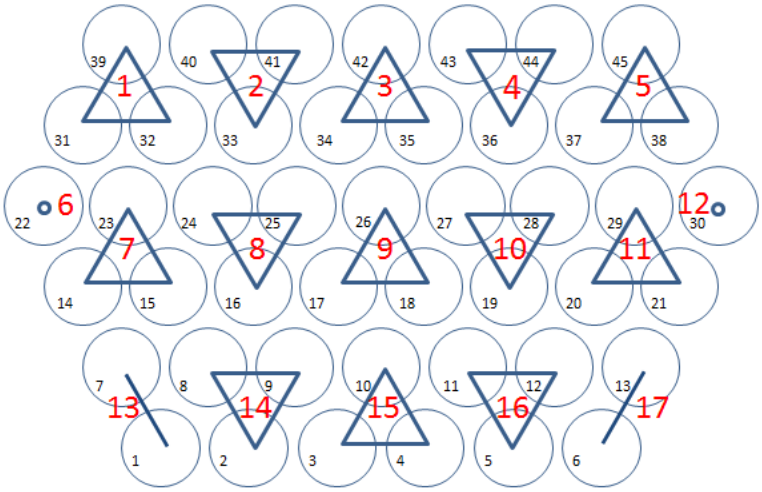

Figure 7.36: Arrangement of RPC systems and clusters

Where it is not possible to cluster together three rotors one or two rotors are clustered. It is advantageous for rotors 22 and 30 to not form part of a cluster as they are furthest from the yaw axis and so have the greatest contribution to the yaw moment.

A Matlab script (adapted from[26]) using the Sandia method [27] is used to create the wind field across the entire structure. Point wind speeds are created in a plane perpendicular to the mean wind direction. The Sandia method uses Taylor's frozen wake theory where under certain conditions turbulent structures move as frozen entities transported by a mean wind speed. In this way a wind field is created over time. With a turbulent wind field in place the effective wind speed is found using a model based on the method described in [24]. The model is used to find the effective wind speed given an input of a point wind speed.

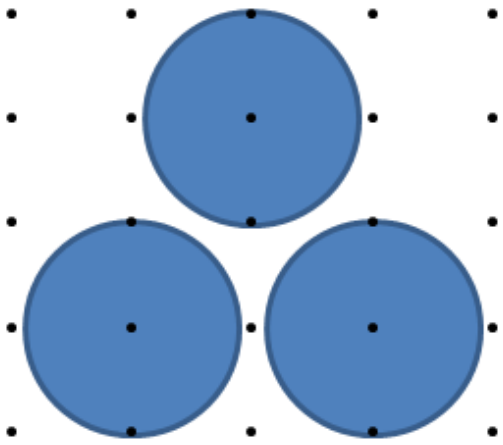

Figure 7.37: Wind field and rotor arrangement

Figure 7.37 shows the wind field and rotors of one cluster represented by the black dots and blue circles respectively. The input to find the effective wind speed for each rotor is taken from the point wind speed that lies at the centre of each rotor.

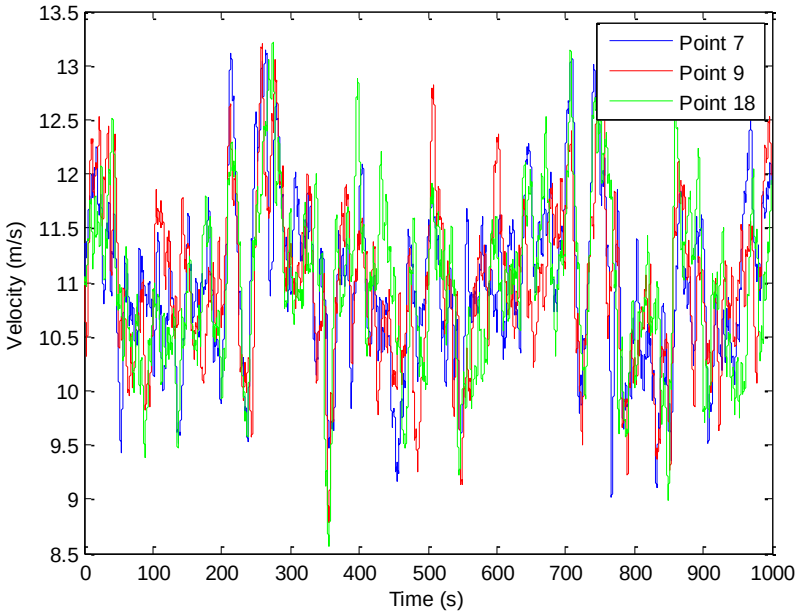

Figure 7.38: Effective wind speeds at three points

Figure 7.38 shows the resultant effective wind speed for each of the three points. It can be seen that there is a significant variation between the three points. Two methods are proposed to effectively represent the clustering of rotors.

1) **Individual technique:** Choose one the effective wind speeds arbitrarily and feed through the RPC system model to calculate the thrust and power. Multiply the relevant outputs by the number of rotors in the cluster.

2) **Averaging Technique:** Take the average of the effective wind speeds at each rotor in the cluster and feed it through the RPC system model. Multiply the relevant outputs by the number of rotors in the cluster.

These two methods are investigated further with a three turbine cluster used as an example. Results generated from taking three effective wind speeds, feeding them through three individual RPC system models and summing together are referred to as the" real" results.
For an average wind speed of 11m/s both the power and the thrust are examined. Figure 7.39 shows the real power of the three turbines summed together in red as well as that of averaging technique in blue. Initial results are positive especially when compared to Figure 7.40 which is a comparison between the real power and the individual technique. Clearly if the wind speed at this rotor happens to lie further from the average, the results will be poor.

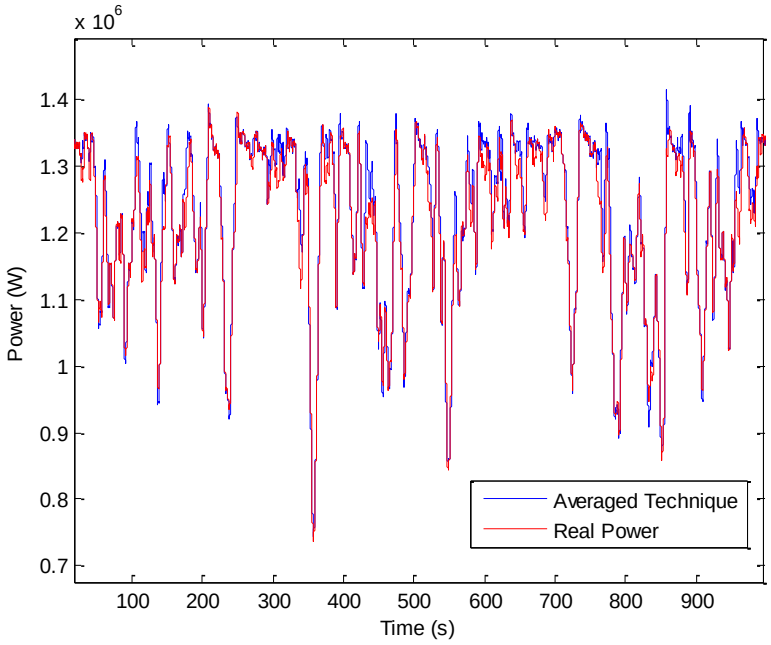

Figure 7.39: Power (Averaged wind multiplied by 3 vs total of 3 individual points) around rated wind speed

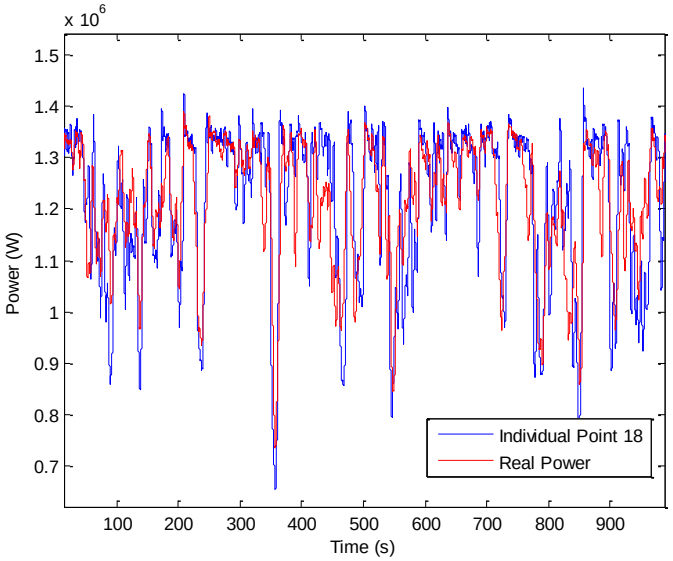

Figure 7.40: Power (Point 18 multiplied by 3 vs a total of 3 individual points) around rated wind speed

Accuracy in thrust values is arguably more important given the thrust on the rotors will act as the yaw mechanism. Figure 7.41 shows the thrust over time for the same scenario as in Figure 7.39.

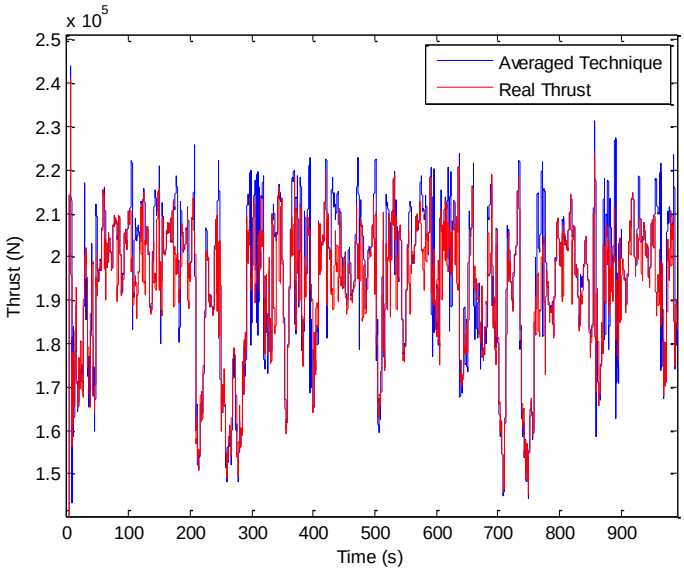

Figure 7.41: Thrust (Averaged wind multiplied by 3 vs total of three individual points) around rated wind speed

The results show a greater disparity compared with the power. To evaluate this, the steady state thrust curve must be looked at in Figure 7.42. Above and below 11 m/s the thrust drops off sharply. The averaging of wind speeds therefore causes greater discrepancies in the thrust at this wind speed.

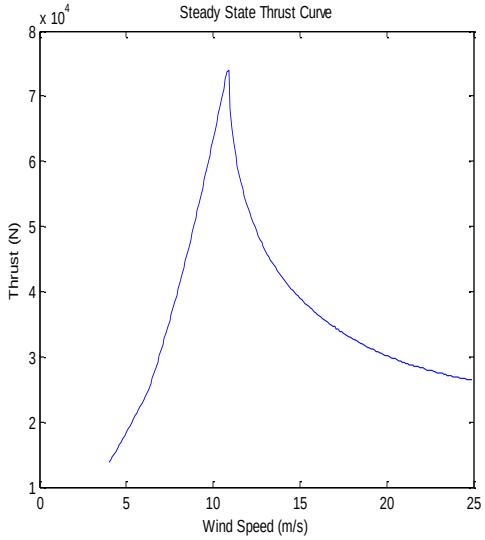

Figure 7.42: Steady state thrust curve

Discrepancies in the power seen in Figure 7.39 can be explained using the steady state power curve. At 11m/s there is a sharp change in the power curve which can be seen in Figure 7.43. It is not as great as the rapid change in thrust with wind speed explaining why greater accuracy is seen in the results for power.

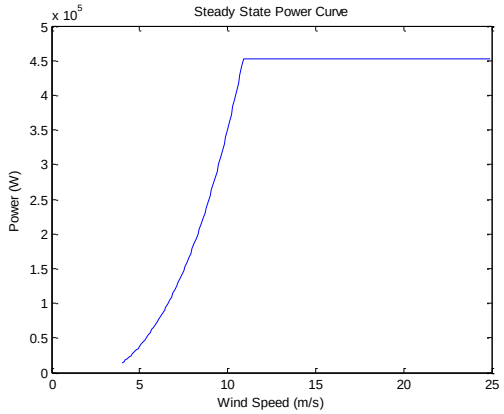

Figure 7.43: Steady state power curve

The impact on power and thrust of the two approaches is examined for a below rated wind speed, in this case 6m/s. Figure 7.44 again shows that the individual technique is not as accurate as the combined average approach.

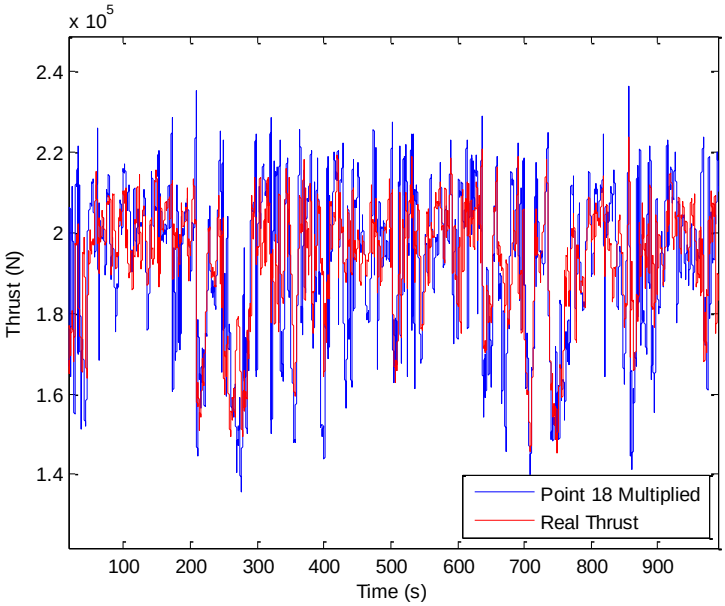

Figure 7.44: Thrust (Point 18 multiplied by 3 vs total of 3 individual points) below rated wind speed

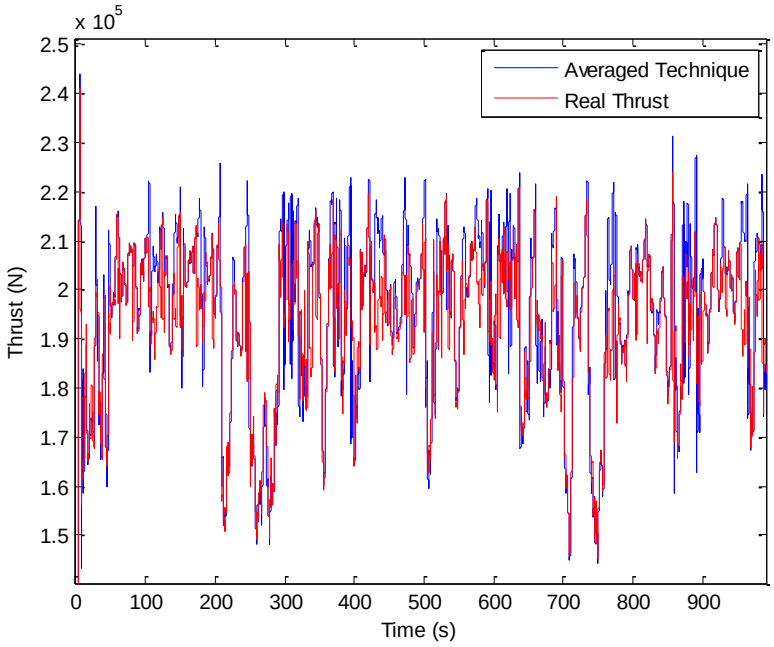

Figure 7.45: Thrust (Average wind multiplied by 3 vs total of 3 individual points) below rated wind speed

Comparison of Figure 46 and Figure 7.47 with Figure 7.39 and Figure 7.41 shows that more accurate results are obtained for the below rated simulations. This is due to lower rate of change of thrust with respect to wind speed and the lower rate of change of power with respect to wind speed.

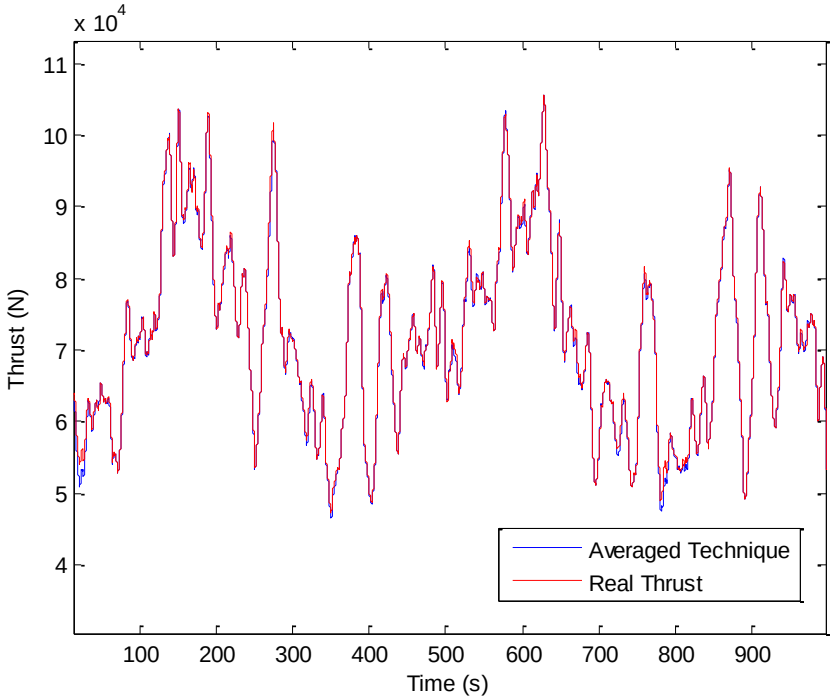

Figure 46: Thrust (Average wind multiplied by 3 vs total of 3 individual points) below rated wind speed

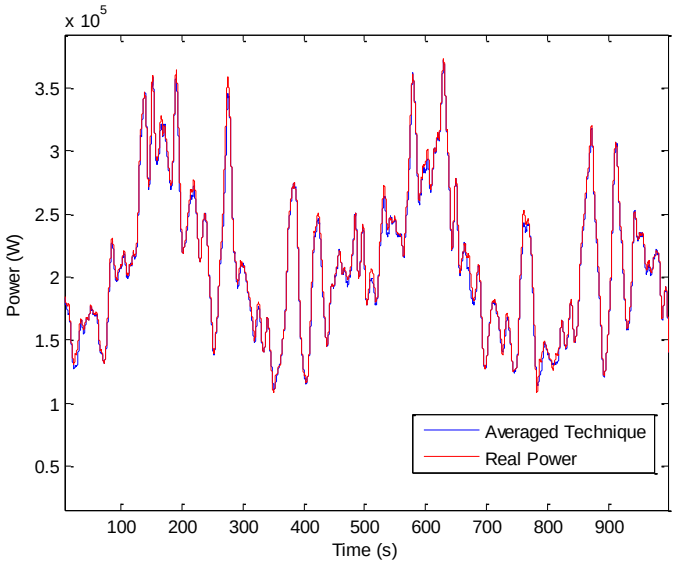

Figure 7.47: Power (Average wind multiplied by 3 vs total of 3 individual points) below rated wind speed

For completeness the averaged technique was also used for a wind speed well above rated (17m/s), with the results given in Figure 7.48 and Figure 7.49. As would be expected, the averaged technique gives an excellent approximation for both power and thrust in above rated conditions.

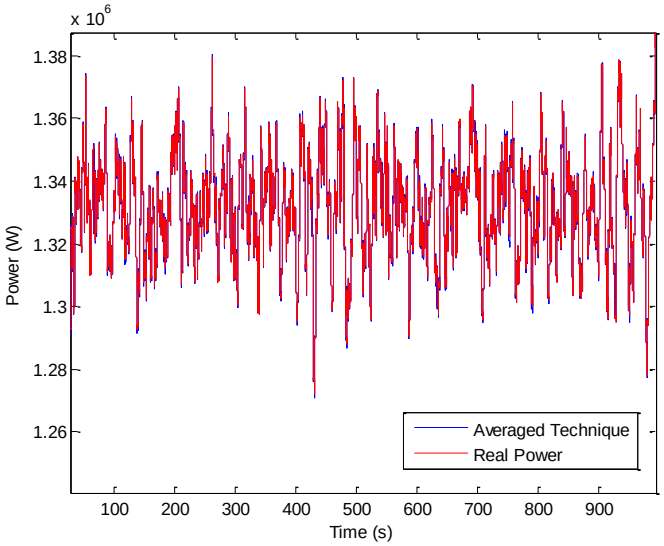

Figure 7.48: Power (Average wind multiplied by 3 vs total of 3 individual points) above rated wind speed

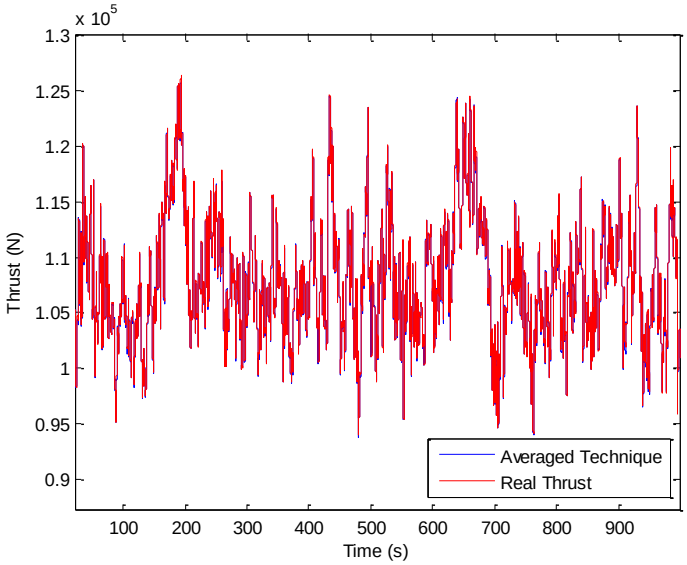

Figure 7.49: Thrust (Average wind multiplied by 3 vs total of 3 individual points) above rated wind speed

The results presented clearly show that using the averaging technique delivers far greater accuracy than the individual technique. Although the averaging technique is not mathematically equivalent to using three individual effective wind speeds (the real values), for the purpose of a MRS model for controller design the technique is a reasonable approximation. By breaking down the MRS into smaller areas and then averaging the different effective wind speeds, wind shear and other variations in speed are taken into account as long as the clustering of rotors is done sensibly. Caution must be taken at rated wind speed as the results are significantly less accurate.

The method outlined above is used across the whole MRS to generate effective wind speeds for each cluster. Wind shear is modelled using a power law approximation. An example of the wind speeds experience by each cluster is given in Figure 7.50. RPC systems on the top row are shown in red, those in the middle row are shown in green, and those on the bottom row are shown in blue. The mean wind speed is shown in black. It is clear that, due to wind shear effects, there can be significant differences between the wind speeds experienced at the top and the bottom of the MRS.

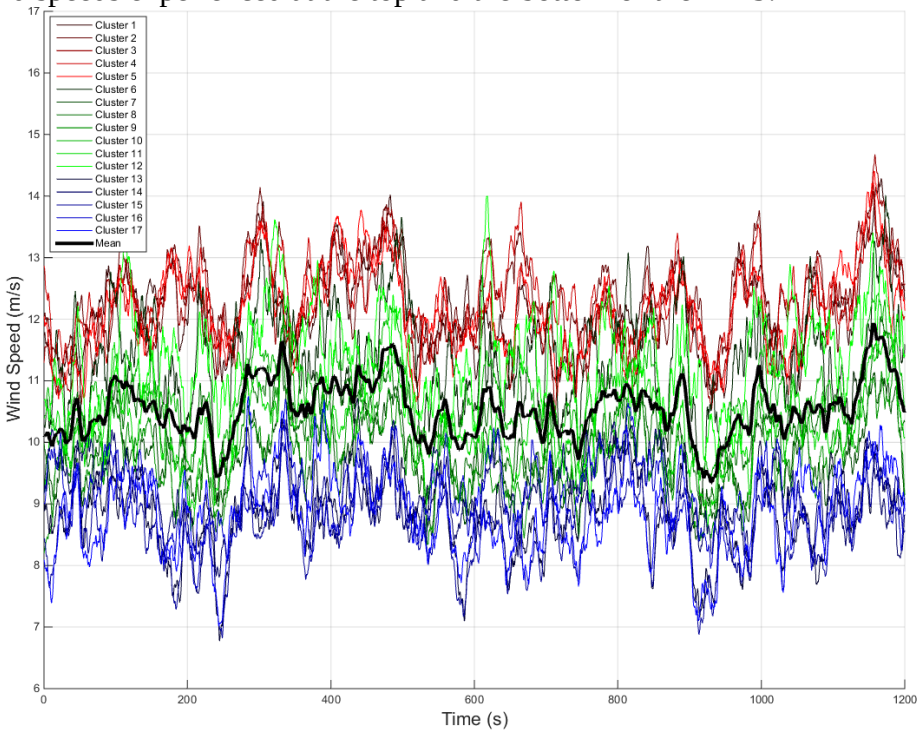

Figure 7.50: Effective wind speeds for each cluster and mean wind speed

7.2.3 Rotor and Power Converter System Controller Design

Each RPC system within the MRS requires a full envelope controller in order to operate effectively. The full envelope controller is required to maximise the power output of the turbine in below rated wind conditions and to output the rated power in above rated wind conditions. In both cases the loads should be minimised. An advantage of the MRS approach over the traditional single rotor approach for very large machines is that RPC systems do not require as much innovation in terms of their design; the RPC systems are familiar to the industry and de-risked, and the dynamics of the RPC systems are comparatively easy to control. Due to these advantages, the full envelope controller does not require the use of more advanced control techniques (e.g. Individual Pitch/Blade Control, Coordinated Control, Tower Feedback Loops). Instead, all that is required is gain scheduling of the above rated controller and the addition of a drive train filter.

The operational strategy chosen for the RPC systems is shown in Figure 7.51.

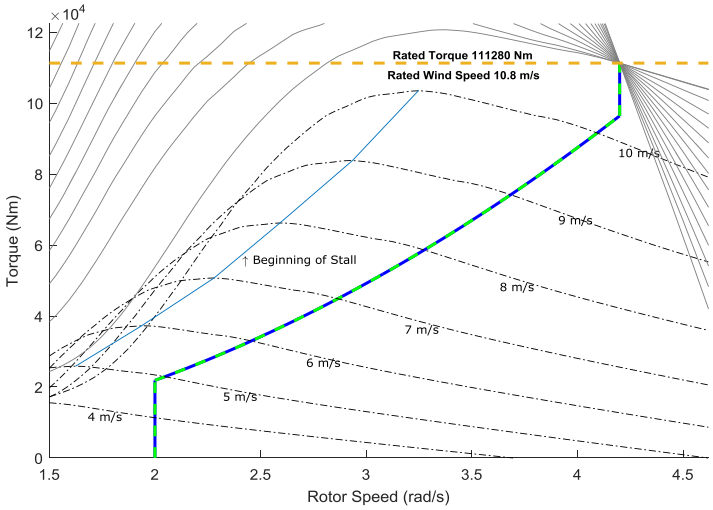

Figure 7.51: Operational strategy for the 444kW RPC system

The maximum power tracking curve is followed between 4.89m/s and 10.2m/s wind speed, with a rotor speed range between 2rad/s and 4.2rad/s.
The full envelope controller is designed using the switching design presented in [28] with below rated and above rated controllers defined as:

$$C_{BR} = \frac{-400000(s + 0.48)}{s(s + 4.85)}$$

$$C_{AR} = \frac{-0.8(s + 0.48)}{s(s + 4.85)}$$

The gain scheduling is performed as a linear approximation of the partial derivative of torque with respect to pitch angle (shown in Figure 7.52). The Bode plots for the controllers for a variety of wind speeds are shown in Figure 7.53.

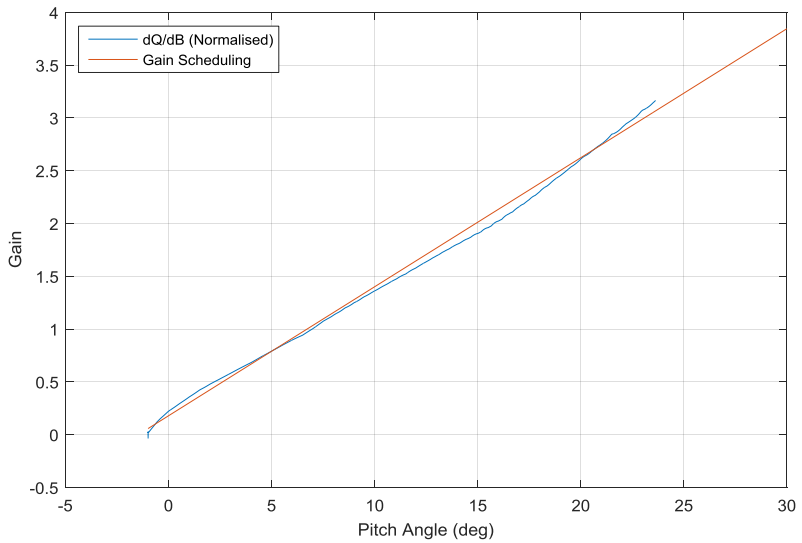

Figure 7.52: Gain scheduling of the RPC systems

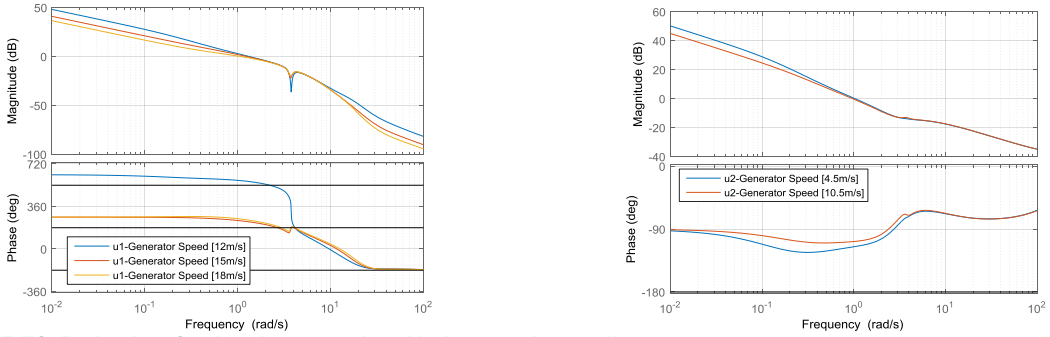

Figure 7.53: Bode plots for the above rated and below rated controllers

7.3 MRS level control

Wind farm level control is a relatively new concept, however, in [29-31] a highly adaptable approach was developed that could be applied to the MRS. This approach utilises a hierarchical structure that can be adapted for the MRS as shown in Figure 7.54.

The MRS controller modifies the set-points for each 444kW rotor and power conversion system (RPC system) via a Power Adjusting Controller (PAC) on each RPC system. The design of the PAC is as a feed forward controller and therefore, no additional feedback loops are introduced for each RPC system and hence the full envelope controller of each RPC system is not compromised. The PAC is capable of fast and slow adjustment of the set points and includes limits to prevent operation outside of a pre-defined safe operational envelope.

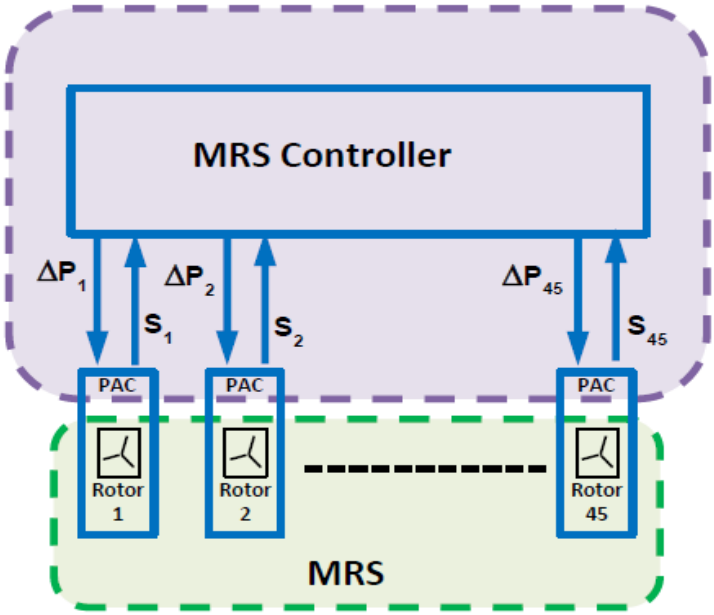

Figure 7.54: Hierarchical structure of the MRS controller

Communication back from each RPC system to the MRS controller is via Boolean flags that provide information regarding the state of each RPC system. In this way, the MRS controller is able to allocate the required change in power appropriately between the RPC systems to meet the control objectives. An expanded diagram for the MRS controller is shown in Figure 7.55.

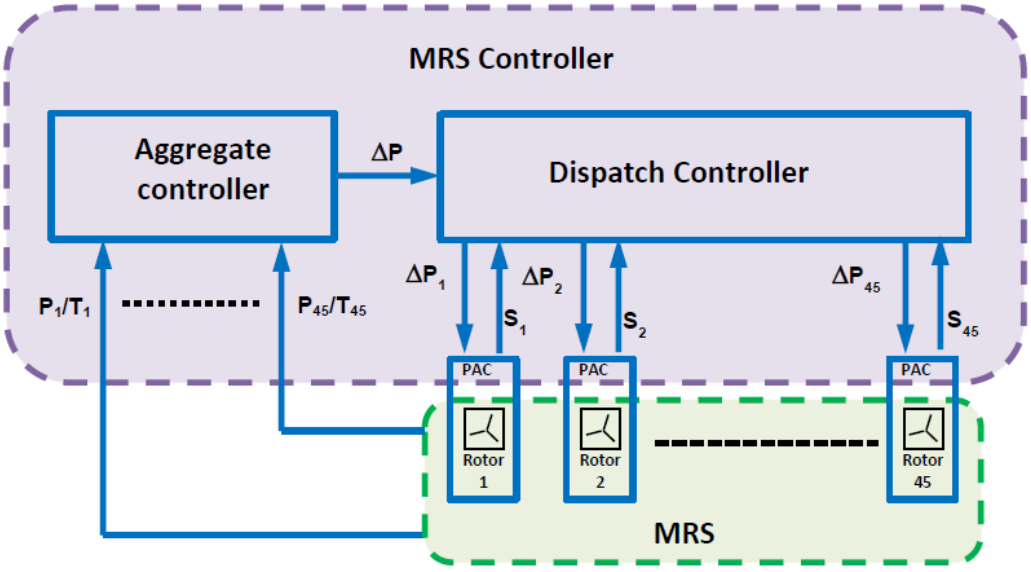

Figure 7.55: Separation of the aggregate and dispatch controllers

In Figure 7.55, the MRS controller is shown to be separated into two separate controllers, an aggregate controller and a dispatch controller. The aggregate controller utilises feedback and delivers a fast acting total change in power ΔP. The feedback introduced around each RPC system through this control action is extremely weak as it is divided between the 45 rotors.
The aggregate controller estimates the total yaw moment and the required reduction in power, ΔP, over a sub-set of rotors required to rebalance the yaw loads with each rotor contributing equally. Included in the aggregate controller is integral action to ensure that the yaw imbalance is driven to zero.
The dispatch controller acts on two different time scales. On a similar time scale to the aggregate controller, the total change in power ΔP is allocated between the RPC systems, taking into account the state of each system identified through the supplied flags (S_{1-45}). On a slower time scale, the dispatch controller acts to adjust the allocations of change in power (ΔP_{1-45}) in order to maximise the total power output. On any RPC system, the feedback involved in maximising the power output is weak due to its slow time scale.

7.3.1 Design of the Power Adjusting Controller (PAC)

In order to implement the MRS level control discussed in the previous section, a Power Adjusting Controller (PAC) must be designed and implemented on each RPC system.
The PAC is designed as a jacket around the full envelope controller (shown in Figure 56), that provides increments to the generator torque and blade pitch angle outputs, and the generator speed input. It is designed as a feed forward controller such that no knowledge of the full envelope controller is required and the operation of the full envelope controller is unaffected by the presence of the PAC.

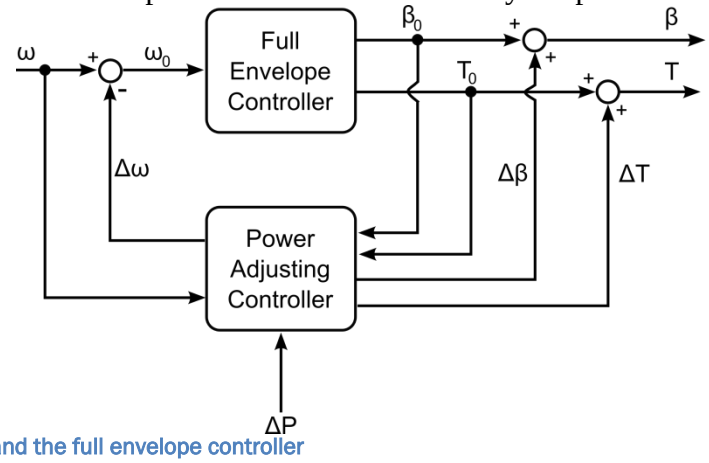

Figure 56: Layout of the PAC and the full envelope controller

The PAC is able to change the power output quickly and accurately through an increment in the torque demand ΔT. The change in torque causes a change in the generator speed. An estimate of this change in generator speed ($\Delta\omega$) is calculated by the PAC and subtracted from the input to the full envelope controller. In this way, the change in generator speed is hidden form the full envelope controller and so the full envelope controller takes no action to counteract the change caused by the PAC.
Simultaneously, a slower acting change to the pitch angle ($\Delta\beta$) alters the aerodynamic torque at the

rotor in order to minimise $\Delta\omega$. The result of these control actions is an effective change to the set point of the controller, without any alteration to the actual full envelope controller required.
The PAC itself can be redrawn as shown in Figure 7.57.

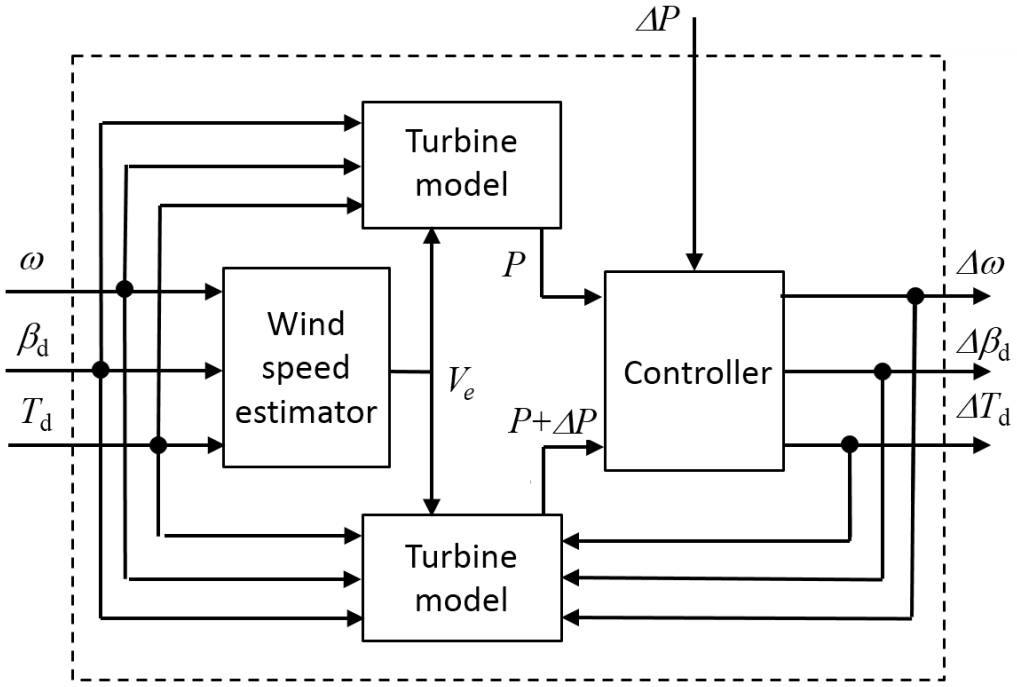

Figure 7.57: Detailed PAC diagram

The components of the PAC shown in Figure 7.57 are as follows:

- A wind speed estimator in which an estimate of the effective wind speed at the rotor in its absence
- Turbine models, which estimate the power with and without the PAC.
- The controller itself, which calculates the required signals for change in torque, pitch, and generator speed to be output.

The controller utilises integral action and is designed as a feedforward controller, and does not introduce strong feedback loops. Hence, the performance of the full envelope controller is not impaired. The aims of the controller are to stabilise the system through the proportional action, and to ensure balanced control such that the pitch response is fast enough to prevent large deviations in the rotor speed when the integral action is included, without introducing high amounts of pitch activity.
The tuning of the PAC is completed using a linearised model of the wind turbine dynamics, and requires the knowledge of the following variables:

- System inertia (rotor, hub and drivetrain combined)
- System damping
- Power and thrust coefficients
- Actuator dynamics

In addition to the gains in the controller, the PAC is gain scheduled using the wind speed estimator as the gain scheduling variable to ensure that similar pitch response is obtained across the operational range.
All variables for the PAC are contained in Appendix 4.

7.3.1.1 Example simulations using one RPC system

In order to demonstrate the PAC, three example simulations are conducted using one RPC system. One simulation uses a below rated wind speed (9m/s), the second uses a wind speed close to rated (11m/s) and the last uses a wind speed above rated (18m/s). A reduction in the power output of 100kW is requested.

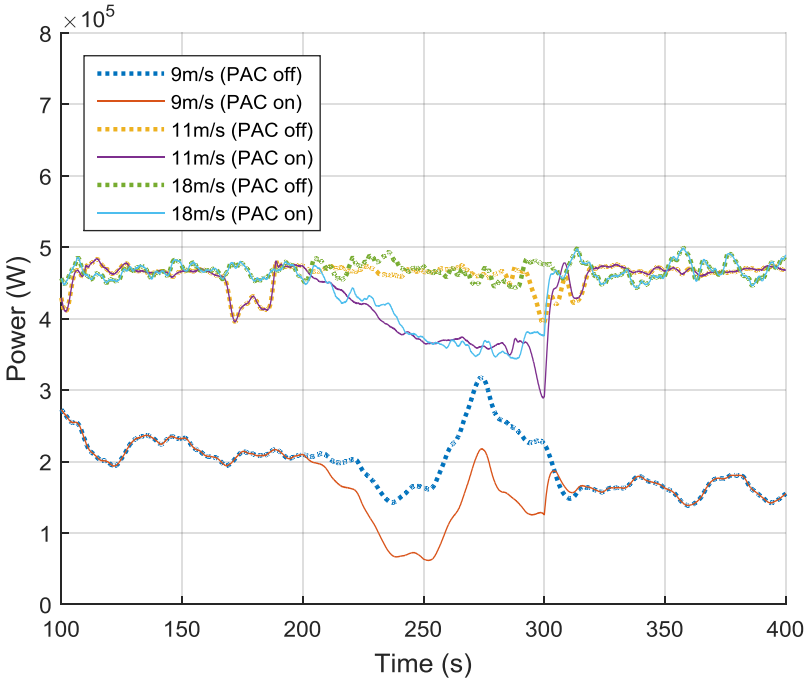

Figure 7.58: Power with and without the PAC in use

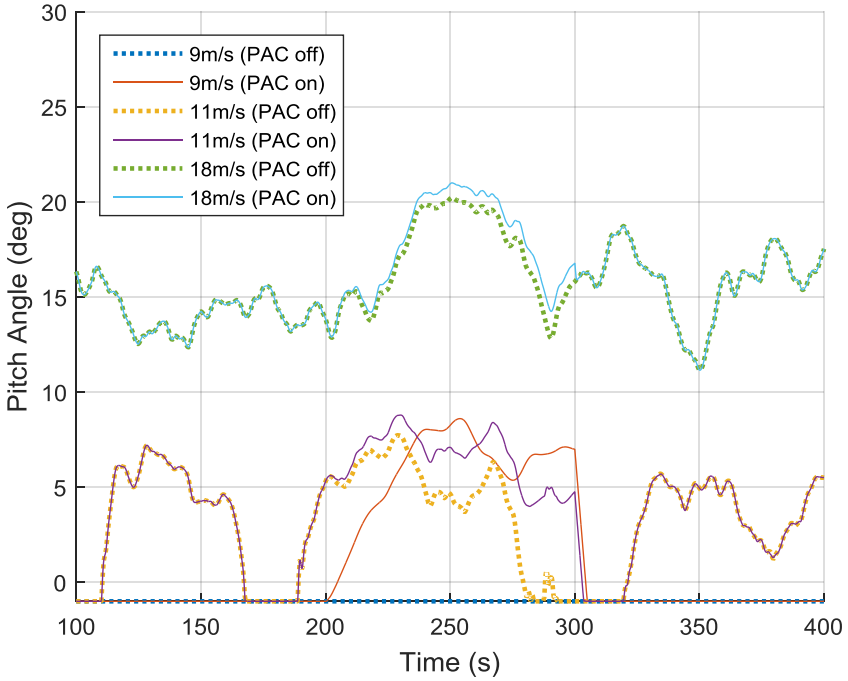

Figure 7.59: Pitch angle with and without the PAC in use

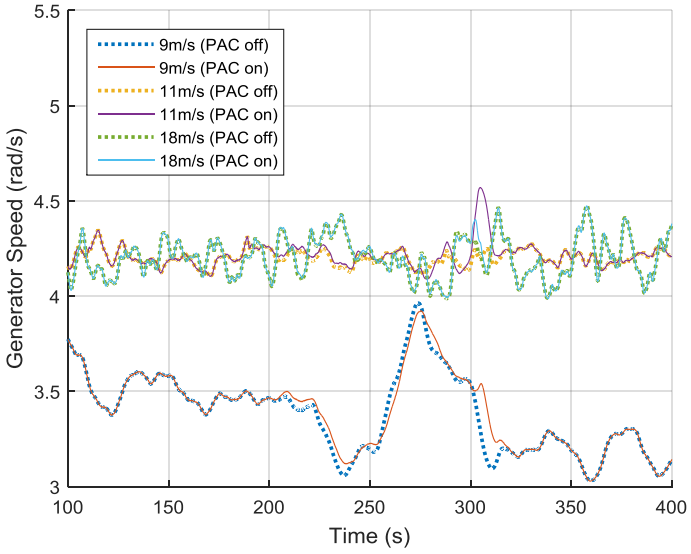

Figure 7.60: Generator speed with and without the PAC in use

Figure 7.58, Figure 7.59, and Figure 7.60 show the results for the power output, the blade pitch angle, and the generator speed respectively, for simulations both without the PAC being used, and with the PAC requesting a reduction of power of 100kW from 200s to 300s.

Figure 7.61 shows the change in power due to the PAC being used.

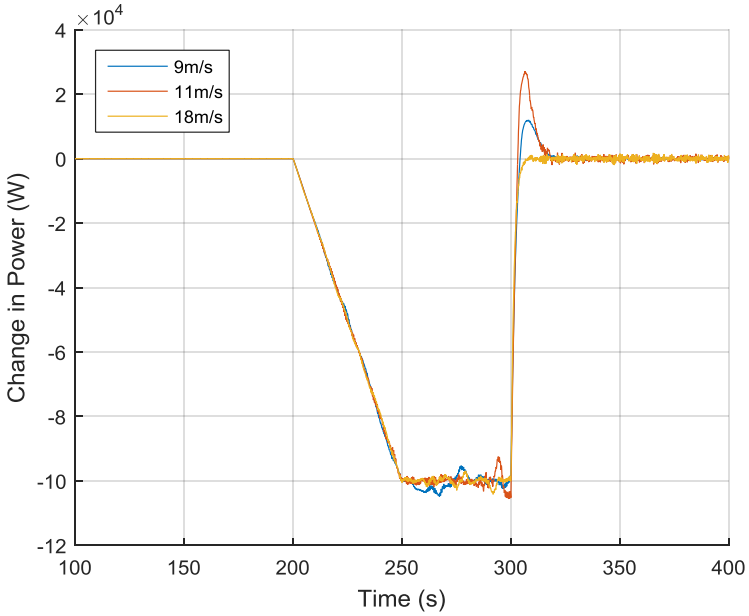

Figure 7.61: Change in power due to use of the PAC

The rate of the reduction in power is limited by the supervisory control (see section 7.4) to a rate of 2kW per second. The power output reduces at the limited rate until the desired change in power (100kW) has been achieved. The reduction in power is then maintained until 300 seconds, at which point the PAC is shut down and it returns the RPC system to normal operation.

Whilst there are some deviations in the change in power output for the 11m/s and 9m/s simulations, these deviations are small and are purely a result of very small changes in the timing of the full envelope controller switching between modes of operation. It can be seen in Figure 7.58 that there are no sharp changes in power output at this time.

In the example presented in Figure 7.61, the recovery is conducted quickly, with some overshoot of the power in below rated wind speeds. The speed of this recovery can be altered. By using different speeds of recovery for different RPC systems within the MRS, the recovery process can be managed such that the change in power across the MRS is smoothed.

Figure 7.59 and Figure 7.60 show that the pitch actuators do not experience a large change in the amount of actuation they are required to perform, and the generator speed does not vary greatly due to the action of the PAC.

7.3.1.2 Supervisory control

As the PAC necessarily moves the operating point of the RPC system away from the normal operating strategy it is important to ensure that the operating point cannot move outside of a predefined safe operational envelope. The "PAC rules" detailed in full in Appendix 3 are designed to meet this requirement. The PAC rules are divided into three types:

1. General supervisory rules

2. Black supervisory rules
3. Traffic light supervisory rules

The general rules contain limits on the maximum, minimum, and rate of change of power and pitch angle. The pitch angle constraint prevents over use of the pitch actuators and/or saturation of the actuators. The limit to the rate of change of power prevents sharp changes in the generator torque to ensure that the instantaneous loads on the drivetrain are no worse than normal operation. With small (compared to modern machines) rotors such as those used in the MRS there is significantly less inertia in the system. The combination of lower rotor inertia and limits on the speed of the pitch actuation (both due to hardware constraints and self-imposed limits to actuator usage) large sharp changes in the generator torque can result in undesirable large and quick changes in the generator speed. The limit to the rate of change of power prevents these large deviations in the generator speed, keeping the variation in generator speed small. As the number of rotors in an MRS system is large, and the yaw dynamics are slow, a slightly restricted speed of response to a change in power request is unlikely to have a significant impact on the yaw control.

The black supervisory rules concern the definition of the black boundaries shown in Figure 7.62. These boundaries are operated such that if the operating point crosses an offset from the black limit (shown as a dotted black line in Figure 7.62), the requested change in power is limited in order to prevent the operating point crossing black limit. Due to the relative lack of inertia of the RPC systems used on the MRS, the size of the offset is required to be significantly larger in proportion than for larger machines. If the operational point remains within the offset region for a period of time greater than 20 seconds the PAC turns off and recovers the operational point back to the normal operating strategy.

In the event that the limits on the change in power applied at the offset are not sufficient to prevent an excursion as far as the black limit, the PAC is set to automatically turn off and recover the operating point to the operational strategy.

The black limits are used on the RPC systems to ensure that the wind turbine does not enter aerodynamic stall, as well as to set an upper and lower bound on the increment to torque.

The traffic light supervisory rules act as a soft limit on the operation of the PAC. The area bounded by the black limits is divided into three areas defined as green (within the green line on Figure 7.62), amber (between the green and red lines on Figure 7.62), and red (outside of the red line in Figure 7.62). When operation is within the green/amber/red zone a green/amber/red traffic light flag is passed to the MRS controller. The MRS controller is able to use the traffic light flags to inform the distribution of the total requested ΔP amongst the RPC systems within the MRS.

Because of the low amounts of inertia in the RPC system rotors, there is very little room between the operational strategy and the black limit offset in the upper left of Figure 7.62. Because of the limited space, the green and red boundaries are coincident such that there is no amber region.

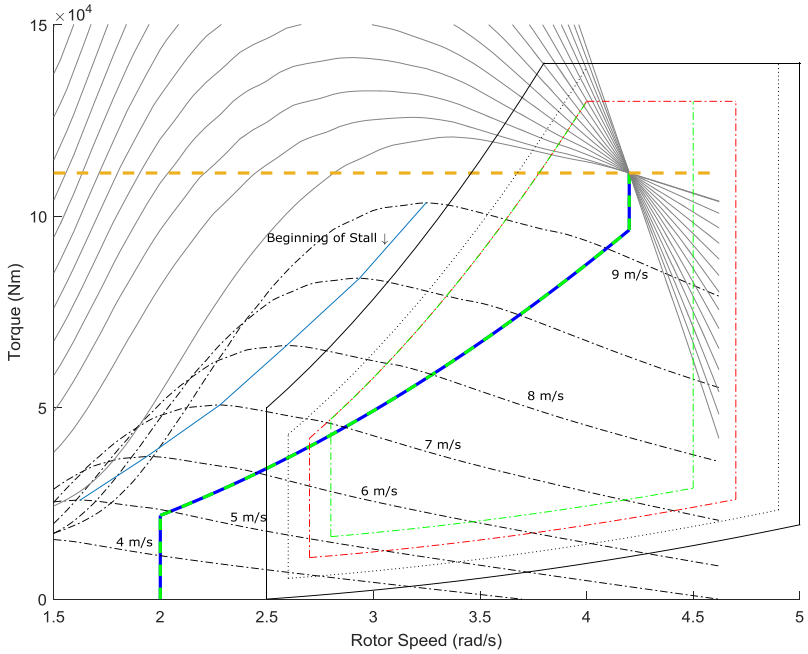

Figure 7.62: Supervisory control regions

7.3.2 Control of the MRS yaw

When studying the stability of the system and developing a controller to yaw the MRS the inertia of the system is critical. The total inertia of the system about the y axis can be modelled as the inertia of the support frame plus the inertia of the rotors. The rotors themselves can reasonably be modelled as point masses. Using this approach, the inertia about the y axis is 20,586 $Mkgm^2$. The yaw dynamics can then be reasonably approximated as a second order dynamic system:

$$\frac{\varphi}{M} = \frac{1}{J_{yaw}s^2 + B_{yaw}s}$$

where J_{yaw} is the inertia of the system, B_{Yaw} is the damping, M is the moment about the y axis, and φ is the error in yaw angle (assuming a constant wind direction). It is assumed that damping losses are approximately 1% of the torque.

The yaw speed results in an addition to the wind speed experienced by each RPC system cluster of $\dot{\theta}r_n$, where $\dot{\theta}$ is the angular speed of yawing and r_n is the distance from the centre of rotation to the centre of the RPC cluster.

With the MRS, RPC systems, and full envelope controllers modelled as described in section 7.3, with the PAC designed as described in the previous section, and with the yaw dynamics as described above, the MRS yaw controller can be designed.

As a baseline, a simulation is conducted whereby no yaw control is provided. The resultant yaw angle for this simulation is shown in Figure 7.63. Note that until 100 seconds simulation time the yaw is fixed at zero to allow for transients related to the start-up of the model to diminish.

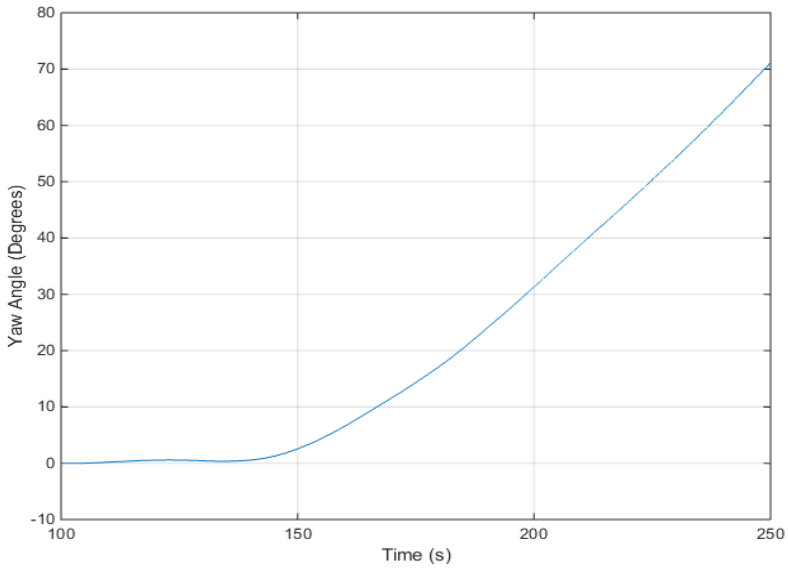

Figure 7.63: Yaw angle, no yaw control 11m/s wind speed

Clearly, without remedial control action the MRS yaw angle is unstable.
As an initial design to test the feasibility of using the wind farm control techniques to control the yaw angle, a simple PID controller is designed based on a feedback of the yaw angle. A diagram of the system is shown in Figure 7.64. Due to the low inertia of the RPC systems it is impractical to increase their power output in below rated conditions, and so only reductions in power are used for the initial design. As the design is purely a proof of concept (i.e. intended to show that the MRS yaw can be controlled in this manner) further simplifications have been made:

1. It is assumed that all the RPC systems on each side of the MRS will receive the same change in power
2. The controller design is concerned solely with the yaw angle, and no attempt is made to maximise nor smooth the power output of the MRS (i.e. the controller design is entirely at the dispatch rather than aggregate controller level).

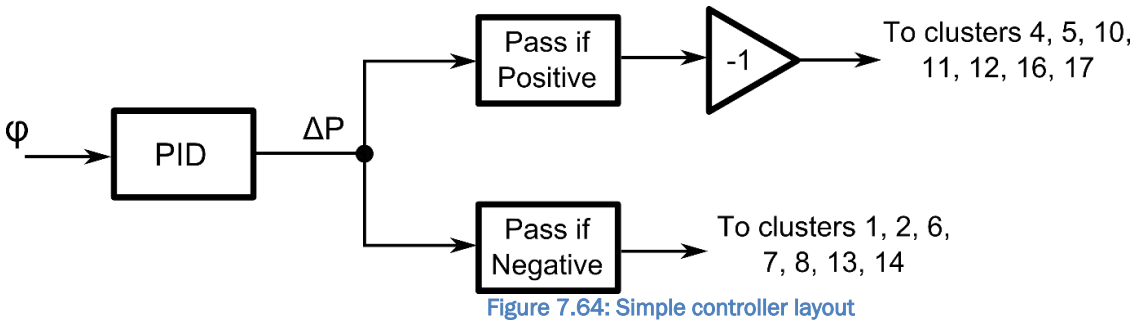

Figure 7.64: Simple controller layout

The PID controller was tuned manually. The yaw angle for the MRS system using the simple PID approach is shown in Figure 7.65, whilst the power output is shown in Figure 7.66 along with the power output of the MRS if held with zero degrees yaw and no yaw control.
Despite the simplistic approach to the controller design, the yaw angle is kept within +/-5 degrees. The impact on the power output is small whilst the yaw angle is small, but the power drops significantly when larger errors in the yaw angle occur as the MRS must reduce the power output by a larger amount to achieve a larger yaw moment to correct the error.

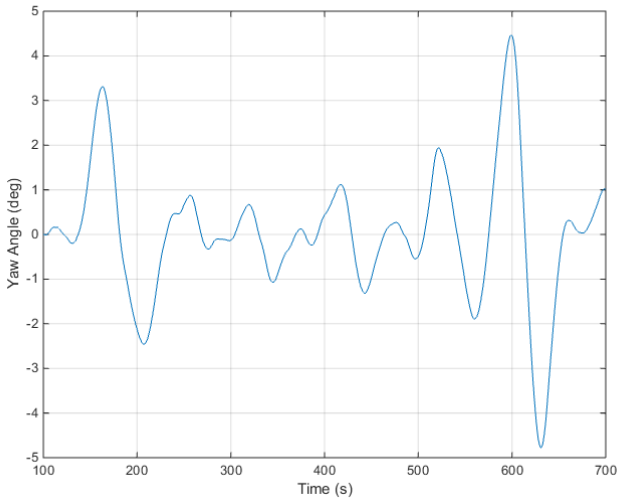

Figure 7.65: Yaw angle against time for a MRS with simple yaw control

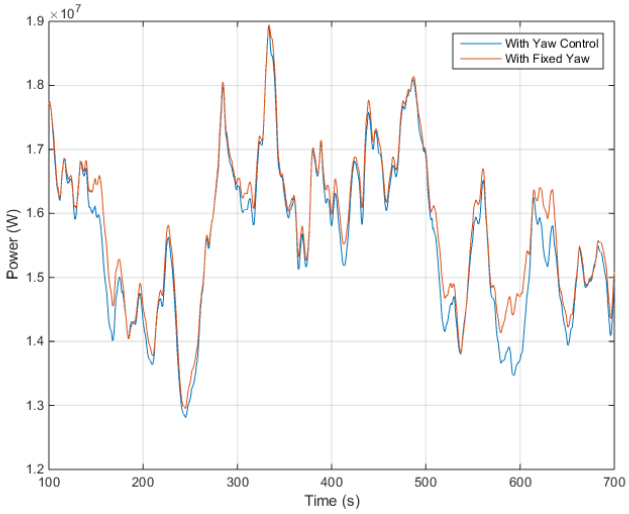

Figure 7.66: Comparison of power output with fixed yaw and power output with simple yaw control

A graph of the yaw rate is presented in Figure 7.67 and illustrates that the MRS can be yawed at a suitably fast rate using the wind farm control technique.

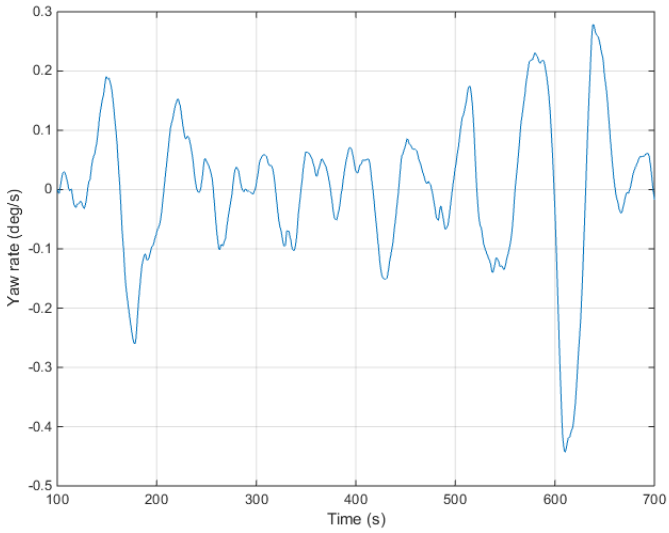

Figure 7.67: Yaw rate for the MRS with simple yaw control

Improving upon the simple manual approach used for the tuning of the PID, instead the open loop transfer function of the system is analysed. The control diagram is shown in Figure 7.68. The RPC blocks are the transfer functions from ΔP, requested by the PAC, to the change in thrust for one rotor. The plant J is simply the transfer function for the yaw dynamics at the beginning of section 7.3, with the input the overall change in moment of the MRS (the moment produced on one side subtracted by the moment produced on the other side). If it is assumed that one side of the MRS is running as normal, then the change in moment due to the PAC will also be the overall change in moment for the MRS. In effect the open loop transfer function is the transfer function of one side of the MRS.

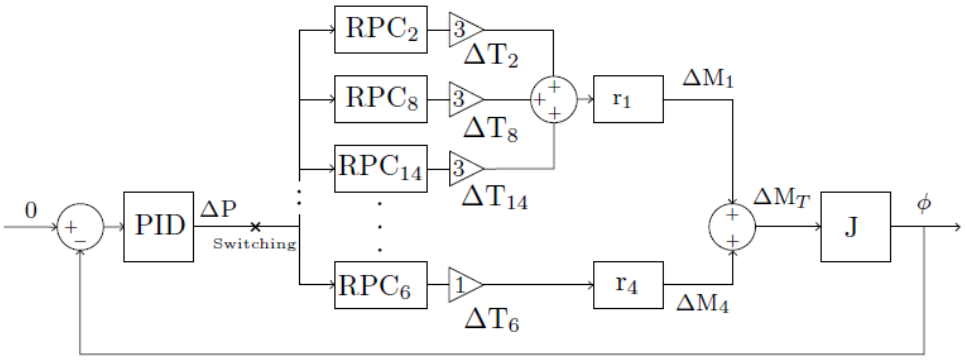

Figure 7.68: Initial control diagram for MRS

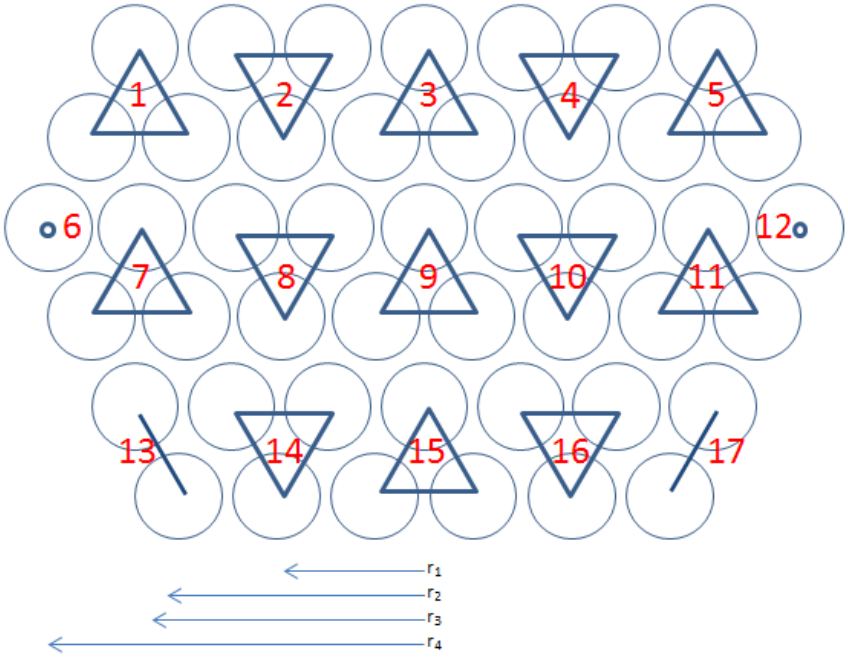

Figure 7.69: Distance of groupings from yaw axis

The control diagram corresponds with both the numbering of the groups and the distance from yaw axis of each group seen in Figure 7.69: Distance of groupings from yaw axis. The switch (or 'if gate') marked with a cross corresponds to the switch seen in Figure 7.64. The 'if gate' dictates on which side of the MRS the power will be reduced. The numbers in Figure 7.68 correspond to the rotors on the left hand side of Figure 7.69: Distance of groupings from yaw axis. A gain is applied to the output thrust of each RPC block to represent the number of rotors in that cluster. Clusters located at the same distance from the yaw axis are then summed together and multiplied by this distance to find a moment. These moments are summed together and the total change in moment is found.

An empirical approach is taken to finding the transfer function of the RPC plant from ΔP to ΔT. A negative step is supplied to a PAC on a single RPC system and the thrust response of the RPC system is analysed. By modelling the RPC as a second order system, an approximation of the dynamics is estimated. Given an input of -20kW; the overshoot and frequency are read from the graph resulting in values for the gain, natural frequency and damping ratio for the transfer function. At each wind speed this response differs and so a transfer function is found across the operational wind speeds of the turbine. Figure 7.70 shows the change in thrust at 8m/s from the step input as well as the output from the modelled transfer function given the same input. As the output of the transfer function is the change in thrust the initial starting value of the actual thrust is added so as to compare the results. The transfer function gives a slightly sharper decrease in thrust however it is clear that a second order transfer function can adequately represent the physical system.

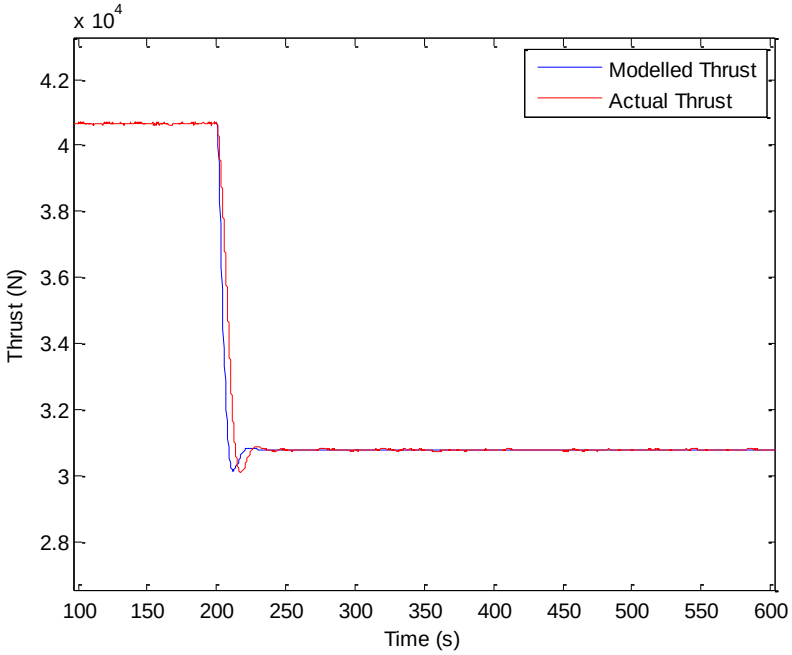

Figure 7.70: Actual thrust and thrust from second order transfer function at 8m/s

The open loop transfer function of the MRS is used to tune the system, however finding adequate gain and phase margins whilst also keeping the gain crossover frequency high is demanding and requires a large derivative gain. Tuning using purely PI control is highly limiting in terms of the achievable gain and phase cross overs. Figure 7. 71 is the bode plot for the MRS plant and shows the low phase crossover system of the system. In effect, a phase lead term has to be introduced. This type of controller would require large amounts of power reducing the energy being supplied to the grid through high amounts of control action.

Instead a double control loop system is used which is shown in Figure 7.72. The first inner loop, working at a faster rate, acts to reduce the yaw rate whilst the slower outer loop acts to reduce the yaw error. The inner loop also includes the switching system seen in Figure 7.64 to ensure that the PAC will only request a reduction in the power, however the input is the yaw rate as opposed to the yaw angle. The transfer function J now outputs $\dot{\emptyset}$ and has the form:

$$\frac{\dot{\emptyset}}{\Delta M_T} = \frac{1}{J_{yaw}s + B_{yaw}}$$

As the value for B_{yaw} is small the transfer function J effectively acts as an integrator. The inner loop therefore only requires a proportional control. An integrator is added to the plant to obtain $\emptyset$ for the outer loop. Again this means integral control is unnecessary and so only proportional control is used for the outer loop.

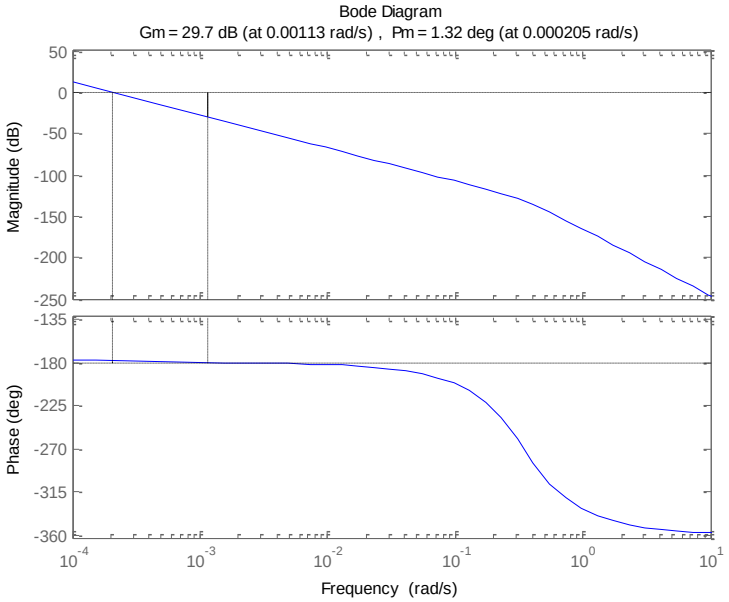

Figure 7. 71: Bode plot for original plant from ΔP to $\emptyset$

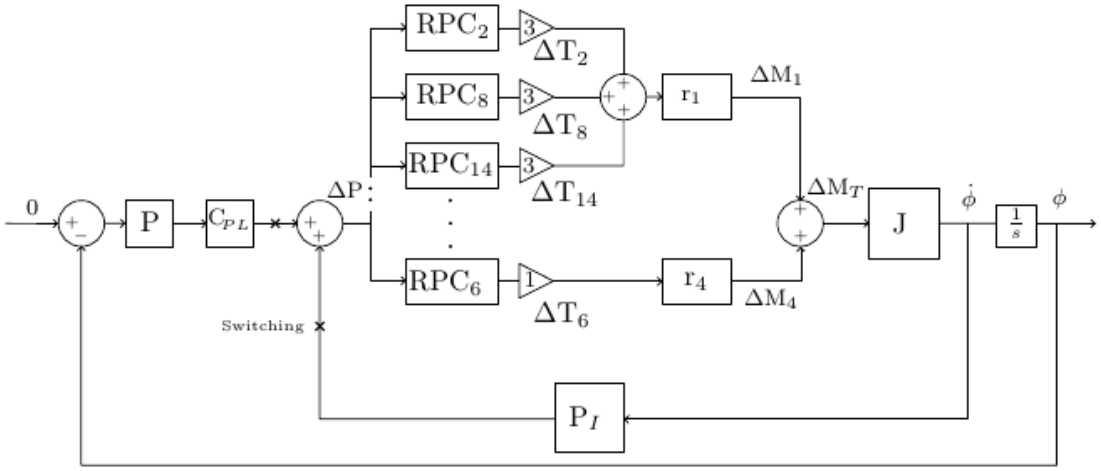

Figure 7.72: New control design for MRS

Figure 7.73 and Figure 7.74 illustrates the ease with which the system can now be tuned. Figure 7.73 shows the open loop transfer function from ΔP to $\dot{\emptyset}$. The phase crossover is much higher and so the inner loop is tuned, using P control only, to a high gain crossover frequency of 0.239 rad/s, at 8m/s, without compromising the gain margin.

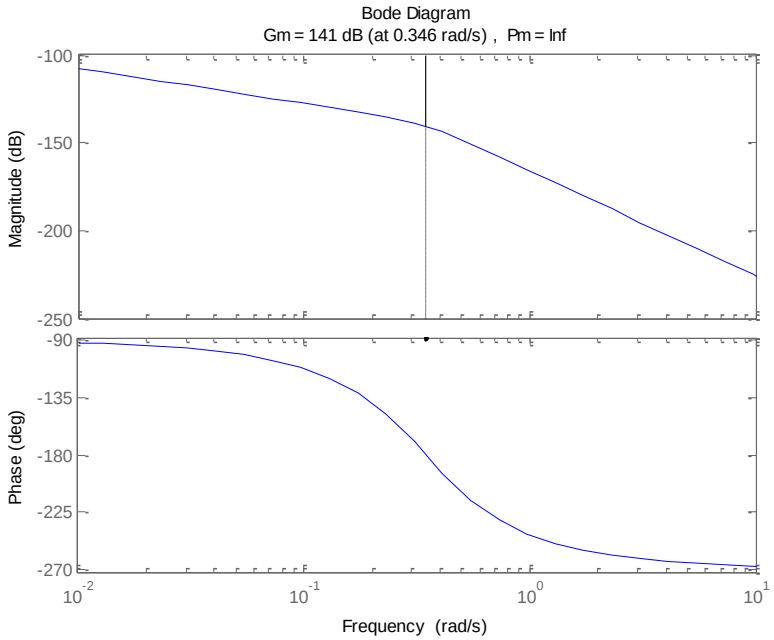

Figure 7.73: Bode plot of open loop transfer function of inner loop ΔP to $\dot{\emptyset}$

With the inner loop tuned, the closed inner loop transfer function combined with the integrator now forms the open loop transfer function for the whole system. The results of tuning at 8m/s with proportional gain only are shown in Figure 7.74. Clearly the phase margin is high and so a phase lag controller is added resulting in a higher crossover frequency of 0.115 rad/s.

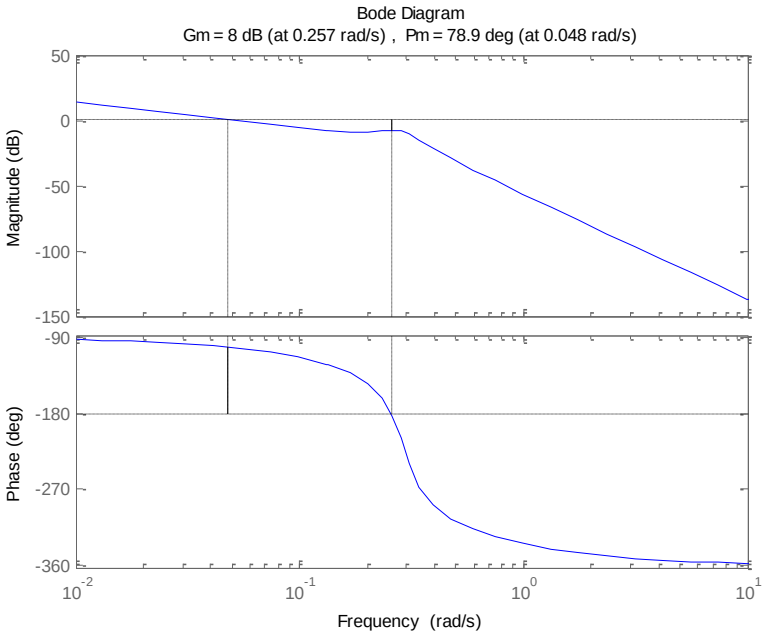

Figure 7.74: Bode plot for open loop transfer function from ΔP to $\emptyset$

Figure 7.75, Figure 7.76 and Figure 7.78: Yaw error at 8 m/s over one hour period show the results for the MRS at 8 m/s. Over a time period of 700s the MRS was kept within a yaw error of 1 degree. The yaw rate remains stable with no fluctuations above 0.06 degrees/s. The power output over this period is compared with power output of zero yaw error in Figure 7.77. The impact on the power is small as would be expected with the small yaw error. Figure 7.78 shows that the MRS remains stable over a long period of time (1 hour), staying within 1.3 degrees. Figure 7.79 again shows the low yaw rate at 8m/s with yaw rate rarely exceeding +/- 0.08 deg/s.

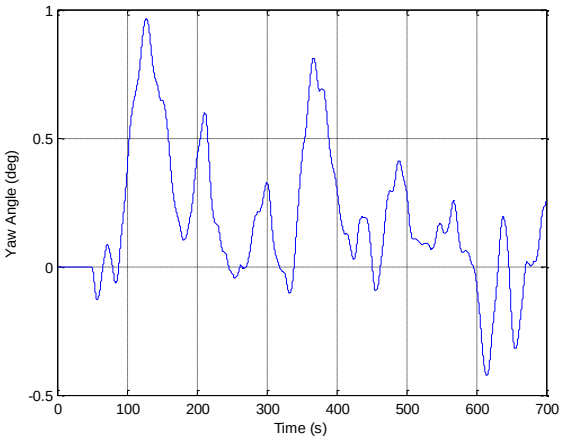

Figure 7.75: Yaw Angle for the MRS

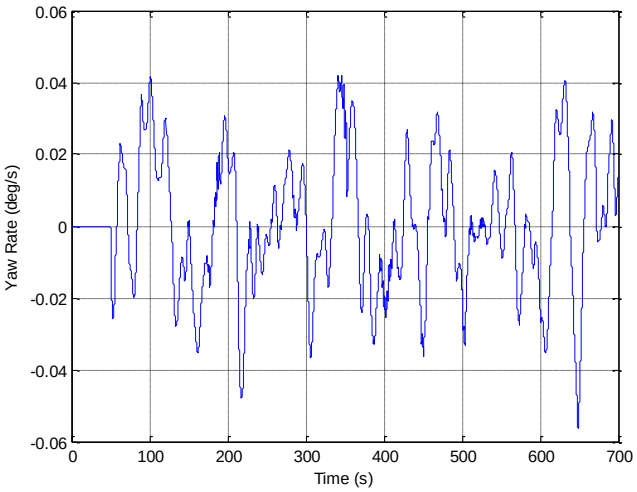

Figure 7.76: Yaw rate for the MRS

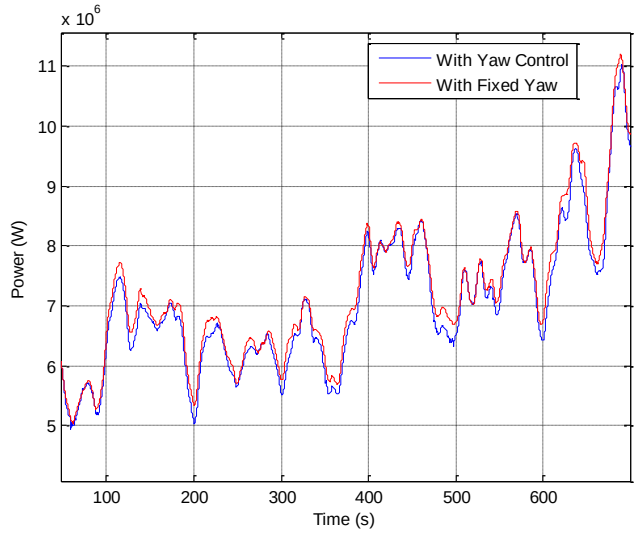

Figure 7.77: Power produced by MRS over 1 hour period both with fixed yaw and yaw control

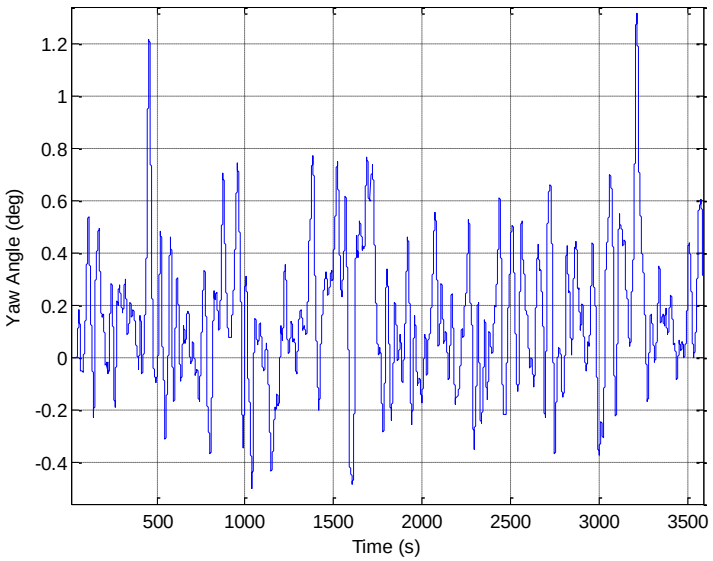

Figure 7.78: Yaw error at 8 m/s over one hour period

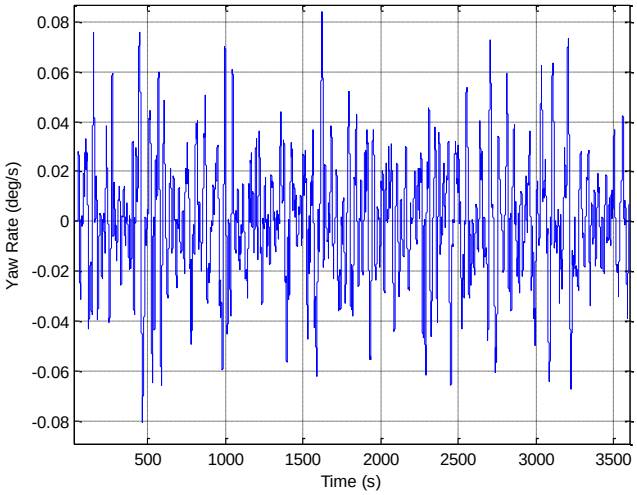

Figure 7.79: Yaw rate at 8m/s over one hour period

The yaw error and yaw rate is tested using turbulent wind conditions with averages both at close to rated (11m/s) and above rated (15m/s). Figure 7.80 and Figure 7.81 show the yaw error and yaw rate respectively at an average wind speed of 11 m/s. The results at rated show greater variation in the yaw angle than in the below rated simulation, keeping the yaw angle within +/-6.5 degrees however the MRS did remain stable over this period. Figure 7.82 and Figure 7.83 show the results at 15 m/s where a maximum yaw error 1.5 degrees is obtained.

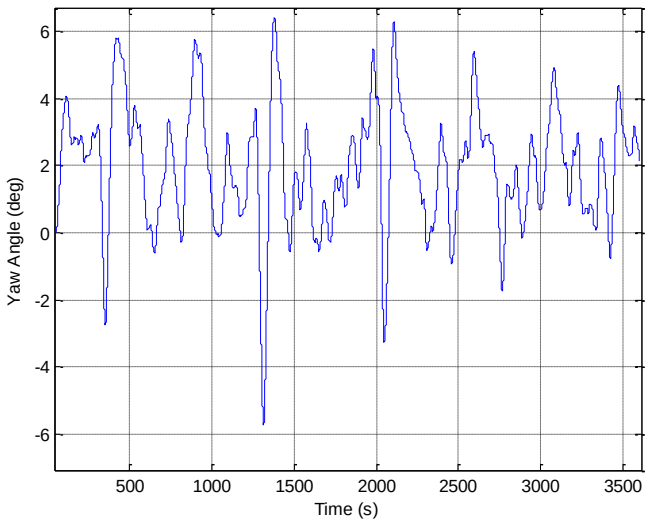

Figure 7.80: Yaw error over one hour period at an average wind speed of 11 m/s

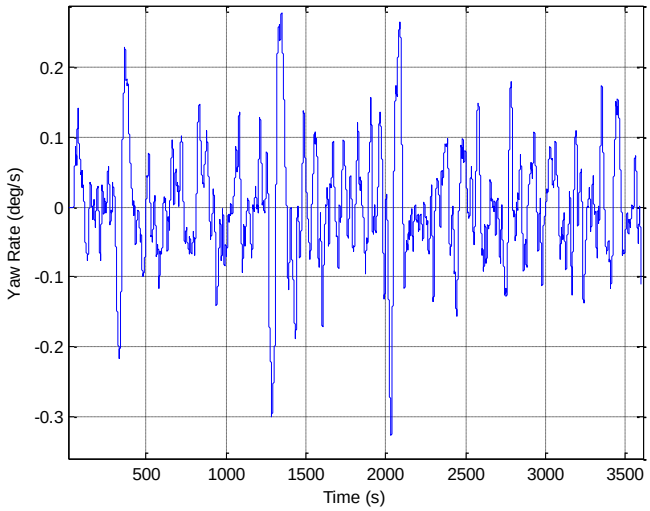

Figure 7.81: Yaw rate over one hour period at an average wind speed of 11 m/s

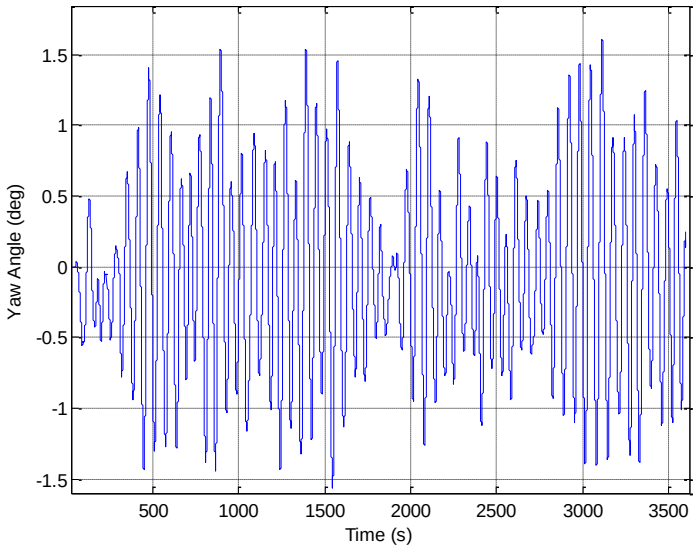

Figure 7.82: Yaw error over one hour period at an average wind speed of 15 m/s

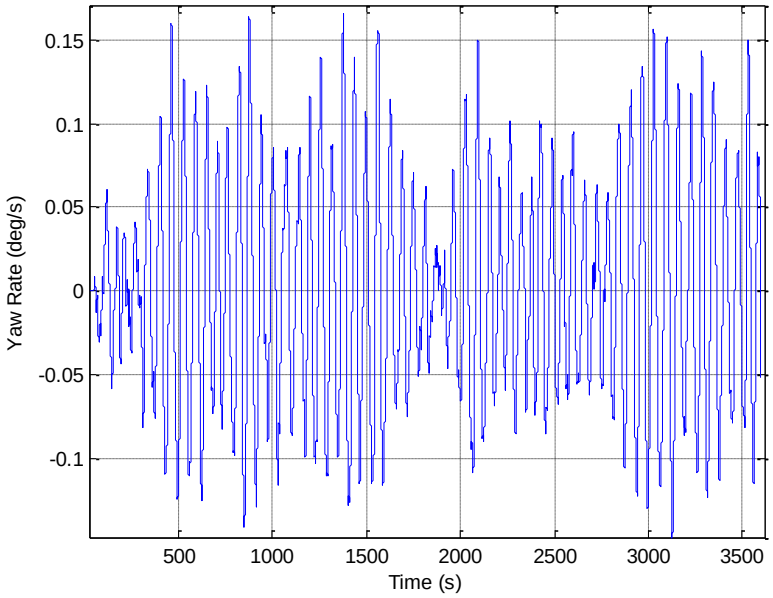

Figure 7.83: Yaw rate over one hour period at an average wind speed of 15 m/s

The power is measured over the 1 hour time periods and compared to a scenario with zero yaw error. The energy lost at 8 m/s, 11m/s and 15 m/s over this period are 213MJ, 870MJ and 3.18GJ respectively. As a percentage this equates to 0.84%, 1.5% and 4.49% of the energy obtained with zero yaw error. The larger percentage loss is expected at higher wind speeds due the lower gain values of

the transfer function from ΔP to ΔT. This means that a higher gain is needed for the proportional controllers above rated, resulting in a larger reduction power for a given reduction in thrust.

7.3.3 Control of Fore-Aft Pitching Motion

The MRS is designed as a floating system for use far offshore. The dynamics of a floating MRS must be modelled to help assess the feasibility of the floating design. In this deliverable, the pitching motion (hereafter referred to as fore-aft pitching motion to prevent confusion with blade pitching) is modelled, and a controller is introduced to provide additional aerodynamic damping to the system. The purpose of this work is to show that damping the fore-aft pitching motion of the MRS through control of the power output of the RPC systems is possible.

7.3.3.1 Modelling the fore-aft motion

In Task 1.3 of INNWIND.EU, several methods for floating the MRS were considered, with the main focus being on the possible cost of energy implications. Clearly, the design of the floater has a direct impact on the dynamics of the MRS. Following discussions between a number of contributors to the deliverable a spar floater design is chosen, as a balance between cost and stability.
For ease of modelling, the spar floater is designed for fore aft motions as shown in Figure 7.84. It is assumed that the rotation takes place about the centre of mass. The buoyancy force is denoted as B, and the total thrust force is denoted as T_F.

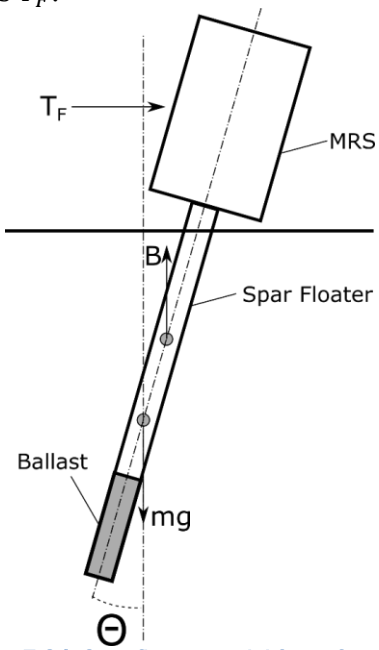

Figure 7.84: Spar floater model fore-aft motion

The floater is designed with a heel angle of 3.5 degrees at rated wind speed. The specification for the floater can be found in Appendix 5.

Spar floaters provide large amounts of inertia to the system, through both the sizable structure that must be constructed and through the mass of the displaced water when said structure moves. These dynamics are modelled as described in [32]. The damping and inertia of a floating structure provided by the water is described by Morison's equation:

$$F = 0.5\rho C_d D|U|U + C_m \rho A\dot{U}$$

where F is the force per unit length of the spar, C_d is the drag coefficient, C_m is the inertia coefficient, ρ is the density of water, D is the spar diameter, A is the spar's cross sectional area, U is the velocity of the flow resolved normal to the spar, and $\dot{U}$ is the acceleration of the flow resolved perpendicular to the spar. Integration of the forces along the length of the spar yields the moment, which, ignoring waves is

$$M = \frac{C_d D\left|\dot{\theta}\right|\dot{\theta} l^3}{3} + \frac{C_m \rho A \dot{\theta} l^2}{2}$$

The velocity and acceleration of the water particles also influence the damping and the inertia, and are dependent upon the motion of the spar and the motion of the waves. These can be modelled using Stoke's wave theory. In the case of the MRS, the size of the spar floater necessitates situating the MRS in deep water, and, as such, the deep water approximation can be used whereby:

$$L = \frac{gT^2}{2\pi}$$

$$A_w = 2\pi\left(\frac{x}{L} - \frac{t}{T}\right)$$

$$U = \frac{\pi H}{T} e^{kz}\cos(A_w)$$

$$W = \frac{\pi H}{T} e^{kz}\sin(A_w)$$

$$\frac{dU}{dt} = \frac{2\pi^2 H}{T^2} e^{kz}\sin(A_w)$$

$$\frac{dW}{dt} = \frac{-2\pi^2 H}{T^2} e^{kz}\cos(A_w)$$

$$k = 2\pi/L$$

where L is the wavelength, A_w and k are useful constants/variables to define, g is the acceleration of gravity, T is the wave period, x is the distance in the direction of the flow, t is time, H is the wave height, z is the distance below the surface of the water, U is the flow velocity in the horizontal direction, and W is the flow velocity in the vertical direction. The deep water approximation is valid when,

$$\frac{d}{gT^2} > 0.08$$

where d is the water depth.

To provide suitably modelled waves, the JONSWAP spectrum is used to provide the wave characteristics. An inverse Fourier transform is then used to generate a time history for implementation in the model. The inputs to the JONSWAP spectrum are found using a wave characteristic diagram

such as that shown in Figure 7.85, with the assumption that fetch is not the limiting factor and with a wind duration of six hours.

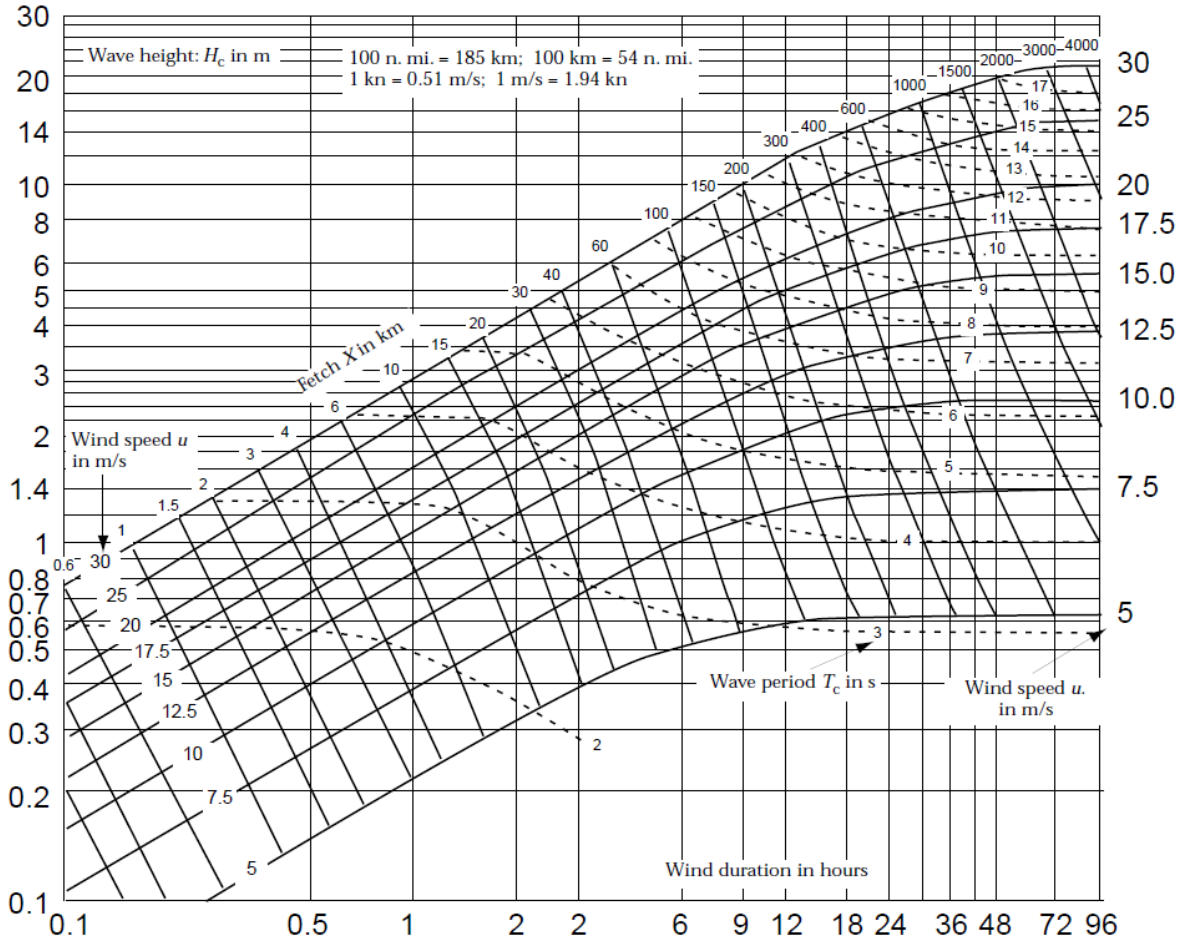

Figure 7.85: Wave characteristic diagram (from [33])

The motion of the MRS in the fore-aft direction has an impact on the wind speed experienced by each RPC system. The wind speed experienced by an RPC system is given by,

$$U = U_{orig}\cos(\theta) + \dot{\theta}r$$

where U is the wind speed, U_{orig} is the original wind speed (assuming no motion), θ is the fore-aft angle, $\dot{\theta}$ is the fore-aft angular speed, and $r$is the vertical distance from the centre of rotation to the RPC system.

The parasitic forces on the MRS structure are modelled using a look up table populated with data for the static thrust at given wind speeds. This look up table uses the average wind speed across the rotor as its input and outputs the parasitic thrust force. This force is assumed to act at the centre of the MRS. In order to damp out the fore-aft motion, the PAC can be used to alter the thrust of RPC systems proportional to the rate of change of fore-aft angle. Above rated wind speed the thrust can be both increased (via an increase in the power output) and decreased (via a reduction in the power output. In

below rated conditions it is not possible to increase the power above the output provided when the PAC is not in use, as, due to the low inertia of the RPC systems, the RPC systems quickly reach the upper torque limit when power increases are requested below rated wind speeds. Because of this, the maximum change in power request in above rated conditions is set to 0.
Figure 7.86 shows that the rate of change of thrust with respect to wind speed is large and positive for below rated conditions however, so the RPC systems provide significant damping without any additional action by the PAC. In above rated conditions however, the rate of change of thrust with respect to wind speed is negative, and so the RPC systems naturally enhance the fore-aft motion without any additional action from the PAC. At higher wind speeds the rate of change of thrust with respect to wind speed is of lesser magnitude, and the effect is at its most pronounced just above rated wind speed.

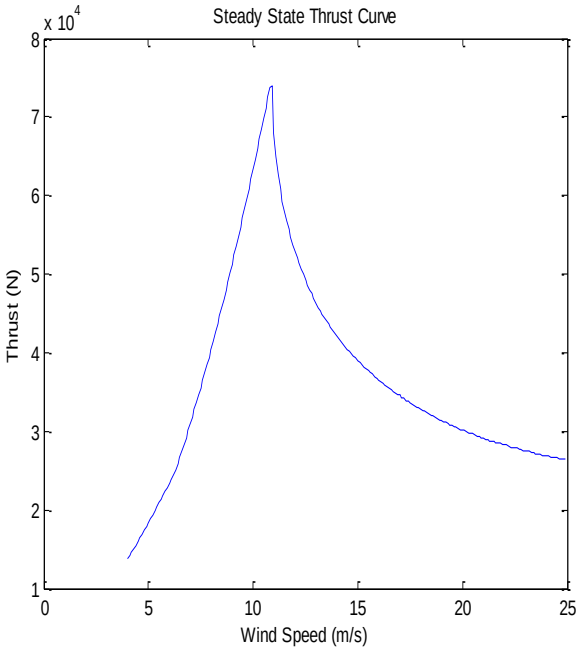

Figure 7.86: Steady state thrust curve

The damping controller provides a change in power response proportional to the rate of change of the fore-aft angle. In below rated conditions, the maximum increase in power output is limited to zero, with the PAC on each RPC system turned off and recovered back to normal operation when the requested change in power is zero or above.

7.3.3.2 Results

The model is run without any fore-aft damping control to provide baseline results for the fore-aft pitch angle and the total power output. The fore-aft pitch and power output with no fore-aft pitching damping control is shown in Figure 7.87 and Figure 7.88. Without any fore-aft pitching damping control the pitch angle varies over a range of up to 7 degrees in above rated winds. In below rated

winds, the natural damping discussed above restricts the fore-aft pitch angle to a tighter range of approximately 1 degree. For wind speeds of 11m/s, 12m/s, and 14m/s the power oscillations are very large. In the case of the 14m/s and 16m/s simulations one or more RPC systems enter stall due to the rapidly changing wind speed induced by the fore-aft motion and the controllers of said RPC systems becomes unstable.

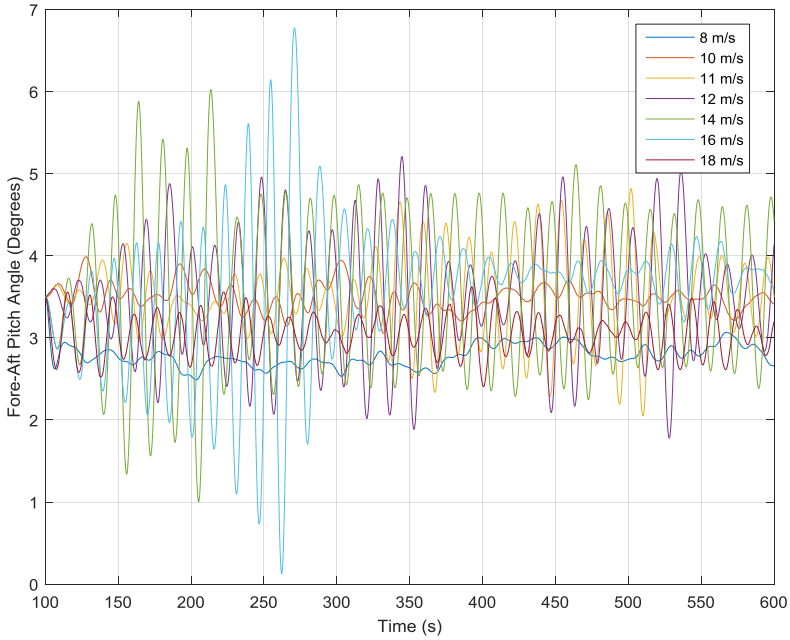

Figure 7.87: Fore-aft pitch angle against time for a variety of wind speeds – no fore-aft damping control

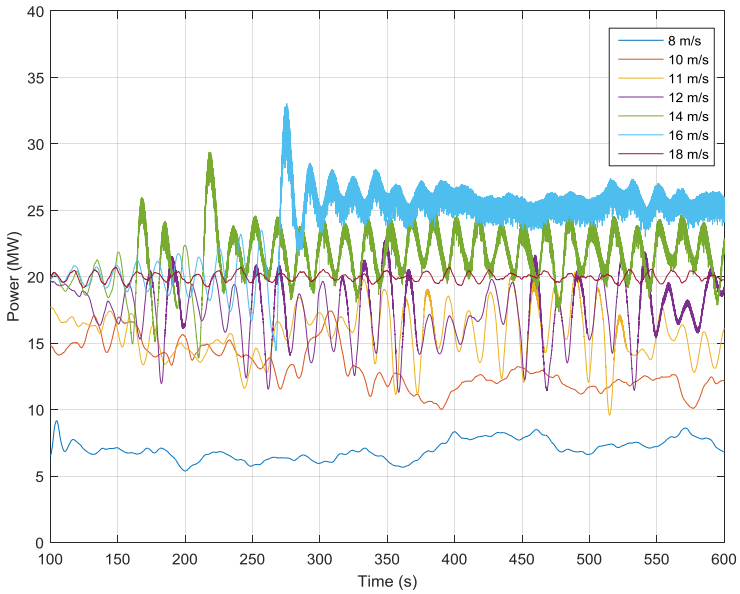

Figure 7.88: Power Output against time for a variety of wind speeds – no fore-aft damping control

Fore-aft pitching damping control is introduced using all the RPC systems. The results for fore-aft angle and power output are shown in Figure 7.89 and Figure 7.90. All the simulations start with a fore-aft pitch angle of 3.5 degrees. The MRS is held perpendicular to the wind for the first 100 seconds. For the first 50 to 150 seconds after the fore-aft motion is turned on in the model there is some transient behaviour.

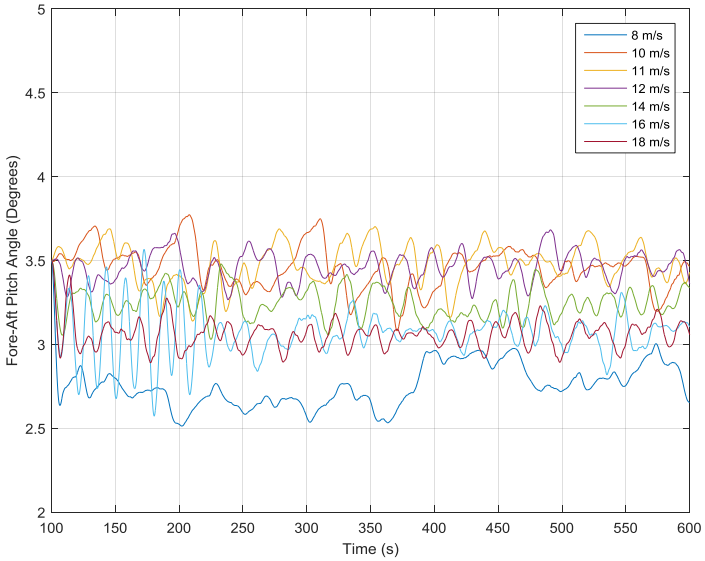

Figure 7.89: Fore-aft pitch angle against time for a variety of wind speeds – with fore-aft damping control

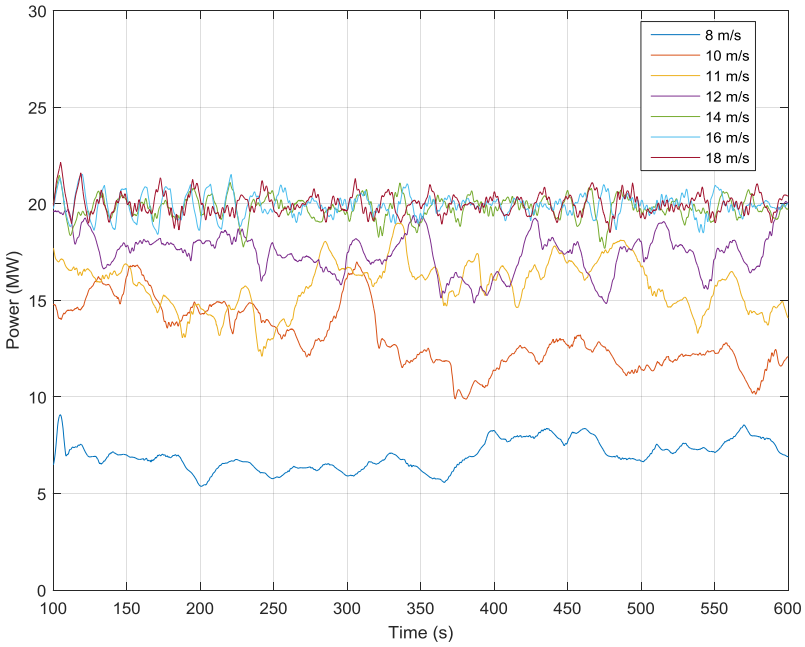

Figure 7.90: Power Output against time for a variety of wind speeds – with fore-aft damping control

It is clear that after the transient period is passed, the fore-aft motions are significantly damped compared to the results without the damping controller. The power output of the MRS is also significantly smoothed. The change in total energy capture is calculated and shown in Table 7.6.

Table 7.6: Change in average power output due to fore-aft control

Wind Speed (m/s)	Average Change in Power Output (kW)	Percentage Change in Power Output
8	-30.646	-0.42
10	-55.92	-0.43
11	28.67	0.18
12	47.287	0.27
14	N/A (unstable without control)	N/A (unstable without control)
16	N/A (unstable without control)	N/A (unstable without control)
18	13.36	0.056

A reduction in the energy capture is expected in below rated conditions, as power is proportional to the square of wind speed, so the increase in power when pitching forward would be expected to be greater than the decrease in power when pitching backwards. In above rated conditions the expectation is for an increase in power capture, as the maximum power is limited by the rating of the MRS. The fatigue loads on the MRS are also likely to be reduced as the amplitude of the loading cycles are greatly reduced. Clearly, at wind speeds above rated wind speed some form of fore-aft pitching damping control is necessary for the MRS to operate.

7.3.3.3 Conclusions on Fore-Aft Pitch Control

The simulations conducted within this deliverable show that without damping of the fore-aft pitching motion, whilst in below rated conditions the fore-aft pitching motion is naturally damped, one or more RPC systems may become unstable in rated and above rated wind conditions. Using the PAC to provide changes in power, and hence changes to the thrust, proportional to the speed of the fore-aft pitching motion can be successfully used to damp the motion, keeping all the RPC systems operating in a stable manner, restricting the fore-aft motion to within approximately one degree across the wind spectrum and significantly smoothing the power output.

7.3.4 Control of the MRS to provide ancillary services

With the increasing contribution of wind energy to the electricity network there is an increasing demand for wind turbines and/or wind farms to provide ancillary services. The MRS is no exception to this. Typical ancillary services include stabilising the grid frequency through the provision of synthetic inertia and droop control.

7.3.4.1 Synthetic Inertia

Synthetic inertia consists of an increase in the power output of a wind turbine/farm proportional to the rate of change of grid frequency. Conventional synchronous plant provide this response naturally, as the generator speed reduces as the grid frequency reduces, with the kinetic energy this releases converted into electrical energy. As modern wind turbine systems including the MRS are asynchronous machines, a change in the grid frequency has no direct effect on the power output without remedial control action.

Grid frequency is related to the power supplied and demanded through the power system via the equation

$$Jf\frac{df}{dt} = P_{Sup} - P_{Dem}$$

Where J is the combined inertia of all the synchronous plant, f is the grid frequency, P_{Sup} is the power supplied and P_{Dem} is the power demand. Conventional, synchronous plant have an inertia constant H of approximately 6s. The inertia constant is related to the rate of change of frequency by

$$\frac{df}{dt} = \frac{\Delta P f}{2HS}$$

where ΔP is the change in power output, f is the grid frequency, and S is the rated power of the machine.

If synthetic inertia is supplied via the relationship

$$\Delta P = K_{Inertia}\frac{df}{dt}$$

Then the equivalent $K_{Inertia}$ for a given inertia constant H is found by

$$K_{Inertia} = -\frac{\Delta P}{\frac{df}{dt}} = \frac{-2SH}{f_{nominal}}$$

As the PAC provides a change in the power output through a change in the generator torque and these dynamics are fast, the PAC is suitable for providing synthetic inertia. This idea was previously explored on multi-megawatt machines, in which it was conclude that large multi-megawatt wind turbines can provide significantly more inertia than typical conventional plant, with an equivalent inertia constant of over 18 seconds possible (in comparison to a typical H constant of 6 seconds for conventional plant). Similar techniques can be applied to the MRS.

A disadvantage of the MRS approach is that, whilst power for a single rotor scales as approximately a square power, inertia scales with approximately a power of five. This means that for a large multi-megawatt machine, the inertia of a traditional horizontal axis machine is an order of magnitude larger than it is far a MRS. For example, comparing 11 of the RPC system rotors (with a total power output of 4.8MW), the total inertia of the system is $11 \times 101370 = 1\,115\,070\ kgm^2$, whereas for a single 5MW machine (in this case the Supergen 5MW Exemplar machine) the total inertia is $43\,883\,576\ kgm^2$, almost forty times larger. For a 20MW machine the difference becomes even larger, with the inertia of the MRS (45 rotors) being $4\,561\,650\ kgm^2$, whereas a 20MW machine, scaled from the Supergen 5MW turbine, has a total inertia of $1\,300\,000\,000\ kgm^2$, almost 285 times the value for the MRS.

Using one RPC system, simulations are conducted using a grid frequency signal equivalent to a very large frequency drop as shown in Figure 7.91.

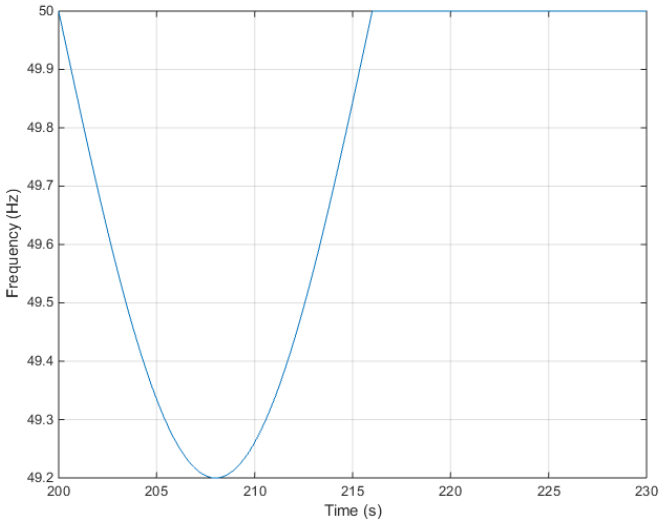

Figure 7.91: Grid frequency for synthetic inertia simulations

Using an equivalent inertia constant of 6 seconds ($K_{Inertia} = -106560$), simulations were conducted at a range of constant below rated wind speeds, with the results plotted on a torque speed graph in red (see Figure 7.92).
Also shown in Figure 7.91 is the output when an equivalent inertia constant of 18s is used ($K_{Inertia} = -319680$). This is the value that a 5MW wind turbine from a previous study was found to be capable of supplying [31].

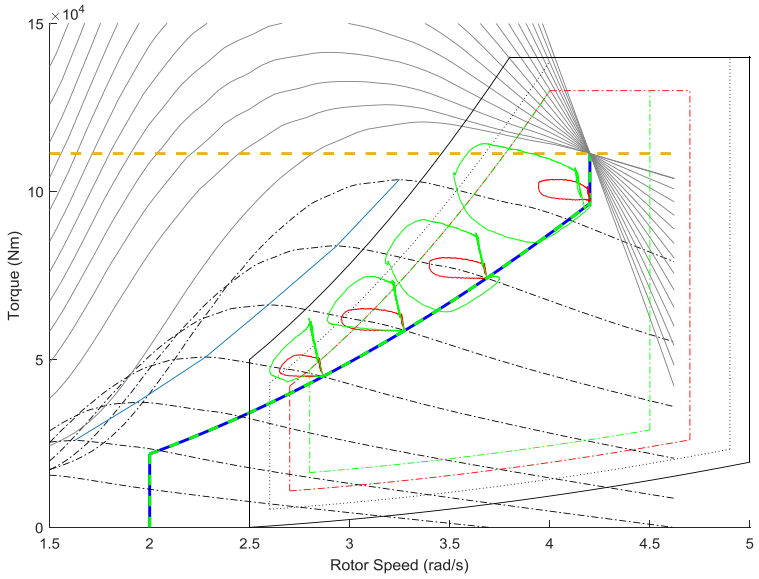

Figure 7.92: Torque-speed graph for an RPC system providing synthetic inertia

Considering the simulations with an equivalent inertia constant of 6s (shown in red in Figure 7.91). For wind speeds of 9m/s and 10.2m/s the RPC system is capable of providing the desired synthetic inertia response. At a wind speed of 7m/s, the operating point soon encounters the black offset and so provision of synthetic inertia is curtailed, and at a wind speed of 8m/s the power output is curtailed late on in the frequency event.

Two factors must be noted about the results presented here. Firstly, the frequency drop simulated is an extreme case. The majority of frequency drops that would be likely to be experienced would be significantly less fast and less long lasting. Secondly however, the simulations presented involve the RPC system immediately returning to normal operation. It is more desirable for a MRS to be able to stagger the recovery of the RPC systems. This would require significantly more inertia in the rotors to allow some RPC systems to maintain a change in power of zero, which, due to the offset from the operational curve would still require conversion of additional kinetic energy to electrical energy, slowing down the rotor.

The simulations with an equivalent inertia constant of 18s (shown in green in Figure 7.91) show that it is unlikely that much additional power can be extracted, as, in these simulations, the power output is quickly curtailed as the operating point enters the upper torque region on the operational diagram.

For comparison, an example is given for a 5MW wind turbine, providing synthetic inertia for the same frequency drop, with an inertia constant of 18 seconds, and holding the change in power at zero for 20 seconds afterwards in Figure 7.93, which shows that despite having a far smaller rated output (5MW rather than the 20MW MRS), a far greater contribution towards synthetic inertia can be made. Even larger conventional wind turbines would be expected to be able to provide even greater contributions for synthetic inertia.

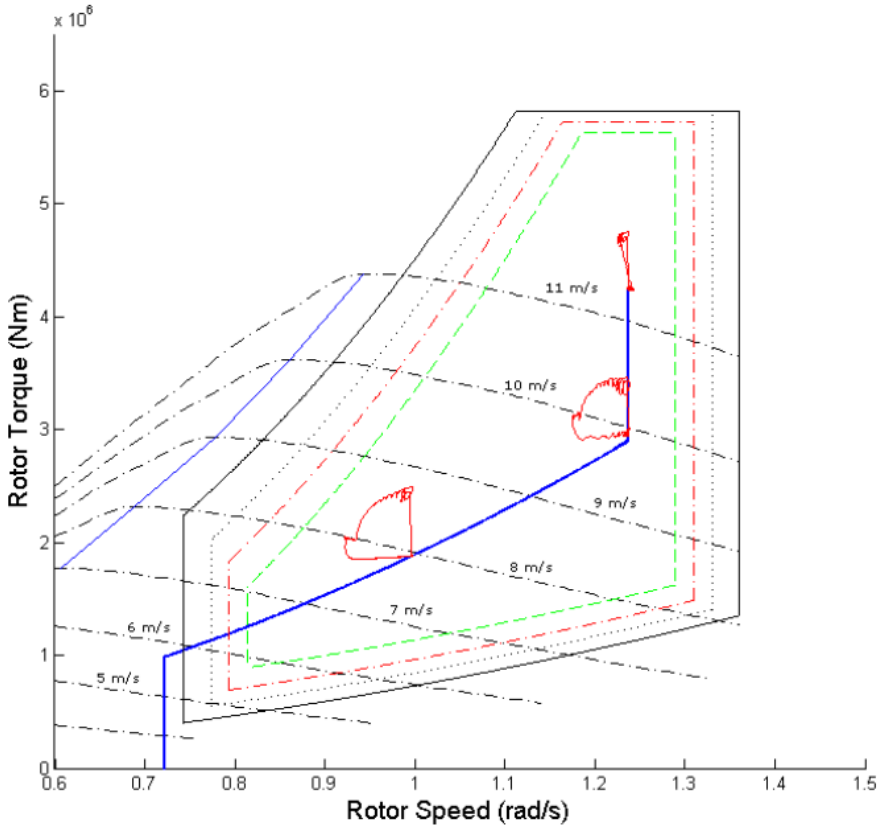

Figure 7.93: 5MW wind turbine providing synthetic inertia with an H value of 18s

In stronger wind conditions it may be possible for the MRS to provide better synthetic inertia response by prioritising the provision of synthetic inertia to turbines operating at more favourable operating points.

Overall however, it is clear that, in comparison to large multi-megawatt wind turbines of conventional design, the MRS is less suitable for provision of synthetic inertia.

7.3.4.2 Droop control

Droop control is the provision of an increment in the power output of a machine provided in proportion to the change in grid frequency. Droop control is a requirement of conventional synchronous generators, though unlike synthetic inertia it is not naturally provided but is instead provided through control action. Provision of droop control using conventional multi-megawatt wind turbines equipped with a PAC was explored in[31] and [30]. Whilst the design of the MRS is unfavourable for synthetic inertia due to the low inertia of the RPC systems, this is less of a concern for droop control, as wind turbines providing droop control are typically curtailed during normal operation to allow head room for under frequency events. As such, the RPC systems on a multi-rotor system providing droop control are not required to provide an increase in power above the normal maximum in below rated wind

conditions, and so the low inertia is less of a concern as the aerodynamic and generator torques can be matched through pitch action.

7.3.4.3 Strategy for Droop Control

The standard requirement for synchronous machines connected to the UK National grid is to provide a droop capability of 3-5% [34]. As such, for the multi-rotor system, a droop capability of 4% is targeted. For a 20MW MRS this translates into a change in power of 10MW/Hz.
As the frequency of the grid is required to be kept between 49.8Hz and 50.2Hz, the maximum change in power output is set to +/-2MW. A deadband is included between 49.95 and 50.05Hz, as is typical for synchronous machines. The droop curve is therefore as shown in Figure 7.94.

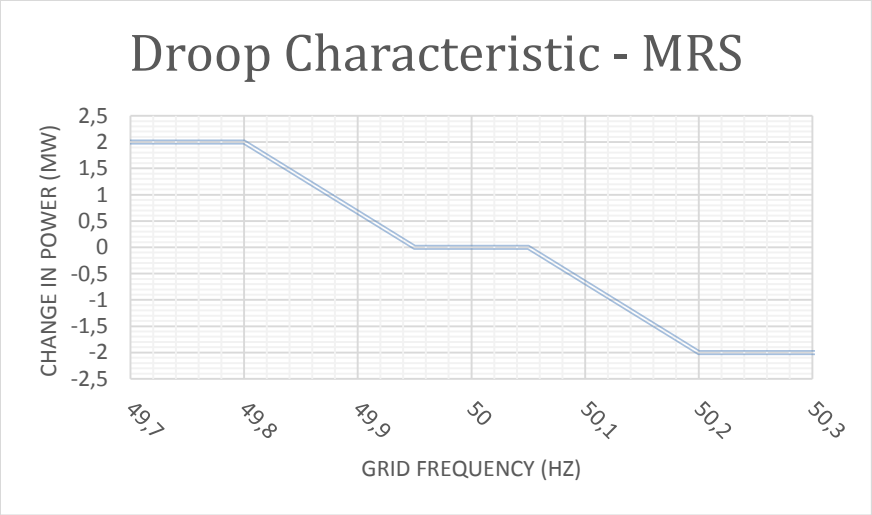

Figure 7.94: Droop characteristic curve for the MRS

It is clear from the results for synthetic inertia discussed in the previous section that any prolonged increase in power below rated wind speed is not feasible, as there is very little inertia in each rotor and it is impossible to balance the aerodynamic and generator torques (and hence stabilise the rotor speed) of each RPC system. When an RPC system is below rated wind speed, it is therefore essential to have a negative offset in power output to allow headroom for power increases. Assuming all the rotors are contributing to droop control, the maximum increase in power is 0.045MW per RPC system, hence an offset of 50kW is used in below rated conditions. Of course not all the rotors may be available for droop control. Some may be experiencing very low wind speeds for instance, or recovering from a different application. The total offset for the below rated machines must therefore be equal to the offset assuming all machines are below rated and available minus -50kW for each above rated machine. A maximum reduction per RPC system is set at -100 000kW. If this limit is reached then a flag is set to inform the operator that the MRS system cannot provide full droop control. To prevent chattering between the above and below rated modes, a hysteresis is used such that the RPC system enters above rated mode (i.e. no offset is used) when the wind speed, as measured by the wind speed estimator, rises above 14m/s, and switches to below rated mode when the wind speed drops below 12m/s. Between

12m/s and 14m/s the RPC system operates in whichever mode it was previously operating in. If the wind speed (as estimated in the PAC) drops below a threshold of 6.5m/s, the PAC will recover the RPC system back to normal operation and no droop control will be provided.
A controller diagram is shown in Figure 7.95.

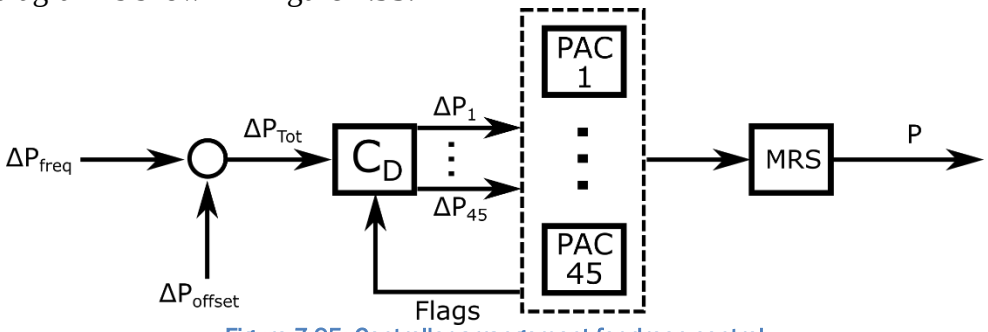

Figure 7.95: Controller arrangement for droop control

The controller is supplied with the required change in power due to the change in grid frequency (ΔP_{freq}), which is added to required offset due to below rated RPC systems (ΔP_{offset}, using flags from the PACs) and then fed into the distribution controller (C_D). The distribution controller includes both rate and saturation limits to ensure that the demand can be met. The total change in power output is then distributed amongst the RPC systems. The RPC systems are assigned into three different groups as shown in Figure 7.96. The RPC systems in group 1 (blue area in Figure 7.96 encompassing clusters 8, 9, 10, 14, 15, and 16) are used first, followed by those in group 2 (green in Figure 7.96 encompassing clusters 1, 2, 4, 5, 6, and 12) and finally by those in group 3 (red in Figure 7.96 encompassing clusters 3, 7, 11, 13, and 17). Groups 1 to 3 become gradually further from the centre of the MRS, and nearer the edges, hence, the preferred machines are those less useful for yaw control and fore-aft pitch control.

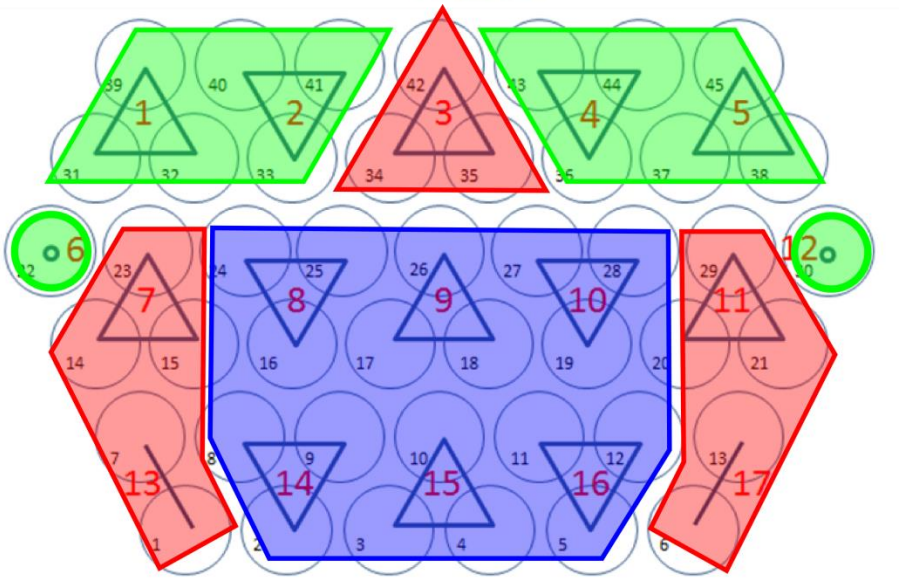

Figure 7.96: Grouping of clusters for droop control

To demonstrate the groupings, simulations are conducted with constant wind speeds (10m/s and 16m/s), with a frequency input as shown in Figure 7.97.

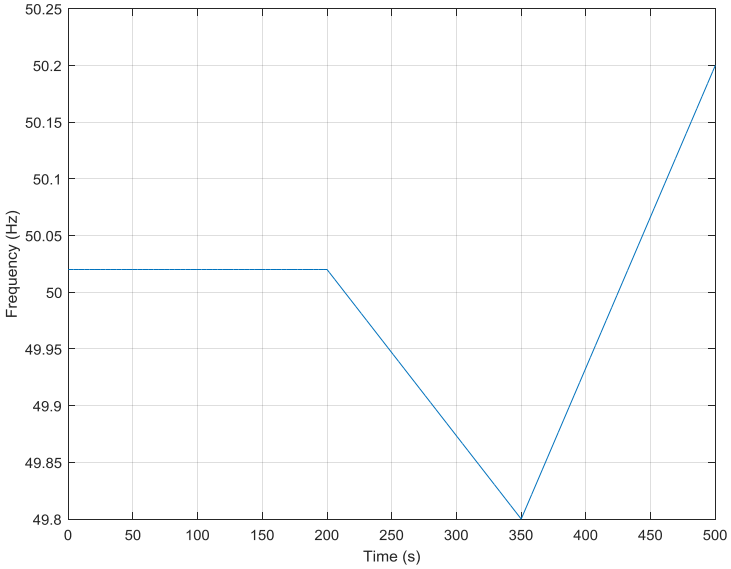

Figure 7.97: Test frequency input

The total power output of the MRS for both simulations is shown in Figure 7.98, along with the requested change in power. It is clear that the change in power achieved is accurate.

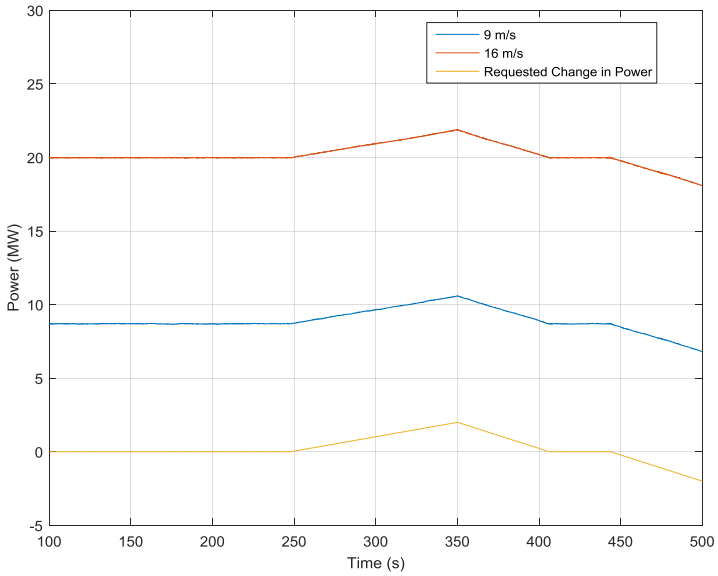

Figure 7.98: Power output for droop control with constant wind speeds

Next simulations are conducted with turbulent winds below rated, close to rated and above rated with the same input and the power output of simulations with no droop control is subtracted. The results are presented in Figure 7.99. The 16m/s simulation shows excellent tracking of the requested change in power. It should be noted that some of the clusters within the MRS are operating with a reduction in power to provide head room, as they are close to rated wind speed, hence the reduced power output before the frequency change.

The 11m/s simulation also tracks the requested change in power well, however there are some minor excursions from the requested value. These excursions have 3 causes:

1- RPC systems switching between working with an offset and working without an offset
2- RPC systems recovering back to normal operation when the wind speed drops below the cut off value
3- Minor changes in the timing of switching between modes of operation by the full envelope controller of the RPC system when using the PAC compared to when the PAC is not in use. When the power output of the MRS without droop control is subtracted from the power output of the MRS with droop control these small changes in timing can result in minor errors in the change in power.

Note that all of the causes are entirely decoupled from the grid frequency, and, as such the small changes in the power output that they cause do not have an impact on the performance of the control action as a droop controller. That is to say that the MRS still provides a proportional response to the frequency change, it is only because the change in power is found via a subtraction of the power with and without droop control active that they are noticeable.

The 8m/s simulation provides an accurate power change until approximately 300 seconds simulation time. At this point, the available RPC systems are providing their maximum power and so the requested change in power cannot be achieved. The slight deviations in the change in power output can be attributed to the same causes as those in the 11m/s simulation.

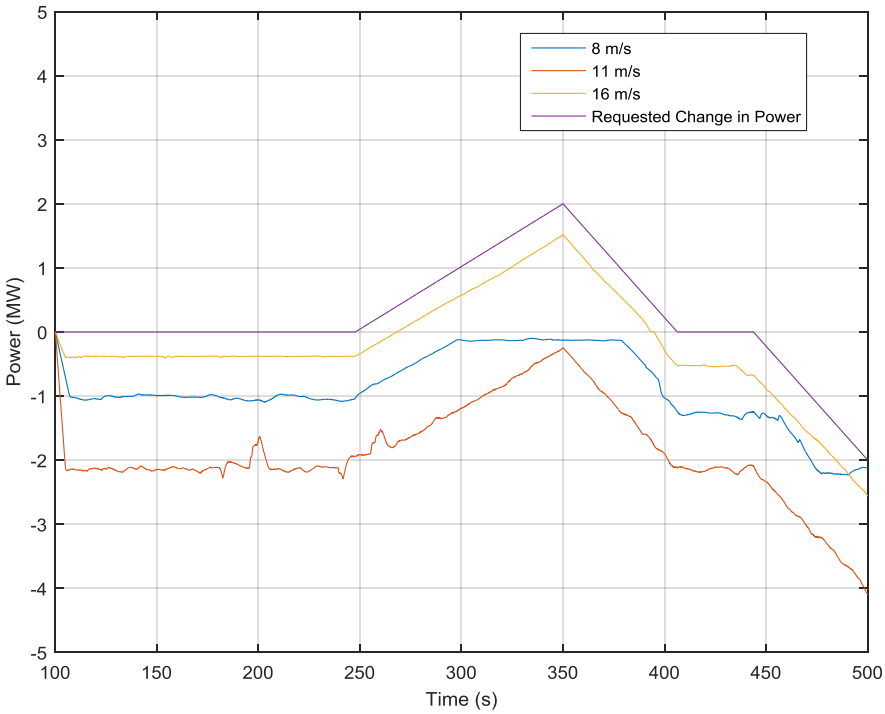

Figure 7.99: Change in power output for simulations with varying wind speed

Finally, a sample frequency signal shown in Figure 7.100, measured on the UK grid on 26th October 2014, is used for simulations below rated, close to rated and above rated.

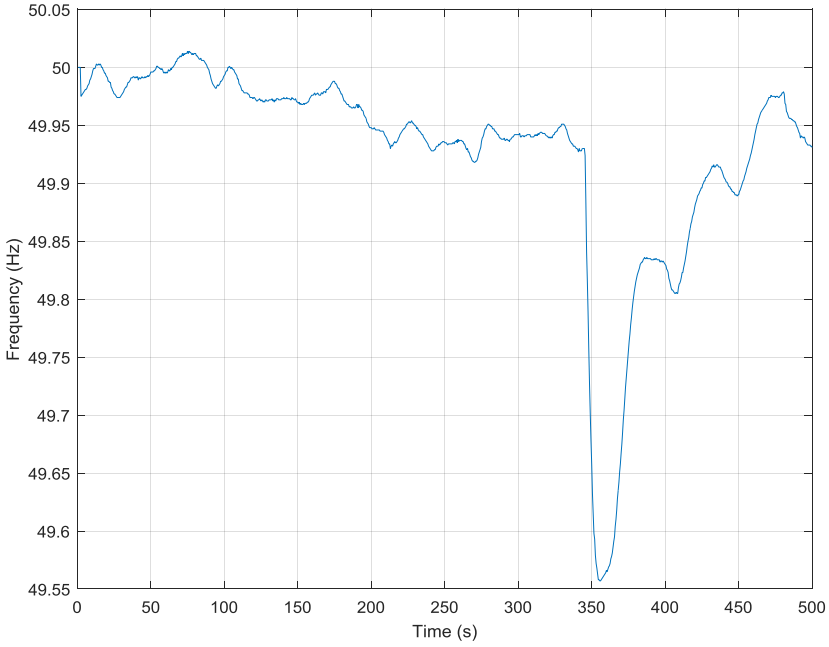

Figure 7.100: Sample grid frequency

The resultant change in power output at the three wind speeds is shown in Figure 7.101.

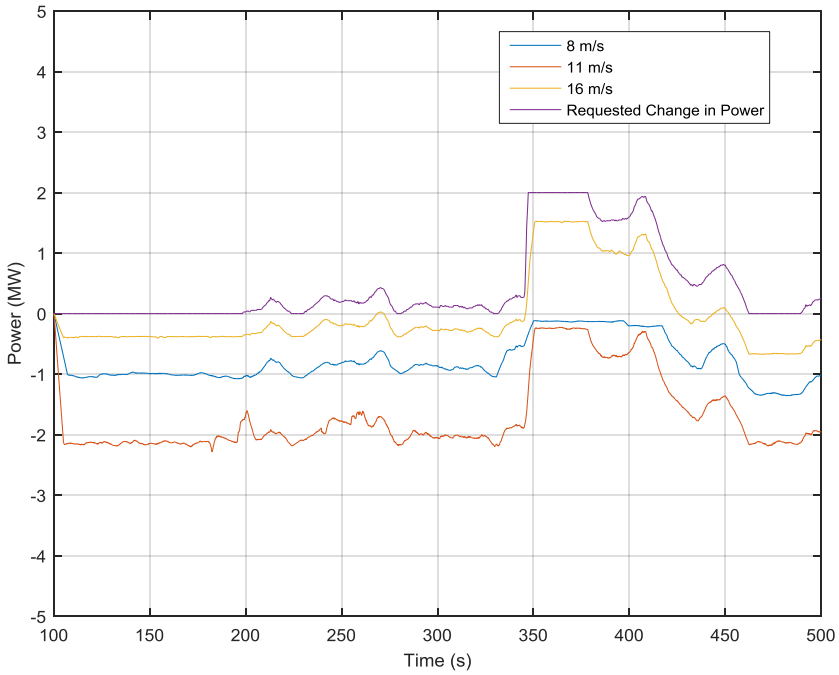

Figure 7.101: Change in power output for droop control in response to sample frequency

Similarly to the previous results, the change in power is well tracked in the 16m/s simulation. In the 11m/s simulation there are some deviations due to the causes identified earlier in this section. In the 8m/s simulation the maximum power increase is again limited by the number of available RPC systems.

7.3.4.4 Conclusion for Ancillary Services

The work presented here shows that an MRS system is capable of providing both synthetic inertia and droop control as ancillary services. In the case of synthetic inertia, due to the scaling factors for power and inertia for the MRS compared to conventional wind turbines, the amount of synthetic inertia that the MRS can provide is significantly less than that of a similarly sized conventional wind turbine, and the possible H constant is lower than that of a 5MW conventional machine. It is however possible to provide synthetic inertia from the MRS with an H value similar to that provided by conventional synchronous generators (6s), even for extreme frequency drops.

In the case of droop control, the MRS is shown to be capable of providing accurate changes in power proportional to the change in frequency, with a droop capability similar to that of conventional synchronous generators. Providing droop control necessarily reduces energy capture as an offset is required below rated to allow head room for power increases. A control strategy is detailed that allows the inner clusters of the MRS to be prioritised for droop control, leaving the clusters higher up the MRS and further to the sides available for fore-aft pitching motion control and yaw control.

7.4 Conclusions for the Multi Rotor Control

The scope of this section of deliverable 1.42 was to examine methods to maximally exploit the additional capability of distributed control to improve the performance relative to current control systems; specifically multi-rotor wind turbine control as a distributed control scheme was to be examined, involving:

a) Management of power and distributed thrust loadings over the array of a multi rotor
b) Stabilization of floating structure via low frequency pitch activity and torque reaction

The work on yaw control and fore-aft concerns the management of distributed thrust loadings over the array of a multi-rotor, as well as stabilization of the floating structure via low frequency pitch activity and torque reaction. Management of power over the array of a multi-rotor is explored in the work on droop control and synthetic inertia.

It was found that it is feasible to control the yaw of a multi-rotor system using distributed control via the incorporation of power adjusting controllers on each RPC system on the multi-rotor. The yaw of the multi-rotor is stabilised through control of the thrust on the rotors. A suitable spar floater was designed for the multi-rotor, taking into account both the aerodynamic and hydrodynamic loads. This model was used to demonstrate the feasibility of damping the fore-aft pitching of the multi-rotor through distributed control. It was demonstrated that without remedial action the fore aft motion of the multi-rotor could cause instability of the RPC system controllers. Distributed control reduces the fore-aft pitching motion, maintaining stability of the RPC system controllers and improving power quality. The capability of the multi-rotor to provide synthetic inertia was examined, and, whilst the multi-rotor does not have the capability to provide synthetic inertia at the same levels as a conventional wind turbine it is possible to provide synthetic inertia equivalent to the inertia of synchronous machines at most wind speeds.
A distributed control scheme to provide droop control was implemented and demonstrated. The control scheme includes a priority system to ensure that the RPC systems least useful for yaw and fore aft pitch control are used first. The control scheme is shown to be able to provide accurate droop control with a droop capability of 4%, similar to conventional synchronous machines.

8 Conclusions

Various types of controller for the INNWIND.EU reference 10 MW were detailed and their advantages and limitations were presented. Simple collective pitch feedback control with active tower damping, drivetrain damping and tower resonance exclusion zone is able to meet performance targets for the turbine, but is not able to limit the fatigue loads on the jacket sub structure, whose lifetime can therefore be limited. In that sense, the key performance indicator (KPI) for the effectiveness of the controls algorithm is the reduction of tower base fatigue loads without reducing the power capture. Based on active tower damping and exclusion zone tuning, the fatigue on the tower base can be reduced by 20%-30% as compared to the standard reference controller

LIDAR based feed forward control assuming perfect reading of the wind conditions ahead of the turbine is able to further reduce the tower base fatigue by a further 20%. Model predictive control with LIDARs can further benefit this KPI, by reducing the pitch activity required and greatly eliminating the tower fore-aft load variations, but again assuming that the wind turbulence can be effectively measured by the LIDAR. However LIDAR based wind observations are dependent on the type of LIDAR, its resolution and scanning frequency, as well as on atmospheric conditions. Based on the pollutants in the air or absence of aerosols, it may result in the signal being degraded or unreliable. Conditions such as thick fog, heavy precipitation, and very clean air can cause the LIDAR signal to be poorly read due to lack of transparency, insufficient particles or aerosol droplets to reflect the laser light. The prevalence of such conditions will be very site-dependent. In practice the probability of such conditions occurring is likely to be largely unknown.

A very focused modelling and controller design for the multi rotor wind turbine was delineated and it was found that it is feasible to control the yaw of a multi-rotor system using distributed control via the incorporation of power adjusting controllers. The yaw of the multi-rotor is stabilised through control of the thrust on the rotors. A suitable spar floater was designed for the multi-rotor, taking into account both the aerodynamic and hydrodynamic loads. It was demonstrated that without remedial action the fore aft motion of the multi-rotor could cause instability of the RPC system controllers and that distributed control reduces the fore-aft pitching motion, maintaining stability of the RPC system controllers and improving power quality. Droop control for varying electrical grid frequencies was explained wherein the control scheme was shown to provide a droop capability of 4%.

REFERENCES

1. E A Bossanyi, T Delouvrié and S Lindahl, " Long-term simulations for optimising yaw control and start-stop strategies", Proc. European Wind Energy Conference, Vienna, EWEA 2013.
2. K Kragh et al, "Rotor Speed Dependent Yaw Control of Wind Turbines Based on Empirical Data", Proc. 50th AIAA Aerospace Sciences Meeting, Nashville, Tennessee, January 2012.
3. E A Bossanyi, A Kumar and O Hugues-Salas, "Wind turbine control applications of turbine-mounted LIDAR", , Proc. Torque from Wind conference, Oldenburg, 2012.
4. E Bossanyi, B Savini, M Iribas, M Hau, B Fischer, D Schlipf, T van Engelen, M Rossetti and C E Carcangiu "Advanced controller research for multi-MW wind turbines in the UPWIND project", Wind Energy vol. 15 pp 119–145, 2012.
5. D. Schlipf, E. Bossanyi, C. E. Carcangiu, T. Fischer, T. Maul and M Rossetti, "LIDAR assisted collective pitch control", UPWIND, Stuttgart, 2011
6. Qin, S. J., & Badgwell, T. A., An Overview Of Industrial Model Predictive Control Technology.1996
7. Henriksen, L. C. Model Predictive Control of a Wind Turbine. Master's thesis, Technical University of Denmark, Informatics and Mathematical Modelling, 2007
8. IEC 61400-3 International Standard, Wind Turbines – Part 3: Design requirements for Offshore Wind Turbines. First Edition 2009-02.
9. Hansen, M.H. and Henriksen, L.C., Basic DTU Wind Energy controller. Technical Report E-0028, DTU Wind Energy, 2013.
10. Bak., C. et, al. , Description of the DTU 10 MW Reference Wind Turbine. DTU Wind Energy Report-I-0092, 2013.
11. Hansen, M. O. , Aerodynamics of Wind Turbines. Earthscan,2008
12. I. Elorza, M. Iribas, E. Miranda, "On the feasibility and limits of extreme load reduction for wind turbines via advanced sensing: a LIDAR case study". Proceedings of the American Control Conference (ACC), 2013, Washington, DC, 2013; 1436–1441.
13. W.V. Rietveld, "Wind speed feedforward control for a wind turbine using LIDAR",TUDelf, 2013
14. Baotic, M., Optimal Control of Piecewise Affine Systems -- a Multi-parametric Approach,. Ph.D. dissertation, ETH, Zurich, 2005
15. Geyer, T. Low Complexity Model Predictive Control in Power Electronics and Power Systems. Ph.D. dissertation. ETH, Zurich, 2005
16. Maciejowski, J., Predictive control with constraints. Essex: Pearson Education Lim, 2002.
17. Jonkman, J. M., & Buhl., M. L., FAST User's Guide. Tech. rep., National Renewable Energy Laboratory, Golden, CO, 2005.

18. Mirzaei, M., Niemann, H. H., & Poulsen, N. K., “A mu-Synthesis Approach to Robust Control of a Wind Turbine. the 50th IEEE Conference on Decision and Control and European Control Conference”, Orlando, Florida, United States, 2011, pp. 645-650.
19. Mirzaei, M., Poulsen, N. K., & Niemann, H. H. (2012). Model Predictive Control of a Nonlinear System with Known Scheduling Variable. Proceedings of the 17th Nordic Process Control Workshop, 163-168.
20. Jonkman, B. (2009). TurbSim User's Guide: Version 1.50. Tech. rep., National Renewable Energy Laboratory, 1617 Cole Boulevard, Golden, Colorado 80401-3393 303-275-3000.
21. International Standard Wind Turbines—Part 1: Design Requirements IEC 61400–1 Ed. 3, Amendment 1, 2010
22. T. von Borstel; Deliverable 4.3.1 “Design Report – Reference Jacket”, INNWind.EU Project. October 2013.
23. P. Jamieson, M. Branney, K. Hart, P. K. Chaviaropoulos, G. Sieros, S. Voutsinas, P. Chasapogiannis, and J. M. Prospathopoulos, “INNWIND Deliverable 1.3.3 - Innovative Turbine Concepts – Multi-Rotor System,” 2014.
24. [2] V. W. Neilson, “Individual Blade Control for Fatigue Load Reduction of Large-scaled Wind Turbines: Theory and Modelling,” University of Strathclyde, 2010.
25. [3] M. Gala-Santos, “Aerodynamic and Wind Field Models for Wind Turbine Control,” University of Strathclyde, Thesis to be submitted.
26. [4] F. Perrone, “Generation of coherent wind fields via Veers method,” 2013. [Online]. Available: http://www.mathworks.com/matlabcentral/fileexchange/35867-3d-turbulent-wind-field-simulation-by-means-of-sandia-method-for-wind-energy-applications.
27. [5] P. S. Veers, “Three Dimensional Wind Simulation,” Sandia Report, Sep. 1988.
28. [6] A. P. Chatzopoulos, “Full Envelope Wind Turbine Controller Design for Power Regulation and Tower Load Reduction,” 2011.
29. [7] A. Stock and W. Leithead, “Providing Grid Frequency Support Using Variable Speed Wind Turbines with Augmented Control,” in Proc. European Wind Energy Association Conference 2012, 2012, pp. 152–156.

30. [8] A. Stock and W. Leithead, “Providing Frequency Droop Control Using Variable Speed Wind Turbines with Augmented Control,” in Proc. European Wind Energy Conference 2014, 2014.
31. [9] A. Stock, “Augmented Control for Flexible Operation of Wind Turbines,” University of Strathclyde, 2015.
32. [10] N. D. P. Barltrop and A. J. Adams, Dynamics of fixed marine structures (3rd edn), 3rd ed. Butterworth-Heinemann, 1991.
33. [11] World Meteorological Organization, Guide to Wave Analysis and Forecasting, 2nd ed., vol. 702. Geneva, 1998.
34. [12] National Grid Electricity Transmission plc, “The Grid Code,” 2013.

Appendix 1 Loads Simulated using CENER IPC CONTROL

Under assumptions of reduced load cases, CENER added IPC to its baseline controller for the Bladed INNWIND.EU 10MW mounted on a Jacket. The obtained results in terms of fatigue and extreme loads are summarized in the following tables.

Fatigue Loads:

Inverse SN slope [.]	Blade 1 Mx	Blade 1 My	Blade 1 Mxy	Blade 1 Mz
	[Nm]	[Nm]	[Nm]	[Nm]
3	4.63E+07	2.63E+07	2.71E+07	367985
4	3.90E+07	2.34E+07	2.37E+07	316616
5	3.52E+07	2.27E+07	2.27E+07	299115
6	3.29E+07	2.26E+07	2.25E+07	293162
7	3.14E+07	2.28E+07	2.26E+07	292255
8	3.03E+07	2.32E+07	2.29E+07	293856
9	2.95E+07	2.36E+07	2.32E+07	296769
10	2.89E+07	2.40E+07	2.36E+07	300352
11	2.84E+07	2.44E+07	2.40E+07	304233
12	2.80E+07	2.48E+07	2.43E+07	308192

Table 7.- Lifetime weighted equivalent loads CENER IPC: blade root

Inverse SN slope [.]	Rotating hub Mx	Rotating hub My	Rotating hub Mz	Rotating hub Myz
	[Nm]	[Nm]	[Nm]	[Nm]
3	3.41E+06	3.08E+07	3.09E+07	2.15E+07
4	3.81E+06	2.62E+07	2.62E+07	1.73E+07
5	4.27E+06	2.44E+07	2.44E+07	1.56E+07
6	4.68E+06	2.37E+07	2.38E+07	1.48E+07
7	5.01E+06	2.35E+07	2.37E+07	1.45E+07
8	5.30E+06	2.37E+07	2.38E+07	1.45E+07
9	5.54E+06	2.40E+07	2.41E+07	1.45E+07
10	5.74E+06	2.44E+07	2.45E+07	1.47E+07
11	5.91E+06	2.49E+07	2.50E+07	1.49E+07
12	6.06E+06	2.54E+07	2.54E+07	1.51E+07

Table 8.- Lifetime weighted equivalent loads CENER IPC: hub (rotating coordinates)

Inverse SN slope [.]	Stationary hub Mx	Stationary hub My	Stationary hub Mz	Stationary hub Myz
	[Nm]	[Nm]	[Nm]	[Nm]
3	3.41E+06	3.14E+07	2.92E+07	2.15E+07
4	3.81E+06	2.62E+07	2.47E+07	1.73E+07
5	4.27E+06	2.43E+07	2.30E+07	1.56E+07
6	4.68E+06	2.35E+07	2.24E+07	1.48E+07
7	5.01E+06	2.33E+07	2.24E+07	1.45E+07
8	5.30E+06	2.33E+07	2.26E+07	1.45E+07
9	5.54E+06	2.36E+07	2.29E+07	1.45E+07
10	5.74E+06	2.39E+07	2.34E+07	1.47E+07
11	5.91E+06	2.43E+07	2.39E+07	1.49E+07
12	6.06E+06	2.47E+07	2.44E+07	1.51E+07

Table 9.- Lifetime weighted equivalent loads CENER IPC: hub (stationary coordinates)

Inverse SN slope [.]	Yaw bearing Mx	Yaw bearing My	Yaw bearing Mxy	Yaw bearing Mz
	[Nm]	[Nm]	[Nm]	[Nm]
3	4.60E+06	3.27E+07	1.18E+07	3.22E+07
4	4.49E+06	2.71E+07	1.01E+07	2.69E+07
5	4.77E+06	2.50E+07	9.55E+06	2.49E+07
6	5.12E+06	2.42E+07	9.49E+06	2.42E+07
7	5.46E+06	2.40E+07	9.61E+06	2.40E+07
8	5.75E+06	2.41E+07	9.83E+06	2.42E+07
9	6.00E+06	2.44E+07	1.01E+07	2.45E+07
10	6.22E+06	2.48E+07	1.04E+07	2.49E+07
11	6.41E+06	2.52E+07	1.06E+07	2.54E+07
12	6.57E+06	2.57E+07	1.09E+07	2.59E+07

Table 10.- Lifetime weighted equivalent loads CENER IPC: yaw bearing

Inverse SN slope [.]	Tower Mx, Location=Mbr 323 End 1.	Tower My, Location=Mbr 323 End 1.	Tower Mz, Location=Mbr 323 End 1.	Tower Myz, Location=Mbr 323 End 1.
	[Nm]	[Nm]	[Nm]	[Nm]
3	3.22E+07	2.35E+07	2.31E+07	1.18E+07
4	2.69E+07	1.95E+07	1.92E+07	1.01E+07
5	2.49E+07	1.80E+07	1.78E+07	9.55E+06
6	2.42E+07	1.74E+07	1.72E+07	9.49E+06
7	2.40E+07	1.72E+07	1.71E+07	9.61E+06
8	2.42E+07	1.73E+07	1.72E+07	9.83E+06
9	2.45E+07	1.75E+07	1.74E+07	1.01E+07
10	2.49E+07	1.77E+07	1.76E+07	1.04E+07
11	2.54E+07	1.80E+07	1.79E+07	1.06E+07
12	2.59E+07	1.83E+07	1.83E+07	1.09E+07

Table 11.- Lifetime weighted equivalent loads CENER IPC: tower top

Inverse SN slope [.]	Tower Mx, Location=Mbr 314 End 2.	Tower My, Location=Mbr 314 End 2.	Tower Mz, Location=Mbr 314 End 2.	Tower Myz, Location=Mbr 314 End 2.
	[Nm]	[Nm]	[Nm]	[Nm]
3	3.29E+07	8.38E+07	1.03E+08	1.18E+08
4	2.74E+07	7.45E+07	9.03E+07	1.04E+08
5	2.54E+07	7.20E+07	8.60E+07	9.99E+07
6	2.46E+07	7.19E+07	8.48E+07	9.93E+07
7	2.44E+07	7.27E+07	8.49E+07	1.00E+08
8	2.46E+07	7.38E+07	8.57E+07	1.02E+08
9	2.49E+07	7.51E+07	8.68E+07	1.03E+08
10	2.53E+07	7.64E+07	8.81E+07	1.05E+08
11	2.58E+07	7.76E+07	8.94E+07	1.07E+08
12	2.63E+07	7.88E+07	9.07E+07	1.08E+08

Table 12.- Lifetime weighted equivalent loads CENER IPC: tower base

Extreme Loads:

			Mx	My	Mxy	Mz	Fx	Fy	Fxy	Fz
		Load case	kNm	kNm	kNm	kNm	kN	kN	kN	kN
Mx	Max	dlc13cb1	24113	47405	53185	-131.6	931.7	-727.7	1182.2	1400.6
Mx	Min	dlc13eb1	-21468	16071	26817	-134.6	377.3	643.1	745.7	1561.5
My	Max	dlc13bb1	-8116.4	54630	55230	275.8	1127.6	435.6	1208.9	1697.9
My	Min	dlc23ca_2	6569.8	-25804	26628	202.7	-476.6	-51.2	479.3	1792.1
Mxy	Max	dlc13cb1	20249	53383	57095	22.2	1106.4	-685.6	1301.6	1088.6
Mxy	Min	dlc62j_h_1_1	-6.4	-13.2	14.6	-174	176.8	61.3	187.1	-253.2
Mz	Max	dlc23da_3	20486	-24297	31781	600.7	-317.2	-542.5	628.4	1593.6
Mz	Min	dlc61ab_h_1_1	-5806.7	-12290	13593	-542.2	-52.4	244	249.5	-59.4
Fx	Max	dlc13bb1	-8067.3	54193	54790	257.1	1140.4	443.8	1223.7	1719.1
Fx	Min	dlc61ab_h_1_1	-1791.7	-18887	18972	-28.5	-671.1	97.9	678.2	266
Fy	Max	dlc13db1	-20227	5282.6	20905	-185.8	87.9	703.5	709	1608.9
Fy	Min	dlc13ab1	22826	36904	43392	-45.8	798.1	-759.1	1101.5	1410.3
Fxy	Max	dlc13cb1	21057	52520	56584	22.2	1116.4	-691.8	1313.3	1131.3
Fxy	Min	dlc62d_l_1_1	653.4	6047.8	6083	64.8	0.64	0.54	0.84	-321.7
Fz	Max	dlc13db1	4057.5	12643	13278	-107.8	399.2	-70.2	405.3	2532.3
Fz	Min	dlc61ab_h_2_1	-1110	1486.4	1855.1	-126.1	-1.06	70.7	70.7	-575

Table 13.-Ultimate loads CENER IPC: blade root

			Mx	My	Mz	Myz	Fx	Fy	Fz	Fyz
		Load case	kNm	kNm	kNm	kNm	kN	kN	kN	kN
Mx	Max	dlc13db1	16710	4680.4	-12551	13396	1485.2	2795.9	806.1	2909.8
Mx	Min	dlc14ab	-8063.6	-4980.5	-3196	5917.7	388.2	-1847	2398.2	3027
My	Max	dlc13eb1	12632	28609	9205	30053	596	1536.2	2419.1	2865.6
My	Min	dlc14cb	12428	-32708	993.6	32723	128.7	-1421.3	2557.4	2925.8
Mz	Max	dlc14cb	13006	17176	36001	39888	34.7	2915.9	-106.4	2917.8
Mz	Min	dlc13db1	13368	19147	-43897	47890	1087.2	2076.5	2492.3	3243.9
Myz	Max	dlc13db1	13368	19147	-43897	47890	1087.2	2076.5	2492.3	3243.9
Myz	Min	dlc62d_h_1_1	-234.7	-1.09	4.59	4.72	520.8	-1300.4	1677.8	2122.7
Fx	Max	dlc14bb	16074	-3677.6	2114.6	4242.2	2769	-1697.5	-2508.8	3029.1
Fx	Min	dlc23ca_2	-318	-1902	3689.2	4150.7	-1478.1	829.1	2355.7	2497.3
Fy	Max	dlc11k1	14494	-20884	-15436	25969	1404.5	3470.5	-153.1	3473.9
Fy	Min	dlc13db1	14607	9969	13216	16554	947.3	-3534.3	919.4	3652
Fz	Max	dlc11j1	14008	-2123.3	-14125	14284	1068.3	228.3	3393.4	3401
Fz	Min	dlc13db1	14664	-16656	12085	20578	1023.3	-388.4	-3456.7	3478.5
Fyz	Max	dlc13db1	14607	9969	13216	16554	947.3	-3534.3	919.4	3652
Fyz	Min	dlc62a_l_2_1	-261.9	-697.1	388.5	798.1	327.1	-930.9	-1272	1576.3

Table 14.-Ultimate loads CENER IPC: hub (rotating coordinates)

			Mx	My	Mz	Myz	Fx	Fy	Fz	Fyz
		Load case	kNm	kNm	kNm	kNm	kN	kN	kN	kN
Mx	Max	dlc13db1	16710	-13330	-1324	13396	1485.2	66.2	-2909.1	2909.8
Mx	Min	dlc14ab	-8063.6	5867.6	-768.8	5917.7	388.2	-134.7	-3024	3027
My	Max	dlc14cb	13002	38110	-12436	40087	77.9	-279.4	-2971	2984.1
My	Min	dlc13db1	13368	-44333	18114	47890	1087.2	249.4	-3234.3	3243.9
Mz	Max	dlc13db1	14547	-368.7	28917	28919	789	151.6	-3240.1	3243.6
Mz	Min	dlc13eb1	13839	-5484.4	-31731	32202	976.8	-160.3	-2686.1	2690.9
Myz	Max	dlc13db1	13368	-44333	18114	47890	1087.2	249.4	-3234.3	3243.9
Myz	Min	dlc62d_h_1_1	-234.7	-2.19	-4.18	4.72	520.8	-121	-2119.3	2122.7
Fx	Max	dlc14bb	16074	-4234.5	-255.2	4242.2	2769	-38.9	-3028.8	3029.1
Fx	Min	dlc23ca_2	-318	2971.7	-2897.8	4150.7	-1478.1	-41	-2497	2497.3
Fy	Max	dlc61ab_l_2_1	-443.1	-6439.7	-5959.2	8773.9	390	995.9	-2867	3035.1
Fy	Min	dlc61ab_h_2_1	-209.6	-6421.9	1226.7	6538	268.6	-1200.9	-2733.3	2985.4
Fz	Max	dlc62d_h_1_1	-60.1	1341.9	4279.1	4484.6	303.6	-178.5	-1566.4	1576.6
Fz	Min	dlc13db1	14607	-15858	4751.9	16554	947.3	366.9	-3633.5	3652
Fyz	Max	dlc13db1	14607	-15858	4751.9	16554	947.3	366.9	-3633.5	3652
Fyz	Min	dlc62a_l_2_1	-261.9	-796.4	-51.3	798.1	327.1	-92.8	-1573.5	1576.3

Table 15.-Ultimate loads CENER IPC: hub (stationary coordinates)

			Mx	My	Mz	Myz
		Load case	kNm	kNm	kNm	kNm
Mx	Max	dlc13db1	29829	-11770	11687	16587
Mx	Min	dlc13eb1	-34460	-15663	-492.8	15671
My	Max	dlc14cb	-13970	13574	31741	34521
My	Min	dlc13db1	14709	-44099	-23731	50079
Mz	Max	dlc14cb	-10154	13251	31986	34622
Mz	Min	dlc13db1	10555	-43913	-24387	50230
Myz	Max	dlc13db1	10555	-43913	-24387	50230
Myz	Min	dlc62g_h_2_1	-1856.1	7.8	4.38	8.95

Table 16.-Ultimate loads CENER IPC: tower top

			Mx	My	Mz	Myz
		Load case	kNm	kNm	kNm	kNm
Mx	Max	dlc13db1	30320	66904	62543	91585
Mx	Min	dlc13eb1	-34855	29580	39650	49468
My	Max	dlc61ab_l_1_1	-4506.5	171023	44097	176616
My	Min	dlc23da_4	-5171.4	-160038	-103674	190684
Mz	Max	dlc61ab_h_1_1	8061.1	14384	221644	222110
Mz	Min	dlc61ab_l_2_1	-4931	97829	-142114	172531
Myz	Max	dlc21cd	1401.9	168691	192818	256194
Myz	Min	dlc13ab1	-638.8	-0.65	22.4	22.4

Table 17.-Ultimate loads CENER IPC: tower base

Appendix 2 Loads Simulated with IPC and LIDAR based Feed Forward CONTROL PERFORMANCE

The obtained load results for the LIDAR based feed forward control with IPC design by CENER in terms of fatigue and extreme loads are summarized in the following tables.

Fatigue Loads:

Inverse SN slope [.]	Blade 1 Mx	Blade 1 My	Blade 1 Mxy	Blade 1 Mz
	[Nm]	[Nm]	[Nm]	[Nm]
3	4.63E+07	2.53E+07	2.61E+07	357174
4	3.89E+07	2.22E+07	2.26E+07	305575
5	3.51E+07	2.14E+07	2.15E+07	287134
6	3.28E+07	2.13E+07	2.12E+07	280006
7	3.13E+07	2.15E+07	2.12E+07	277849
8	3.02E+07	2.18E+07	2.15E+07	278200
9	2.94E+07	2.22E+07	2.18E+07	279905
10	2.88E+07	2.27E+07	2.21E+07	282351
11	2.84E+07	2.31E+07	2.24E+07	285185
12	2.80E+07	2.35E+07	2.27E+07	288193

Table 18.- Lifetime weighted equivalent loads CENER IPC FF: blade root

Inverse SN slope [.]	Rotating hub Mx	Rotating hub My	Rotating hub Mz	Rotating hub Myz
	[Nm]	[Nm]	[Nm]	[Nm]
3	3.28E+06	3.07E+07	3.09E+07	2.14E+07
4	3.70E+06	2.59E+07	2.63E+07	1.72E+07
5	4.16E+06	2.41E+07	2.45E+07	1.55E+07
6	4.56E+06	2.34E+07	2.39E+07	1.48E+07
7	4.90E+06	2.32E+07	2.37E+07	1.45E+07
8	5.18E+06	2.34E+07	2.39E+07	1.45E+07
9	5.41E+06	2.37E+07	2.42E+07	1.45E+07
10	5.61E+06	2.41E+07	2.46E+07	1.47E+07
11	5.78E+06	2.46E+07	2.50E+07	1.49E+07
12	5.92E+06	2.51E+07	2.55E+07	1.51E+07

Table 19.- Lifetime weighted equivalent loads CENER IPC FF: hub (rotating coordinates)

Inverse SN slope [.]	Stationary hub Mx	Stationary hub My	Stationary hub Mz	Stationary hub Myz
	[Nm]	[Nm]	[Nm]	[Nm]
3	3.28E+06	3.13E+07	2.92E+07	2.14E+07
4	3.70E+06	2.62E+07	2.46E+07	1.72E+07
5	4.16E+06	2.42E+07	2.29E+07	1.55E+07
6	4.56E+06	2.35E+07	2.23E+07	1.48E+07
7	4.90E+06	2.33E+07	2.23E+07	1.45E+07
8	5.18E+06	2.34E+07	2.25E+07	1.45E+07
9	5.41E+06	2.37E+07	2.28E+07	1.45E+07
10	5.61E+06	2.41E+07	2.33E+07	1.47E+07
11	5.78E+06	2.45E+07	2.37E+07	1.49E+07
12	5.92E+06	2.50E+07	2.42E+07	1.51E+07

Table 20.- Lifetime weighted equivalent loads CENER IPC FF: hub (stationary coordinates)

Inverse SN slope [.]	Yaw bearing Mx	Yaw bearing My	Yaw bearing Mxy	Yaw bearing Mz
	[Nm]	[Nm]	[Nm]	[Nm]
3	4.46E+06	3.25E+07	1.17E+07	3.22E+07
4	4.37E+06	2.69E+07	9.96E+06	2.69E+07
5	4.67E+06	2.48E+07	9.47E+06	2.49E+07
6	5.04E+06	2.40E+07	9.46E+06	2.41E+07
7	5.37E+06	2.38E+07	9.66E+06	2.40E+07
8	5.67E+06	2.39E+07	9.97E+06	2.41E+07
9	5.92E+06	2.43E+07	1.03E+07	2.44E+07
10	6.14E+06	2.47E+07	1.07E+07	2.48E+07
11	6.33E+06	2.52E+07	1.11E+07	2.53E+07
12	6.49E+06	2.57E+07	1.14E+07	2.58E+07

Table 21.- Lifetime weighted equivalent loads CENER IPC FF: yaw bearing

Inverse SN slope [.]	Tower Mx, Location=Mbr 323 End 1.	Tower My, Location=Mbr 323 End 1.	Tower Mz, Location=Mbr 323 End 1.	Tower Myz, Location=Mbr 323 End 1.
	[Nm]	[Nm]	[Nm]	[Nm]
3	3.22E+07	2.34E+07	2.30E+07	1.17E+07
4	2.69E+07	1.94E+07	1.91E+07	9.96E+06
5	2.49E+07	1.78E+07	1.76E+07	9.47E+06
6	2.41E+07	1.72E+07	1.70E+07	9.46E+06
7	2.40E+07	1.70E+07	1.69E+07	9.66E+06
8	2.41E+07	1.71E+07	1.70E+07	9.97E+06
9	2.44E+07	1.73E+07	1.73E+07	1.03E+07
10	2.48E+07	1.75E+07	1.76E+07	1.07E+07
11	2.53E+07	1.79E+07	1.80E+07	1.11E+07
12	2.58E+07	1.82E+07	1.84E+07	1.14E+07

Table 22.- Lifetime weighted equivalent loads CENER IPC FF: tower top

Inverse SN slope [.]	Tower Mx, Location=Mbr 314 End 2.	Tower My, Location=Mbr 314 End 2.	Tower Mz, Location=Mbr 314 End 2.	Tower Myz, Location=Mbr 314 End 2.
	[Nm]	[Nm]	[Nm]	[Nm]
3	3.29E+07	7.76E+07	9.77E+07	1.10E+08
4	2.74E+07	6.88E+07	8.61E+07	9.75E+07
5	2.53E+07	6.64E+07	8.24E+07	9.41E+07
6	2.45E+07	6.62E+07	8.16E+07	9.40E+07
7	2.43E+07	6.69E+07	8.21E+07	9.52E+07
8	2.45E+07	6.80E+07	8.32E+07	9.70E+07
9	2.48E+07	6.92E+07	8.46E+07	9.89E+07
10	2.52E+07	7.04E+07	8.61E+07	1.01E+08
11	2.57E+07	7.15E+07	8.75E+07	1.03E+08
12	2.62E+07	7.26E+07	8.90E+07	1.04E+08

Table 23.- Lifetime weighted equivalent loads CENER IPC FF: tower base

Extreme Loads:

			Mx	My	Mxy	Mz	Fx	Fy	Fxy	Fz
		Load case	kNm	kNm	kNm	kNm	kN	kN	kN	kN
Mx	Max	dlc13cb1	24804	47550	53631	-64.2	969.8	-782.6	1246.2	1459.5
Mx	Min	dlc13db1	-21421	19450	28934	-96.5	363.1	743.4	827.4	1711.4
My	Max	dlc13cb1	-3002.6	51883	51970	216.6	1050.7	295.4	1091.5	1497.2
My	Min	dlc61ab_h_2_1	6882.4	-24997	25927	-114.8	-604	-80.4	609.3	-553.7
Mxy	Max	dlc13cb1	23899	48069	53682	-82.5	989	-752.3	1242.7	1455.8
Mxy	Min	dlc62j_h_1_1	-6.4	-13.2	14.6	-174	176.8	61.3	187.1	-253.2
Mz	Max	dlc13cb1	-9074	43540	44475	365.5	819.9	404.3	914.2	1693.7
Mz	Min	dlc13eb1	-7688.4	-7346.2	10634	-548.3	92.6	155.7	181.2	1204.8
Fx	Max	dlc13ab1	8706.6	49571	50330	95	1099.1	-266.4	1131	1935.4
Fx	Min	dlc61ab_h_1_1	-1791.7	-18887	18972	-28.5	-671.1	97.9	678.2	266
Fy	Max	dlc13db1	-21421	19450	28934	-96.5	363.1	743.4	827.4	1711.4
Fy	Min	dlc13cb1	24804	47550	53631	-64.2	969.8	-782.6	1246.2	1459.5
Fxy	Max	dlc13cb1	24804	47550	53631	-64.2	969.8	-782.6	1246.2	1459.5
Fxy	Min	dlc62d_l_1_1	653.4	6047.8	6083	64.8	0.64	0.54	0.84	-321.7
Fz	Max	dlc11e1	-3461	19223	19532	-93.2	486.3	119.7	500.8	2416.9
Fz	Min	dlc61ab_h_2_1	-1110	1486.4	1855.1	-126.1	-1.06	70.7	70.7	-575

Table 24.-Ultimate loads CENER IPC FF: blade root

			Mx	My	Mz	Myz	Fx	Fy	Fz	Fyz
		Load case	kNm	kNm	kNm	kNm	kN	kN	kN	kN
Mx	Max	dlc13eb1	16403	2698.1	13271	13542	909.7	1936	2108.1	2862.2
Mx	Min	dlc14ab	-7846.8	-6620.4	-349.7	6629.6	295.9	-329.2	3002.3	3020.3
My	Max	dlc13db1	14191	29954	-2016.7	30022	1365.6	2195.8	-1864	2880.3
My	Min	dlc13db1	14597	-35243	-3795.8	35447	1465	792.4	-2982.1	3085.6
Mz	Max	dlc13eb1	15489	3590.2	33457	33649	1528.8	-2324.7	-2167.6	3178.5
Mz	Min	dlc14cb	13925	16633	-33298	37221	262.7	-1819.2	-2281.5	2918
Myz	Max	dlc14cb	13931	17509	-32979	37338	268	-1619.7	-2415	2907.8
Myz	Min	dlc62d_h_1_1	-234.7	-1.09	4.59	4.72	520.8	-1300.4	1677.8	2122.7
Fx	Max	dlc21bb	14725	-1034.7	9138.6	9197	2642.3	-3058.6	-590.4	3115.1
Fx	Min	dlc23ca_2	-112.6	269.1	4846.5	4854	-1059.6	257.4	2485.6	2498.9
Fy	Max	dlc13eb1	15063	-13083	-22802	26289	1377.2	3568.5	-22.2	3568.6
Fy	Min	dlc13db1	15136	16166	4243.8	16713	1000.1	-3534.1	-739.3	3610.6
Fz	Max	dlc13eb1	13994	12001	-16518	20417	751.4	79.7	3550	3550.9
Fz	Min	dlc13db1	14767	-9818.3	17633	20182	1245.8	-380.8	-3478.1	3498.9
Fyz	Max	dlc13db1	15136	16166	4243.8	16713	1000.1	-3534.1	-739.3	3610.6
Fyz	Min	dlc62a_l_2_1	-261.9	-697.1	388.5	798.1	327.1	-930.9	-1272	1576.3

Table 25.-Ultimate loads CENER IPC FF: hub (rotating coordinates)

			Mx	My	Mz	Myz	Fx	Fy	Fz	Fyz
		Load case	kNm	kNm	kNm	kNm	kN	kN	kN	kN
Mx	Max	dlc13eb1	16403	7265.6	-11428	13542	909.7	68.7	-2861.3	2862.2
Mx	Min	dlc14ab	-7846.8	6601.8	-606.6	6629.6	295.9	-106.2	-3018.4	3020.3
My	Max	dlc14cb	14202	33453	-11378	35335	180.8	-284.5	-2979.2	2992.8
My	Min	dlc13db1	14597	-35297	3255.3	35447	1465	186.4	-3080	3085.6
Mz	Max	dlc13eb1	15215	6624.9	29379	30117	945.2	-156.4	-3096.6	3100.6
Mz	Min	dlc13eb1	14010	-5069.9	-31552	31957	1064.3	30.6	-2619	2619.2
Myz	Max	dlc14cb	13931	31505	-20040	37338	268	-216.6	-2899.8	2907.8
Myz	Min	dlc62d_h_1_1	-234.7	-2.19	-4.18	4.72	520.8	-121	-2119.3	2122.7
Fx	Max	dlc21bb	14725	-9190.5	344.6	9197	2642.3	126	-3112.6	3115.1
Fx	Min	dlc23ca_2	-112.6	196.2	-4850	4854	-1059.6	-18.2	-2498.9	2498.9
Fy	Max	dlc61ab_l_2_1	-443.1	-6439.7	-5959.2	8773.9	390	995.9	-2867	3035.1
Fy	Min	dlc61ab_h_2_1	-209.6	-6421.9	1226.7	6538	268.6	-1200.9	-2733.3	2985.4
Fz	Max	dlc62d_h_1_1	-60.1	1341.9	4279.1	4484.6	303.6	-178.5	-1566.4	1576.6
Fz	Min	dlc13db1	15136	-293.1	16711	16713	1000.1	-119.1	-3608.6	3610.6
Fyz	Max	dlc13db1	15136	-293.1	16711	16713	1000.1	-119.1	-3608.6	3610.6
Fyz	Min	dlc62a_l_2_1	-261.9	-796.4	-51.3	798.1	327.1	-92.8	-1573.5	1576.3

Table 26.-Ultimate loads CENER IPC FF: hub (stationary coordinates)

			Mx	My	Mz	Myz
		Load case	kNm	kNm	kNm	kNm
Mx	Max	dlc13db1	31525	-14428	9386.3	17213
Mx	Min	dlc13db1	-35507	-7680.1	8987.1	11822
My	Max	dlc14cb	-17590	10169	28857	30596
My	Min	dlc13db1	373.5	-36799	-16379	40280
Mz	Max	dlc14cb	-10619	9207.5	29736	31129
Mz	Min	dlc13db1	-819	-36455	-16409	39978
Myz	Max	dlc13db1	373.5	-36799	-16379	40280
Myz	Min	dlc62g_h_2_1	-1856.1	7.8	4.38	8.95

Table 27.-Ultimate loads CENER IPC FF: tower top

			Mx	My	Mz	Myz
		Load case	kNm	kNm	kNm	kNm
Mx	Max	dlc13db1	32150	47217	55193	72634
Mx	Min	dlc13db1	-36244	23930	37808	44745
My	Max	dlc61ab_l_1_1	-4506.5	171023	44097	176616
My	Min	dlc23ca_2	-5305.3	-133454	-110760	173429
Mz	Max	dlc61ab_h_1_1	8061.1	14384	221644	222110
Mz	Min	dlc61ab_l_2_1	-4931	97829	-142114	172531
Myz	Max	dlc21cd	683.7	168707	189489	253708
Myz	Min	dlc13bb1	-837	2	-26.2	26.2

Table 28.-Ultimate loads CENER IPC FF: tower base

Appendix 3 Power Adjusting Controller PAC Variables

Variable Name	Variable Symbol	Variable Value
System Inertia	J_{PAC}	101370
System Damping	B_{PAC}	1460
Proportional Gain	K_P	0.05
Integral Gain	K_I	0.025

Appendix 4 Power Adjusting Controller PAC supervisory rules

The PAC supervisory rules are implemented in the PAC to ensure that the turbine is kept in a safe operating regime. The occurrence of events triggered by these rules is communicated between the PAC and wind farm controller using flags residing in the PAC. (Capital letters are used to indicate flag names with sub-flags in bracketed italics) There are two sets of rules, black rules defined by a boundary on the torque/speed plane that act as a hard limit and traffic light rules, defined by two concentric boundaries contained within the black rules boundary, that act as soft limits. Maximum aerodynamic and drive-train torque boundaries apply. The regions inside the inner traffic light boundary, between the inner and outer traffic light boundaries and outside the outer traffic light boundary are designated green, amber and red, respectively.

General supervisory rules:

- The requested change in power, rate of change in power and pitch rates are subject to limits and the permissible turbulence intensity and wind speed are subject to upper and lower limits, respectively. These limits and events designated high priority, e.g. requests for synthetic inertia, are defined with agreement and cannot be changed without agreement of the OEM.
- The PAC is turned on when the PAC ON flag is set at a request from the wind farm controller.
- The PAC is turned off when the PAC ON flag is reset by either the PAC itself or by the PAC at a request from the wind farm controller. The PAC goes into recovery mode and the RECOVERY flag is set. The speed of recovery is fast or slow depending on the setting of the RECOVERY (*Fast/Slow*) flag and sub-flag. The sub-flag (*Fast/Slow*) can be reset at the request of the wind farm controller. The default setting is RECOVERY (*Fast*). During the recovery mode the PAC rejects any requested change in power. The REJECTION (*Recovery*) flag is set by the PAC. On completion of recovery mode the RECOVERY (*Complete*) flag and sub-flag are set and the PAC ON flag is reset.
- Only black supervisory rules apply to high priority events. The PRIORITY flag is set by the PAC at a request from the wind farm controller.
- If the limit for requested change in power is exceeded, the REJECTION (*Power*) flag is set by the PAC.

- If the limit for requested change of power rate limit is exceeded and the PRIORITY flag is not set, the rate limit applies and the REJECTION (*Power rate*) flag is set by the PAC.
- If the turbulence intensity limit is exceeded, the PAC ON flag is reset and latched and the PAC ON (*Turbulence*) sub-flag is set and latched by the PAC.
- If the actuator pitch rate limits are violated by the turbine full envelope controller, the PAC ON flag is reset indefinitely and the PAC ON (*Actuator*) sub-flag set indefinitely by the PAC.
- If the low wind speed limit is exceeded, the PAC ON flag is reset and latched and the PACON (*Wind Speed*) sub-flag is set and latched by the PAC.
- If the turbine state is divergent such that normal operation is unreachable, the DIVERGENT flag is set by the PAC.

Black supervisory rules:

- The boundary and maximum possible generator reaction torque are set with agreement and cannot be changed without agreement of the OEM.
- The boundary should not be crossed under any circumstances. If the turbine state is outside the boundary the PAC ON flag is reset by the PAC.
- On the turbine state reaching the boundary, the REJECTION (*Limit*) flag and sub-flag are set by the PAC.
- If the turbine state remains on the boundary beyond a pre-set time limit, the PAC ON flag is reset by the PAC.
- On a section of the boundary corresponding to the maximum possible generator reaction torque, the permitted time limit before resetting the PAC ON flag is zero.

Traffic light supervisory rules:

- The boundaries can be set at a request from wind farm controller.
- The maximum magnitude of change of power in all regions can be set by the wind farm controller subject to the fixed upper limit, the maximum magnitude for the amber region being less than the maximum for the green region and the maximum/minimum change of power for that part of the red region to the left/right of the operating strategy being zero.
- When the turbine state is in the green/amber/red region, the corresponding GREEN/AMBER/RED flag is set by the PAC.
- When the demanded change in power exceeds the maximum or minimum, the corresponding REJECTION (*Green Limit*)/(*Amber Limit*)/(*Red Limit*) flag and sub-flag are set by the PAC.

Appendix 5 Multi Rotor Spar floater design

Inputs	Symbol	Value	Unit
Ballast Mass	Mb	42,500,000.00	kilograms
Radius of cylinder	Rs	15.00	metres
Thickness of wall	ts	0.06	metres
Outputs	**Symbol**	**Value**	**Unit**
Length of Ballast	Lb	22.27	metres
Length of Cylinder	Ls	65.03	metres
Length of whole thing	Ltot	87.30	metres
Angle	theta	3.49	degrees
Total Inertia	Jtot	66586915473	kilogram metres squared
Constants	**Symbol**	**Value**	**Unit**
Weight of MRS	Wmrs	34,000,000.00	Newtons
Height of MRS CoM	Hmrs	98.00	metres
Assumed Thrust	T	6,400,000.00	Newtons
Centre of Thrust	Ht	131.00	metres
Density of Steel	rhofe	7,850.00	kilograms per metre cubed
g	g	9.81	metres per second per second
Density of Ballast	rhob	2,700.00	kilograms per metre cubed
Density of water	rhod	1,000.00	kilograms per metre cubed
Calculated Variables	**Symbol**	**Value**	**Unit**
Mass of MRS	**Mmrs**	**3,465,851.17**	**kilograms**
Ballast Weight	**Wb**	**416,925,000.00**	**Newtons**
Weight of Floater	**Ws**	**434,601.86**	**Newtons**
Buoyancy	**Wtot**	**451,403,903.79**	**Newtons**
Total Mass	**Mtot**	**46,010,153.10**	**kilograms**
Total CoM	**Hmtot**	**-63.00**	**metres**
Volume for buoyancy	**Vs**	**45,965.85**	**cubic metres**

Area of Cylinder cross section	As	706.86	square metres
Mass of Floater	Ms	44,301.92	kilograms
Floater CoM	Hms	-32.51	metres
Floater CoB	Hbs	-32.51	metres
Ballast CoM	Hb	-76.16	metres
Volume of Ballast	Vb	15,740.74	cubic metres
Radius of Ballast	Rb	15.00	metres
Cross sectional area of Ballast	Ab	706.86	square metres
Inertia of multi-rotor	Jmrs	45269607881	kilogram metres squared
Volume of solid cylinder for ballast part of spar	Vbc	15740.74074	cubic metres
Volume of ballast for ballast part of spar	Vba	15615.06667	cubic metres
Mass of solid cylinder for ballast part of spar	Mbc	123564814.8	kilograms
Mass of steel removed to make cylinder (Ballast)	Mbs	122578273.3	kilograms
length of A	Lca	24.29564403	metres
length of B	Lcb	63.00132596	metres
Volume cylinder A	Vca	17173.57878	cubic metres
Mass cylinder A	Mca	134812593.4	kilograms
Mass cylinder B	Mcb	349584153.1	kilograms
Mass of Steel removed from A	Mcar	133736249.7	kilograms
Mass of steel removed from B	Mcbr	346793073.2	kilograms
Mass of A	Mca2	1076343.746	kilograms
Mass of B	Mcb2	2791079.878	kilograms
Inertia of cylinder A	Jca	332386077.8	kilogram metres squared
Inertia of cylinder B	Jcb	4005497129	kilogram metres squared
Total inertia of buoyant spar	Jbs	4337883207	kilogram metres squared
Inertia of Ballast	Jb2	35064111281	kilogram metres squared
Inertia of MRS	Jmrs2	59026150233	kilogram metres squared
New Total Inertia	Jtot2	66586915473	kilogram metres squared
Inertia of water	Jw	3222882033	kilogram metres

			squared
Mass of Ballast	Mba	42160680	kilograms